

The Absorption and Emission of Neutral Hydrogen around High-Redshift Star-Forming Galaxies

Thesis by
Yuguang Chen

In Partial Fulfillment of the Requirements for the
Degree of
Doctor of Philosophy

The logo for the California Institute of Technology (Caltech), featuring the word "Caltech" in a bold, orange, sans-serif font.

CALIFORNIA INSTITUTE OF TECHNOLOGY
Pasadena, California

2022
Defended August 2, 2021

© 2022

Yuguang Chen

ORCID: 0000-0003-4520-5395

All rights reserved

To those who look up and wonder

ACKNOWLEDGEMENTS

I have been longing to write this part of my thesis, but actually laying down the words proved to be an incredibly difficult task. From a kid who was greatly attracted to the night sky to an astronomer, I owe great debt to so many wonderful people during this journey.

First and foremost, I am very grateful to my advisor, Chuck Steidel. Without his wisdom and selflessness, this thesis would never have been possible. When we had different opinions, or when I wrote something for him to read, I am afraid that I have caused many head-scratching moments for him. But this never stopped him from allowing me to explore the KBSS survey as much as I could, and from giving me an incredible amount of help when I needed it. He also entrusted me to play a major role in organizing and observing for the KBSS-KCWI survey, which is and will continue to be one of the most important surveys in the field in the years to come. Since he is never shy of sharing his experiences and knowledge, our discussions are always valuable and inspiring.

I would like to acknowledge all my thesis committee members: Evan Kirby, Phil Hopkins, Chris Martin, and Dimitri Mawet. They all helped me in many ways, not just academically, during my time at Caltech. I would also like to acknowledge Lynne Hillenbrand and Richard Ellis, whom I knew before I even came here, and they often checked on my progress and well-being ever since. I also would like to acknowledge my collaborators who have helped me significantly, including Cameron Hummels, Gwen Rudie, Allison Strom, Ryan Trainor, David Law, Rachel This, Dawn Erb, and Donal O'Sullivan. I would also like to thank the staff members of the Keck Observatory for their hard work, without which this thesis would not exist.

I would like to acknowledge all the friends I made here at Caltech over the years. Especially, I am grateful to Ivanna Escala, Anna Ho, Bhawna Motwani, and Kaew Tinyanont. Being in the same year, we shared this great journey together, and I could never have asked for a better match. I would like to acknowledge Cameron Hummels. We had great moments collaborating on research and outreach. I thank Quanzhi Ye, Zheng Cai, Yiqiu Ma, Suoqing Ji, Lile Wang, Fei Dai, Shibo Shu, Bin Ren, and all astro grads at Caltech for their friendship.

Through my journey, I am thankful to all the teachers who have taught me before. I am especially grateful to Qiao Junying, my first astronomy teacher in high school.

Without her, I would have never found the right path to become an astronomer. I would like to acknowledge my other astronomy teachers, including Dong Ruiling and Lu Mingyu, and my physics teachers, including Xiong Wen and Zhang Liguo. I am grateful to Greg Herczeg, my first research advisor at Peking University. He taught me the many principles of how to be a good researcher, and advised me on life-changing decisions. I also would like to acknowledge Luis Ho, Xiaohui Fan, and Xue-Bing Wu, who helped me during my years as an undergraduate student.

Before 2020, I had never expected that our lives could be so dramatically affected by a global health crisis. Yet during my last year as a graduate student, humanity has been stricken hard by the COVID-19 pandemic. As we start to see the light at the end of the tunnel, I would like to thank everyone who has helped fight this pandemic.

Finally, I would like to thank my family. I am grateful to my parents, Wang Xiaoshen and Chen Bingqin, and my fiancée, Hongjie Zhu, for their tremendous and unreserved support. I also thank my grandparents, aunts, uncles, and cousins for their inspiration and encouragement. Among them, Chen Xiaoyan, Wang Xiaojing, Chen Xiufang, and Xie Junlai had made huge contributions to my upbringing.

ABSTRACT

The circumgalactic medium (CGM) mediates the interaction between galaxies and their surrounding gas, and ultimately controls the evolutionary trajectory of its host galaxies. Among the CGM gas, neutral hydrogen (H I) constitutes an important component observationally. This thesis focuses on characterizing the circumgalactic H I around $z = 2\text{--}3$ star-forming galaxies using absorption and emission techniques in the Keck Baryonic Structure Survey (KBSS) fields.

Chapter 2 provides a new statistical measurement of the distribution and kinematics of H I in the CGM using Lyman-alpha ($\text{Ly}\alpha$) absorption signatures. We constructed the KBSS Galaxy Pair Sample (KGPS), which contains $> 200,000$ distinctive foreground-background galaxy pairs with projected distances of 0.02–4 Mpc. We compared the observed H I absorption map with a cosmological zoom-in simulation, and found qualitative agreement. Furthermore, using an analytic model, we show that the observed H I distribution can be explained by a combination of outflow, accretion, and Hubble expansion.

Chapters 3 and 4 explore the $\text{Ly}\alpha$ emission, one of the strongest spectral features of H I, from the spatially resolved spectroscopy, by using the new high-sensitivity integral field unit, Keck Cosmic Web Imager (KCWI). We introduce the use of “cylindrically projected 2D (CP2D) spectra,” which map the average $\text{Ly}\alpha$ spectral profile over a specified range of azimuthal angle, as a function of impact parameter, around galaxies. We find that the averaged CP2D spectrum is most consistent with the expected signatures of $\text{Ly}\alpha$ resonant scattering through outflowing gas.

Furthermore, Chapter 3 investigates the statistical relation between $\text{Ly}\alpha$ emission and its orientation relative to the galaxy major axis for 59 galaxies that have been observed with both KCWI and high-spatial-resolution imaging instruments. We find that the extended $\text{Ly}\alpha$ emission along the galaxy projected major and minor axes are statistically indistinguishable at projected distance $\lesssim 30$ physical kpc, indicating that resonant scattering of $\text{Ly}\alpha$ by outflowing H I occurs in a statistically uniform halo, independent of galaxy orientation.

Chapter 4 provides ongoing research on the connection between $\text{Ly}\alpha$ emission in the CGM and the host galaxy properties. Our preliminary result from 110 star-forming galaxies at $z \approx 2\text{--}3$ demonstrates that the host galaxy affects the production and escape of $\text{Ly}\alpha$ emission at $\lesssim 15$ kpc as expected. However, the faint envelopes of

$\text{Ly}\alpha$ emission reach to similar spatial distances ($\gtrsim 30$ kpc) regardless of their host galaxies.

Finally, we document the standard data reduction procedure and data products of the KBSS-KCWI survey in Appendix A.

PUBLISHED CONTENT AND CONTRIBUTIONS

Chen, Yuguang et al. (Dec. 2020). “The Keck Baryonic Structure Survey: Using foreground/background galaxy pairs to trace the structure and kinematics of circumgalactic neutral hydrogen at $z \sim 2$ ”. *MNRAS* 499.2, pp. 1721–1746. DOI: 10.1093/mnras/staa2808. arXiv: 2006.13236 [astro-ph.GA].

Y.C. participated in the conception of this project, conducted part of the observations, organized the data, developed analysis software, and wrote the manuscript.

Chen, Yuguang et al. (Apr. 2021). “The KBSS-KCWI Survey: The connection between extended $\text{Ly}\alpha$ halos and galaxy azimuthal angle at $z \sim 2-3$ ”, arXiv:2104.10173. (in press with MNRAS), arXiv:2104.10173. arXiv: 2104.10173 [astro-ph.GA].

Y.C. participated in the conception of this project, conducted the observations, reduced and organized the data, developed analysis software, and wrote the manuscript.

TABLE OF CONTENTS

Acknowledgements	iv
Abstract	vi
Published Content and Contributions	viii
Table of Contents	viii
List of Illustrations	x
List of Tables	xxvi
Chapter I: Introduction	1
1.1 The Circumgalactic Medium	2
1.2 $\text{Ly}\alpha$ in the Circumgalactic Medium	5
1.3 This Thesis	6
Chapter II: The Keck Baryonic Structure Survey: Using foreground/background galaxy pairs to trace the structure and kinematics of circumgalactic neutral hydrogen at $z \sim 2$	13
2.1 Introduction	14
2.2 Sample and Analysis	18
2.3 HI Absorption	31
2.4 Discussion	39
2.5 Summary	64
Chapter III: The KBSS-KCWI Survey: The connection between extended $\text{Ly}\alpha$ halos and galaxy azimuthal angle at $z \sim 2-3$	82
3.1 Introduction	83
3.2 The KBSS-KCWI Galaxy Sample	88
3.3 Observations and Reductions	92
3.4 Galaxy Azimuthal Angle	101
3.5 Analyses	113
3.6 Integrated Line Flux and Azimuthal Asymmetry	126
3.7 Finer Division of Galaxy Azimuthal Angles	130
3.8 Discussion	131
3.9 Summary	136
Chapter IV: Circumgalactic $\text{Ly}\alpha$ Emission and Its Host Galaxies	150
4.1 Continuum Subtraction	150
4.2 The Average $\text{Ly}\alpha$ Emission	153
4.3 $\text{Ly}\alpha$ CP2D Spectrum and the Host Galaxies	159
4.4 Looking Forward	160
Chapter V: Conclusion	172
Appendix A: The Standard KBSS-KCWI Reduction Procedure	176
A.1 Level 1: Improved Data Reduction Pipeline	176
A.2 Level 2: Stacked Data Cube for Each Pointing	179
A.3 Level 3: Extracting Signal	182

LIST OF ILLUSTRATIONS

<i>Number</i>	<i>Page</i>
1.1 A schematic diagram of the circumgalactic medium (from Tumlinson, Peebles, and Werk, 2017). The CGM gas normally consists of outflow, inflow, and recycled gas, with a large range of physical conditions.	3
2.1 Randomly-selected examples of individual rest-UV spectra of background galaxies in KGPS. Wavelengths are in the observed frame, with red triangles marking the position of Ly α λ 1215.67 at wavelengths $1215.67(1+z_{\text{fg}})$ Å for each foreground galaxy with projected distance $D_{\text{tran}} \leq 500$ pkpc. The solid (open) triangles correspond to foreground galaxies whose systemic redshifts are based on z_{neb} (z_{UV}). Their typical redshift uncertainties, in terms of observed wavelength, are ~ 0.2 Å (1.8 Å) at $z = 2.2$ as estimated in §2.2. The y-coordinate of each triangle indicates D_{tran} for the foreground galaxies, with reference to the scale marked on the righthand side of each plot. The light shaded regions are those that would be masked prior to using the spectrum to form composites stacked in the rest frame of foreground galaxies (see §2.2 & Table 2.2), to minimise contamination by spectral features at $z = z_{\text{bg}}$. The yellow vertical lines indicate UV absorption lines arising in the ISM of the background galaxy. Note that some foreground galaxies have clear counterparts in the Ly α forest, even in low-resolution spectra.	22
2.2 Distribution of velocity differences between $z_{\text{Ly}\alpha}$ ($\Delta v_{\text{Ly}\alpha}$, in red) or z_{IS} (Δv_{IS} , in blue) and the systemic redshift measured from z_{neb} . Top-right of each panel shows the median shift in velocity and its error estimated by dividing the standard deviation by the square-root of the number of galaxies. These distributions have been used to calibrate the systemic redshifts of galaxies in Equations 2.1–2.3, for which only the UV spectral features are available.	24

- 2.3 The cumulative number of pairs as a function of impact parameter $D_{\text{tran}}(z_{\text{fg}})$ for the KGPS-Full sample (green), the KGPS- z_{neb} sample (yellow). The solid curves are the actual number of pairs, and the dashed-dotted lines are quadratic fits over the range $50 \text{ pkpc} < D_{\text{tran}} < 500 \text{ pkpc}$ for each of the KGPS samples. The smaller number of pairs (relative to the quadratic extrapolation) at very small D_{tran} results from observational biases caused by geometrical slit-mask constraints and finite angular resolution of the ground-based images used for target selection. At large D_{tran} , the pair count falls below the quadratic fit as the angular separation approaches the size of the KBSS survey regions. 26
- 2.4 Distribution of z_{fg} (top) and $\Delta z_{\text{fb}}/(1 + z_{\text{fg}})$ (bottom) for foreground-background galaxy pairs with $D_{\text{tran}} < 4.7 \text{ pMpc}$. The vertical lines mark the median values of each distribution. The KGPS-Full and KGPS- z_{neb} samples have similar distributions of both z_{fg} and $\Delta z_{\text{fb}}/(1 + z_{\text{fg}})$ 28
- 2.5 Example composite spectra near $\text{Ly}\alpha$ in the rest frame of foreground galaxies for four different bins of D_{tran} . The left panel shows the spectra before continuum-normalization. The black curves with dots are the fitted continua and spline points used for cubic interpolation. The legend indicates the range in pkpc for the bin in D_{tran} . The right-hand panel shows normalized spectra near $\text{Ly}\alpha$, along with their 1σ uncertainty (shaded histogram). In both panels, the spectra shown have been shifted relative to one another by 0.5 in y for display purposes. The vertical dashed line is the rest wavelength of $\text{Ly}\alpha$, 1215.67 \AA . The $\text{Ly}\alpha$ absorption profiles in the composite spectra clearly vary in both depth and width with D_{tran} . The clear asymmetry in the velocity profiles of the two middle spectra ([50-100] and [160-319] pkpc) is discussed in §2.4 below. 31

- 2.6 $W_\lambda(\text{Ly}\alpha)$ as a function of D_{tran} measured from the KGPS-Full sample. Each black dot (connected with the solid line segments) is a measurement made from a composite spectrum in a bin spanning a factor of 2 in D_{tran} where the point marks the geometric mean D_{tran} within the bin. The light blue shaded region represents the $\pm 1\sigma$ uncertainty based on bootstrap resampling of the spectra comprising each composite in each bin. The single dot with error bars below the legend box shows the bin size used to make composite spectra; i.e., the bins were evaluated at intervals smaller than the bin size, thus adjacent points on smaller than the bin size are correlated. The purple dash-dotted line is the best single-power-law fit to the $W_\lambda(\text{Ly}\alpha)$ - D_{tran} relation, with slope $\beta = -0.40 \pm 0.01$. The new measurements are compared with Steidel et al. (2010, brown squares) and Turner et al. (2014, magenta diamonds), where the latter are based on HIRES QSO/galaxy pairs in KBSS. 34
- 2.7 The line-of-sight velocity structure of HI absorbers around foreground galaxies. Each column of pixels in each plot corresponds to a measurement of $\tau_{\text{ap}}(v_{\text{LOS}})$ evaluated from the corresponding composite spectrum in the bin of D_{tran} made from the KGPS-Full sample (left) and the KGPS- z_{neb} sample (right). The black dots with horizontal error bars show the range of D_{tran} used to make each column of the map; the effective velocity resolution of the map is shown as a vertical error bar. Solid contours correspond to positive optical depth τ_{ap} , with dotted contours indicating negative values, which are consistent with the $1\text{-}\sigma$ uncertainties. The contour levels are separated by $\Delta\tau_{\text{ap}} = 0.1$ 36
- 2.8 Maps of τ_{ap} with the blue and red sides folded to increase the signal-to-noise ratio. The three maps are (top to bottom): $\tau_{\text{ap}}(|v_{\text{los}}|, D_{\text{tran}})$, $\tau_{\text{ap}} \times D_{\text{tran}}^{0.4}$ (to better illustrate the structure at large D_{tran}), and the map of the SNR per \AA of the τ_{ap} measurement. The contour decrements are 0.1 for the τ_{ap} map, 0.02 for the $\tau_{\text{ap}} \times D_{\text{tran}}^{0.4}$ map, and 3 for the SNR map. The half-aperture in which the $W_\lambda(\text{Ly}\alpha)$ is measured in §2.3 is shown as the orange dashed line in the SNR map. 37
- 2.9 Same as the top plot of Figure 2.8, but for the KGPS- z_{neb} sample. . . 38

- 2.10 Maps of $dN_{\text{HI}}/dv_{\text{LOS}}$ in the FIRE-2 simulation (h350), as seen by an observer, projected onto the $v_{\text{LOS}}-D_{\text{tran}}$ plane. *Left:* Snapshots from a single time step ($z = 2.20$) as viewed from two orthogonal viewing angles. *Right:* The median-stack of 22 such maps: 11 time steps at intervals of $\delta z = 0.05$ for $2.0 \leq z \leq 2.4$ from each of two orthogonal viewing angles. Contours based on the observed map of τ_{ap} for the KGPS-Full sample (Figure 2.8) are overlaid for comparison. Note that the D_{tran} -axis has been zoomed in from that of Figure 2.8 because of the limited size (a few times r_{vir}) of the high-resolution zoom-in region of the FIRE-2 simulation. 40
- 2.11 The galactocentric radial velocity versus galactocentric radius for neutral hydrogen in the same $z = 2.20$ snapshot as shown in the lefthand panels of Figure 2.10. Positive and negative values indicate net outward and net inward radial motion, respectively. The vertical strips are due to the outflow of the satellite galaxies. The colorbar represents the total HI mass in each pixel. The gradual decrease of HI content beyond 500 pkpc is artificial because of the limited volume within which the gas simulation is conducted. 42
- 2.12 A cartoon illustration of the parametrization of the analytic model described in §2.4. The model comprises of two isotropic, non-interacting, purely radial components: “outflow” (red) and “inflow” (blue). Each component has free parameters describing its radial velocity profile $v(r)$ and apparent absorption coefficient $\alpha_{\text{ap}}(r)$ (defined in Equations 2.14, 2.15, and 2.16). The outflow component is truncated at the point that it slows to $v_{\text{out}} = 0$ 45
- 2.13 The best-fit radial profiles of v_r and α_{ap} as functions of galactocentric radius (i.e., before projection to the observed $v_{\text{LOS}} - D_{\text{tran}}$ plane). The model parameters are as in Table 2.3. The red curves correspond to the outflow component and blue curves to the inflow. The best-fit model for the KGPS-Full sample is shown with solid lines, while the best-fit model for the KGPS- z_{neb} is shown with dashed lines. 48

- 2.14 Comparison of the observed KGPS-Full map (left) with the best-fit model (middle). The right-most plots are residuals after subtraction of the model from the observed map. The top panel shows τ_{ap} as a function of D_{tran} and v_{LOS} , while the bottom panel shows τ_{ap} multiplied by $D_{\text{tran}}^{0.4}$. The colorbars and contour levels are identical to those shown in Figure 2.8. 49
- 2.15 The best fitting parametrizations of alternative models, to be compared with that of the fiducial model shown in Figure 2.14. Both maps show the quantity $\tau_{\text{ap}} \times D_{\text{tran}}^{-0.4}$, as in the bottom panels of Figure 2.14. (*Top:*) Same as fiducial, but with the outflow velocity $v_{\text{out}}(r)$ as power law. (*Bottom:*) A (ballistic) outflow-only model that eliminates the infall component completely. The power law model fits the data similarly to the fiducial; the outflow-only model is a poor fit. 52
- 2.16 Same as the $\tau_{\text{ap}} \times D_{\text{tran}}^{0.4}$ map in Figure 2.8, except that instead of averaging the blue and red sides, the left (right) map is the *subtraction* of the blue (red) side from the red (blue) side. Significant asymmetry can be seen at $D_{\text{tran}} \simeq 100$ pkpc. Again, the solid (dotted) contours represent positive (negative) values. The excess blueshifted absorption at $D_{\text{tran}} \lesssim 50$ pkpc could be due to sample variation, while the excess redshifted absorption with $D_{\text{tran}} = 50 - 200$ pkpc is likely real. 55
- 2.17 Expected contribution to $W_{\lambda}(\text{Ly}\alpha)$ by $\text{Ly}\alpha$ emission surrounding foreground galaxies (red), compared to the observed $W_{\lambda}(\text{Ly}\alpha)$ in absorption (black, same as in Figure 2.6). The dashed magenta curve shows the absorption after correction for the estimated contribution from emission filling. The yellow dashed curve shows the fraction of $W_{\lambda}(\text{Ly}\alpha)$ contributed by asymmetry, calculated by integrating the blue/red halves of the absorption profiles spectra within $|\Delta v_{\text{LOS}}| < 700 \text{ km s}^{-1}$ and subtracting one from the other. 58
- 2.18 Same as the τ_{ap} map in Figure 2.8, with the radial dependence of the escape velocity (v_{esc} , red dashed) and circular velocity (v_{circ} , green dash-dotted) for an NFW halo with $M_{\text{h}} = 10^{12} M_{\odot}$ superposed (assuming that D_{tran} is equivalent to the galactocentric distance r .) 60

2.19 Same as the top-left plot of Figure 2.8, except here the y-axis has been converted to line-of-sight distance assuming that v_{LOS} is entirely due to Hubble expansion. The two axes have been adjusted so that any departures from symmetry indicate the presence of peculiar motions of gas with respect to the Hubble flow. The red vertical dashed lines and black horizontal dashed lines correspond to the locations of extracted profiles in Figure 2.20. 61

2.20 Comparison of the extracted τ_{ap} profiles (see Figure 2.19) in the D_{tran} (black) and D_{LOS} (red) directions. Numbers on the top-right corner of the plots are the distances in pkpc to the center of the galaxy in the direction orthogonal to that over which the profile is extracted. 62

2.21 The impact of different stacking methods on $W_{\lambda}(\text{Ly}\alpha)$ measurements: each panel shows $W_{\lambda}(\text{Ly}\alpha)(\text{top})$; the SNR of $W_{\lambda}(\text{Ly}\alpha)(\text{middle})$; the SNR of the continuum near $\text{Ly}\alpha(\text{bottom})$. The 3 panels (left to right) show the results for sigma clipping, *iterative* sigma clipping, and min-max rejection. For min-max rejection, the x-axis shows the fraction of data points rejected from each side of the sample distribution. Within each panel, the black filled points correspond to a sample with $(D_{\text{tran}}/\text{pkpc}) \leq 100$ and the skeletal boxes to a sample with $500 \leq (D_{\text{tran}}/\text{pkpc}) \leq 550$; the horizontal red lines show the corresponding values for a median stack with no other rejection algorithm applied. 68

2.22 Width of the Gaussian kernel (σ_{Δ}) used in convolution to match the line profile of C II $\lambda 1334$, between stacks with pure 600/4000 spectra and ones with a fraction of the 400/3400 grism spectra (f_{400}). The red line is the best-fit model using Equation 2.25. 70

2.23 Spectroscopic resolution for 400/3400 and 600/4000 grisms plotted as 1- σ error in velocity space. *Top*: Absolute value estimated from arc spectra with 1.2-arcsec slit width. *Bottom*: Ratio between σ_{400} and σ_{600} , which remains unchanged with varying object size in slits. 71

2.24 Similar to Figure 2.22, but the x-axis is the fraction of objects in the stacks whose z_{sys} is determined using rest-UV spectral features (f_{zuv}). The red curve is the best-fit of Equation 2.23, and the blue line is a simple linear fit. 72

- 3.1 Redshift distribution of the galaxy sample. The blue histogram represents the full sample of 59 galaxies. The orange histogram shows the distribution for the 38 galaxies with nebular redshift measurements from MOSFIRE near-IR spectra, while the rest are calibrated based on Chen et al. (2020b) using rest-UV absorption lines or Ly α emission from Keck/LRIS and/or KCWI spectra. The mean (median) redshift of the full sample is 2.42 (2.29). 90
- 3.2 Distribution of SFR and M_* of 56/59 galaxies in this sample; the remaining 3 galaxies have insufficient photometric measurements for reliable SED fitting. The normalized distributions of the parent KBSS sample are shown in the orange 1-D histograms. The SFR and M_* of galaxies used in this work are similar to those of the parent KBSS sample; the values are all based on the BPASS-v2.2-binary spectral synthesis models (Stanway and Eldridge, 2018), assuming stellar metallicity $Z = 0.002$, SMC extinction as described by Theios et al. (2019), and a Chabrier (2003) stellar initial mass function. . . . 91
- 3.3 Distribution of $W_\lambda(\text{Ly}\alpha)$ for the sample (blue histogram). The orange skeletal histogram shows the normalized $W_\lambda(\text{Ly}\alpha)$ distribution from Reddy and Steidel (2009), which is a subset of the current KBSS sample large enough to be representative. The sample discussed in this work is slightly biased toward Ly α -emitting galaxies compared to the parent sample of $z \sim 2 - 3$ KBSS galaxies. 92
- 3.4 A schematic diagram of how the galaxy azimuthal angle (ϕ) is defined in this work and how it might be related to the origin and kinematics of gas in the CGM under common assumptions of a bi-conical outflow with accretion along the disk plane. Suppose that we are viewing a galaxy projected on the sky in this diagram, naively, one would expect to see inflow aligning with the projected galaxy major axis, and outflow aligning with the minor axis. Impact parameter, D_{tran} is defined as the projected distance from the center of the galaxy. The galaxy azimuthal angle, ϕ is defined as the projected angle on the sky with respect to the center of the galaxy, and starts from the projected galaxy major axis. 101

- 3.5 HST images of the 35 galaxies whose PA_0 were determined from Methods i and ii. For each image, shown in the four corners, from top-left in clockwise direction, are the KBSS identifier, the FWHM of PSF, redshift, and the instrument and filter that the image was taken with. The dashed red line, dash-dotted yellow line, and the solid white line indicate the direction of PA_0 measured from GALFIT, pixel moment, and the average between the two. 104
- 3.6 Same as Figure 3.5, except that the galaxies do not have a clear central SB peak. Therefore, their PA_0 were determined only from the pixel moment (white solid line). 105
- 3.7 Similar to Figure 3.5, showing the PA_0 of galaxies with both Keck/OSIRIS $H\alpha$ maps from Law et al. (2009) and HST continuum images. For each panel, the left image shows the OSIRIS $H\alpha$ map, in which the cyan dashed line is PA_0 measured from this map using second pixel moment. The right image shows the HST image, where the red dashed line and the yellow dash-dotted line show the PA_0 measured from GALFIT fitting and second moment from this image when present. The white solid lines are the final PA_0 determined for each galaxy by averaging the OSIRIS and HST measurements¹. 106
- 3.8 *Left:* HST WFC3-F160W image of Q2343-BX442. *Right:* $H\alpha$ velocity map of Q2343-BX442 by Law et al. (2012c). The PA_0 (white solid line) is defined to be perpendicular to its rotational axis. 106
- 3.9 Comparison of PA_0 values measured using different methods. Blue points compare methods (i) and (ii), while orange points compare methods (i) and (iii). The overall RMS = 11.4 deg. 110
- 3.10 The kernel density estimate (KDE; blue shaded region) of PA_0 for the galaxy sample, normalized so that a uniform distribution would have a constant KDE = 1. The KDE was constructed using Gaussian kernels of fixed $\sigma = 10^\circ$, corresponding to an opening angle represented by the black block at the top-right. The orange solid lines indicate the values of PA_0 for the individual galaxies. There is an apparent excess in the KDE of galaxies with $PA_0 \simeq 10 - 40^\circ$, which we attribute to sample variance. 110

- 3.11 (a) Histogram of the relative contribution of measurements made at different slicer azimuthal angles (ϕ_{slicer}) in units of total exposure time. The distribution of ϕ_{slicer} is relatively uniform, with a small excess near $\phi_{\text{slicer}} \sim 10^\circ$. (b) Stacks of the galaxy continuum images for which the major and minor axes of each galaxy were aligned with the X and Y axes prior to averaging. Each panel shows (i) the pseudo-narrow-band image (rest frame $1230 \pm 6 \text{ \AA}$) of the KCWI galaxy continuum, (ii) the stacked HST continuum image, after aligning the principal axes in the same way, (iii) the HST image convolved with a Gaussian kernel of $\text{FWHM} = 1''.02$ to match the KCWI continuum, (iv) the residual between the KCWI continuum and the HST image convolved with the KCWI PSF, (v) a 2D circular Gaussian profile with $\text{FWHM} = 1.21 \text{ arcsec}$ as the best symmetric Gaussian profile from a direct fit of the KCWI continuum image, and (vi) the residual between the KCWI continuum and the model in (v) isotropic Gaussian profile. The color map of (i), (ii), (iii), and (v) is in log scale, with linear red contours in the decrement of 0.17. The color map of (iv) and (vi) is in linear scale. The residual map in panel (vi) shows a clear dipole residual in the Y (minor axis) direction that is not present in (iv). The RMS values in panels (iv) and (vi) were calculated within $|\Delta x| < 1 \text{ arcsec}$ and $|\Delta y| < 1 \text{ arcsec}$ to reflect the dipole residual. The “boxiness” of the KCWI stack is likely due to the undersampling of KCWI in the spatial direction. Taken together, (b) demonstrates that the KCWI PSF is axisymmetric (with $\text{FWHM} = 1''.02$), and that the KCWI continuum image is capable of distinguishing the galaxy major and minor axes. 112
- 3.12 Stacked images of the galaxy continuum (*Left*) and the continuum-subtracted $\text{Ly}\alpha$ emission (*Right*) with the X- and Y-axes aligned with the galaxy major and minor axes, respectively. The color coding is on a log scale, while the contours are linear. The intensity scales have been normalized to have the same peak surface brightness intensity at the center. The $\text{Ly}\alpha$ emission is more extended than the continuum emission. 113

- 3.13 *Top panel:* The average Ly α surface brightness profile of the continuum-subtracted composite Ly α image shown the righthand panel of Figure 3.12. Red points represent the median surface brightness evaluated over all azimuthal angles ($0^\circ < \phi \leq 90^\circ$) as a function of projected distance from the galaxy center. Orange and purple curves show the profiles evaluated over $0^\circ < \phi \leq 45^\circ$ (major axis) and $45^\circ < \phi < 90^\circ$ (minor axis) azimuthal angles. Dashed cyan curve shows the best-fit profile of the two-component exponential model. Dotted cyan curves show the two component separately. The grey profile shows the normalized continuum for comparison. *Bottom:* The residual surface brightness profile formed by subtracting the all-azimuth average from the major and minor axis profiles. The residuals are consistent with zero aside from a marginally-significant difference at $\theta_{\text{tran}} < 1''0$, where the the Ly α emission is slightly stronger along the major axis. Unless otherwise noted, the conversion between θ_{tran} and D_{tran} for this and later figures assumes a redshift of 2.3, the median redshift of the sample. 114
- 3.14 *Top:* A schematic diagram explaining cylindrically projected 2D (CP2D) spectra. Spaxels with similar D_{tran} are averaged to create the emission map in $D_{\text{tran}}-\Delta v$ space. *Bottom:* The composite CP2D spectra of the continuum-subtracted Ly α emission line map averaged over all 59 galaxies, at all azimuthal angles (ϕ). The color-coding of the Ly α surface intensity is on a log scale to show the full extent of the emission, whereas the contours are spaced linearly and marked as white lines in the colorbar. The stack was formed by shifting the wavelengths of each galaxy data cube to the rest frame, leaving the surface brightness in observed units. The black ellipse at the top right shows the effective resolution of the stacked maps, with principal axes corresponding to the spectral resolution FWHM and the spatial resolution FWHM (see §3.4). Pixels with $\theta_{\text{tran}} < 0.1$ arcsec have been omitted to suppress artifacts owing to the singularity in the cylindrical projection. 117

- 3.15 *Left:* The stacked CP2D spectra along the galaxy major ($0^\circ \leq \phi < 45^\circ$; top) and minor ($45^\circ \leq \phi \leq 90^\circ$; bottom) axes. Both the color-coding and the contours are on linear scales. *Right:* The residual CP2D maps: the top panel shows the difference between the Major axis and Minor axis maps, in the same units of surface intensity as in the lefthand panels, where blue colors indicate regions with excess Ly α surface intensity along the Major axis; orange colors indicate regions where Ly α is brighter in the Minor axis map. The bottom panel shows the same residual map in units of the local noise level. The most prominent feature is excess Ly α emission along the galaxy major axis relative to that along the minor axis), at $\Delta v \sim +300 \text{ km s}^{-1}$, extending to $\theta_{\text{tran}} \sim 2''.0$ or $D_{\text{tran}} \sim 15 \text{ pkpc}$ 119
- 3.16 Distribution of the difference in Ly α flux integrated over velocity and angular distance in the bins of azimuthal angle corresponding to “major” and “minor” axes. Positive (negative) values indicate that Ly α emission is stronger along the major (minor) axis. The integration is conducted within $0 < \Delta v / (\text{km s}^{-1}) < 500$ and $\theta_{\text{tran}} \leq 2 \text{ arcsec}$ (top) and $0 < \Delta v / (\text{km s}^{-1}) < 1000$ and $\theta_{\text{tran}} \leq 3 \text{ arcsec}$ (bottom). There are two outliers in the first integration (top panel), while one remains in the second (bottom panel). 120
- 3.17 Same as Figure 3.15, but without Q0142-BX165, which is the strongest outlier in terms of excess Ly α emission along the galaxy major axis. 121
- 3.18 Same as Figure 3.15, but without Q0142-BX165 and Q2343-BX418, the two most significant outliers in the top panel of Figure 3.16. Significant excess emission that is larger than a resolution element for the redshifted peak no longer exists. 121
- 3.19 Same as Figure 3.16, but with a different velocity range of $-700 < \Delta v / (\text{km s}^{-1}) \leq -200$ and $\theta_{\text{tran}} \leq 2.5 \text{ arcsec}$ that focuses on the blueshifted component of Ly α emission. No individual galaxy is an extreme outlier in terms of excess blueshifted Ly α along the minor axis. 123

- 3.20 *Top*: Same as the top-right panel of Figure 3.15, but for a single galaxy, Q0142-BX165, which has the strongest excess Ly α emission along the galaxy major axis. Note that the color scale is 10 times that of Figure 3.15. *Bottom*: The HST F160W image of Q0142-BX165, overlaid with contours from the KCWI continuum image (left) and the narrow-band Ly α image (right). 124
- 3.21 Same as Figure 3.20, but for Q2343-BX418, the object with the second strongest major axis Ly α asymmetry. 125
- 3.22 Relationship between the flux measurements of anisotropic (excess) Ly α emission ($\Delta F_{\text{Ly}\alpha} = F_{\text{major}} - F_{\text{minor}}$) of the blueshifted component (left) and redshifted component (right) of Ly α emission and properties of the integrated Ly α halo [*Top*: central Ly α equivalent width, $W_{\lambda}(\text{Ly}\alpha)$; *Middle*: total Ly α flux, $F_{\text{Ly}\alpha}(\text{tot})$; *Bottom*: the ratio between the total blueshifted and redshifted components, $F_{\text{Ly}\alpha}(\text{blue})/F_{\text{Ly}\alpha}(\text{red})$]. Galaxies without reliable F_{red} are omitted in the bottom panel since their $F_{\text{Ly}\alpha}(\text{blue})/F_{\text{Ly}\alpha}(\text{red})$ are dominated by noise. The pink lines and shaded regions show the results and their 1σ uncertainties of a linear regression accounting for the errors in both x- and y-directions. The vertical dashed line in each panel marks the median value of the (x-axis) property for the full sample. The yellow diamond in each panel marks the location of Q2343-BX418, the outlier that caused the excess emission of the redshifted peak along the galaxy major axis as discussed in §3.5. 127
- 3.23 The difference between the CP2D spectra of Ly α emission for the major and minor axes. The maps show the residual for CP2D stacks for two sub-samples representing those below (left) and above (right) the sample median, From top to bottom, the Ly α halo properties are the central Ly α equivalent width ($W_{\lambda}(\text{Ly}\alpha)$), the integrated Ly α flux ($F_{\text{Ly}\alpha}(\text{tot})$), and the flux ratio between the blueshifted and redshifted components ($F_{\text{Ly}\alpha}(\text{blue})/F_{\text{Ly}\alpha}(\text{red})$). This figure confirms that the blueshifted excess Ly α emission favours weak Ly α emitting galaxies. 129

- 3.24 Similar to the right panel of Figure 3.15, but residual maps are between the major and minor (left), major and intermediate (middle), and intermediate and minor (right) axes with each bin size of only $\Delta\phi = 30^\circ$. The strong residual beyond $\theta_{\text{tran}} > 4$ arcsec is caused by a contaminating source near a single object. No sign of a bimodal distribution of Ly α emission is present. The sample in this figure is the same as in Figure 3.17. (Q0142-BX165: discarded; Q2343-BX418: included). 131
- 4.1 *Left*: The composite 1D spectrum of the full sample (black) and the composite stellar continuum model (orange). Before stacking, each individual galaxy spectrum was normalized with $F_\lambda(1450 \text{ \AA}) = 1$, and the stacking method was a sigma-clipped mean with $N_\sigma = 2.5$. *Right*: The composite continuum-subtracted spectrum (brown). In both panels, the grey spectrum is the 1σ error spectrum derived from bootstrap resampling. The vertical lines with labels mark the selected spectral features in the range, where different colors indicate their primary physical origin: ISM (green), nebular (blue), stellar (red), and non-resonant emission (purple). Our continuum model works well in continuum subtraction. 152
- 4.2 This figure shows how different parameters or assumptions affect the modeled continuum spectrum. The black and orange spectra are the same as in Figure 4.1, which show the composite 1D spectra of the galaxies and their fiducial continuum models. From left to right: The change of the continuum spectrum by varying age (left) and stellar metallicity (middle), and by ignoring the IGM + CGM component or the ISM component (right). Our fiducial model closely resembles the continuum around Ly α in the composite 1D spectrum. 153

- 4.3 (a) The composite CP2D spectrum constructed from a stack of all 110 star-forming galaxies in the sample. Before stacking, the CP2D spectrum of each object was extracted and normalized based on its median flux density at $1400 - 1500 \text{ \AA}$. The stacking was made with iterative sigma-clipped mean with $N_\sigma = 2.5$. The color map is on a log scale to highlight the low SB halo, while the white contours are linear increments of 0.4, as shown in the color bar. The ellipse on the top-right is the effective “beam” size of the map, where the vertical size is the FWHM of the typical seeing (1 arcsec), and the horizontal size corresponds to the typical spectral resolution (210 km s^{-1}), as estimated in C21. (b) Error of the composite CP2D spectrum, estimated using bootstrap resampling with 500 realizations. The color map is the same as in panel (a). (c) The S/N map of the composite CP2D spectrum formed by dividing panel (a) by panel (b). Both the color map and contours are on a linear scale. 154
- 4.4 *Top:* The composite spatial profiles of the normalized $\text{Ly}\alpha$ surface brightness. The black points show the total $\text{Ly}\alpha$ emission. The red and blue points show the redshifted and blueshifted emission components accordingly. The black, red, and blue lines show the best-fit exponential profiles to the corresponding points. All profiles are continuum-subtracted. The gray line shows the continuum profile. *Bottom:* The ratio between the blue and redshifted emission as a function of θ_{tran} . The blue line is the best-fit line in log-linear space. 157
- 4.5 The $W_\lambda(\text{Ly}\alpha)$ spatial curve of growth for the stacked CP2D spectra as shown in Figure 4.3. The black curve is the measured value, with the gray shade marks the 1σ error. The orange curve is the best-fit model from an exponential profile with a constant background. The purple line shows this best-fit model, after removing the background component. 158
- 4.6 The composite CP2D spectra for three sets of galaxies divided into bins of $E(B - V)$. The top left corner of each panel shows the median value of $E(B - V)$, and the number of galaxies that went into each bin. The colormap is in log space, while the white contours are linear. Both are shown in the colorbars on the right side. The unit of the colorbars is normalized SB units. 161
- 4.7 Same as in Figure 4.6, for galaxies binned in $\log(M_*/M_\odot)$ 162

4.8	Same as in Figure 4.6, for galaxies binned in $\log(\text{SFR})$, where SFR is based on best-fit SED models.	163
4.9	Same as in Figure 4.6, for galaxies binned in $\log(\text{sSFR})$	164
4.10	Same as in Figure 4.6, for galaxies binned in observed $F_{\text{H}\alpha}$ from 1D extracted slit-spectroscopy.	165
4.11	Same as in Figure 4.6, for galaxies binned in $\log([\text{OIII}]/\text{H}\beta)$	166
4.12	Same as in Figure 4.6, for galaxies binned in the DTB $W_\lambda(\text{Ly}\alpha)$	167
4.13	Same as in Figure 4.6, for galaxies binned in $F_{\text{blue}}(\text{tot})/F_{\text{red}}(\text{tot})$	168
5.1	A schematic diagram for H I in the CGM around a typical star-forming galaxy at $z = 2 - 3$, as a qualitative summary of the major results of this thesis. Outflows originating from regions of rapid star formation inside galaxies from star-forming regions inside galaxies dominates the H I kinematics in all directions at $D_{\text{tran}} \lesssim 50$ pkpc. At $D_{\text{tran}} \gtrsim 100$ pkpc, accretion flows and/or ambient CGM that carries H I from > 1 pMpc, likely in the form of “cold accretion” streams based on recent cosmological simulations, gradually takes over.	173
A.1	Flowchart of the three-level data products of the KBSS-KCWI survey.	177
A.2	Pseudo-white-light images before (<i>left</i>) and after (<i>right</i>) subtracting the median-filtered cube. This procedure is capable of removing low-frequency background (<i>top</i>) residuals and scattered light from bright objects (<i>bottom</i>).	178
A.3	The inverse sensitivity (<i>top</i>) and effective aperture curves of (<i>bottom</i>) measured from spectrophotometric two standard stars (Feige 34 and Feige 110). This figure includes data from three consecutive observing nights in November 2019. The colored curves are included in the final calibration. The gray ones were observed at either the end of the first night or the beginning of the second night when it was cloudy, and are discarded. The dashed cyan curve in the top panel is modeled ISC from all curves observed in clear conditions. The vertical dashed curves mark the boundary generated by the IDL DRP, in which the reduction is reliable.	180
A.4	<i>Top</i> : Pseudo-white-light images of two exposures on the same pointing. The red box marks the location of the alignment box, in which the cross-correlation is calculated. <i>Bottom</i> : The cross-correlation map of two images. The red cross marks the location of the local maximum, which is the relative offset between the two exposures.	181

A.5 *Left:* Pseudo-white-light image of a pointing in the KBSS-KCWI survey. The red circle marks the boundary, from which the 1D spectrum is extracted. The object in it is Q0100-BX172. The boundary is drawn from the segment map generated by SExtractor. *Right:* Comparison between the optimally extracted 1D spectrum (top) and a direct sum of the spaxels in the aperture (bottom). The direct sum is significantly noisier than the optimally extracted spectrum. . . . 183

LIST OF TABLES

<i>Number</i>	<i>Page</i>
2.1 Field-by-field summary of the properties of the KBSS Galaxy Pair Sample.	19
2.2 Masked background spectral regions	29
2.3 Best-fit model parameters	47
3.1 Summary of the galaxy sample and the observations (I).	93
3.1 — <i>continued.</i>	94
3.2 Summary of the galaxy sample and the observations (II).	95
3.2 — <i>continued.</i>	96
3.2 — <i>continued.</i>	97
3.3 Summary of HST observations	100

Chapter 1

INTRODUCTION

In its nearly 14 billion years of life, our universe has staged a series of fantasies for the curious cosmic audience – from the Big Bang, to the birth of the first stars and galaxies, and eventually to the birth of us. During the *ksana*¹ existence of human beings to date, we were able to determine, with a fair degree of confidence, that our current universe is made of 68.9% dark energy, 26.2% dark matter, and 4.9% baryons (Planck Collaboration et al., 2020). Despite being a small part of the universe, baryons, with their diverse and complex physical processes, still determine how we see the universe.

Galaxies like our Milky Way are the building blocks of the universe. After the Big Bang, primordial density fluctuations of dark matter grow into dark matter halos under the effect of gravity. These halos subsequently grow and merge with other halos. During this time, baryons, mostly in the form of gas, are also attracted by gravitational potential. They cool and collapse into clumps of star-forming regions, which are essentially the first galaxies. The birth of the first galaxies occurred earlier than $z \sim 11$ (current record holder of the earliest galaxy: GN-z11, $z = 11.09$; Oesch et al., 2016), although galaxies at even higher redshifts will likely be discovered after the launch of the James Webb Space Telescope (JWST). The ultraviolet (UV) radiation from the first stars and active galactic nuclei (AGN) is likely responsible for the reionization of the universe at $z \gtrsim 6$, which turns most of the hydrogen in the intergalactic medium (IGM) from neutral (H I) to ionized (H II) (see Loeb and Barkana, 2001, for a review).

Meanwhile, fresh gas in the intergalactic medium (IGM) along the “cosmic web” continues to feed the star formation within galaxies. At the same time, galaxy formation creates energetic winds and radiation through stars, supernovae (SN), and AGN, limiting the amount of gas falling into the galaxies, creating a “feedback” loop that regulates the star-formation rate (SFR). This feedback process constantly shapes galaxies. The departure of the galaxy stellar mass (M_*) function (e.g., Schechter, 1976) from the power-law dark matter halo mass function predicted by cosmological simulations is a manifestation of feedback. Meanwhile, galaxies in the

¹Sanskrit: An extremely short period of time.

current universe show clear bimodality in appearance (Hubble sequence; Hubble, 1926), color-magnitude diagram and star-formation rate (SFR; e.g., Strateva et al., 2001; Bell et al., 2004). However, earlier in the universe’s history, galaxies did not resemble their present-day descendants. We know that the star formation rate density and black hole activity all peaked at $z \sim 2$, with an intensity ~ 9 times higher than the present-day values (Madau and Dickinson, 2014). Morphologically, high-redshift star-forming galaxies appear to be “clumpy” and cannot be well-described as disks. These differences between galaxies in high and low redshifts, and drop of star-formation activities in the recent history of the universe suggests that certain mechanism related to feedback is responsible in either stopping gas falling into galaxies and/or stopping gas from making stars. Either way, it is important to look at the surrounding gas of galaxies, where inflow and outflow take place.

1.1 The Circumgalactic Medium

Understanding the process of galaxy formation requires studying the interaction between galaxies and the diffuse baryons outside of galaxies, the circumgalactic medium (CGM). CGM has been drawing increasingly more attention, thanks to the recent development of high-sensitivity ground and space-based telescopes, e.g., the Keck observatories and the Hubble Space Telescope (HST). Nevertheless, there is no consensus definition of the CGM as yet—but what is usually meant is gas in the immediate surrounding of a galaxy (see Figure 1.1 for a schematic diagram). Historically, the boundary between the CGM and the more diffuse intergalactic medium (IGM) is often imagined near the virial radius of a galaxy (R_{vir}). Recently, the concept of the “splash-back radius” (R_{sp} ; More, Diemer, and Kravtsov, 2015), where infalling dark matter particles first hit the apocenter, has been proposed as a more robust physical definition of a galaxy’s size, since it corresponds to a sharp drop in the density of dark matter in numerical simulations. However, there is no observational evidence for sudden physical changes of *gas* properties near either R_{vir} or R_{sp} , and a galaxy often has influence well beyond either.

Observing the CGM is relatively difficult because the CGM gas is diffuse. Nevertheless, significant progress has been made in recent decades. Currently, CGM observations span the entire electromagnetic spectrum, including radio/far-IR (e.g., [C II] 158 μm emission; Le Fèvre et al., 2020; using fast radio bursts; Ravi, 2019), infrared (IR; e.g., using broad components of nebular emission lines as tracer of outflows; Freeman et al., 2019), and x-ray emission (e.g., Anderson et al., 2015; Li et al., 2017); however, the vast majority of observations have been made in the rest-

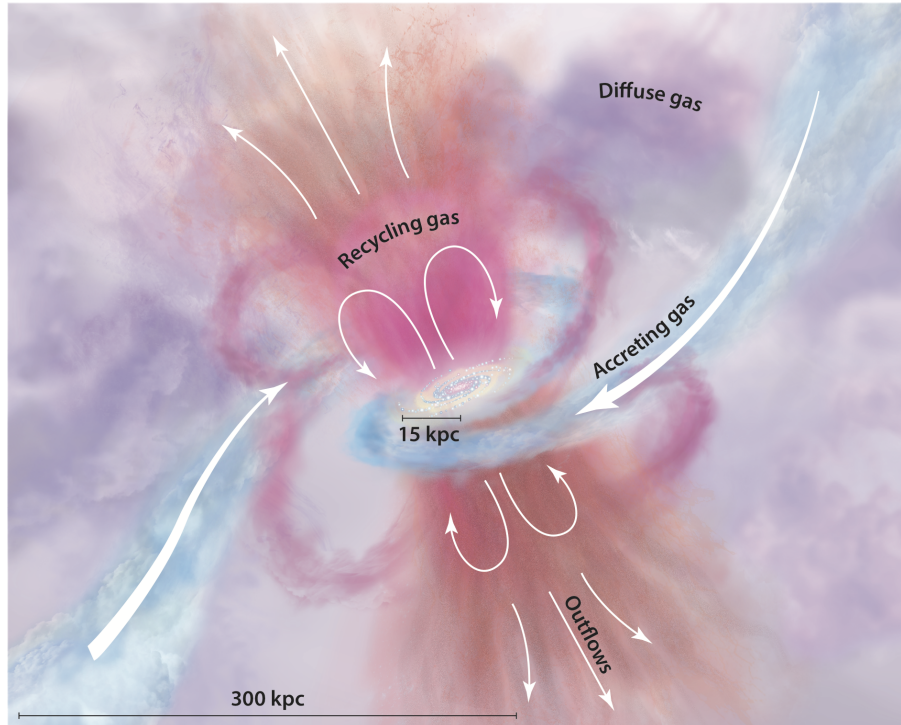


Figure 1.1: A schematic diagram of the circumgalactic medium (from Tumlinson, Peeples, and Werk, 2017). The CGM gas normally consists of outflow, inflow, and recycled gas, with a large range of physical conditions.

frame ultraviolet (UV), where absorption lines corresponding to transitions from the ground-state to first excited state of astrophysically-abundant ions easily detected in the spectra of background continuum sources along lines of sight near galaxies, e.g., H I, Si II, Si III, Si IV, C II, C IV, and Mg II, are located at. These spectral features are also observed in “down-the-barrel” (DTB) spectra – i.e., arising in gas located along the direct line of sight to a star-forming galaxy (e.g., Steidel et al., 2010). More recently, it has become feasible to detect the same transitions in emission from the CGM (e.g., Mg II; Burchett et al., 2021).

With help from these recent observations, we have learned that the CGM gas is extremely complex and multiphase, with density spanning > 6 orders of magnitude, and temperature ranging from 10^4 to 10^7 K. The mostly-ionized gas in the CGM could easily comprise $\gtrsim 50\%$ of the total cosmic baryon budget (see Tumlinson, Peeples, and Werk, 2017, for a review). However, many detailed properties (e.g., kinematics, composition, physical scale, mass-flow rate) of the CGM have not yet been determined with high fidelity.

Outflows resulting from stellar and/or AGN feedback are commonly observed in DTB spectra, particularly for starburst galaxies in the local universe, and for nearly all galaxies at high redshifts. The rest-UV absorption lines are almost always observed to be blueshifted with respect to the galaxy systemic redshift (e.g., Shapley et al., 2003; Steidel et al., 2010), indicating that clumpy outflowing gas covers a large fraction of the central continuum source of rapidly star-forming galaxies. On the other hand, direct evidence of gas accretion—believed to be ubiquitous—has only rarely been observed directly (e.g., Rubin et al., 2012)². This suggests that, although accretion must play a crucial role in galaxy formation, its observational signatures are more subtle than those of outflows, due to quieter velocity fields and, possibly, smaller cross-section presented to individual lines of sight. Historically, gas accreting from the IGM was believed to be shocked heated to the virial temperature (T_{vir}) near R_{vir} , which for individual galaxy halo masses would result in hot (10^6 K) atmospheres surrounding central galaxies that would gradually cool out and rain onto the central galaxy (e.g., Rees and Ostriker, 1977). However, with the more recent development of cosmological hydrodynamical simulations, the picture has been revised for all but the most massive dark matter halos: instead of the cool gas accretion rate depending on the cooling rate from high temperature, most accreting gas is not shocked, but instead flows in a relatively cool state directly onto the central regions of the halo, called “cold-mode accretion” (e.g., Kereš et al., 2005; Dekel et al., 2009; Benson and Bower, 2011; Martin et al., 2019).

The physical scale of structure in the CGM has also been a focus of the field in recent years, especially because the physical processes on small scales have direct implications for the origin and content of the multiphase CGM. If CGM were in pure hydrostatic equilibrium, the typical gas temperature of the MW CGM would be $\sim 10^6$ K, too hot for the significant presence of neutral gas that observations have revealed. In recent years, idealized simulations have proposed several physical processes that might explain the multiphase nature of the CGM, including cosmic-ray feedback (e.g., Ji et al., 2020), magnetic fields (e.g., van de Voort et al., 2021), and shattering (e.g., McCourt et al., 2018). Even though cosmological simulations, especially zoom-in simulations such as the Feedback In Realistic Environments (FIRE; Hopkins et al., 2014; Hopkins et al., 2018), have been increasingly successful in matching observations, each increase in spatial resolution in the CGM leads to significant changes in predicted gas properties, i.e., small-scale physical processes

²It is difficult to separate inflow and outflow for gas observed along lines of sight through CGM gas that are not “DTB”, as discussed in this thesis.

in the CGM are still not fully resolved (Hummels et al., 2019).

1.2 Ly α in the Circumgalactic Medium

Neutral hydrogen is a major component of the CGM, representing the cold (neutral) phase CGM (Tumlinson, Peebles, and Werk, 2017). Despite that the use of other transitions (mostly Balmer and other lines in the Lyman series), Lyman-alpha (Ly α ; at 1215.67 Å) is the strongest spectral feature created by H I and the primary tool for CGM to study CGM H I. Ly α corresponds to the $n = 2$ to 1 transition of H I atoms, and is thus a resonant transition. At $z > 2$, Ly α conveniently shifts into the optical atmospheric window, making it accessible by ground-based telescopes. Therefore, Ly α is one of the most popular spectral features for CGM observations.

The resonant nature of the Ly α line makes it rather difficult to understand the full radiative transfer process. Since the presence of H I atoms is common in the CGM, once a Ly α photon is emitted, it would be almost immediately absorbed by a nearby H I atom, creating a cascade of events where Ly α photons are constantly being absorbed and re-emitted, in a process known as “resonant scattering”. Effectively, a Ly α photon undergoes a random walk in both the physical space and frequency space, until it has walked far enough that it reaches a region where the H I is optically thin, and the photon can escape (see Dijkstra, 2014, for a review). Because of resonant scattering, predicting Ly α emission is difficult and requires knowledge of both the kinematics and spatial distribution of H I and the distribution of initial sources of Ly α . Reasonable approximations can be made in order to predict the emergent Ly α emission properties using semi-analytic models (e.g., Verhamme, Schaerer, and Maselli, 2006; Scarlata and Panagia, 2015), realistic Ly α radiative transfer models, including realistic treatment of the small-scale structure of the ambient medium, require computationally-expensive photon-tracing Monte-Carlo (MC) simulations (Gronke et al., 2016).

Observationally, aided by recently-developed high-sensitivity integral field units (IFU) on large telescopes – e.g., the Keck Cosmic Web Imager (KCWI; Morrissey et al., 2018) and the Multi Unit Spectroscopic Explorer (MUSE; Bacon et al., 2010) – Ly α emission from the CGM (often referred to as the “Ly α halo”) has been shown to be much more extended than the host galaxy starlight, and appears to be a common feature at low redshift and nearly ubiquitous at high redshifts: see, e.g., ($z < 1$: Hayes et al., 2013; $2 < z < 3$: Steidel et al., 2011; $z > 3$: Wisotzki et al., 2018). Meanwhile, 1D Ly α spectra are nearly always observed to possess a

dominant component that is redshifted with respect to the galaxy systemic redshift, accompanied by either a weaker blueshifted component with a minimum close to the systemic redshift, or blueshifted absorption component. While this spectral morphology is consistent with resonant scattering of Ly α produced by a central source (e.g., recombination of gas photoionized by massive stars or AGN) propagating through an extended gas distribution in the CGM, this is not necessarily the only explanation. Alternative explanations include: (1) *in situ* photoionization of H I by the metagalactic UV ionizing radiation field combined with local sources and followed by recombination (sometimes called “fluorescence”) (2) accreting gas losing energy via collisional excitation of Ly α (sometimes referred to as “gravitational cooling”) (3) emission from unresolved satellite galaxies in the halos of larger central galaxies (see Ouchi, Ono, and Shibuya, 2020, for a review). It is also clear from observations that Ly α emission from galaxies evolves with redshift, in the sense that the average ratio of Ly α to stellar continuum luminosity increases with redshift at least over the range $2 \lesssim z \lesssim 6$, with an apparent decrease by $z \simeq 7$ – possibly indicating the IGM phase transition expected near the epoch of reionization (e.g., Mesinger et al., 2015).

For Ly α absorption, the physical picture is much simpler. When background light passes through H I gas in the CGM of a foreground galaxy, an absorption line at the corresponding redshift is recorded. With sufficient S/N and spectral resolution of the background source (hence the use of QSOs), the column density, kinematics, and thermal broadening of H I and metallic ions in the CGM can be measured using either profile fitting (e.g., Rudie et al., 2012; Rudie et al., 2019) or more statistical approaches such as the so-called “pixel optical depth” method (e.g., Rakic et al., 2012; Turner et al., 2014). Bright QSOs are ideal for the purpose of making quantitative measurements in this way, but they are far too rare to allow multiple sightlines through the CGM of a single galaxy, and thus cannot provide spatial information on intervening gaseous structures on scales smaller than their mean separation on the sky (tens to hundreds of Mpc).

1.3 This Thesis

The Keck Baryonic Structure Survey (KBSS; Rudie et al., 2012; Steidel et al., 2014; Trainor et al., 2015; Strom et al., 2017) is built with 15 independent densely-sampled survey fields. The majority of galaxies in the KBSS survey were photometrically selected Lyman break galaxies (LBG) using BX, BM (Adelberger et al., 2004; Steidel et al., 2004), MD, C, D, M (Steidel et al., 2003), and RK criteria (Strom et

al., 2017), as well as Ly α emitting galaxies using narrow-band photometry (Trainor and Steidel, 2012; Trainor and Steidel, 2013; Trainor et al., 2015). In total, 3631 galaxies (2986 continuum-selected + 645 Ly α -selected) have been spectroscopically identified.

This thesis marks a milestone in a continuous effort to characterize HI around star-forming galaxies using the Ly α transition at $z > 2$. We present two samples, the KBSS Galaxy Pair Sample (KGPS) and the KBSS-KCWI sample, which have the potential to greatly improve our understanding of the CGM. The KGPS sample (presented in Chapter 2) consists of ~ 3000 galaxies whose spectra were observed with the Low Resolution Imaging Spectrograph (LRIS; Oke et al., 1995). By matching these galaxies in foreground-background non-interacting pairs, the sample includes $> 200,000$ independent sightlines sampling the CGM within 3 Mpc around galaxies. The KBSS-KCWI sample utilizes the newly commissioned Keck Cosmic Web Imager, which is a highly sensitive IFU on the Keck II telescope with a wide field of view (FoV). This sample consists of observations of Ly α observation of ~ 100 star-forming galaxies with a typical integration time ~ 5 hours, achieving a limiting surface-brightness (SB) threshold of 10^{-19} ergs s $^{-1}$ cm $^{-2}$ arcsec $^{-2}$ in the composite spectral cube. This sample is presented in Chapters 3 and 4. We will also present a concluding remark with future perspectives in Chapter 5, and an appendix on the data reduction process of the KBSS-KCWI survey in Appendix A. Unless otherwise noticed, we assume a Λ CDM cosmology with $\Omega_m = 0.3$, $\Omega_\Lambda = 0.7$, and $h = 0.7$. Distances are given in proper units, i.e., physical kpc (pkpc).

References

- Adelberger, Kurt L. et al. (May 2004). “Optical Selection of Star-forming Galaxies at Redshifts $1 < z < 3$ ”. *ApJ* 607.1, pp. 226–240. DOI: 10.1086/383221. arXiv: astro-ph/0401445 [astro-ph].
- Anderson, Michael E., Massimo Gaspari, Simon D. M. White, Wenting Wang, and Xinyu Dai (June 2015). “Unifying X-ray scaling relations from galaxies to clusters”. *MNRAS* 449.4, pp. 3806–3826. DOI: 10.1093/mnras/stv437. arXiv: 1409.6965 [astro-ph.CO].
- Bacon, R. et al. (July 2010). “The MUSE second-generation VLT instrument”. *Ground-based and Airborne Instrumentation for Astronomy III*. Ed. by Ian S. McLean, Suzanne K. Ramsay, and Hideki Takami. Vol. 7735. Society of Photo-Optical Instrumentation Engineers (SPIE) Conference Series, p. 773508. DOI: 10.1117/12.856027.

- Bell, Eric F. et al. (June 2004). “Nearly 5000 Distant Early-Type Galaxies in COMBO-17: A Red Sequence and Its Evolution since $z \sim 1$ ”. *ApJ* 608.2, pp. 752–767. DOI: 10.1086/420778. arXiv: astro-ph/0303394 [astro-ph].
- Benson, Andrew J. and Richard Bower (Feb. 2011). “Accretion shocks and cold filaments in galaxy formation”. *MNRAS* 410.4, pp. 2653–2661. DOI: 10.1111/j.1365-2966.2010.17641.x.
- Burchett, Joseph N. et al. (Mar. 2021). “Circumgalactic Mg II Emission from an Isotropic Starburst Galaxy Outflow Mapped by KCWI”. *ApJ* 909.2, 151, p. 151. DOI: 10.3847/1538-4357/abd4e0. arXiv: 2005.03017 [astro-ph.GA].
- Dekel, A. et al. (Jan. 2009). “Cold streams in early massive hot haloes as the main mode of galaxy formation”. *Nature* 457.7228, pp. 451–454. DOI: 10.1038/nature07648. arXiv: 0808.0553 [astro-ph].
- Dijkstra, Mark (Oct. 2014). “Ly α Emitting Galaxies as a Probe of Reionisation”. *Publ. Astron. Soc. Australia* 31, e040, e040. DOI: 10.1017/pasa.2014.33. arXiv: 1406.7292 [astro-ph.CO].
- Freeman, William R. et al. (Mar. 2019). “The MOSDEF Survey: Broad Emission Lines at $z = 1.4$ – 3.8 ”. *ApJ* 873.2, 102, p. 102. DOI: 10.3847/1538-4357/ab0655.
- Gronke, Max, Mark Dijkstra, Michael McCourt, and S. Peng Oh (Dec. 2016). “From Mirrors to Windows: Lyman-alpha Radiative Transfer in a Very Clumpy Medium”. *ApJ* 833.2, L26, p. L26. DOI: 10.3847/2041-8213/833/2/L26. arXiv: 1611.01161 [astro-ph.GA].
- Hayes, Matthew et al. (Mar. 2013). “The Lyman Alpha Reference Sample: Extended Lyman Alpha Halos Produced at Low Dust Content”. *ApJ* 765.2, L27, p. L27. DOI: 10.1088/2041-8205/765/2/L27. arXiv: 1303.0006 [astro-ph.CO].
- Hopkins, Philip F. et al. (Nov. 2014). “Galaxies on FIRE (Feedback In Realistic Environments): stellar feedback explains cosmologically inefficient star formation”. *MNRAS* 445.1, pp. 581–603. DOI: 10.1093/mnras/stu1738. arXiv: 1311.2073 [astro-ph.CO].
- Hopkins, Philip F. et al. (Oct. 2018). “FIRE-2 simulations: physics versus numerics in galaxy formation”. *MNRAS* 480.1, pp. 800–863. DOI: 10.1093/mnras/sty1690. arXiv: 1702.06148 [astro-ph.GA].
- Hubble, E. P. (Dec. 1926). “Extragalactic nebulae.” *ApJ* 64, pp. 321–369. DOI: 10.1086/143018.
- Hummels, Cameron B. et al. (Sept. 2019). “The Impact of Enhanced Halo Resolution on the Simulated Circumgalactic Medium”. *ApJ* 882.2, 156, p. 156. DOI: 10.3847/1538-4357/ab378f. arXiv: 1811.12410 [astro-ph.GA].
- Ji, Suoqing et al. (Aug. 2020). “Properties of the circumgalactic medium in cosmic ray-dominated galaxy haloes”. *MNRAS* 496.4, pp. 4221–4238. DOI: 10.1093/mnras/staa1849. arXiv: 1909.00003 [astro-ph.GA].

- Kereš, Dušan, Neal Katz, David H. Weinberg, and Romeel Davé (Oct. 2005). “How do galaxies get their gas?” *MNRAS* 363.1, pp. 2–28. DOI: 10.1111/j.1365-2966.2005.09451.x. arXiv: astro-ph/0407095 [astro-ph].
- Le Fèvre, O. et al. (Nov. 2020). “The ALPINE-ALMA [CII] survey. Survey strategy, observations, and sample properties of 118 star-forming galaxies at $4 < z < 6$ ”. *A&A* 643, A1, A1. DOI: 10.1051/0004-6361/201936965. arXiv: 1910.09517 [astro-ph.CO].
- Li, Jiang-Tao et al. (Dec. 2017). “The Circum-Galactic Medium of Massive Spirals. II. Probing the Nature of Hot Gaseous Halo around the Most Massive Isolated Spiral Galaxies”. *ApJS* 233.2, 20, p. 20. DOI: 10.3847/1538-4365/aa96fc. arXiv: 1710.07355 [astro-ph.GA].
- Loeb, Abraham and Rennan Barkana (Jan. 2001). “The Reionization of the Universe by the First Stars and Quasars”. *ARA&A* 39, pp. 19–66. DOI: 10.1146/annurev.astro.39.1.19. arXiv: astro-ph/0010467 [astro-ph].
- Madau, Piero and Mark Dickinson (Aug. 2014). “Cosmic Star-Formation History”. *ARA&A* 52, pp. 415–486. DOI: 10.1146/annurev-astro-081811-125615. arXiv: 1403.0007 [astro-ph.CO].
- Martin, D. Christopher et al. (July 2019). “Multi-filament gas inflows fuelling young star-forming galaxies”. *Nature Astronomy* 3, pp. 822–831. DOI: 10.1038/s41550-019-0791-2. arXiv: 1904.11465 [astro-ph.GA].
- McCourt, Michael, S. Peng Oh, Ryan O’Leary, and Ann-Marie Madigan (Feb. 2018). “A characteristic scale for cold gas”. *MNRAS* 473.4, pp. 5407–5431. DOI: 10.1093/mnras/stx2687. arXiv: 1610.01164 [astro-ph.GA].
- Mesinger, Andrei et al. (Jan. 2015). “Can the intergalactic medium cause a rapid drop in Ly α emission at $z > 6$?” *MNRAS* 446.1, pp. 566–577. DOI: 10.1093/mnras/stu2089. arXiv: 1406.6373 [astro-ph.CO].
- More, Surhud, Benedikt Diemer, and Andrey V. Kravtsov (Sept. 2015). “The Splash-back Radius as a Physical Halo Boundary and the Growth of Halo Mass”. *ApJ* 810.1, 36, p. 36. DOI: 10.1088/0004-637X/810/1/36. arXiv: 1504.05591 [astro-ph.CO].
- Morrissey, Patrick et al. (Sept. 2018). “The Keck Cosmic Web Imager Integral Field Spectrograph”. *ApJ* 864.1, 93, p. 93. DOI: 10.3847/1538-4357/aad597. arXiv: 1807.10356 [astro-ph.IM].
- Oesch, P. A. et al. (Mar. 2016). “A Remarkably Luminous Galaxy at $z=11.1$ Measured with Hubble Space Telescope Grism Spectroscopy”. *ApJ* 819.2, 129, p. 129. DOI: 10.3847/0004-637X/819/2/129. arXiv: 1603.00461 [astro-ph.GA].
- Oke, J. B. et al. (Apr. 1995). “The Keck Low-Resolution Imaging Spectrometer”. *PASP* 107, p. 375. DOI: 10.1086/133562.

- Ouchi, Masami, Yoshiaki Ono, and Takatoshi Shibuya (Aug. 2020). “Observations of the Lyman- α Universe”. *ARA&A* 58, pp. 617–659. DOI: 10.1146/annurev-astro-032620-021859. arXiv: 2012.07960 [astro-ph.GA].
- Planck Collaboration et al. (Sept. 2020). “Planck 2018 results. VI. Cosmological parameters”. *A&A* 641, A6, A6. DOI: 10.1051/0004-6361/201833910. arXiv: 1807.06209 [astro-ph.CO].
- Rakic, Olivera, Joop Schaye, Charles C. Steidel, and Gwen C. Rudie (June 2012). “Neutral Hydrogen Optical Depth near Star-forming Galaxies at $z \approx 2.4$ in the Keck Baryonic Structure Survey”. *ApJ* 751.2, 94, p. 94. DOI: 10.1088/0004-637X/751/2/94. arXiv: 1109.4944 [astro-ph.CO].
- Ravi, Vikram (Feb. 2019). “Measuring the Circumgalactic and Intergalactic Baryon Contents with Fast Radio Bursts”. *ApJ* 872.1, 88, p. 88. DOI: 10.3847/1538-4357/aafb30. arXiv: 1804.07291 [astro-ph.HE].
- Rees, M. J. and J. P. Ostriker (June 1977). “Cooling, dynamics and fragmentation of massive gas clouds: clues to the masses and radii of galaxies and clusters.” *MNRAS* 179, pp. 541–559. DOI: 10.1093/mnras/179.4.541.
- Rubin, Kate H. R., J. Xavier Prochaska, David C. Koo, and Andrew C. Phillips (Mar. 2012). “The Direct Detection of Cool, Metal-enriched Gas Accretion onto Galaxies at $z \sim 0.5$ ”. *ApJ* 747.2, L26, p. L26. DOI: 10.1088/2041-8205/747/2/L26. arXiv: 1110.0837 [astro-ph.CO].
- Rudie, Gwen C. et al. (May 2012). “The Gaseous Environment of High- z Galaxies: Precision Measurements of Neutral Hydrogen in the Circumgalactic Medium of $z \sim 2-3$ Galaxies in the Keck Baryonic Structure Survey”. *ApJ* 750.1, 67, p. 67. DOI: 10.1088/0004-637X/750/1/67. arXiv: 1202.6055 [astro-ph.CO].
- Rudie, Gwen C. et al. (Nov. 2019). “Column Density, Kinematics, and Thermal State of Metal-bearing Gas within the Virial Radius of $z \sim 2$ Star-forming Galaxies in the Keck Baryonic Structure Survey”. *ApJ* 885.1, 61, p. 61. DOI: 10.3847/1538-4357/ab4255. arXiv: 1903.00004 [astro-ph.GA].
- Scarlata, C. and N. Panagia (Mar. 2015). “A Semi-analytical Line Transfer Model to Interpret the Spectra of Galaxy Outflows”. *ApJ* 801.1, 43, p. 43. DOI: 10.1088/0004-637X/801/1/43. arXiv: 1501.07282 [astro-ph.GA].
- Schechter, P. (Jan. 1976). “An analytic expression for the luminosity function for galaxies.” *ApJ* 203, pp. 297–306. DOI: 10.1086/154079.
- Shapley, Alice E., Charles C. Steidel, Max Pettini, and Kurt L. Adelberger (May 2003). “Rest-Frame Ultraviolet Spectra of $z \sim 3$ Lyman Break Galaxies”. *ApJ* 588.1, pp. 65–89. DOI: 10.1086/373922. arXiv: astro-ph/0301230 [astro-ph].
- Steidel, Charles C. et al. (Aug. 2003). “Lyman Break Galaxies at Redshift $z \sim 3$: Survey Description and Full Data Set”. *ApJ* 592.2, pp. 728–754. DOI: 10.1086/375772. arXiv: astro-ph/0305378 [astro-ph].

- Steidel, Charles C. et al. (Apr. 2004). “A Survey of Star-forming Galaxies in the $1.4 \lesssim Z \lesssim 2.5$ Redshift Desert: Overview”. *ApJ* 604.2, pp. 534–550. DOI: 10.1086/381960. arXiv: astro-ph/0401439 [astro-ph].
- Steidel, Charles C. et al. (July 2010). “The Structure and Kinematics of the Circumgalactic Medium from Far-ultraviolet Spectra of $z \sim 2-3$ Galaxies”. *ApJ* 717.1, pp. 289–322. DOI: 10.1088/0004-637X/717/1/289. arXiv: 1003.0679 [astro-ph.CO].
- Steidel, Charles C. et al. (Aug. 2011). “Diffuse Ly α Emitting Halos: A Generic Property of High-redshift Star-forming Galaxies”. *ApJ* 736.2, 160, p. 160. DOI: 10.1088/0004-637X/736/2/160. arXiv: 1101.2204 [astro-ph.CO].
- Steidel, Charles C. et al. (Nov. 2014). “Strong Nebular Line Ratios in the Spectra of $z \sim 2-3$ Star Forming Galaxies: First Results from KBSS-MOSFIRE”. *ApJ* 795.2, 165, p. 165. DOI: 10.1088/0004-637X/795/2/165. arXiv: 1405.5473 [astro-ph.GA].
- Strateva, Iskra et al. (Oct. 2001). “Color Separation of Galaxy Types in the Sloan Digital Sky Survey Imaging Data”. *AJ* 122.4, pp. 1861–1874. DOI: 10.1086/323301. arXiv: astro-ph/0107201 [astro-ph].
- Strom, Allison L. et al. (Feb. 2017). “Nebular Emission Line Ratios in $z \approx 2-3$ Star-forming Galaxies with KBSS-MOSFIRE: Exploring the Impact of Ionization, Excitation, and Nitrogen-to-Oxygen Ratio”. *ApJ* 836.2, 164, p. 164. DOI: 10.3847/1538-4357/836/2/164. arXiv: 1608.02587 [astro-ph.GA].
- Trainor, Ryan and Charles C. Steidel (Sept. 2013). “Constraints on Hyperluminous QSO Lifetimes via Fluorescent Ly α Emitters at $Z \sim 2.7$ ”. *ApJ* 775.1, L3, p. L3. DOI: 10.1088/2041-8205/775/1/L3. arXiv: 1308.1678 [astro-ph.CO].
- Trainor, Ryan F. and Charles C. Steidel (June 2012). “The Halo Masses and Galaxy Environments of Hyperluminous QSOs at $z \sim 2.7$ in the Keck Baryonic Structure Survey”. *ApJ* 752.1, 39, p. 39. DOI: 10.1088/0004-637X/752/1/39. arXiv: 1204.3636 [astro-ph.CO].
- Trainor, Ryan F., Charles C. Steidel, Allison L. Strom, and Gwen C. Rudie (Aug. 2015). “The Spectroscopic Properties of Ly α -Emitters at $z \sim 2.7$: Escaping Gas and Photons from Faint Galaxies”. *ApJ* 809.1, 89, p. 89. DOI: 10.1088/0004-637X/809/1/89. arXiv: 1506.08205 [astro-ph.GA].
- Tumlinson, Jason, Molly S. Peeples, and Jessica K. Werk (Aug. 2017). “The Circumgalactic Medium”. *ARA&A* 55.1, pp. 389–432. DOI: 10.1146/annurev-astro-091916-055240. arXiv: 1709.09180 [astro-ph.GA].
- Turner, Monica L., Joop Schaye, Charles C. Steidel, Gwen C. Rudie, and Allison L. Strom (Nov. 2014). “Metal-line absorption around $z \approx 2.4$ star-forming galaxies in the Keck Baryonic Structure Survey”. *MNRAS* 445.1, pp. 794–822. DOI: 10.1093/mnras/stu1801. arXiv: 1403.0942 [astro-ph.CO].

- van de Voort, Freeke et al. (Mar. 2021). “The effect of magnetic fields on properties of the circumgalactic medium”. *MNRAS* 501.4, pp. 4888–4902. DOI: 10.1093/mnras/staa3938. arXiv: 2008.07537 [astro-ph.GA].
- Verhamme, A., D. Schaerer, and A. Maselli (Dec. 2006). “3D Ly α radiation transfer. I. Understanding Ly α line profile morphologies”. *A&A* 460.2, pp. 397–413. DOI: 10.1051/0004-6361:20065554. arXiv: astro-ph/0608075 [astro-ph].
- Wisotzki, L. et al. (Oct. 2018). “Nearly all the sky is covered by Lyman- α emission around high-redshift galaxies”. *Nature* 562.7726, pp. 229–232. DOI: 10.1038/s41586-018-0564-6. arXiv: 1810.00843 [astro-ph.GA].

Chapter 2

THE KECK BARYONIC STRUCTURE SURVEY: USING
FOREGROUND/BACKGROUND GALAXY PAIRS TO TRACE
THE STRUCTURE AND KINEMATICS OF CIRCUMGALACTIC
NEUTRAL HYDROGEN AT $z \sim 2$

Chen, Yuguang et al. (Dec. 2020). “The Keck Baryonic Structure Survey: Using foreground/background galaxy pairs to trace the structure and kinematics of circumgalactic neutral hydrogen at $z \sim 2$ ”. *MNRAS* 499.2, pp. 1721–1746. DOI: 10.1093/mnras/staa2808. arXiv: 2006.13236 [astro-ph.GA].

Yuguang Chen¹, Charles C. Steidel¹, Cameron B. Hummels,¹ Gwen C. Rudie², Bili Dong³, Ryan F. Trainor⁴, Milan Bogosavljević⁵, Dawn K. Erb⁶, Max Pettini^{7,8}, Naveen A. Reddy⁹, Alice E. Shapley¹⁰, Allison L. Strom², Rachel L. Theios¹, Claude-André Faucher-Giguère¹¹, Philip F. Hopkins¹, and Dušan Kereš³

¹Cahill Center for Astronomy and Astrophysics, California Institute of Technology, MC249-17, Pasadena, CA 91125, USA

²The Observatories of the Carnegie Institution for Science, 813 Santa Barbara Street, Pasadena, CA 91101, USA

³Department of Physics, Center for Astrophysics and Space Sciences, University of California at San Diego, 9500 Gilman Drive, La Jolla, CA 92093, USA

⁴Department of Physics and Astronomy, Franklin & Marshall College, 637 College Ave., Lancaster, PA 17603, USA

⁵Division of Science, New York University Abu Dhabi, P.O. Box 129188, Abu Dhabi, UAE

⁶The Leonard E. Parker Center for Gravitation, Cosmology and Astrophysics, Department of Physics, University of Wisconsin-Milwaukee, 3135 North Maryland Avenue, Milwaukee, WI 53211, USA

⁷Institute of Astronomy, University of Cambridge, Madingley Road, Cambridge CB3 0HA, UK

⁸Kavli Institute for Cosmology, University of Cambridge, Madingley Road, Cambridge CB3 0HA, UK

⁹Department of Physics and Astronomy, University of California, Riverside, 900 University Avenue, Riverside, CA 92521, USA

¹⁰Department of Physics and Astronomy, University of California, Los Angeles, 430 Portola Plaza, Los Angeles, CA 90095, USA

¹¹Department of Physics and Astronomy and Center for Interdisciplinary Exploration and Research in Astrophysics (CIERA), Northwestern University, 2145 Sheridan Road, Evanston, IL 60208, USA

Abstract

We present new measurements of the spatial distribution and kinematics of neutral hydrogen in the circumgalactic and intergalactic medium surrounding star-forming galaxies at $z \sim 2$. Using the spectra of ≈ 3000 galaxies with redshifts $\langle z \rangle = 2.3 \pm 0.4$ from the Keck Baryonic Structure Survey, we assemble a sample of more than 200,000 distinct foreground-background pairs with projected angular separations of $3'' - 500''$ and spectroscopic redshifts, with $\langle z_{\text{fg}} \rangle = 2.23$ and $\langle z_{\text{bg}} \rangle = 2.57$ (foreground, background redshifts, respectively.) The ensemble of sightlines and foreground galaxies is used to construct a 2-D map of the mean excess H I Ly α optical depth relative to the intergalactic mean as a function of projected galactocentric distance ($20 \lesssim D_{\text{tran}}/\text{pkpc} \lesssim 4000$) and line-of-sight velocity. We obtain accurate galaxy systemic redshifts, providing significant information on the line-of-sight kinematics of H I gas as a function of projected distance D_{tran} . We compare the map with cosmological zoom-in simulation, finding qualitative agreement between them. A simple two-component (accretion, outflow) analytical model generally reproduces the observed line-of-sight kinematics and projected spatial distribution of H I. The best-fitting model suggests that galaxy-scale outflows with initial velocity $v_{\text{out}} \approx 600 \text{ km s}^{-1}$ dominate the kinematics of circumgalactic H I out to $D_{\text{tran}} \approx 50 \text{ kpc}$, while H I at $D_{\text{tran}} \gtrsim 100 \text{ kpc}$ is dominated by infall with characteristic $v_{\text{in}} \lesssim$ circular velocity. Over the impact parameter range $80 \lesssim D_{\text{tran}}/\text{pkpc} \lesssim 200$, the H I line-of-sight velocity range reaches a minimum, with a corresponding flattening in the rest-frame Ly α equivalent width. These observations can be naturally explained as the transition between outflow-dominated and accretion-dominated flows. Beyond $D_{\text{tran}} \approx 300 \text{ pkpc}$ ($\sim 1 \text{ cMpc}$), the line of sight kinematics are dominated by Hubble expansion.

2.1 Introduction

Galaxy formation involves a continuous competition between gas cooling and accretion on the one hand, and feedback-driven heating and/or mass outflows on the other. The outcome of this competition, as a function of time, controls nearly all observable properties of galaxies: e.g., the star-formation rate, the fraction of galactic baryons converted to stars over the galaxy lifetime, and the fraction of baryons that remain bound to the galaxy. This competition eventually halts star formation and the growth of supermassive black hole mass. The exchange of gaseous baryons between the diffuse intergalactic medium (IGM) and the central regions of galaxies (the interstellar medium; ISM) involves an intermediate baryonic reservoir that has

come to be called the “circumgalactic medium” (CGM) (e.g., Steidel et al., 2010; Rudie, Steidel, and Pettini, 2012; Tumlinson, Peebles, and Werk, 2017.)

Although there is not yet a consensus, one possible working definition of the CGM is the region containing gas that is outside of the interstellar medium of a galaxy, but that is close enough that the physics and chemistry of the gas and that of the central galaxy are causally connected. For example, the CGM may be 1) the baryonic reservoir that supplies gas, via accretion, to the central regions of the galaxy, providing fuel for star formation and black hole growth; 2) the CGM may also consist of gas that has already been part of the ISM at some point in the past, but has since been dispersed or ejected to large galactocentric radii; or 3) the physical state of the gas can be otherwise affected by energetic processes (mechanical or radiative) originating in the galaxy’s central regions, e.g., via galactic winds, radiation pressure, ionization, etc. Therefore, the CGM represents a galaxy’s evolving “sphere of influence”.

Since being postulated by Bahcall and Spitzer (1969) more than 50 years ago, evidence for extended (~ 100 pkpc) halos of highly-ionized, metal-enriched gas around galaxies has continuously accumulated. In recent years, there has been increasing attention given to understanding the physics and chemistry of CGM gas as a function of galaxy properties, e.g., environment (Johnson, Chen, and Mulchaey, 2015; Burchett et al., 2016; Nielsen et al., 2018), mass and star-formation rate (Adelberger et al., 2005a; Chen et al., 2010; Tumlinson et al., 2011; Rakic et al., 2012; Johnson et al., 2017; Rubin et al., 2018), and cosmic epoch (Nelson et al., 2019; Hafen et al., 2019; Hummels et al., 2019). In large part, the increased focus on the CGM is attributable to a growing appreciation that diffuse gas outside of galaxies is a laboratory where many of the most important, but poorly understood, baryonic processes can be observed and tested.

Redshifts near the peak of cosmic star formation history, at $z \simeq 2 - 3$ (Madau and Dickinson, 2014), are especially attractive for observations of galaxies and their associated diffuse CGM/IGM gas, due to the accessibility of spectroscopic diagnostics in the rest-frame far-UV (observed optical) and rest-frame optical (observed near-IR) using large ground-based telescopes (see, e.g., Steidel et al., 2014). The most sensitive measurements of neutral hydrogen and metals in diffuse gas in the outer parts of galaxies along the line of sight require high-resolution ($\text{FWHM} \lesssim 10 \text{ km s}^{-1}$), high signal-to-noise ratio (SNR) of bright background continuum sources – i.e., quasi-stellar objects (QSOs). However, QSOs bright enough to be observed in this way are extremely rare, thereby limiting the number of galaxies whose CGM

can be probed. Moreover, each sightline to a suitable background QSO provides at most a single sample, at a single galactocentric distance, for any identified foreground galaxy. This inefficiency makes the assembly of a statistical picture of the CGM/IGM around galaxies at a particular redshift, or having particular properties, very challenging.

Improved efficiency for such QSO sightline surveys can be realized by conducting deep galaxy surveys in regions of the sky *selected* to include the lines of sight to one or more background QSOs, with emission redshifts chosen to optimize the information content of absorption lines in the QSO spectrum given the galaxy redshift range targeted by the survey (e.g., Lanzetta et al., 1995; Chen et al., 2001; Adelberger et al., 2003; Adelberger et al., 2005a; Morris and Jannuzi, 2006; Prochaska et al., 2011; Crighton et al., 2011.) The Keck Baryonic Structure Survey (KBSS¹; Rudie et al., 2012; Steidel et al., 2014; Strom et al., 2017) was designed along these lines, specifically to provide a densely-sampled spectroscopic survey of star-forming galaxies in the primary redshift range $1.9 \lesssim z_{\text{gal}} \lesssim 2.7$ in 15 survey regions, each of which is centered around the line of sight to a very bright QSO with $z \sim 2.7 - 2.8$. The Keck/HIRES spectra of the QSOs, together with the positions and redshifts of the galaxies in each survey region, have been analysed in detail to measure neutral hydrogen (H I) and metals associated with the foreground galaxies. Absorption has been measured as a function of projected galactocentric distance to the QSO sightline and as a function of line-of-sight velocity with respect to the galaxy systemic redshift, using both Voigt profile fitting (Rudie et al., 2012; Rudie et al., 2013; Rudie et al., 2019) and “pixel optical depth” techniques (Rakic et al., 2012; Rakic et al., 2013; Turner et al., 2014; Turner et al., 2015). These studies have shown that there is H I and C IV significantly in excess of the intergalactic mean extending to at least 2.5 physical Mpc around identified galaxies, but with the most prominent excess of both H I and metals lying within $D_{\text{tran}} \sim 200 - 300$ pkpc and $\Delta v_{\text{LOS}} \lesssim 300 - 700$ km s⁻¹. The statistical inferences were based on ~ 900 QSO/galaxy pairs with projected separation $D_{\text{tran}} < 3$ Mpc, but only (90,26,10) sample the CGM within $D_{\text{tran}} \leq (500, 200, 100)$ pkpc. Thus, in spite of the large observational effort behind KBSS, the statistics of diffuse gas surrounding $z \simeq 2 - 2.7$ galaxies is limited to relatively small samples within the inner CGM.

Alternatively, as shown by Steidel et al. (2010) (S2010; see also Adelberger et al., 2005a), it is also possible to use the grid of background *galaxies* – which comes

¹The complete spectroscopic catalogs of the galaxies used in this paper and the processed data can be found at the KBSS website: <http://ramekin.caltech.edu/KBSS>.

“for free” with a densely sampled spectroscopic survey – to vastly increase the number of lines of sight sampling the CGM of foreground galaxies, particularly for small transverse distances (or impact parameter, $D_{\text{tran}} \lesssim 500$ pkpc.) The penalty for increased spatial sampling is, unavoidably, the vastly reduced spectral resolution and SNR – and the associated loss of the ability to resolve individual components and measure column densities along individual sightlines, compared to the HIRES QSO spectra. S2010 used a set of ~ 500 galaxy foreground/background angular pairs with separation $\theta \leq 15''$ to trace the rest-frame equivalent width of Ly α and several strong metal lines as a function of impact parameter over the range $20 \leq D_{\text{tran}}/\text{pkpc} \leq 125$ at $\langle z \rangle = 2.2$. In this paper, we extend the methods of S2010, with significant improvements in both the size and quality of the galaxy sample, to characterize HI absorption over the full range of 20 – 4000 pkpc. Compared to the earlier KBSS QSO/galaxy pairs, the new galaxy/galaxy analysis includes ~ 3000 galaxies, with a factor > 100 increase in the number of sightlines sampled with $D_{\text{tran}} \leq 500$ pkpc.

As discussed by S2010, background galaxies are spatially extended², unlike QSOs, and thus each absorption line probe is in effect averaging over a spatially extended line of sight through the circumgalactic gas associated with the foreground galaxies. CGM gas is known to be clumpy, with indications that the degree of “clumpiness” (i.e., the size scale on which significant variations of the ionic column density are observed) depends on ionization level, with low-ionization species having smaller coherence scales (see Rauch, Sargent, and Barlow, 1999; Rudie et al., 2019). In general, this means that the strength of an absorption feature produced by gas in a foreground galaxy as recorded in the spectrum of a background galaxy will depend on three factors: the fraction of the beam covered by a significant column of the species, the column density in the beam, and the range of line-of-sight velocity (v_{LOS}) sampled by the roughly cylindrical volume through the CGM. The dynamic range in total HI column density measurable using stacks of background galaxy spectra is much smaller (and less quantitative) than could be measured from high-resolution, high SNR QSO spectra. However, using galaxy-galaxy pairs provides much more rapid convergence to the mean CGM absorption as a function of impact parameter, where samples of QSO-galaxy pairs would be limited by sample variance. This improvement – along with the larger sample size – allows us to probe more details in the kinematics and the spatial distribution of HI compared to that obtained from QSO sightlines (e.g. Rudie et al., 2012; Turner et al., 2014; Tummuangpak

²Typical galaxies in the spectroscopic sample have physical sizes of $d \approx 4$ kpc. The diameter of the beam as it traverses a galaxy with $z_{\text{fg}} \approx z_{\text{bg}} - 0.3$ would have a similar physical extent.

et al., 2014; Bielby et al., 2017; and Ryan-Weber, 2006; Tejos et al., 2014 at lower redshifts).

This paper is organized as follows. In §2.2, we describe the KBSS galaxy spectroscopic sample and the steps used in the analysis; §2.3 presents the principal results of the analysis. We discuss the implications of the results in §2.4. Particularly, in §2.4, we compare the results with cosmological zoom-in simulations, and in §2.4, we develop a simple analytic model to describe the 2-D spatial and kinematic distribution of H I on scales $0.020 - 4.0$ pMpc ($\approx 0.06 - 12.0$ cMpc) surrounding typical star-forming galaxies at $z \sim 2$. We summarize our conclusions in §2.5.

Unless stated otherwise, throughout the paper we assume a Λ CDM cosmology with $\Omega_m = 0.3$, $\Omega_\Lambda = 0.7$, and $h = 0.7$. Units of distance are generally given in terms of physical kpc (pkpc) or physical Mpc (pMpc).

2.2 Sample and Analysis

Table 2.1 provides a summary of the KBSS galaxy pairs sample, described in more detail in the remainder of this section.

The KBSS galaxy pairs sample (hereafter KGPS) is drawn from 2862 galaxies in 19 densely sampled survey regions (Table 2.1), of which 15 comprise the nominal KBSS survey (Rudie et al., 2012; Steidel et al., 2014) of bright QSO sightlines. KGPS includes 4 additional fields (GOODS-N, Q1307, GWS, and Q2346) observed using the same selection criteria and instrumental configurations as the KBSS fields, and thus have a similar redshift selection function and similarly-dense spectroscopic sampling. GWS and GOODS-N³ were observed as part of a Lyman break galaxy (LBG) survey targeting primarily the redshift range $2.7 \lesssim z \lesssim 3.4$ (Steidel et al., 2003), but were subsequently supplemented by observations favoring the slightly lower redshift range $1.9 \lesssim z \lesssim 2.7$ selected using a different set of rest-UV color criteria. For all 19 fields, two groups of photometric pre-selection of candidates are included: at $z \sim 3.0 \pm 0.4$, using the MD, C, D, and M criteria described by Steidel et al. (2003); and at $z \sim 2.3 \pm 0.4$, using the BX and BM criteria described by Adelberger et al. (2004) and Steidel et al. (2004), as well as the RK criteria from Strom et al. (2017). The limiting apparent magnitude of the photometric selection is $\mathcal{R} \leq 25.5$ (AB). The galaxies were observed spectroscopically over the period 2002-2016, with the goal of achieving the densest-possible sampling of galaxies in the redshift range $2 \lesssim z \lesssim 3$.

³Referred to as “Westphal” and “HDF-N”, respectively, by Steidel et al. (2003).

Table 2.1: Field-by-field summary of the properties of the KBSS Galaxy Pair Sample.

Field Name	RA ^a (J2000.0)	DEC ^a (J2000.0)	Area ^b (arcmin ²)	N_{gal} ($z > 1.9$)	N_{pair}^c (Full/ z_{neb}) ^d	$\langle z_{\text{fg}} \rangle$ (Full/ z_{neb}) ^d	$\Delta z_{\text{fb}} / (1 + z_{\text{fg}})$ (Full/ z_{neb}) ^d
Q0100	01:03:11	+13:16:27	7.6 × 5.6	153	762/441	2.11/2.11	0.108/0.111
Q0105	01:08:08	+16:35:30	7.4 × 5.3	137	519/296	2.15/2.12	0.103/0.108
Q0142	01:45:15	-09:45:30	7.2 × 5.2	131	572/320	2.21/2.22	0.113/0.116
Q0207	02:09:52	-00:05:22	7.0 × 5.4	133	480/296	2.15/2.15	0.130/0.140
Q0449	04:52:14	-16:40:29	6.5 × 5.0	128	561/297	2.28/2.23	0.108/0.105
Q0821	08:21:05	+31:07:42	7.3 × 5.5	124	413/242	2.35/2.35	0.112/0.113
Q1009	10:11:55	+29:41:36	7.2 × 5.2	141	552/325	2.44/2.31	0.125/0.129
Q1217	12:19:33	+49:40:46	6.9 × 5.1	93	242/90	2.19/2.19	0.101/0.109
GOODS-N ^e	12:36:52	+62:14:20	14.3 × 10.4	249	590/209	2.27/2.31	0.108/0.142
Q1307	13:07:54	+29:22:24	10.0 × 11.0	71	93/—	2.13/—	0.113/—
GWS	14:17:47	+52:28:49	15.1 × 14.8	228	270/12	2.82/2.92	0.081/0.084
Q1442	14:44:54	+29:19:00	7.3 × 5.1	137	613/373	2.29/2.34	0.124/0.122
Q1549	15:51:55	+19:10:53	7.1 × 5.2	144	605/297	2.36/2.29	0.111/0.131
Q1603	16:04:57	+38:11:50	7.2 × 5.4	112	354/166	2.27/2.28	0.083/0.080
Q1623	16:25:52	+26:47:58	16.1 × 11.6	284	781/239	2.18/2.24	0.108/0.104
Q1700	17:01:06	+64:12:02	11.5 × 11.0	210	585/337	2.29/2.29	0.103/0.103
Q2206	22:08:54	-19:43:35	7.5 × 5.4	119	457/183	2.15/2.16	0.113/0.116
Q2343	23:46:20	+12:47:28	11.5 × 6.3	224	859/610	2.17/2.17	0.096/0.103
Q2346	23:48:31	+00:22:42	11.8 × 10.3	44	43/7	2.07/2.03	0.067/0.070
All			1447	2862	9351/4741	2.23/2.22	0.106/0.113

^a Mean coordinates for galaxies with spectroscopic redshifts $z > 1.9$.

^b Angular size of field over which spectroscopy was performed; (long axis × short axis, both in arc minutes).

^c The number of distinct foreground/background galaxy pairs with $D_{\text{tran}} < 500$ pkpc. Numbers for other ranges of D_{tran} can be estimated based on Figure 2.3.

^d The KGPS-Full sample and the KGPS- z_{neb} subsample. See §2.2 for definitions.

^e Full catalog published in Reddy et al., 2006; the majority of nebular redshifts in the GOODS-N region are as reported by the MOSDEF survey (Kriek et al., 2015).

The survey regions listed in Table 2.1 are identical to those included in the analysis of galaxy-galaxy pairs by Steidel et al. (2010); however the current spectroscopic catalog is larger by $\sim 30\%$ in terms of the number of galaxies with spectroscopic redshifts in the most useful range ($1.9 \lesssim z \lesssim 3.0$), increasing the number of pairs sampling angular scales of interest by $\gtrsim 70\%$. More importantly, as detailed in §2.2 below, $\sim 50\%$ of the foreground galaxies in KGPS pairs have precisely-measured systemic redshifts (z_{neb}) from nebular emission lines observed in the near-IR, compared with only a handful available for the S2010 analysis.

We use the substantial subset of galaxies with nebular emission line measurements to improve the calibrations of systemic redshifts inferred from measurements of spectral features in the rest-frame UV (observed frame optical) spectra (§2.2). The much improved redshift precision and accuracy⁴ – as well as a more careful construction of composite (stacked) spectra (§2.2) – allow us to extend the technique using galaxy foreground-background pairs to angular separations far beyond the $\theta = 15$ arcsec ($D_{\text{tran}} \simeq 125$ pkpc) used by Steidel et al. (2010). The various improvements represented by KGPS significantly increase the sampling density and S/N ratio (SNR) of the H I absorption measurements as a function of impact parameter (D_{tran}). As we show in the next section, this leads to a major improvement compared to S2010, allowing us to resolve and model details of the kinematic structure of the H I with respect to the galaxies.

Subsets of the KGPS sample have figured prominently in many previous investigations involving galaxies and the CGM/IGM at $1.9 \lesssim z \lesssim 3.5$. In what follows below, we direct the reader to the most relevant references for more information on some of the details. All of the rest-UV spectra were obtained using the Low Resolution Imaging Spectrograph (LRIS; Oke et al., 1995) on the Keck I telescope; the vast majority were obtained after June 2002, when LRIS was upgraded to a dual-channel configuration (see Steidel et al., 2004).

A small subset of the $z \sim 2$ – 2.6 galaxies in earlier catalogs in some of the fields listed in Table 2.1 was observed in the near-IR using Keck/NIRSPEC (Erb et al., 2006b; Erb et al., 2006c; Erb et al., 2006a); the sample was used to calibrate UV measurements of systemic redshifts by Steidel et al. (2010). However, the vast majority of the nebular redshifts used in this paper were obtained using the Multi-Object Spectrometer for InfraRed Exploration (MOSFIRE; McLean et al., 2012;

⁴The number of galaxies with insecure or incorrect redshifts is also greatly reduced compared to S2010.

Steidel et al., 2014) beginning in 2012 April. MOSFIRE observations in all but the GOODS-N field⁵ were obtained as part of KBSS-MOSFIRE (see Steidel et al., 2014; Strom et al., 2017 for details.)

The statistical properties of the galaxies in the KGPS sample are as described in previous work: stellar masses $8.6 \lesssim \log(M_*/M_\odot) \lesssim 11.4$ (median ≈ 10.0), star formation rates $2 \lesssim SFR/(M_\odot yr^{-1}) \lesssim 300$ (median ≈ 25) (Shapley et al., 2005; Erb et al., 2006b; Erb et al., 2006c; Reddy et al., 2008; Reddy et al., 2012; Steidel et al., 2014; Strom et al., 2017; Theios et al., 2019), and clustering properties indicate host dark matter halos of typical mass $\langle \log(M_h/M_\odot) \rangle = 11.9 \pm 0.1$ (Adelberger et al., 2005b; Trainor and Steidel, 2012).

Rest-Frame Far-UV Spectra

All of the rest-UV spectra used in this work were obtained with the Low Resolution Imaging Spectrometer (LRIS; Oke et al., 1995; Steidel et al., 2004) on the Keck I 10m telescope; most were obtained between 2002 and 2016, after LRIS was upgraded to a dual-beam spectrograph. Most of the spectra used here were obtained using the blue channel (LRIS-B), with one of two configurations: a 400 line/mm grism blazed at 3400 Å in first order, covering 3200-6000 Å, or a 600 line/mm grism blazed at 4000 Å, typically covering 3400-5600 Å. Approximately half of the slitmasks were observed with each configuration. Further details on the observations and reductions with LRIS-B are given in, e.g., Steidel et al. (2004), Steidel et al. (2010), and Steidel et al. (2018).

The total integration time for individual objects ranges from 5400s to >54,000s. About 40% of the galaxies were observed with two or more masks, particularly in the KBSS fields for which the field size is comparable to the 5'5 by 7'5 field of view of LRIS. Examples of typical reduced 1-D spectra are shown in Figure 2.1. The wavelength solutions for the LRIS-B spectra were based on polynomial fits to arc line lamp observations using the same mask and instrument configuration, which have typical residuals of ≈ 0.1 Å. Small shifts between the arc line observations and each 1800s science exposure were removed during the reduction process with reference to night sky emission features in each science frame. The wavelength calibration uncertainties make a negligible contribution to the redshift measurement errors (§2.2).

⁵Nebular redshifts of 89 galaxies in our catalog were obtained by the MOSFIRE Deep Evolution Field Survey (MOSDEF; Kriek et al., 2015.)

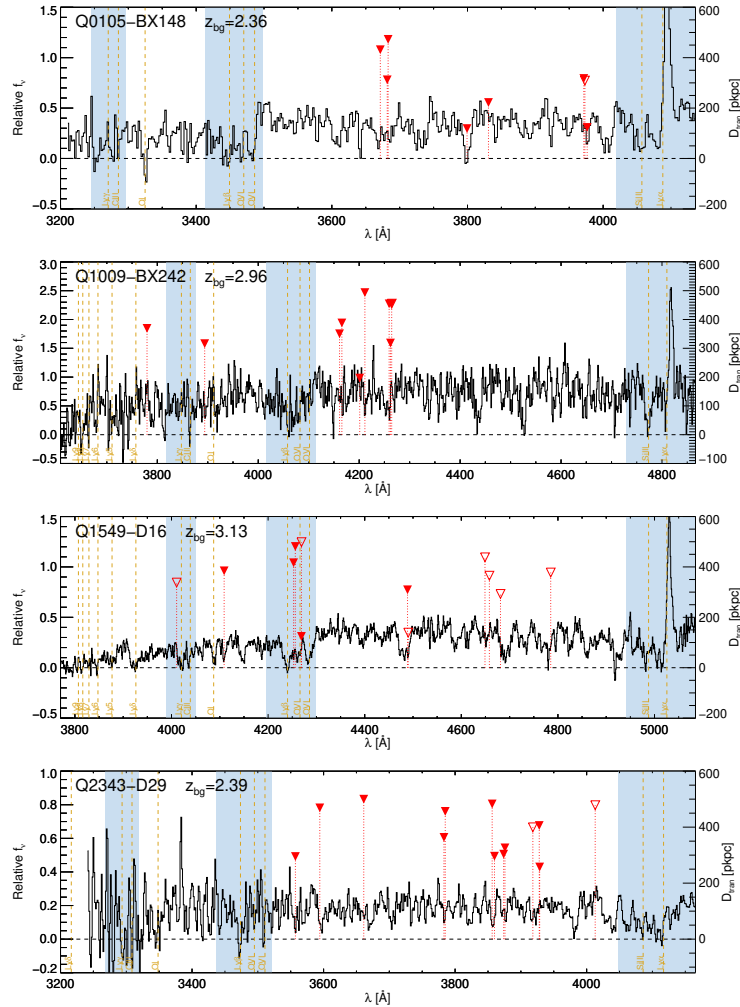


Figure 2.1: Randomly-selected examples of individual rest-UV spectra of background galaxies in KGPS. Wavelengths are in the observed frame, with red triangles marking the position of Ly α $\lambda 1215.67$ at wavelengths $1215.67(1 + z_{\text{fg}})$ \AA for each foreground galaxy with projected distance $D_{\text{tran}} \leq 500$ pkpc. The solid (open) triangles correspond to foreground galaxies whose systemic redshifts are based on z_{neb} (z_{UV}). Their typical redshift uncertainties, in terms of observed wavelength, are ~ 0.2 \AA (1.8 \AA) at $z = 2.2$ as estimated in §2.2. The y-coordinate of each triangle indicates D_{tran} for the foreground galaxies, with reference to the scale marked on the righthand side of each plot. The light shaded regions are those that would be masked prior to using the spectrum to form composites stacked in the rest frame of foreground galaxies (see §2.2 & Table 2.2), to minimise contamination by spectral features at $z = z_{\text{bg}}$. The yellow vertical lines indicate UV absorption lines arising in the ISM of the background galaxy. Note that some foreground galaxies have clear counterparts in the Ly α forest, even in low-resolution spectra.

Each reduced 1-D spectrum⁶ was examined interactively, in order to mask regions of very low SNR, poor background subtraction, unphysical flux calibration, or previously unmasked artifacts (e.g., cosmic rays, bad pixels) that were not recognized during data reduction. A total of 280 spectra (out of nearly 10,000 in total) were entirely discarded because of generally poor quality or unphysical continuum shape. Spectra of the same object observed on multiple masks and/or with multiple spectroscopic setups were assigned individual weights according to spectral quality, based on a combination of visual inspection and exposure time. They were then resampled onto a common wavelength grid with the finest sampling of the individual spectra to preserve the spectral resolution (using cubic-spline interpolation), and averaged together to create a single spectrum for each object.

Calibration of Systemic Redshifts

Spectral features commonly observed in the far-UV spectra of high redshift star-forming (SF) galaxies – Ly α emission, when present, and interstellar (IS) absorption from strong resonance lines of, e.g., Si II, Si IV, C II, C IV, O I—are rarely found at rest with respect to the stars in the same galaxy due to gas motions and radiative transfer effects (e.g., Steidel et al., 1996; Franx et al., 1997; Lowenthal et al., 1997; Pettini et al., 2001; Shapley et al., 2003; Erb et al., 2006c). Clearly, measuring the kinematics of diffuse gas in the CGM of foreground galaxies benefits from the most accurate available measurements of each galaxy’s systemic redshift (z_{sys}).

The centroids of nebular emission lines from ionized gas (i.e., H II regions) are less strongly affected by galaxy-scale outflows and radiative transfer effects, and are generally measured with significantly higher precision, than the rest-FUV features. As previously noted, 50% of the foreground galaxies used in this work have measurements of one or more strong nebular emission lines in the rest-frame optical (observed frame J, H, K bands) using MOSFIRE. Independent observations of the same galaxies with MOSFIRE have demonstrated redshift precision (i.e., rms repeatability) of $\sigma_v \simeq 18 \text{ km s}^{-1}$ (Steidel et al., 2014).

For the 50% of foreground galaxies lacking nebular emission line measurements, we used estimates of z_{sys} based on the full KBSS-MOSFIRE sample (Steidel et al., 2014; Strom et al., 2017) with $z_{\text{neb}} > 1.9$ and existing rest-UV LRIS spectra. These were used to calibrate relationships between z_{sys} and redshifts measured from features in the rest-frame FUV spectra, strong interstellar absorption lines

⁶For galaxies observed on multiple masks, each independent 1-D spectrum was examined separately.

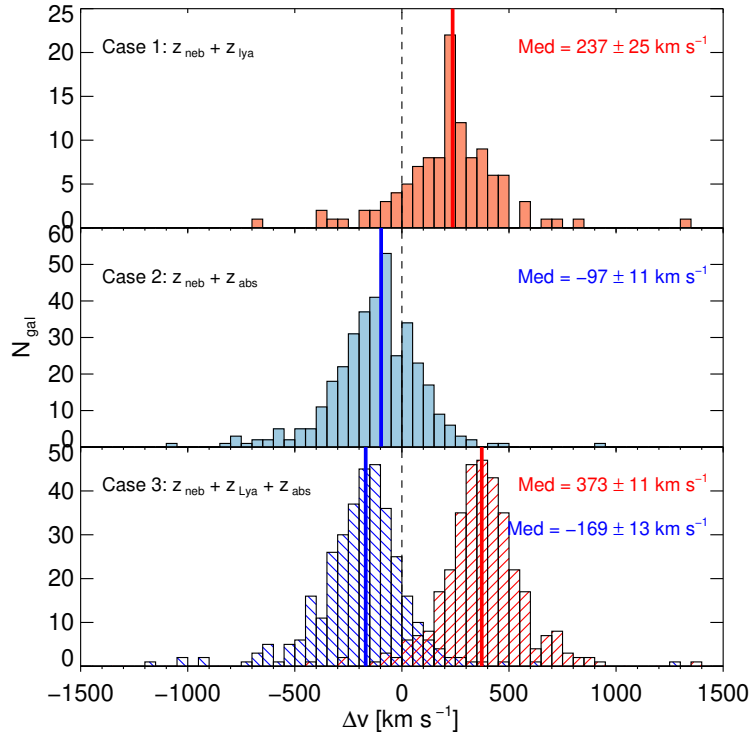


Figure 2.2: Distribution of velocity differences between $z_{\text{Ly}\alpha}$ ($\Delta v_{\text{Ly}\alpha}$, in red) or z_{IS} (Δv_{IS} , in blue) and the systemic redshift measured from z_{neb} . Top-right of each panel shows the median shift in velocity and its error estimated by dividing the standard deviation by the square-root of the number of galaxies. These distributions have been used to calibrate the systemic redshifts of galaxies in Equations 2.1–2.3, for which only the UV spectral features are available.

(z_{IS}) and/or the centroid of Lyman- α emission ($z_{\text{Ly}\alpha}$). As for previous estimates of this kind (e.g., Adelberger et al., 2003; Steidel et al., 2010; Rudie et al., 2012), we adopt rules that depend on the particular combination of features available in each spectrum. Figure 2.2 shows the distribution of velocity offsets of the UV redshift measurements relative to z_{neb} , $\Delta v_{\text{Ly}\alpha} = c(z_{\text{Ly}\alpha} - z_{\text{neb}})/(1 + z_{\text{neb}})$ and/or $\Delta v_{\text{IS}} = c(z_{\text{IS}} - z_{\text{neb}})/(1 + z_{\text{neb}})$ for the three cases below. The median velocity offsets (see Figure 2.2) for the three sub-samples were then used to derive the following relationships that map UV redshift measurements to an estimate of z_{sys} :

- Case 1: $z_{\text{Ly}\alpha}$ only,

$$z_{\text{sys}} = z_{\text{Ly}\alpha} - \frac{237 \text{ km s}^{-1}}{c}(1 + z_{\text{Ly}\alpha}), \quad (2.1)$$

- Case 2: z_{IS} only,

$$z_{\text{sys}} = z_{\text{IS}} + \frac{97 \text{ km s}^{-1}}{c} (1 + z_{\text{IS}}). \quad (2.2)$$

- Case 3: $z_{\text{Ly}\alpha}$ and z_{IS} ,

if $z_{\text{Ly}\alpha} > z_{\text{IS}}$,

$$z_{\text{sys}} = \frac{1}{2} \left\{ \left[z_{\text{Ly}\alpha} - \frac{373 \text{ km s}^{-1}}{c} (1 + z_{\text{Ly}\alpha}) \right] + \left[z_{\text{IS}} + \frac{169 \text{ km s}^{-1}}{c} (1 + z_{\text{IS}}) \right] \right\}; \quad (2.3)$$

otherwise,

$$z_{\text{sys}} = \frac{1}{2} (z_{\text{Ly}\alpha} + z_{\text{abs}}). \quad (2.4)$$

When the above relations are used to estimate $z_{\text{sys,uv}}$ on an object-by-object basis, applied to the UV measurements of the redshift calibration sample on an object-by-object basis, the outlier-clipped mean and rms of the velocity difference between z_{neb} and $z_{\text{sys,uv}}$ are

$$\langle c(z_{\text{sys,uv}} - z_{\text{neb}})/(1 + z_{\text{neb}}) \rangle = -5 \pm 143 \text{ km s}^{-1}, \quad (2.5)$$

implying that we expect negligible systematic offset in cases where only $z_{\text{sys,uv}}$ is available, with $\sigma_z \simeq 140 \text{ km s}^{-1}$.

In what follows below, we define the subsample of galaxy foreground-background pairs for which $z_{\text{sys,fg}}$ is based on z_{neb} as the ‘‘KGPS- z_{neb} ’’ sample, with $\sigma_z \simeq 18 \text{ km s}^{-1}$; the ‘‘KGPS-Full’’ sample includes all of KGPS- z_{neb} plus the remaining pairs for which $z_{\text{sys,fg}}$ is estimated from the rest-UV spectra according to Equations 2.1–2.3. The fraction of pairs with $z_{\text{sys,fg}}$ estimated from rest-UV features is consistently $\simeq 50\%$ at $D_{\text{tran}} < 1 \text{ pMpc}$, but gradually decreases to $\simeq 40\%$ from $D_{\text{tran}} \simeq 1 \text{ pMpc}$ to 4 pMpc .

Assembly of Galaxy Foreground-Background Pairs

We assembled samples of KGPS galaxy pairs ($z_{\text{fg}}, z_{\text{bg}}$) according to several criteria designed to optimize the measurement of weak absorption lines near the redshift z_{fg} in the spectrum of the background galaxy:

1. The background galaxy has one or more LRIS spectra.

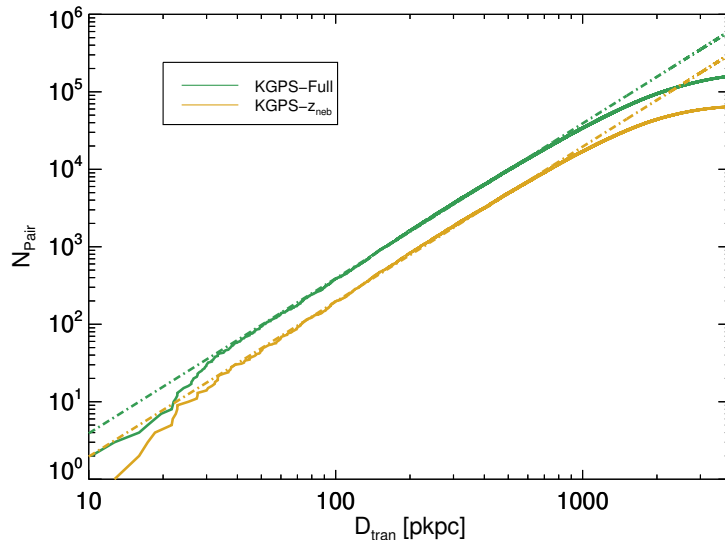


Figure 2.3: The cumulative number of pairs as a function of impact parameter $D_{\text{tran}}(z_{\text{fg}})$ for the KGPS-Full sample (green), the KGPS- z_{neb} sample (yellow). The solid curves are the actual number of pairs, and the dashed-dotted lines are quadratic fits over the range $50 \text{ pkpc} < D_{\text{tran}} < 500 \text{ pkpc}$ for each of the KGPS samples. The smaller number of pairs (relative to the quadratic extrapolation) at very small D_{tran} results from observational biases caused by geometrical slitmask constraints and finite angular resolution of the ground-based images used for target selection. At large D_{tran} , the pair count falls below the quadratic fit as the angular separation approaches the size of the KBSS survey regions.

2. The foreground galaxy does not host a known Type I or Type II active galactic nucleus⁷.
3. The paired galaxies have redshifts $(z_{\text{fg}}, z_{\text{bg}})$ such that

$$0.017(1 + z_{\text{fg}}) < \Delta z_{\text{fb}} < 0.3(1 + z_{\text{fg}}), \quad (2.6)$$

where $\Delta z_{\text{fb}} = z_{\text{bg}} - z_{\text{fg}}$. This is equivalent to $5100 \text{ km s}^{-1} < \Delta v_{\text{LOS}} < 90000 \text{ km s}^{-1}$, or $37 \text{ pMpc} < D_{\text{LOS}} < 520 \text{ pMpc}$ at $z = 2.2$, assuming pure Hubble flow, where Δv_{LOS} and D_{LOS} are velocity difference and distance in the line-of-sight direction.

The lower limit on Δz_{fb} ensures that the two galaxies are not physically associated, so that any absorption features detected near z_{fg} are well-separated from features at z_{bg} and are not part of the same large scale structure in which the background

⁷Pairs for which the foreground object harbors an AGN will be considered in a separate paper

galaxy resides. An upper limit on $\Delta z_{\text{fb}}/(1+z_{\text{fg}})$ was set by S2010 to maximise the detectability of C IV $\lambda\lambda 1548, 1550$ at z_{fg} by ensuring that it would fall longward of the Ly α forest in the spectrum of the background galaxy, i.e.

$$(1+z_{\text{fg}})1549\text{\AA} > (1+z_{\text{bg}})1215.67\text{\AA} \quad (2.7)$$

for typical $z_{\text{bg}} \sim 2.4$. In the present case, using a more empirical approach, we tested different upper limits on $\Delta z_{\text{fb}}/(1+z_{\text{fg}})$ in order to optimize the SNR of the final stacks. In principle, if one is interested in detecting Ly α absorption, large $\Delta z_{\text{fb}}/(1+z_{\text{fg}})$ would increase the relative contribution of the shorter wavelength, noisier portions of the background galaxy spectra, particularly when regions shortward of Ly β at $z = z_{\text{bg}}$ [i.e., $\lambda \leq (1+z_{\text{bg}})1025.7\text{\AA}$] are included. On the other hand, choosing a small upper limit on $\Delta z_{\text{fb}}/(1+z_{\text{fg}})$ would increase the noise by significantly decreasing the number of spectra contributing. Depending on the strength of the Ly α absorption, we found that the SNR does not depend strongly on the upper limit so long as it is close to $\Delta z_{\text{fb}}/(1+z_{\text{fg}}) \simeq 0.30$, similar to the upper limit used by Steidel et al. (2010) ($\Delta z_{\text{fb}}/(1+z_{\text{fg}}) \simeq 0.294$ for $z_{\text{bg}} \simeq 2.4$).

Figure 2.3 shows the cumulative number of galaxy pairs as a function of D_{tran} between the foreground galaxy and the line of sight to the background galaxy, evaluated at z_{fg} . The cumulative number of distinct pairs varies as D_{tran}^2 (dashed lines in Figure 2.3; as expected for uniform sampling of a constant surface density of galaxies) over the range $50 \leq D_{\text{tran}}/\text{pkpc} \leq 500$. The departure of the observed number of pairs falls below the quadratic extrapolation for $D_{\text{tran}} < 30\text{ pkpc}$ (angular scales of $\theta \lesssim 3''.6$ at $z \sim 2.2$) due to a combination of limited spatial resolution of the ground-based images used to select targets, and the constraints imposed by slit assignment on LRIS slitmasks. For $D_{\text{tran}} \gtrsim 1\text{ pMpc}$ ($\theta \gtrsim 2\text{ arcmin}$ at $z = 2.2$), the number of pairs begins to be limited by the size of individual survey regions (see Table 2.1). Over the range $30 < D_{\text{tran}}/\text{pkpc} < 1000$, the number of pairs is well represented by a quadratic function,

$$\text{KGPS-Full: } N_{\text{pair}}(< D_{\text{tran}}) = 39069 \times \left(\frac{D_{\text{tran}}}{1\text{ pMpc}} \right)^2, \quad (2.8)$$

and

$$\text{KGPS-}z_{\text{neb}}: N_{\text{pair}}(< D_{\text{tran}}) = 19577 \times \left(\frac{D_{\text{tran}}}{1\text{ pMpc}} \right)^2. \quad (2.9)$$

Figure 2.4 shows the distributions of z_{fg} and $\Delta z_{\text{fb}}/(1+z_{\text{fg}})$ for both the KBSS-Full and KBSS- z_{neb} samples. The difference in the z_{fg} distributions is caused

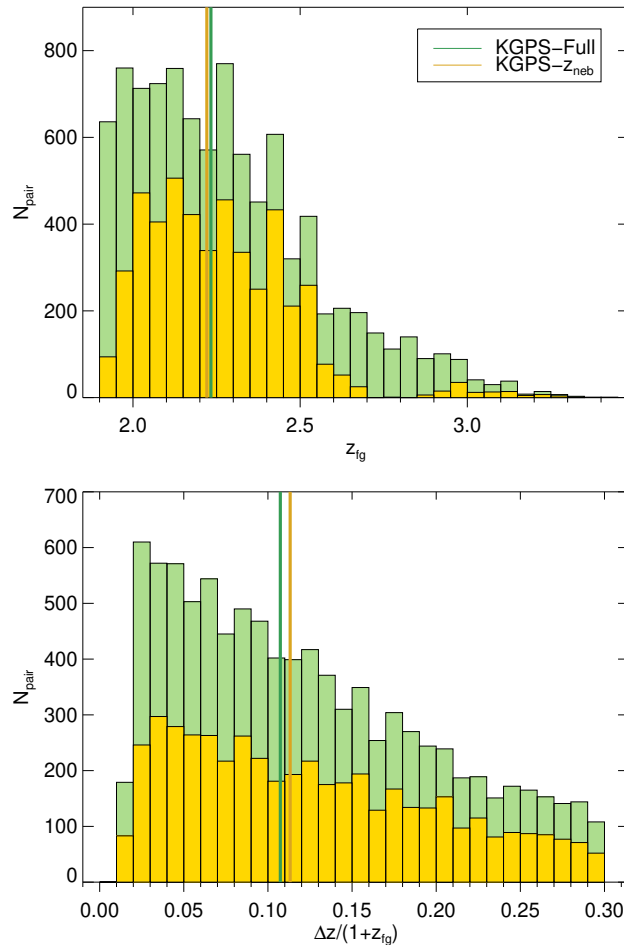


Figure 2.4: Distribution of z_{fg} (top) and $\Delta z_{fb}/(1 + z_{fg})$ (bottom) for foreground-background galaxy pairs with $D_{\text{tran}} < 4.7$ pMpc. The vertical lines mark the median values of each distribution. The KGPS-Full and KGPS- z_{neb} samples have similar distributions of both z_{fg} and $\Delta z_{fb}/(1 + z_{fg})$.

by gaps in redshift for the KBSS- z_{neb} sample that correspond to regions of low atmospheric transmission between the J, H, and K bands. However, in spite of this, the distributions of $\Delta z_{fb}/(1 + z_{fg})$ remain very similar. The median foreground galaxy redshift is $\langle z_{fg} \rangle_{\text{med}} = 2.23$ for the KGPS-Full sample, and $\langle z_{fg} \rangle_{\text{med}} = 2.22$ for the KGPS- z_{neb} sample; the median value of the redshift differences between the foreground and background galaxies are $\Delta z_{fb}/(1 + z_{fg}) = 0.106$ and 0.113 , respectively.

Composite Spectra

The typical spectrum of an individual galaxy in the KGPS sample has SNR per spectral resolution element of only 1–6 in the region shortward of $\text{Ly}\alpha$ in the galaxy

Table 2.2: Masked background spectral regions

λ (Å)	$\Delta z_{\text{fb}}/(1 + z_{\text{fg}})$	Spectral Features
965 – 980	0.2405 – 0.2598	Ly γ , C III λ 977
1015 – 1040	0.1689 – 0.1977	Ly β , O VI λ 1031,1036
1195 – 1216	0 – 0.0173	Si III λ 1206, Ly α

rest frame. Individual spectra also include absorption from other spectral lines due to the interstellar and circumgalactic medium of the galaxy itself – whose locations are predictable – and intervening absorption caused by gas at redshifts different from the foreground at which a measurement of Ly α absorption is made ⁸. Both problems – limited SNR of faint background galaxy spectra, and contamination from absorption at other redshifts – are mitigated by forming “stacks” of many spectra sampling a particular range of D_{tran} for an ensemble of foreground galaxies probed by background galaxies.

A distinct advantage of stacking, particularly when it comes to detecting absorption lines arising from gas at a particular redshift, is that one naturally suppresses small-wavelength-scale noise caused by contamination from absorption lines at redshifts other than that of the foreground galaxies of interest. With a suitable number of spectra comprising a stack, unrelated (stochastic) absorption will produce a new, lower, effective continuum level against which the Ly α absorption due to the foreground galaxy ensemble can be measured. The amount by which the continuum is lowered depends on z_{fg} , and is expected to be close to the mean Ly α forest flux decrement $D_A(z)$ (Oke and Korycansky, 1982). At $z \sim 2$ –2.5 most relevant for the KGPS sample, $D_A \simeq 0.2$, i.e., a reduction in the apparent continuum level near Ly α of $\simeq 20\%$. Thus, any residual Ly α absorption is equivalent to an H I “overdensity”, in the sense that it signals the amount by which H I gas associated with the foreground galaxy exceeds the mean IGM absorption at the same redshift.

We arranged galaxy pairs into bins of D_{tran} , and stacked the spectra of all of the background galaxies in the same bin of D_{tran} after (1) normalizing the flux-calibrated background galaxy spectra to have unity median flux density evaluated over the z_{bg} -frame rest wavelength interval $1300 \leq \lambda_{\text{bg},0}/\text{Å} \leq 1400$; (2) masking regions of the background galaxy spectra corresponding to the locations of strong absorption lines or sets of absorption lines at $z = z_{\text{bg}}$; the relevant spectral ranges are given in

⁸In the case of QSO sightlines, the problem of contamination also exists, but is partially overcome by observing at very high spectral resolution.

Table 2.2; (3) shifting the result to the rest-frame of the foreground galaxy, i.e.,

$$\lambda_{\text{fg},0} = \lambda_{\text{bg,obs}} / (1 + z_{\text{fg}}) \quad ; \quad (2.10)$$

and (4) resampling the normalized, masked, and z_{fg} -shifted spectra onto a common range of rest wavelength and combining to form a composite rest-frame spectrum representing the bin in D_{tran} .

The normalization in (1) was performed in order to give roughly equal weight to each galaxy pair in a given bin of D_{tran} without requiring an actual continuum fit to each low-SNR spectrum. We found that continuum fitting is less prone to large systematic errors (e.g., Faucher-Giguère et al., 2008) when it is performed for the composite spectra after stacking, rather than for individual spectra, particularly within the Ly α forest where it would be difficult to perform the fit reliably in the face of both shot noise and real Ly α forest absorption. Error spectra for each stack were generated using bootstrap resampling of the galaxy ensemble, which should account for both sample variance and random (Poisson) errors. Step (2) was implemented in order to reduce contamination by unrelated absorption features near z_{bg} by excluding pixels known to be contaminated; the wavelength ranges listed in Table 2.2 were adopted based on tests using larger or smaller masked intervals⁹. For step (3), we used the best available systemic redshift of the foreground galaxy (§2.2).

We experimented with several different methods for accomplishing step (4) before adopting a straight median of unmasked pixels at each dispersion point; details of the tests are summarized in Appendix 2.5. The median algorithm produces composite spectra with SNR comparable to the best σ -clipped mean algorithm, but has the added benefit of computational and conceptual simplicity.

To remove the continuum, each composite spectrum was divided into 200-Å segments; for each segment, we calculated the mean value (with 2.5- σ clipping applied) of the flux density; the mean flux density and mean wavelength within each segment were then used to constrain a cubic spline fit to the continuum flux density as a function of wavelength, as illustrated in Figure 2.5. The composite spectra were then divided by the initial continuum fit, after which the continuum level of each normalized spectrum was further adjusted by dividing by the linear interpolation of pixels within two windows fixed in velocity relative to the nominal rest-wavelength

⁹Note that masking a particular range of rest-wavelength in the frame of each background galaxy is similar to eliminating pairs having a particular range of $\Delta z_{\text{fb}} / (1 + z_{\text{fg}})$. These intervals are also provided in Table 2.2.

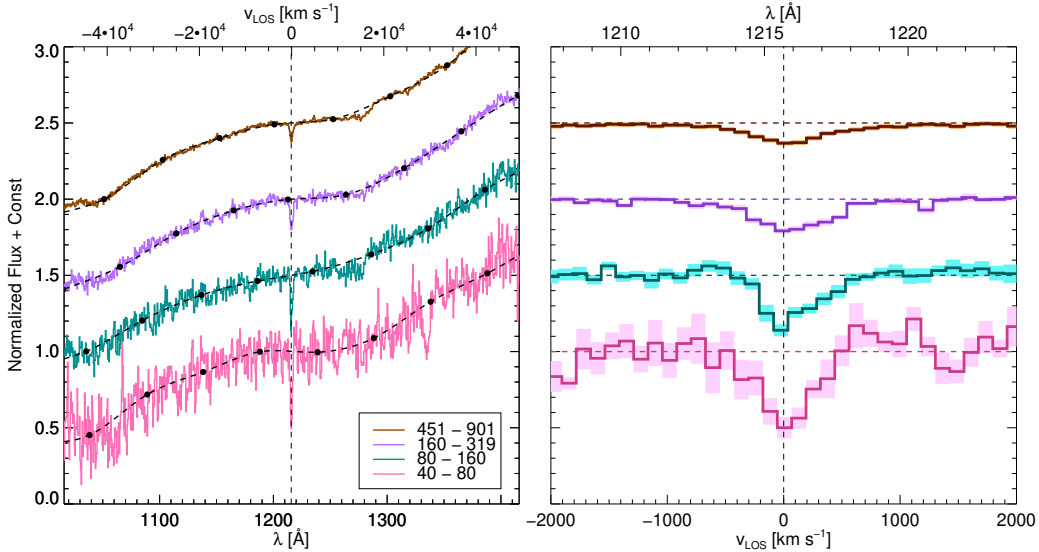


Figure 2.5: Example composite spectra near $\text{Ly}\alpha$ in the rest frame of foreground galaxies for four different bins of D_{tran} . The left panel shows the spectra before continuum-normalization. The black curves with dots are the fitted continua and spline points used for cubic interpolation. The legend indicates the range in pkpc for the bin in D_{tran} . The right-hand panel shows normalized spectra near $\text{Ly}\alpha$, along with their 1σ uncertainty (shaded histogram). In both panels, the spectra shown have been shifted relative to one another by 0.5 in y for display purposes. The vertical dashed line is the rest wavelength of $\text{Ly}\alpha$, 1215.67 Å. The $\text{Ly}\alpha$ absorption profiles in the composite spectra clearly vary in both depth and width with D_{tran} . The clear asymmetry in the velocity profiles of the two middle spectra ([50-100] and [160-319] pkpc) is discussed in §2.4 below.

of $\text{Ly}\alpha$: $3000 \text{ km s}^{-1} < |\Delta v_{\text{Ly}\alpha}| < 5000 \text{ km s}^{-1}$. Figure 2.5 shows examples of the z_{fg} -frame stacked spectra before and after dividing by a fitted continuum. Both the velocity width and the depth of the excess $\text{Ly}\alpha$ absorption associated with the foreground galaxies clearly varies with D_{tran} .

2.3 HI Absorption

$\text{Ly}\alpha$ Rest Equivalent Width [$W_\lambda(\text{Ly}\alpha)$]

Expressing the total strength of $\text{Ly}\alpha$ absorption in terms of the rest-frame equivalent width [hereafter $W_\lambda(\text{Ly}\alpha)$] is appropriate in the present case, where the velocity structure is only marginally resolved. Because $W_\lambda(\text{Ly}\alpha)$ does not depend on the spectral resolution of the observed spectra (provided it is sufficient to allow accurate placement of the continuum level), it is also useful for comparisons among samples obtained with different spectral resolution. $W_\lambda(\text{Ly}\alpha)$ is also entirely empirical,

and does not depend on any assumptions regarding the fine-scale kinematics or component structure of the absorbing gas.

In KGPS, which uses composite spectra of many background galaxies, $W_\lambda(\text{Ly}\alpha)$ is modulated by a potentially complex combination of the mean integrated covering fraction of absorbing gas, its line-of-sight (LOS) kinematics for an ensemble of sightlines falling within a range of D_{tran} relative to foreground galaxies, and the total column density of H I. As discussed above (see also S2010), the finite “footprint” of the image of a background galaxy projected onto the gas distribution surrounding a foreground galaxy also means that the $\text{Ly}\alpha$ absorption profile may depend on the spatial variations on scales of a few pkpc¹⁰ for CGM sightlines near individual galaxies. However, given a sample of foreground galaxies, the average dependence of $W_\lambda(\text{Ly}\alpha)$ on D_{tran} should be identical for extended (galaxy) and point-like (QSO) background sources so long as the number of sightlines is large enough to overcome sample variance within each bin of D_{tran} .

For a sample of galaxy pairs as large as KGPS, where both the width and depth of the $\text{Ly}\alpha$ profile varies with D_{tran} (Figure 2.5), it is desirable to develop a robust method for automated measurement of $W_\lambda(\text{Ly}\alpha)$ while maximizing the SNR. For spectra of limited continuum SNR – particularly where the absorption line profile has a spectral shape that is unknown *a priori*, the size of the measurement aperture has a significant effect on the SNR of the $\text{Ly}\alpha$ line; it should not be unnecessarily large, which would contribute unwanted noise without affecting the net signal, nor so small that it would exclude significant absorption signal. We set the integration aperture using 2-D maps of apparent optical depth (Figure 2.8; to be discussed in detail in §2.3): when $D_{\text{tran}} < 100$ pkpc, we set the aperture width to $\Delta v = 1400 \text{ km s}^{-1}$ ($\Delta\lambda_0 \approx 11.35 \text{ \AA}$), centered on the nominal rest wavelength of $\text{Ly}\alpha$; otherwise, the width of the aperture is set to,

$$\Delta v = 1000 \langle \log(D_{\text{tran}}/\text{pkpc}) \rangle - 600 \text{ km s}^{-1}, \quad (2.11)$$

also centered on rest-frame $\text{Ly}\alpha$.

Figure 2.6 shows $W_\lambda(\text{Ly}\alpha)$ measured from the KGPS-Full sample as a function of D_{tran} with the bin size in D_{tran} set to be 0.3 dex, together with measurements from S2010 for galaxy-galaxy foreground/background pairs and from Turner et al. (2014) for foreground galaxy-background QSO pairs from the KBSS survey. The points

¹⁰The typical effective radius of the background galaxies in the KBSS sample is $r_e \approx 1.5$ pkpc (Law et al., 2012).

from Turner et al. (2014) were measured from the spectra of only 17 background QSOs in the 15 KBSS fields, evaluated at the redshifts of foreground galaxies within ≈ 4.2 drawn from essentially the same parent galaxy sample as KGPS. For $D_{\text{tran}} > 400$ pkpc, where the sample variance of QSO-galaxy sightlines is relatively small, there is excellent agreement between KGPS-Full and Turner et al. (2014), as expected. At smaller D_{tran} , the QSO sightline measurements are not as detailed, although they remain statistically consistent given the larger uncertainties. Although the QSO spectra used by Turner et al. (2014) are far superior to the KGPS galaxy spectra in both resolution ($\sigma_v \approx 8 \text{ km s}^{-1}$ versus $\sigma_v \approx 190 \text{ km s}^{-1}$) and SNR (≈ 100 versus \approx a few), the QSO-based measurements are less precise for the ensemble. This is because both the local continuum level and the net absorption profile contribute to the uncertainty. In the case of the QSO sightlines, the stochastic variations in the mean Ly α forest opacity in the QSO spectra in the vicinity of z_{fg} modulate the apparent continuum against which excess Ly α absorption at z_{fg} is evaluated, and have a large sample variance in the absorption strength at fixed D_{tran} . The points in Figure 2.6 from S2010 were measured using stacked LRIS spectra of a subset of the current KGPS sample, with a comparable range of z_{fg} and overall galaxy properties, and are consistent with our measurements within the uncertainties.

Figure 2.6 clearly shows that excess Ly α absorption is detected to transverse distances of at least $D_{\text{tran}} \approx 3500$ pkpc. A single power law reasonably approximates the dependence of $W_\lambda(\text{Ly}\alpha)$ on D_{tran} , with power law index $\beta = -0.40 \pm 0.01$:

$$W_\lambda(\text{Ly}\alpha) = (0.429 \pm 0.005 \text{ \AA}) \left(\frac{D_{\text{tran}}}{\text{pMpc}} \right)^{(-0.40 \pm 0.01)}. \quad (2.12)$$

This power law is also shown in Figure 2.6. There is evidence from the new KGPS results for subtle differences in slope over particular ranges of D_{tran} . Specifically, at $D_{\text{tran}} < 100$ pkpc, $\beta = -1.0 \pm 0.1$; for $100 < D_{\text{tran}}/\text{pkpc} \leq 300$, $\beta = 0.0 \pm 0.1$; and $300 < D_{\text{tran}}/\text{pkpc} \leq 2000$, $\beta = -0.48 \pm 0.02$. Details are discussed in §2.4 below.

Kinematics

In order to interpret observations of the kinematics of Ly α absorption, one must first develop a detailed understanding of the effective spectral resolution, including the net contribution of redshift uncertainties. We showed in §2.2 that redshift uncertainties are negligible for the KGPS- z_{neb} galaxies, but that $\approx 50\%$ of the KGPS-Full sample whose z_{fg} was estimated using Equations 2.1–2.3 have larger redshift uncertainties, $\sigma_z \lesssim 140 \text{ km s}^{-1}$. In the latter case, redshift uncertainties would make a non-negligible contribution to the effective spectral resolution of

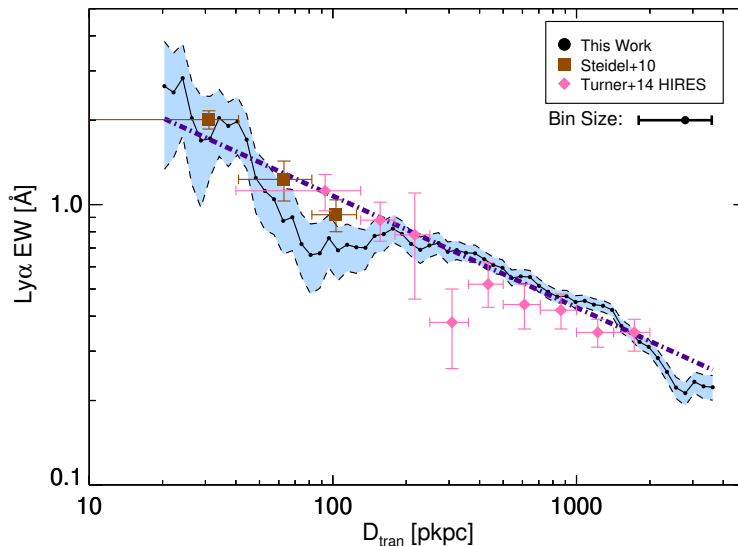


Figure 2.6: $W_\lambda(\text{Ly}\alpha)$ as a function of D_{tran} measured from the KGPS-Full sample. Each black dot (connected with the solid line segments) is a measurement made from a composite spectrum in a bin spanning a factor of 2 in D_{tran} where the point marks the geometric mean D_{tran} within the bin. The light blue shaded region represents the $\pm 1\sigma$ uncertainty based on bootstrap resampling of the spectra comprising each composite in each bin. The single dot with error bars below the legend box shows the bin size used to make composite spectra; i.e., the bins were evaluated at intervals smaller than the bin size, thus adjacent points on smaller than the bin size are correlated. The purple dash-dotted line is the best single-power-law fit to the $W_\lambda(\text{Ly}\alpha)$ - D_{tran} relation, with slope $\beta = -0.40 \pm 0.01$. The new measurements are compared with Steidel et al. (2010, brown squares) and Turner et al. (2014, magenta diamonds), where the latter are based on HIRES QSO/galaxy pairs in KBSS.

the stacked spectra. We determined the effective spectral resolution applicable to composites formed from the KGPS- z_{neb} and KGPS-Full samples separately, using procedures whose details are described in Appendix 2.5.

In fact, Appendix 2.5 concludes that the effective spectral resolution, including the contribution of redshift uncertainties, is nearly identical for the two subsamples: $\sigma_{\text{eff}} = 189 \text{ km s}^{-1}$ (KGPS- z_{neb}) and $\sigma_{\text{eff}} = 192 \text{ km s}^{-1}$ (KGPS-Full). As explained in the appendix, this suggests that the contribution of redshift uncertainties to the effective spectral resolution is small compared to that of the instrumental resolution¹¹: $\sigma_{z,\text{eff}} \simeq \sqrt{\sigma_{\text{eff}}^2(\text{Full}) - \sigma_{\text{eff}}^2(z_{\text{neb}})} \lesssim 60 \text{ km s}^{-1}$. This implies that the additional degradation in the effective spectral resolution caused by the use of calibrated z_{UV}

¹¹The KGPS-Full and KGPS- z_{neb} samples comprise a comparable mix of the two LRIS instrumental configurations.

redshifts for the $\sim 50\%$ of the KGPS-Full sample lacking measurements of z_{neb} is not significant. The contribution is smaller than the redshift error estimated in §2.2 for galaxies with only rest-UV measurements; we suggest that the reason for the apparent discrepancy is that the earlier estimate included both the uncertainty in the mean offsets between z_{UV} and z_{neb} , and the noise associated with the measurement of spectral features in individual spectra, which are effectively averaged out in applying the fits in Equations 1-4. Nevertheless, we retain the KGPS- z_{neb} sample as a sanity check to eliminate unknown systematic uncertainties that may be present in the KGPS-Full sample.

As discussed above (§2.3), for composite spectra of modest spectral resolution, much of the physical information that could be measured from high-resolution QSO spectra through the same ensemble of sightlines is sacrificed in order to increase the spatial sampling. However, from the smaller samples of QSO sightlines through the CGM of a subset of the KGPS galaxies (Rudie et al., 2012), we know that the Ly α absorption profile resolves into a number of individual components of velocity width $\sigma_v \simeq 20 - 50 \text{ km s}^{-1}$ that do not fully occupy velocity space within $\pm 700 \text{ km s}^{-1}$ of the galaxy's systemic redshift. The total absorption strength tends to be dominated by components with $N_{\text{HI}} \gtrsim 10^{14} \text{ cm}^{-2}$, whose Ly α transitions are saturated. Thus, Ly α profiles in stacked spectra at low resolution can be usefully thought of as smoothed, statistical averages of a largely bimodal distribution of pixel intensities that is modulated by whether or not a saturated absorber is present.

Nevertheless, the Ly α line profiles in the KGPS composites encode useful information on the total Ly α absorption as a function of line-of-sight velocity relative to the galaxy systemic redshifts, and the large number of pairs allows us to map these parameters as a function of D_{tran} . To describe the absorption profiles with sufficient dynamic range, we use the apparent optical depth, defined as

$$\tau_{\text{ap}}(v) = -\ln \frac{F(v)}{F_{\text{cont}}(v)}, \quad (2.13)$$

where $F(v)$ is the flux density of the composite spectrum as a function of velocity, $F_{\text{cont}}(v)$ is the continuum level, and v is the line-of-sight velocity relative to z_{sys} . For continuum-normalized spectra, $F_{\text{cont}}(v) = 1$. Since we know that HI gas is clumpy and normally saturated, τ_{ap} is relatively weakly dependent on N_{HI} for $N_{\text{HI}} > 10^{14} \text{ cm}^{-2}$. Rather, $\tau_{\text{ap}}(v)$ is modulated by both the covering fraction (f_c) of the clumps, and the typical line of sight velocity range over which significant absorption is present.

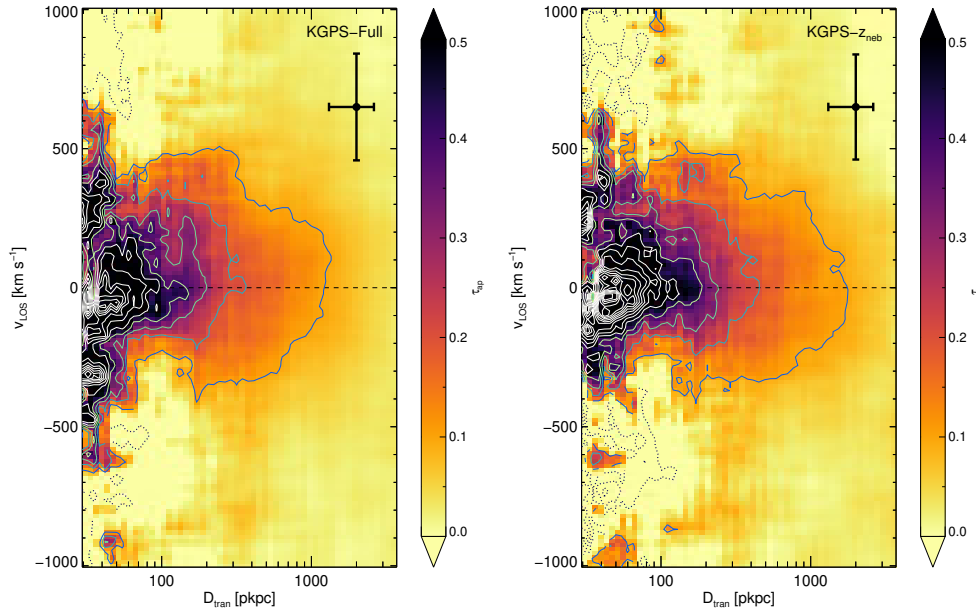


Figure 2.7: The line-of-sight velocity structure of HI absorbers around foreground galaxies. Each column of pixels in each plot corresponds to a measurement of $\tau_{\text{ap}}(v_{\text{LOS}})$ evaluated from the corresponding composite spectrum in the bin of D_{tran} made from the KGPS-Full sample (left) and the KGPS- z_{neb} sample (right). The black dots with horizontal error bars show the range of D_{tran} used to make each column of the map; the effective velocity resolution of the map is shown as a vertical error bar. Solid contours correspond to positive optical depth τ_{ap} , with dotted contours indicating negative values, which are consistent with the $1\text{-}\sigma$ uncertainties. The contour levels are separated by $\Delta\tau_{\text{ap}} = 0.1$.

Figure 2.7 shows the map of τ_{ap} in the $v_{\text{LOS}} - D_{\text{tran}}$ plane for the KGPS-Full and the KGPS- z_{neb} sample. Each column in the maps represents a stacked spectrum for sightlines within a bin of D_{tran} , each of which represents an equal logarithmic interval $\Delta(\log D_{\text{tran}}) = 0.3$, as in Figure 2.6. Assuming that the cumulative number of pairs is proportional to D_{tran}^2 (see Figure 2.3), the average D_{tran} weighted by number of sightlines within a bin is ~ 0.18 dex greater than the lower bin edge, and ~ 0.12 dex smaller than the higher bin edge. The map of τ_{ap} vs. D_{tran} is symmetric between the blue and red sides across all D_{tran} except between ~ 50 pkpc and ~ 200 pkpc, where the total τ_{ap} for $v_{\text{LOS}} > 0$ (i.e., the side redshifted with respect to the galaxy systemic redshift) is larger by $> 50\%$ than that of the blueshifted side. The possible origin of the asymmetry is discussed in §2.4.

To further increase the SNR, the red and blue sides of the τ_{ap} map are folded together in Figure 2.8 for the KGPS-Full sample and Figure 2.9 for the KGPS- z_{neb} sample.

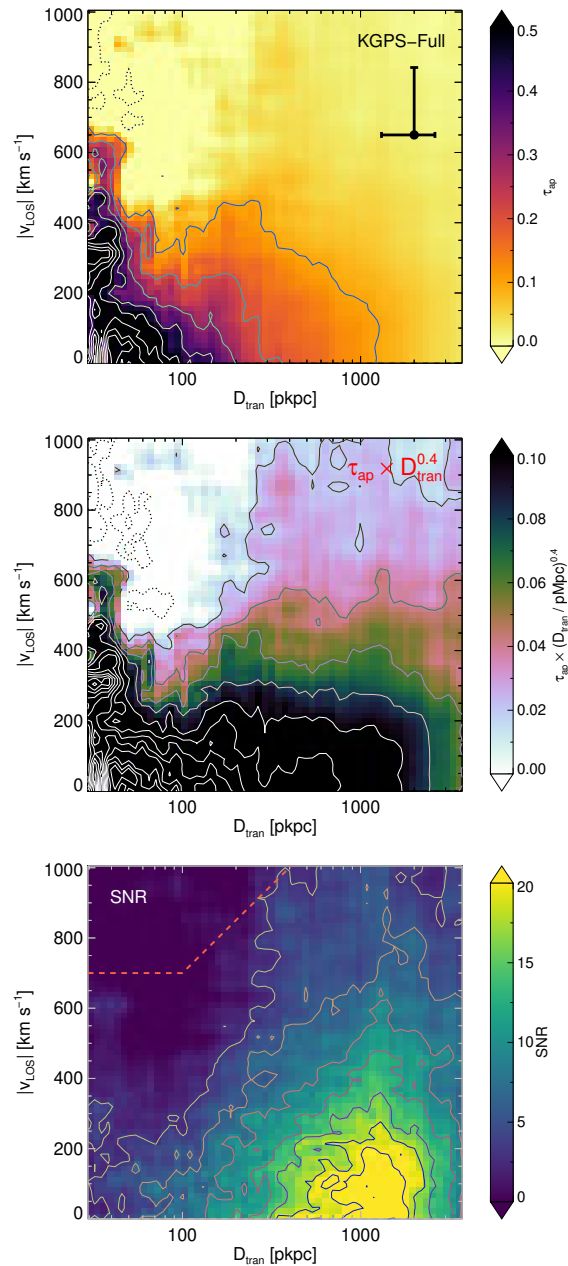


Figure 2.8: Maps of τ_{ap} with the blue and red sides folded to increase the signal-to-noise ratio. The three maps are (top to bottom): $\tau_{\text{ap}}(|v_{\text{los}}|, D_{\text{tran}})$, $\tau_{\text{ap}} \times D_{\text{tran}}^{0.4}$ (to better illustrate the structure at large D_{tran}), and the map of the SNR per \AA of the τ_{ap} measurement. The contour decrements are 0.1 for the τ_{ap} map, 0.02 for the $\tau_{\text{ap}} \times D_{\text{tran}}^{0.4}$ map, and 3 for the SNR map. The half-aperture in which the $W_{\lambda}(\text{Ly}\alpha)$ is measured in §2.3 is shown as the orange dashed line in the SNR map.

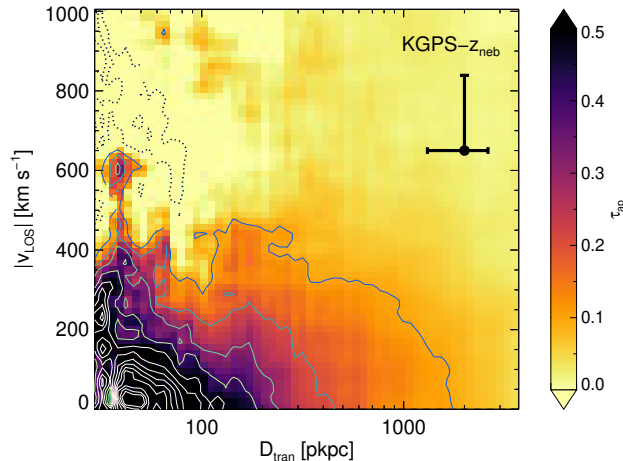


Figure 2.9: Same as the top plot of Figure 2.8, but for the KGPS- z_{neb} sample.

Also shown in Figure 2.8 (top-right) is the map of $\tau_{\text{ap}} \times D_{\text{tran}}^{0.4}$, in order to accentuate the structure at large D_{tran} ; the power 0.4 was chosen to approximately counteract the overall decrease in absorption strength with increasing D_{tran} (Equation 2.12). Equal size bins in $\Delta \log D_{\text{tran}}$ means that fewer sightlines are being averaged when D_{tran} is smaller, so that the uncertainties are larger for pixels on the lefthand side of the τ_{ap} maps: the SNR (per \AA) maps are shown in the bottom panels of Figure 2.8. The SNR was calculated by bootstrap resampling the ensemble of spectra contributing to each D_{tran} bin 2000 times, and then rescaling so that the units are SNR per \AA in the rest frame of z_{fg} . The values in the uncertainty estimation are also supported by the strength of apparent negative τ_{ap} (dotted contours) in the τ_{ap} maps, which are consistent with the $1-\sigma$ errors from the bootstrap determinations.

The maps of the KGPS-Full and KGPS- z_{neb} samples show similar features and are consistent within the uncertainties after convolution of the KGPS- z_{neb} map with a $\sigma_z = 60 \text{ km s}^{-1}$ Gaussian kernel in the v_{LOS} direction.

Figure 2.8 confirms trends in Ly α absorption strength versus D_{tran} based on QSO sightlines in KBSS (Rudie et al., 2012; Rakic et al., 2012; Turner et al., 2014) – a sample with much smaller number of foreground galaxies – and similar surveys at comparable (Adelberger et al., 2003; Adelberger et al., 2005a; Tummuangpak et al., 2014; Bielby et al., 2017) or lower redshifts (Ryan-Weber, 2006; Tejos et al., 2014). It is also consistent with analytic modeling from Kakiichi and Dijkstra (2018) and the mock observations of QSO sightlines from the Evolution and Assembly of Galaxies and their Environments (EAGLE) simulations (Rakic et al., 2013; Turner

et al., 2017), who proposed measuring the typical halo mass of the host galaxies based on matching the observed pixel optical depth as a function of D_{tran} to dark matter halos in the simulation.

The KGPS maps show that, at small D_{tran} , excess Ly α absorption reaches velocities $|v_{\text{LOS}}| \gtrsim 500 \text{ km s}^{-1}$ relative to the systemic redshifts of foreground galaxies, and that excess absorption over and above that of the average IGM extends to transverse distances of at least 3.5 pMpc in D_{tran} direction. Figure 2.8 suggests several interesting features in the 2-D maps of τ_{ap} , moving from small to large D_{tran} :

1. A region with high line-of-sight velocity spread ($\langle |v_{\text{LOS}}| \rangle \gtrsim 300\text{--}400 \text{ km s}^{-1}$) on transverse distance scales $D_{\text{tran}} \lesssim 50 \text{ pkpc}$.
2. An abrupt compression of the v_{LOS} profile beginning near $D_{\text{tran}} \approx 70 \text{ pkpc}$, extending to $D_{\text{tran}} \sim 150 \text{ kpc}$, with a local minimum near $D_{\text{tran}} \approx 100 \text{ pkpc}$.
3. A gradual broadening of the Ly α velocity profile beginning at $D_{\text{tran}} \gtrsim 150 \text{ pkpc}$ with $|v_{\text{LOS}}| \sim 500 \text{ km s}^{-1}$ and extending to $> 4 \text{ pMpc}$ with $\sim 1000 \text{ km s}^{-1}$ (most evident in the upper righthand panel of Figure 2.8).

We show in §2.4 that feature (iii) is a natural consequence of the Hubble expansion coupled with decreasing HI overdensity, causing the absorption to become weaker and broader as D_{tran} increases. Eventually, one would expect that the profile would broaden and weaken until it becomes indistinguishable from the ambient IGM – recalling that τ_{ap} is the *excess* Ly α optical depth over the intergalactic mean.

We address the likely origin of each of the enumerated features in §2.4.

2.4 Discussion

Comparison to Cosmological Zoom-In Simulations

To aid in the interpretation of the observed τ_{ap} maps, we compared them to the distribution of N_{HI} as a function of v_{LOS} in a subset of simulations taken from the Feedback In Realistic Environments (FIRE) cosmological zoom-in simulations (Hopkins et al., 2014; Hopkins et al., 2018). The selected simulations are intended to reproduce LBG-like galaxies at $z \sim 2$; they were originally run at lower spatial resolution using the FIRE-1 feedback model (Faucher-Giguère et al., 2015), but have since been migrated to FIRE-2 with improved mass resolution of $m_{\text{gas}} \sim m_{\text{star}} \sim 700 M_{\odot}$. We randomly selected a single main simulated galaxy whose halo mass (M_{h}), stellar mass ($M_{\text{*}}$), and star formation rate (SFR) roughly match values inferred for

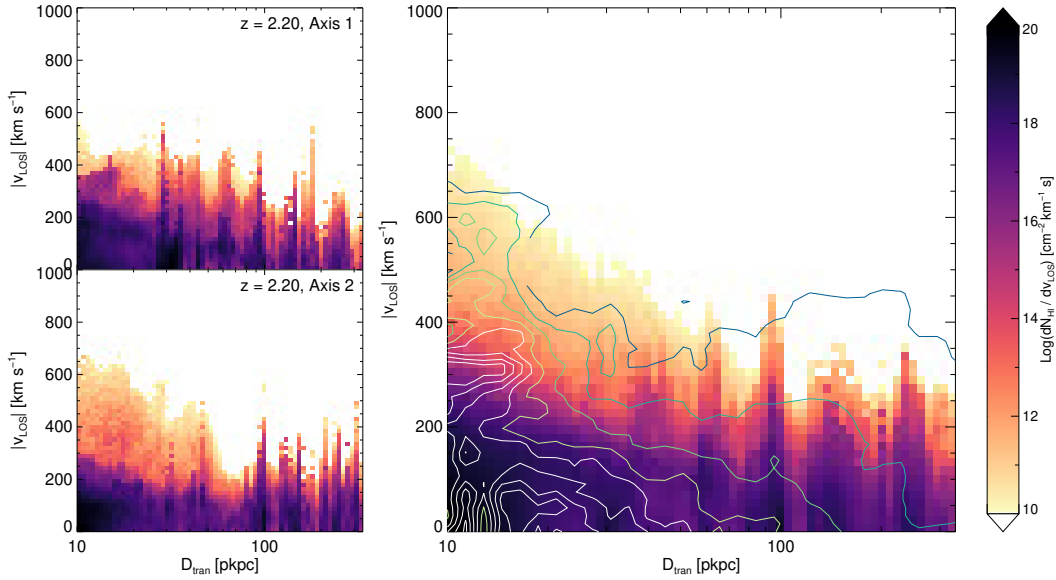


Figure 2.10: Maps of $dN_{\text{HI}}/dv_{\text{LOS}}$ in the FIRE-2 simulation (h350), as seen by an observer, projected onto the $v_{\text{LOS}}-D_{\text{tran}}$ plane. *Left*: Snapshots from a single time step ($z = 2.20$) as viewed from two orthogonal viewing angles. *Right*: The median-stack of 22 such maps: 11 time steps at intervals of $\delta z = 0.05$ for $2.0 \leq z \leq 2.4$ from each of two orthogonal viewing angles. Contours based on the observed map of τ_{ap} for the KGPS-Full sample (Figure 2.8) are overlaid for comparison. Note that the D_{tran} -axis has been zoomed in from that of Figure 2.8 because of the limited size (a few times r_{vir}) of the high-resolution zoom-in region of the FIRE-2 simulation.

a typical galaxy in the KGPS sample: $\log M_{\text{h}}/M_{\odot} \sim 12$, $\log M_{*}/M_{\odot} \sim 10.5$, and $\langle \text{SFR}/(M_{\odot} \text{ yr}^{-1}) \rangle \sim 30$ at $z \sim 2.2$.

We selected 11 snapshots evenly distributed in redshift between $z = 2.4$ and $z = 2.0$ ¹². In each time step, we chose two random (but orthogonal) viewing angles, and calculated the projected quantity $dN_{\text{HI}}/dv_{\text{LOS}}$ (a proxy for the observed τ_{ap}) projected onto the “observed” $D_{\text{tran}} - v_{\text{LOS}}$ plane; example maps for the $z = 2.20$ time step are shown in the lefthand panels of Figure 2.10. We then median-stacked the 22 N_{HI} maps (11 snapshots for each of two viewing angles); the result is shown in the righthand panel of Figure 2.10). Note that the range shown on the D_{tran} axis is smaller than that used for the observations (e.g., Figure 2.8) because of the limited size of the full-resolution volume of the zoom-in simulation.

Thanks to the large dynamic range in the simulation, one can see that the highest v_{LOS} values ($v_{\text{LOS}} \sim 400 - 700 \text{ km s}^{-1}$) are found within $D_{\text{tran}} \lesssim 50 \text{ pkpc}$ and

¹²The interval $\delta z = 0.05$ corresponds to intervals of cosmic time in the range $\delta t \simeq 70 \pm 10 \text{ Myr}$ over the redshift range included in our analysis.

are associated with material having total $N_{\text{HI}} \simeq dN_{\text{HI}}/dv \times \Delta v \simeq 10^{14.5-15.0} \text{ cm}^{-2}$, whereas the slower material with $v_{\text{LOS}} < 200 \text{ km s}^{-1}$ has N_{HI} typically 100-1000 times larger. While essentially all pixels in the map that are significantly above the background in Figure 2.10 would give rise to Ly α absorption detectable in KGPS, the low spectral resolution coupled with the inherent loss in dynamic range in $\tau(\text{Ly}\alpha)$ for $\log N_{\text{HI}} \gtrsim 14.5$ makes a detailed quantitative comparison of the KGPS observed map and the simulation map more challenging. Part of the difficulty stems from the limited depth along the line of sight ($\sim 1 \text{ pMpc}$) over which the high-resolution zoom-in simulations were conducted, meaning they could be missing potential high-velocity material in the IGM. However, we conclude that the general morphology of the N_{HI} map from the averaged zoom-in simulations is qualitatively consistent with that of the observed τ_{ap} map.

Individual snapshots provide insight into the physical origin of features in the time-averaged map. For example, the most prominent features in Figure 2.10 are the vertical “spikes” evident at $D_{\text{tran}}/\text{pkpc} \gtrsim 50$ – these are due to the passing of satellite galaxies through the simulation box, giving rise to line-of-sight components of velocity due both to their motion relative to the central galaxy and their internal gas motions, including outflows; e.g., Faucher-Giguère et al. (2016), Anglés-Alcázar et al. (2017), and Hafen et al. (2019). Some of these features remain even in the median of 22 snapshots (righthand panel of Figure 2.10), caused by gradual decay of orbits of galaxies destined to merge with the central galaxy. Such features would not be expected to remain in an average over many galaxies, each observed at a particular time (as in the KGPS data), except insofar as there might be a characteristic range of galactocentric radius and relative velocity affected by satellites, so that a net signal might be detected statistically.

With the above *caveats* in mind, the envelope of v_{LOS} as a function of D_{tran} in the simulation resembles that of the KGPS observations in several respects: both the highest velocities and the highest optical depths occur within the central 50 pkpc, with a local minimum in the range of v_{LOS} over which significant HI is present somewhere in the range 50–100 pkpc, reminiscent of the expected virial radius for a dark matter halo of $\log(M_{\text{h}}/M_{\odot}) \sim 12$ of $r_{\text{vir}} \simeq 75\text{--}95 \text{ pkpc}$.

Further insight can be gleaned with reference to Figure 2.11, which is essentially a histogram of HI as a function of galactocentric radius and radial velocity¹³. Negative (positive) radial velocities indicate motion toward (away from) the center of

¹³The center of the galaxy is determined by the center of mass of the dark matter halo.

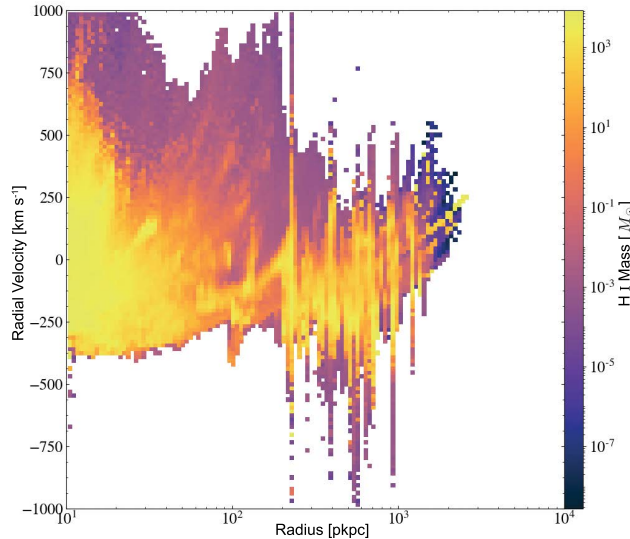


Figure 2.11: The galactocentric radial velocity versus galactocentric radius for neutral hydrogen in the same $z = 2.20$ snapshot as shown in the lefthand panels of Figure 2.10. Positive and negative values indicate net outward and net inward radial motion, respectively. The vertical strips are due to the outflow of the satellite galaxies. The colorbar represents the total H I mass in each pixel. The gradual decrease of H I content beyond 500 pkpc is artificial because of the limited volume within which the gas simulation is conducted.

the galaxy. This type of diagram makes it easier to distinguish gas with substantial outflow velocities, which cause the clear asymmetry of the radial velocity distribution relative to the galaxy center of mass rest frame. In this particular case, there is neutral hydrogen with $v_r > 300 \text{ km s}^{-1}$ at galactocentric radii from $r = 0$ to $r \simeq 200 \text{ pkpc}$, but essentially no gas with $v_r < -300 \text{ km s}^{-1}$ except for that due to satellite galaxies. If one looks at the same diagram in successive time steps, it is clear that the high velocities are associated with episodes of high SFR, and that this particular galaxy is experiencing such an episode at the present time step, which produces most of the high velocity gas with $r \lesssim 50 \text{ kpc}$; the “plume” of high velocity material that peaks near $r = 100 \text{ pkpc}$ is a remnant of a similar episode that occurred $\sim 100 \text{ Myr}$ earlier that has propagated to larger galactocentric radii with somewhat reduced v_r . Such episodic star formation and outflows are typical in high- z galaxies in the FIRE simulation (Muratov et al., 2015). Such plumes are also seen in IllustrisTNG simulations (Nelson et al., 2019), although they are generally due to the implementation of AGN feedback in higher-mass halos, and thus have even larger velocities. One can also see an accretion stream that has $v_r \simeq 0$ at $r \simeq 200 \text{ kpc}$, and evidently has accelerated to $v_r \simeq -200 \text{ km s}^{-1}$ by $r \sim 50 \text{ pkpc}$.

However, the bulk of the H I mass within the virial radius is not obviously accreting or outflowing, with $|v_r| \lesssim 250 \text{ km s}^{-1}$.

A halo with $M_h = 10^{12} M_\odot$ and $r_{\text{vir}} \approx 90 \text{ kpc}$ has a circular velocity of $\approx 220 \text{ km s}^{-1}$, so that if gas were on random orbits one would expect to measure a 1-D velocity dispersion (more or less independent of radius, for realistic mass profiles) of $\sigma_{1D} \approx 220/\sqrt{3} \approx 130 \text{ km s}^{-1}$, with $\sim 95\%$ of particle velocities expected to lie within $|v_{\text{LOS}}| \lesssim 260 \text{ km s}^{-1}$. These expectations could be modulated by the prevalence of mostly-circular or mostly-radial orbits, of course. However, in a statistical sense, gravitationally-induced motions could contribute a fraction of the most extreme velocities (i.e., $|v_r| > 300 \text{ km s}^{-1}$ within $\lesssim 2R_{\text{vir}}$), but are not enough to make up the whole.

A Simple Analytic Model

Context

Inspired by comparisons to the cosmological zoom-in simulations, and to offer an explanation for the general shape of the τ_{ap} map before discussing the details, we constructed a two-component analytic model intended to capture the salient features of Figure 2.8.

To construct a model in 3-D physical space, a parameter must be chosen to represent Ly α absorption strength. As discussed in §2.2, $\tau_{\text{ap}}(v_{\text{LOS}})$ is affected by a combination of the total N_{HI} , which is known to depend on D_{tran} (e.g., Rudie et al., 2012), the average distribution of v_{LOS} at a given D_{tran} , and the fraction of sightlines that give rise to detectable absorption at a given D_{tran} . The relative importance of these effects depends on galactocentric distance (i.e., D_{tran}) in a complex manner that cannot be resolved from an ensemble of low-resolution spectra, which also cannot be expected to reveal the level of detail that could be measured from individual sightlines observed at very high spectral resolution. However, some general statements about the “sub-grid” behavior of Ly α absorption may be helpful in providing some intuition.

At large D_{tran} , given the minimum total equivalent width detected of $\approx 0.2 \text{ \AA}$ (see Figure 2.6), the lowest column density that could be measured for a single Ly α absorption line is $\log N_{\text{HI}} \approx 13.6$, assuming a linear curve of growth; for a typical value of the Doppler parameter $b_d \approx 25 \text{ km s}^{-1}$ ($\sigma_d \equiv b_d/\sqrt{2} \approx 17.7 \text{ km s}^{-1}$), the single line would have an optical depth at line center of $\tau_0 \approx 2.4$, which if resolved would produce a minimum flux density relative to the continuum of

$F_{v,0} \sim 0.09$. However, given the effective spectral resolution of $\sigma_{\text{eff}} \simeq 190 \text{ km s}^{-1}$, the observed line profile of the same line would have $\sigma_{\text{LOS}} \simeq 190 \text{ km s}^{-1}$ and central *apparent* optical depth of only $\tau_{\text{ap},0} \simeq 0.2$, or $F_{v,0}/F_{v,\text{cont}} \simeq 0.82$. In fact, at large D_{tran} we measure $\sigma_{\text{LOS}} \simeq 600 \text{ km s}^{-1}$, and a maximum apparent optical depth $\tau_{\text{ap}} \lesssim 0.06$. This suggests that at large D_{tran} we are measuring a small total N_{HI} excess [$\log(N_{\text{HI}}/\text{cm}^{-2}) < 14$] spread over a large range of v_{LOS} ; the apparent line width is best interpreted as a probability distribution in v_{LOS} of the small excess absorption over that of the general IGM.

At small D_{tran} , the situation is very different; in most cases, if observed at high spectral resolution, one would see several components within a few hundred km s^{-1} of the galaxy systemic velocity, most of which would be strongly saturated ($\log N_{\text{HI}}/\text{cm}^{-2} \gtrsim 14.5$) and complexes of absorption could often produce large swaths of velocity space with $F_v = 0$ (e.g., Rudie et al., 2012). At $D_{\text{tran}} \lesssim 50 \text{ kpc}$, the total $W_\lambda(\text{Ly}\alpha) \simeq 2 \text{ \AA}$ with maximum $\tau_{\text{ap},0} \simeq 1$ and $\sigma_{\text{LOS}} \sim 320 \text{ km s}^{-1}$. Once saturation occurs, the equivalent width contributed by individual absorbers grows very slowly with increasing N_{HI} until Lorentzian damping wings begin to become important ($\log(N_{\text{HI}}/\text{cm}^{-2}) \gtrsim 19.0$). At high spectral resolution, $\exp(-\tau_0) \simeq 0$ independent of N_{HI} so that additional absorbers in the same range of v_{LOS} might have little or no effect on the absorption profile, especially when observed at low spectral resolution. However, a relatively small amount of HI with larger $|v_{\text{LOS}}|$ – if it is a common feature of $D_{\text{tran}} \lesssim 50 \text{ pkpc}$ sightlines – would be easily measured.

parametrization

Figure 2.12 illustrates the parametrization of our model. In the interest of simplicity, our model makes no attempt to capture the detailed radiative processes (e.g., Kakiichi and Dijkstra, 2018) of individual absorption components that would be revealed by high resolution QSO spectra. Instead, in order to unify the two extreme scenarios described in §2.4 above, we treated HI in the CGM as a continuous medium in which the absorption strength per unit pathlength is represented by an absorption coefficient,

$$\alpha_{\text{ap}} = \frac{d\tau_{\text{ap}}}{dl}, \quad (2.14)$$

where dl is the differential path length. In essence, α_{ap} represents the overdensity of HI relative to the average in the IGM, accounting for some of the non-linearity that results from curve-of-growth effects that remain unresolved by the data.

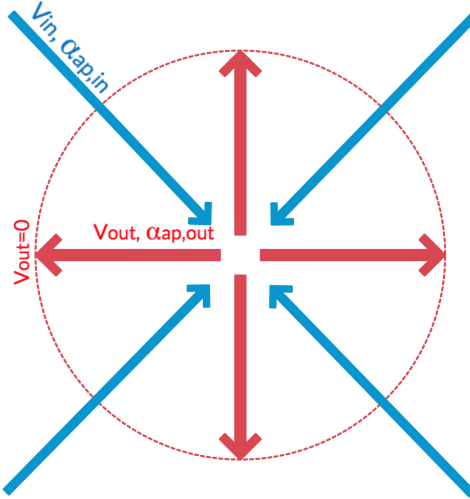


Figure 2.12: A cartoon illustration of the parametrization of the analytic model described in §2.4. The model comprises of two isotropic, non-interacting, purely radial components: “outflow” (red) and “inflow” (blue). Each component has free parameters describing its radial velocity profile $v(r)$ and apparent absorption coefficient $\alpha_{\text{ap}}(r)$ (defined in Equations 2.14, 2.15, and 2.16). The outflow component is truncated at the point that it slows to $v_{\text{out}} = 0$.

We assumed that the HI surrounding galaxies is composed of two isotropic (non-interacting) components: one moves radially outward (“outflow”), the other radially inward (“inflow”). Each has α_{ap} parametrized as an independent radial power law:

$$\alpha_{\text{ap,out}}(r) = \alpha_{0,\text{out}} r_{100}^{-\gamma_{\text{out}}} \quad (2.15)$$

$$\alpha_{\text{ap,in}}(r) = \alpha_{0,\text{in}} r_{100}^{-\gamma_{\text{in}}}, \quad (2.16)$$

where $\alpha_{0,\text{out}}$ and $\alpha_{0,\text{in}}$ are normalization constants, γ_{out} and γ_{in} are power law indices, and $r_{100} = r/100$ pkpc is the galactocentric radius.

For simplicity, we assumed that the velocity fields of the two components are also isotropic and purely radial; clearly this is unrealistic. However, since only the line-of-sight component of gas velocity is measured, random motions of gas moving in the galaxy potential is partly degenerate with our treatment of gas accretion. In the context of the simplified model, one can think of the “inflow” component as a proxy for all gas motions that are induced by the galaxy’s potential. Under these assumptions, there is a simple geometric relationship between the line-of-sight component of velocity $v_{\text{LOS}}(D_{\text{tran}}, l)$ at each point along a sightline through

the CGM and the radial velocity $v_r(r)$

$$v_{\text{LOS}}(D_{\text{tran}}, l) = \frac{l}{r} v_r(r), \quad (2.17)$$

where l is the line of sight coordinate distance measured from the tangent point where $v_{\text{LOS}} = 0$, i.e., where $r = D_{\text{tran}}$, and in general, $r^2 = l^2 + D_{\text{tran}}^2$. Within this paradigm, specification of $v_{\text{out}}(r)$, $v_{\text{in}}(r)$, $\alpha_{\text{ap,out}}(r)$, and $\alpha_{\text{ap,in}}(r)$ can be transformed to maps of $\tau_{\text{ap}}(D_{\text{tran}}, v_{\text{LOS}})$ directly analogous to those in Figure 2.8.

For the outflow component velocity field $v_{\text{out}}(r)$, we assume that the gas has been accelerated to an initial “launch” velocity v_1 at a galactocentric radius $r = 1$ pkpc, beyond which its trajectory is assumed to be purely ballistic (i.e., no pressure gradient or mass loading is accounted for) within an NFW halo (Navarro, Frenk, and White, 1996) density profile. The outflow component is truncated (i.e., $\alpha_{\text{ap,out}} = 0$) at the radius where $v_{\text{out}}(r) \rightarrow 0$. With these assumptions,

$$v_{\text{out}}(r) = \sqrt{v_1^2 + A \left(-\ln \frac{R_s + 1}{R_s} + \frac{1}{r} \ln \frac{R_s + r}{R_s} \right)}, \quad (2.18)$$

where R_s is the NFW scale radius in pkpc, and

$$A = \frac{8\pi G \rho_0 R_s^3}{1 \text{ pkpc}} \quad (2.19)$$

$$\simeq 1.2 \times 10^7 \text{ km}^2 \text{ s}^{-2}. \quad (2.20)$$

Following Klypin et al. (2016), for a $M_h = 10^{12} M_\odot$ NFW halo with concentration parameter $c = 3.3$ at $z = 2.3$, $R_s = 27$ pkpc (i.e. $R_{\text{vir}} \simeq 90$ pkpc).

For the inflow component, we make the simplifying assumption that $v_{\text{in}}(r)$ is just a constant velocity offset relative to the Hubble expansion (similar to Kaiser, 1987),

$$v_{\text{in}}(r) = v_{\text{offset}} + H(z)r, \quad (2.21)$$

where $H(z)$ is the Hubble parameter at redshift z . For our assumed Λ CDM cosmology and given the median redshift of the KGPS foreground galaxies, $\langle z \rangle = 2.2$, we set $H(z) = 227 \text{ km s}^{-1} \text{ pMpc}^{-1}$.

Given the parametrization in Equations 2.15, 2.16, 2.18, and 2.21, for each realization of the MCMC we projected both components independently to the $|v_{\text{LOS}}|$ - D_{tran} plane, in the process of which α_{ap} was converted to τ_{ap} by integration. Subsequently, $\tau_{\text{ap,in}}$ and $\tau_{\text{ap,out}}$ are added in $D_{\text{tran}} - v_{\text{LOS}}$ space, and convolved with the effective resolution of the observed τ_{ap} maps as determined in §2.3.

Table 2.3: Best-fit model parameters

	Parameter	KGPS-Full	KGPS- z_{neb}
Inflow	v_{offset} (km s $^{-1}$)	-84^{+6}_{-6}	-110^{+8}_{-9}
	$\alpha_{0,\text{in}}$ (pkpc $^{-1}$)	$0.0083^{+0.0011}_{-0.0008}$	$0.0095^{+0.0018}_{-0.0013}$
	γ_{in}	$0.58^{+0.03}_{-0.02}$	$0.62^{+0.04}_{-0.03}$
Outflow	v_1 (km s $^{-1}$)	603^{+5}_{-11}	575^{+7}_{-3}
	$\alpha_{0,\text{out}}$ (pkpc $^{-1}$)	$0.031^{+0.010}_{-0.008}$	$0.034^{+0.057}_{-0.012}$
	γ_{out}	$2.0^{+0.1}_{-0.1}$	$1.1^{+0.4}_{-0.1}$

Results

The best fit model parameters were estimated using a Markov-Chain Monte Carlo (MCMC) method to fit to the observed maps of τ_{ap} . Prior to fitting, in order to reduce pixel-to-pixel correlations, the observed maps were resampled to a grid with $\Delta v_{\text{LOS}} = 101 \text{ km s}^{-1}$ and $\Delta \log(D_{\text{tran}}) = 0.126$. These pixel dimensions represent one standard deviation of the fitted 2-D Gaussian covariance profile determined from bootstrap resampling of over-sampled maps.

Even with the simplified model, we found it was necessary to fit the inflow and outflow serially, rather than simultaneously, to achieve convergence in the MCMC. Specifically, the inflow component was fit in the region of $D_{\text{tran}} > 400 \text{ pkpc}$, assuming that this part of the τ_{ap} map is dominated by inflow¹⁴. Once the inflow parameters ($\alpha_{0,\text{in}}, \gamma_{\text{in}}, v_{\text{offset}}$) were obtained, they were held fixed and combined with the as-yet-undetermined outflow model to fit the whole τ_{ap} map. For the inflow MCMC, the priors were assumed to be flat in linear space with positive values (except for v_{offset} , which is negative for inflow). The outflow MCMC, however, adopts the most probable posterior of the inflow parameters and fixes them; this may be viewed as a strong prior on the resulting outflow parameters, which are otherwise assumed to be flat and positive-valued.

The best-fit model parameters are summarized in Table 2.3, and the $\alpha(r)$ and $v_r(r)$ profiles for the KGPS-Full and the KGPS- z_{neb} samples are shown in Figure 2.13. In general, the fitted parameters for the two maps are consistent with one another within the estimated uncertainties; the main difference is in the exponent γ_{out} , the inferred radial dependence of the outflow component (see Figure 2.13). In the case of the sparser KGPS- z_{neb} sample, γ_{out} is not very well constrained, likely due to sample variance at small D_{tran} caused by the relatively small number of independent

¹⁴The region was chosen by eye based on Figure 2.8 to minimize the contamination from outflow.

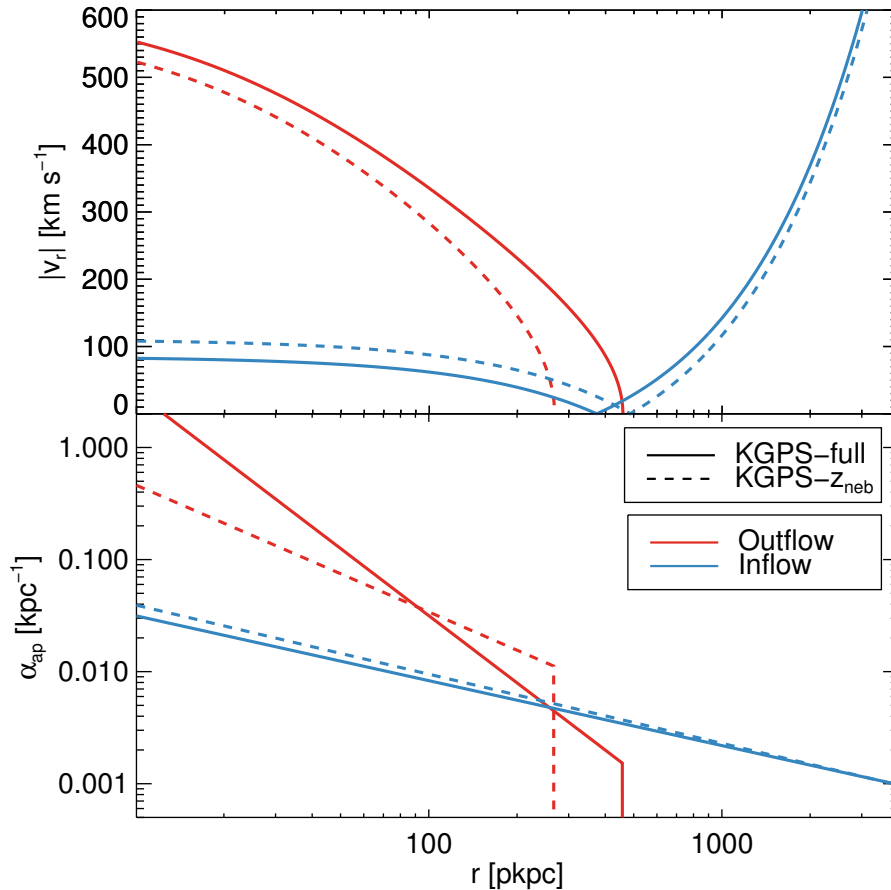


Figure 2.13: The best-fit radial profiles of v_r and α_{ap} as functions of galactocentric radius (i.e., before projection to the observed $v_{\text{LOS}} - D_{\text{tran}}$ plane). The model parameters are as in Table 2.3. The red curves correspond to the outflow component and blue curves to the inflow. The best-fit model for the KGPS-Full sample is shown with solid lines, while the best-fit model for the KGPS- z_{neb} is shown with dashed lines.

sightlines. Figure 2.14 compares the observed and modeled τ_{ap} maps and the residual map for the KGPS-Full sample. The best-fit model reproduces the general features of Figure 2.8 reasonably well.

The best-fit outflow models above are, on the face of it, inconsistent with the kinematic outflow model of S2010, in which the radial velocity was constrained primarily by “down-the-barrel” (DTB) profiles of blue-shifted low-ionization metal lines (rather than H I) in galaxy spectra. In the S2010 models, most of the acceleration of outflowing material was inferred to occur within $r \lesssim 5 - 10$ pkpc of the galaxy center, with few constraints on $v(r)$ at larger radii; however, we note that the asymptotic velocity of the fastest-moving material in the S2010 models was

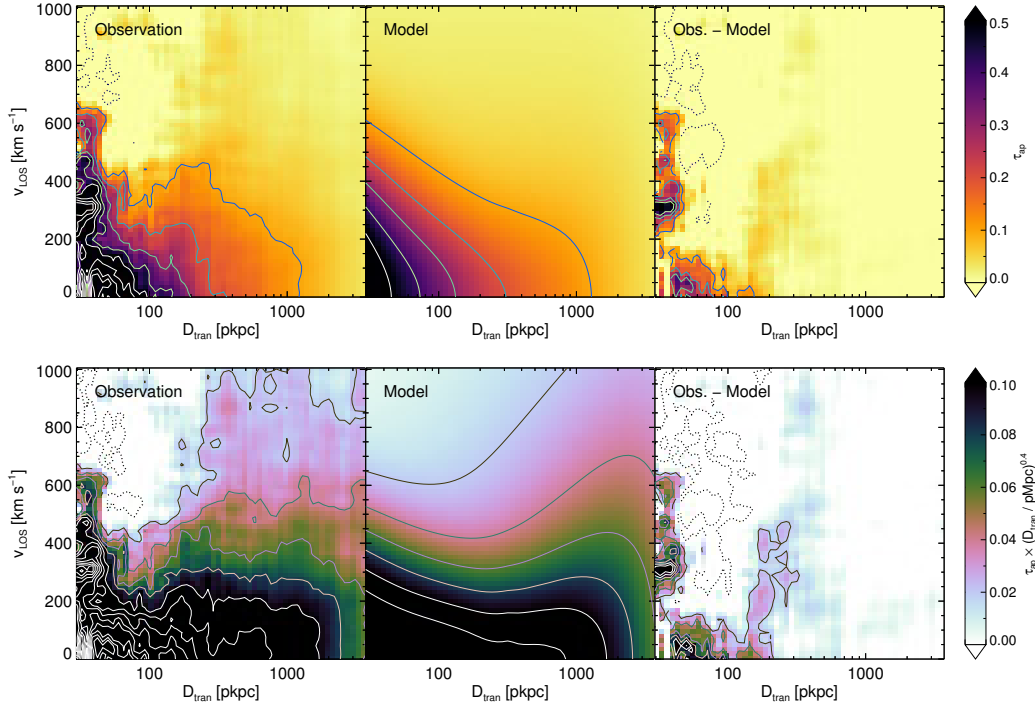


Figure 2.14: Comparison of the observed KGPS-Full map (left) with the best-fit model (middle). The right-most plots are residuals after subtraction of the model from the observed map. The top panel shows τ_{ap} as a function of D_{tran} and v_{LOS} , while the bottom panel shows τ_{ap} multiplied by $D_{\text{tran}}^{0.4}$. The colorbars and contour levels are identical to those shown in Figure 2.8.

$\sim 600 - 700 \text{ km s}^{-1}$, similar to the highest detected v_{LOS} at small D_{tran} in the KGPS optical depth maps (e.g., Figure 2.8). S2010 did not use information from measurements of v_{LOS} profiles as a function of D_{tran} , which has provided the most important new constraints in the present work.

Additionally, although various hydrodynamical simulations of galaxy formation differ substantially in their spatial resolution and feedback implementation, our best-fit outflow velocity of $\sim 600 \text{ km s}^{-1}$ is consistent with the upper range of gas velocities found for simulated galaxies with similar halo mass and redshift. For example, in the FIRE zoom-in simulations, the 95th percentile gas-phase velocity is $\sim 600 \text{ km s}^{-1}$ at $0.25R_{\text{vir}}$ ($r \simeq 25 \text{ pkpc}$) (Muratov et al., 2015); for larger volume simulations, which depend to a greater extent on “sub-grid” treatment of feedback physics, the level of agreement depends on the simulation suite: in the IllustrisTNG simulations, the 95th-percentile gas-phase velocity is $\sim 650 \text{ km s}^{-1}$ at $r = 10 \text{ pkpc}$ (Nelson et al., 2019), whereas in the EAGLE simulations, the 90-percentile gas

velocity between 0.1 and 0.2 r_{vir} (equivalent to $r \sim 10 - 20$ pkpc for the galaxies in our observed sample) is smaller, $\sim 350 \text{ km s}^{-1}$ (Mitchell et al., 2020). It is important to note that the comparison of our observations with the FIRE simulation in §2.4 is more direct, since it was confined to neutral H in the simulation box, while the results quoted above pertain to *all* outflowing gas, regardless of physical state. It will be important in the future to examine simulation results in terms of parameters that are most directly comparable to the available observational constraints.

The simple model framework we adopted is not intended to reproduce all aspects of what is undoubtedly a more complex situation in reality. There are clearly features of the observations that are not successfully captured by the model; these are discussed in §2.4 below. Here we examine whether its basic assumptions – that both infall and outflows are required to reproduce the general behavior of the observed τ_{ap} maps – are justified.

One questionable assumption we adopted for the fiducial model is the kinematic nature of the outflow, which was launched from $r = 1$ pkpc at high velocity and subsequently affected only by gravity. It neglects the possible effects of a pressure gradient in the halo, through which buoyancy forces could conceivably counter-act gravity in determining the velocity of outflowing material as it moves to larger radii (e.g., Ji, Oh, and Masterson, 2019). It also assumes that no ambient gas is entrained by the outflow (i.e., no additional mass loading) as it moves outward, which could reduce the outflow velocity $v_{\text{out}}(r)$ more rapidly than the model presented above.

As a test, we relaxed the ballistic assumption and considered a model in which the outflow velocity is simply a power-law function of galactocentric radius, $v_{\text{out}}(r) = v_1 \cdot r^\beta$. With this parametrization, we found a best-fitting $\beta = -0.7_{-0.2}^{+0.5}$, while the $\alpha_{\text{out}}(r)$ remains largely unchanged for the KGPS-Full sample (see Figure 2.15). The alternative model does result in a more rapid decline in the range of v_{LOS} at $D_{\text{tran}} \sim 100$ pkpc (and thus slightly closer to the observed map in the same range), but the overall fit has χ^2 similar to that of our fiducial model. Moreover, the power law model failed to converge in the case of the smaller KGPS- z_{neb} sample.

Another questionable assumption in the model is that all gas motion is radial with respect to the galaxy center of mass. We acknowledge that with a more sophisticated parameterization, one might be able to reproduce all of the observed features with a combination of radial and non-radial motions, e.g. orbital or random motions. However, the observations measure line-of-sight components of velocity only, so the distinction between infall, random, and circular/orbital motion based on an ensemble

of sightlines would not be evident even with much higher quality data. On the other hand, as long as the line of sight component of velocity is slowly varying with D_{tran} – as expected for typical dark matter halo mass distributions – one can think of the “inflow” component as a generalized proxy for CGM gas whose motion is dictated by the galaxy potential only, whether that motion is radial, random, circular, or some combination.

To test the robustness of the model fits, we tried fitting the outflow component using constant weighting (rather than inverse variance weighting) across the map; the resulting best-fit model parameters change by $\lesssim 10\%$ compared to the weighted fit. We also tried fitting the 2D maps of the “red” and “blue” halves separately: the power of $\alpha_{\text{ap}}(r)$ (i.e., γ) for inflow is $0.40_{-0.04}^{+0.05}$ on the blue side and $0.71_{-0.03}^{+0.03}$ on the red side, almost different by a factor of 2, while other parameters are consistent within 25%.

Finally, we attempted to fit the observed τ_{ap} maps with single component gas distributions, i.e. with infall only or outflow only. The infall model fails to converge because a match to the observations requires an abrupt increase in velocity (by a factor of ~ 3) and in absorption coefficient (by a factor of ~ 5) at $r \sim 50$ pkpc; in any case, as discussed earlier, it is hard to account for $v_{\text{LOS}} > 300$ km s $^{-1}$ with gravitationally-induced infall onto a halo of mass $10^{12} M_{\odot}$. Moreover, we know unequivocally from the kinematics of strong interstellar absorption lines observed in DTB spectra of the foreground galaxies that outflows dominate the kinematics on scales of at least a few pkpc, and that they have maximum outflow velocities similar to the values of v_1 in our model outflows.

Figure 2.15 shows the best-fit outflow-only model to the KGPS-Full sample. The model includes the effects of Hubble expansion, $v_{\text{out-only}}(r) = v_{\text{out}}(r) + H(z)r$, because the behaviour of the observed map would clearly require a substantial fraction of the outflowing gas to escape the halo, after which its kinematics would be dominated by Hubble expansion. For $D_{\text{tran}} \lesssim 100$ pkpc, the model clearly fails to reproduce either the absorption strength or the kinematics of the central region in order to reproduce the behaviour at larger D_{tran} .

Despite the uncertainty in the parametrization of the model, we argue that the observations require both outflowing and accreting components; this assertion is discussed further in the next section.

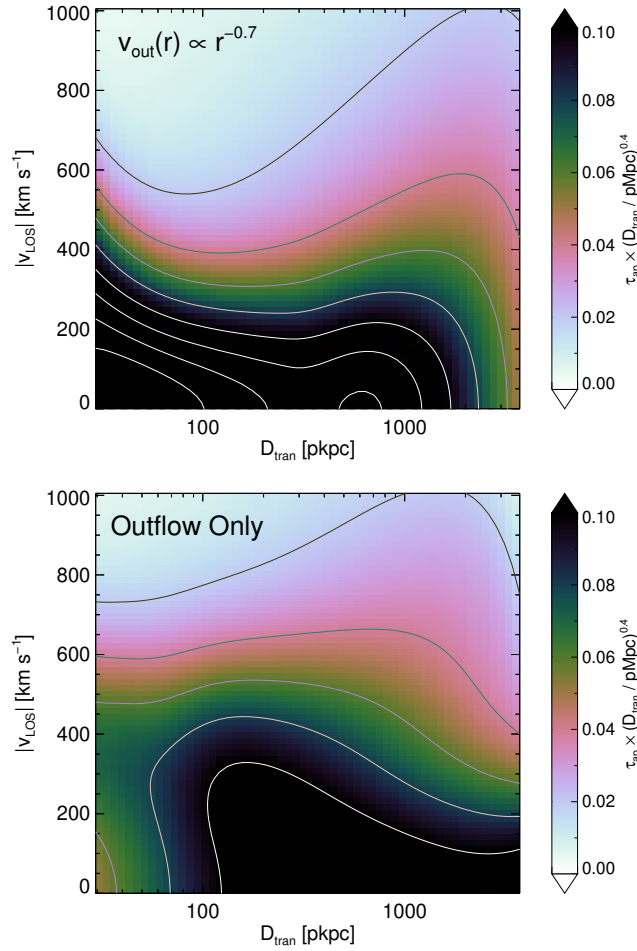


Figure 2.15: The best fitting parametrizations of alternative models, to be compared with that of the fiducial model shown in Figure 2.14. Both maps show the quantity $\tau_{\text{ap}} \times D_{\text{tarn}}^{-0.4}$, as in the bottom panels of Figure 2.14. (*Top:*) Same as fiducial, but with the outflow velocity $v_{\text{out}}(r)$ as power law. (*Bottom:*) A (ballistic) outflow-only model that eliminates the infall component completely. The power law model fits the data similarly to the fiducial; the outflow-only model is a poor fit.

Implications for Detailed CGM H I Kinematics

Despite the ability of the model to reproduce the general features of the observed τ_{ap} maps, there are some details present in the data that are not successfully captured. Most notable is that the data exhibit contours of constant τ_{ap} that change overall shape depending on the contour level, whereas the model contours are relatively smooth and self-similar at different contour levels (Figure 2.14) – i.e. the model lacks kinematic structure within $D_{\text{tran}} < 100$ pkpc and $|v_{\text{LOS}}| < 600$ km s⁻¹, especially the observed compression between 50 and 100 pkpc that characterizes the observed map. Some of the discrepancy could be caused by the relatively small number of sightlines that comprise the measurements on small D_{tran} scales, with the correspondingly larger sample variance, and the lack of non-radial gas motion in the model. However, very similar structure at $D_{\text{tran}} < 100$ pkpc is observed at both positive and negative v_{LOS} in the unfolded maps in Figure 2.7, suggesting that the structure is likely to be real.

The rightmost panels of Figure 2.14 show the residuals between the observed KGPS-Full maps and the corresponding best-fit model. These illustrate that the model systematically under-predicts the apparent optical depth at small D_{tran} , particularly for $v_{\text{LOS}} \gtrsim 200$ km s⁻¹, suggesting that a single, smoothly varying outflowing component whose velocity depends only on r is an oversimplification of the true situation. From high-resolution QSO spectra, it is common to observe complexes of absorption systems at small galactocentric impact parameters, with a wide range of N_{HI} and v_{LOS} (e.g., Rudie et al., 2012), with many pixels reaching zero intensity. Disentangling these complexes often requires measurement of the higher Lyman series lines even in spectra with resolution $\lesssim 10$ km s⁻¹ and very high S/N; it is therefore unsurprising that a simple model fails to capture the details. Nevertheless, the rapid fall-off in the maximum v_{LOS} at relatively high τ_{ap} over the range $D_{\text{tran}} \approx 50 - 100$ pkpc, and the flattening of the profile out to $D_{\text{tran}} \approx 200 - 300$ pkpc, are not present in our fiducial model or the alternatives discussed in the previous section.

As discussed in §2.4, a power-law parametrization of the outflow component provides a fit to the τ_{ap} map (at least, for the KGPS-Full version) with similar χ^2 , and allows for a more rapid decrease in $v_{\text{out}}(r)$ with radius compared to the ballistic model with no mass loading. However, it still cannot account for the changing contour shapes of τ_{ap} present in the data. Better matches might be obtained by treating high- τ_{ap} in the outflow component separately from the remainder, allowing it to experience more rapid deceleration at $D_{\text{tran}} \sim 50$ pkpc than more diffuse gas, or

by a rapid transition from high to low- N_{HI} absorbers for fast-outflowing gas. Both scenarios are consistent with the results of Rudie et al. (2012), in which absorbers with $N_{\text{HI}} > 10^{14.5} \text{ cm}^{-2}$ were found to occupy a smaller range in v_{LOS} than absorbers with $N_{\text{HI}} < 10^{14.5} \text{ cm}^{-2}$ at $D_{\text{tran}} \lesssim 2 \text{ pMpc}$.

At $50 \text{ pkpc} \lesssim D_{\text{tran}} \lesssim 100 \text{ pkpc}$, where the τ_{ap} profile is at its narrowest, the line profile (i.e., the distribution of v_{LOS} at a given D_{tran}) is consistent with the effective velocity resolution of the map ($\sim 190 \text{ km s}^{-1}$), and changes very little out to $D_{\text{tran}} \sim 100\text{--}200 \text{ pkpc}$. As best-seen in the bottom panels of Figure 2.14, beyond $D_{\text{tran}} \sim 100 \text{ pkpc}$, while the optical depth continues to decrease roughly as $D_{\text{tran}}^{-0.4}$, the range of v_{LOS} begins to increase again, by an amount that depends on the contour level. The best fit radial and kinematic profiles shown in Figure 2.13 suggest that the minimum in the line-of-sight velocity field at $D_{\text{tran}} \sim 100\text{--}200 \text{ pkpc}$ may mark a caustic where outflows and infall both reach minimum v_{LOS} , perhaps with opposite sign. The location of this feature also corresponds to the clear change in slope of the relationship between D_{tran} and $W_{\lambda}(\text{Ly}\alpha)$ (Figure 2.6), and is just beyond the expected virial radius given a halo mass of $M_{\text{h}} = 10^{12} M_{\odot}$. Since the escape velocity at 100 pkpc for such a halo is $v_{\text{esc}} \simeq 440 \text{ km s}^{-1}$, we expect that most of the neutral H at $r \lesssim 100 \text{ pkpc}$ remains bound to the central galaxy.

Velocity Asymmetry and Emission Filling

One of the more puzzling features of the 2D maps of τ_{ap} – evident in Figure 2.7 – is the apparent asymmetry of τ_{ap} with respect to v_{LOS} . In the KGPS-Full sample, for D_{tran} between ~ 70 and 150 pkpc , the integrated τ_{ap} for $v_{\text{LOS}} > 0$ is > 1.5 times that of the corresponding value for $v_{\text{LOS}} < 0$, meaning that redshifted Ly α absorption is stronger than blueshifted Ly α absorption. The asymmetry can also be seen in Figure 2.5: for the composite Ly α spectrum for the bin with $80 \leq D_{\text{tran}}/\text{pkpc} \leq 160$, although the maximum depth in the absorption profile occurs at a velocity consistent with $v_{\text{LOS}} = 0$, there is a red wing extending to $v_{\text{LOS}} \sim +500 \text{ km s}^{-1}$, whereas the blue absorption wing reaches only $v_{\text{LOS}} \sim -300 \text{ km s}^{-1}$. Similar asymmetry is also present for the KGPS- z_{neb} sample, suggesting that residual systematic redshift errors are not likely to be the principal cause.

Figure 2.16 shows the result of subtracting the blue (red) component of the $\tau_{\text{ap}} \times D_{\text{tran}}^{0.4}$ map from the red (blue) side for the KGPS-Full sample. The most prominent residual appears at $50 \lesssim D_{\text{tran}}/\text{pkpc} \lesssim 200$ and $200 \lesssim |v_{\text{LOS}}|/\text{km s}^{-1} \lesssim 500$; residuals resulting from differencing of the KGPS- z_{neb} sample are similar. Although the

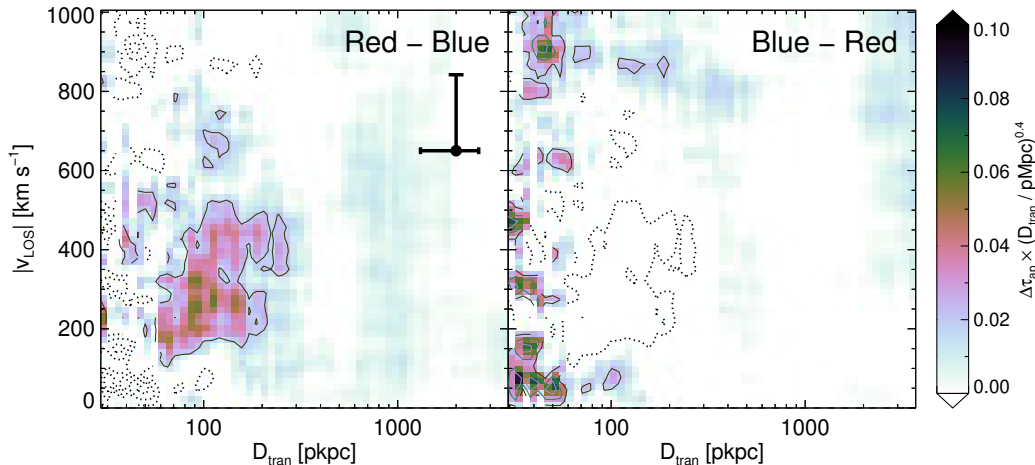


Figure 2.16: Same as the $\tau_{\text{ap}} \times D_{\text{tran}}^{0.4}$ map in Figure 2.8, except that instead of averaging the blue and red sides, the left (right) map is the *subtraction* of the blue (red) side from the red (blue) side. Significant asymmetry can be seen at $D_{\text{tran}} \approx 100$ pkpc. Again, the solid (dotted) contours represent positive (negative) values. The excess blueshifted absorption at $D_{\text{tran}} \lesssim 50$ pkpc could be due to sample variation, while the excess redshifted absorption with $D_{\text{tran}} = 50 - 200$ pkpc is likely real.

residual has modest SNR (≈ 2 per \AA), it extends over a contiguous region larger than the effective resolution of the map, and is therefore significant. There is a fractionally less-significant excess of blueshifted Ly α absorption at $D_{\text{tran}} \lesssim 50$ pkpc (better shown in the righthand panel of Figure 2.16), apparently extending over the full range $0 \leq |v_{\text{LOS}}| / \text{km s}^{-1} \leq 1000$ that could be attributable to the relatively small number of galaxy pairs at small separations (i.e., to sample variance). It is harder to dismiss the excess redshifted absorption in the lefthand panel of Figure 2.16, which is based on a 10-times larger sample (≈ 1000) of galaxy pairs. On the other hand, there is no significant asymmetry in the Ly α absorption profiles beyond $D_{\text{tran}} \sim 200$ pkpc, where the S/N of the map is high.

If the observed asymmetry is of astrophysical origin, it remains to be explained. We considered possible causes of the apparent excess redshifted Ly α absorption, noting that it is confined to the foreground galaxy CGM within $D_{\text{tran}} \approx 200$ pkpc: possibilities include observational selection effects or biases, which might have been introduced by particular properties favored among the foreground or background galaxies that were observed successfully (e.g., compactness, dust attenuation, orientation, etc.). We could not envision a plausible scenario that could explain the asymmetry in the absorption profile.

We also considered the real *temporal* difference between the time light from the background galaxy passes through the “far” and “near” sides of the foreground galaxy CGM, but the relevant timescale would be very short, $\Delta t \lesssim 400 \text{ pkpc}/c \sim 10^5 \text{ yrs}$. As above, it is hard to explain why any time-dependent effect would systematically bias the kinematics of the absorbing gas.

It is now well-known that Ly α emission “halos” are a generic property of star-forming galaxies at high redshift (e.g., Steidel et al., 2011; Wisotzki et al., 2016; Erb, Steidel, and Chen, 2018) and that they extend to projected distances $\sim 5 - 10$ times larger than their UV continuum light. Of the possible explanations, we find the least implausible to be that the Ly α absorption profile has been altered by Ly α emission contamination within the spectroscopic aperture used to record the background galaxy spectra. Most surveys of intervening absorption lines have used bright background point sources, such as QSOs, in which case this possible source of contamination can ordinarily be neglected. One usually thinks of Ly α absorption systems in terms of equivalent width $W_\lambda(\text{Ly}\alpha)$ or column density N_{HI} , but one can also think of a Ly α absorption feature at $z = z_{\text{fg}}$ as a record of the flux removed from the beam of the background source at z_{bg} , scattered out of the line of sight by H I in the CGM of a foreground galaxy. As an example, for an observation of a $m = 18$ QSO at z_{bg} whose sightline passes near to a typical $z_{\text{fg}} = 2.2$ galaxy and produces an absorption feature with rest-frame $W_\lambda(\text{Ly}\alpha) = 1.0 \text{ \AA}$ at z_{fg} , the flux removed from the QSO spectrum would be $\simeq 6 \times 10^{-16} \text{ ergs s}^{-1} \text{ cm}^{-2}$, which is large even in comparison to the *total* Ly α flux from the galaxy (Steidel et al., 2011), and hundreds of times larger than the Ly α flux likely to be collected by a slit located 5-10 arcsec away from the z_{fg} galaxy. For a typical $m = 25$ background galaxy, on the other hand, the same absorption line equivalent width would correspond to a flux smaller by a factor of ~ 630 , or $\simeq 10^{-18} \text{ ergs s}^{-1} \text{ cm}^{-2}$, i.e., approaching the flux expected from the low surface brightness Ly α emission halo of the foreground galaxy. In the latter case, the presence of the Ly α emission could have a measurable effect on the apparent absorption strength if the velocity ranges overlap.

To be more quantitative, we estimated the flux of Ly α emission captured within the aperture used to obtain background galaxy spectra using the average Ly α halo observed by Steidel et al. (2011) (S2011) for a sample of star forming galaxies with similar properties to those in the larger KBSS sample, but with $\langle z \rangle = 2.65$. The mean Ly α surface brightness profile was found to be reasonably well-described by an exponential, $S(b) = C_1 \exp(-b/b_0)$, where $b = D_{\text{tran}}$, $C_1 = 2.4 \times 10^{-18} \text{ ergs s}^{-1}$

$\text{cm}^{-2} \text{ arcsec}^{-2}$, and $b_0 = 25 \text{ pkpc}$. The mean halo is detected down to a surface brightness limit of $S \simeq 10^{-19} \text{ ergs s}^{-1} \text{ cm}^{-2} \text{ arcsec}^{-2}$ at $D_{\text{tran}} \sim 80 \text{ pkpc}$.

By assuming that the intrinsic Ly α luminosity and scale length of the mean Ly α halo of the KGPS foreground galaxies are the same as those of the S2011 sample, we applied the redshift-dependent surface brightness correction to move from $\langle z \rangle = 2.65$ to $\langle z \rangle = 2.25$, and extrapolated the Ly α surface brightness profile to $D_{\text{tran}} = 100 \text{ pkpc}$. The predicted Ly α surface brightness would be $\sim 7.2 \times 10^{-20} \text{ ergs s}^{-1} \text{ cm}^{-2} \text{ arcsec}^2$. Taking the typical extraction aperture for the LRIS spectra to be of angular size $1.35 \text{ arcsec} \times 1.2 \text{ arcsec}$ ($\sim 1.6 \text{ arcsec}^2$), the integrated Ly α emission flux within the slit would be $F_{\text{Ly}\alpha, \text{em}} \sim 1.1 \times 10^{-19} \text{ erg s}^{-1} \text{ cm}^{-2}$.

We estimated the mean background galaxy continuum flux density near 4000\AA (i.e., the wavelength of Ly α at $z \sim 2.25$) by interpolating the flux density between the photometric U_n (3520/600) and G (4730/1100) passbands, with the result $\langle m_{\text{AB}}(4000\text{\AA}) \rangle \simeq 25.3$, or $\langle F_\nu \rangle \simeq 0.26 \mu\text{Jy}$ ($\langle F_\lambda \rangle \simeq 5 \times 10^{-19} \text{ erg s}^{-1} \text{ cm}^{-2} \text{\AA}^{-1}$).

The observed Ly α absorption equivalent width at $D_{\text{tran}} \simeq 100 \text{ pkpc}$ is $\langle W_\lambda(\text{Ly}\alpha)_{\text{obs}} \rangle \simeq 2.7 \text{ \AA}$ (assuming $\langle z \rangle = 2.25$), which removes an average flux from the background galaxy spectrum of $2.7 \times 5 \times 10^{-19} \simeq 1.4 \times 10^{-18} \text{ ergs s}^{-1} \text{ cm}^{-2}$. The fractional perturbation of the total Ly α absorption equivalent width by foreground galaxy Ly α emission is then $1.1 \times 10^{-19} / 1.4 \times 10^{-18} \simeq 0.08$ (8%). Using the same arguments, emission filling at $D_{\text{tran}} \simeq 25 \text{ pkpc}$ – where the mean Ly α surface brightness is ~ 20 times higher (according to S2011) but the absorption rest equivalent width is larger by a factor of only $\simeq 2.5$ (see Figure 2.6) – emission would be predicted to affect the observed $W_\lambda(\text{Ly}\alpha)$ at the $\gtrsim 50\%$ level. Figure 2.17 shows the predicted effect of diffuse emission on the observed $W_\lambda(\text{Ly}\alpha)$ absorption as a function of D_{tran} . Also shown in Figure 2.17 is the amplitude of the observed asymmetry converted to $\Delta W_\lambda(\text{Ly}\alpha)$, the net equivalent width of the $W_\lambda(\text{Ly}\alpha)$ residuals shown in Figure 2.16.

The average equivalent width of the residual shown in the lefthand panel of Figure 2.16 is $\Delta W_\lambda(\text{Ly}\alpha) \simeq 0.2 \text{ \AA}$ for $70 \lesssim D_{\text{tran}}/\text{pkpc} \lesssim 150$, or $\simeq 25 - 30\%$ of the total observed $W_\lambda(\text{Ly}\alpha)$ over the same range of D_{tran} – within a factor of ~ 3 of the estimated effect from emission filling, possibly consistent given the uncertainties. However, if the emission were distributed symmetrically in velocity space with respect to the absorption, its effect would mostly likely have remained unrecognized. The asymmetry in Ly α absorption at $D_{\text{tran}} \sim 100 \text{ pkpc}$, if attributed to emission filling, would require that the bulk of Ly α emission must be *blueshifted* by $\Delta v_{\text{LOS}} \sim 200 - 400 \text{ km s}^{-1}$ with respect to the foreground galaxy systemic

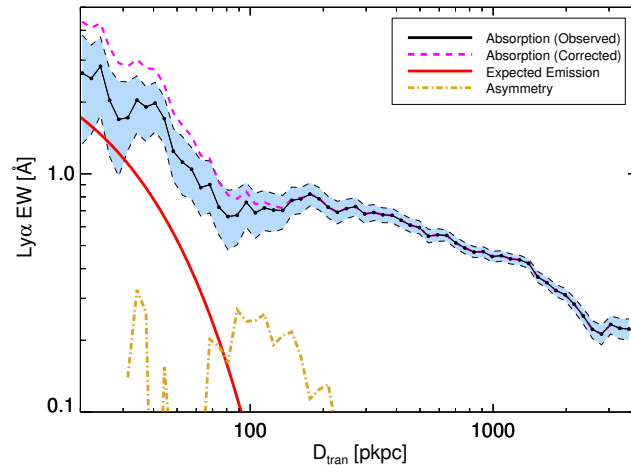


Figure 2.17: Expected contribution to $W_\lambda(\text{Ly}\alpha)$ by $\text{Ly}\alpha$ emission surrounding foreground galaxies (red), compared to the observed $W_\lambda(\text{Ly}\alpha)$ in absorption (black, same as in Figure 2.6). The dashed magenta curve shows the absorption after correction for the estimated contribution from emission filling. The yellow dashed curve shows the fraction of $W_\lambda(\text{Ly}\alpha)$ contributed by asymmetry, calculated by integrating the blue/red halves of the absorption profiles spectra within $|\Delta v_{\text{LOS}}| < 700 \text{ km s}^{-1}$ and subtracting one from the other.

redshift. This is opposite to what is typically observed for $\text{Ly}\alpha$ emission in DTB galaxy spectra, in which the dominant component of $\text{Ly}\alpha$ emission is redshifted by several hundred km s^{-1} for the galaxies in the KBSS sample (e.g., see the top and bottom panels of Figure 2.2.) In this context, it is possibly relevant that the excess emission (if that is indeed the cause) falls in the range of D_{tran} where our kinematic modeling (§2.4) suggested a transition between outflow-dominated and accretion-dominated flows. If the velocity field at $D_{\text{tran}} \simeq 100 \text{ pkpc}$ were dominated by inflows, scattering of $\text{Ly}\alpha$ photons in the observer’s direction would tend to be blueshifted (e.g., Faucher-Giguère et al., 2010; Dijkstra, 2014).

Also qualitatively (but perhaps not quantitatively) consistent with this picture is that the asymmetry on smaller transverse scales ($D_{\text{tran}} \lesssim 40 \text{ pkpc}$) has the opposite sign, i.e., the *absorption* is stronger on the blueshifted side of v_{sys} , which might be attributable to excess redshifted emission, as for typical DTB spectra. However, as shown in Figure 2.17, in order to be consistent with the expected effect of emission filling at small D_{tran} , the kinematic asymmetry of the $\text{Ly}\alpha$ emission would need to comprise only a fraction of the total emission, since the observed net effect on $W_\lambda(\text{Ly}\alpha)$ from the asymmetry is only $\sim 10 - 15\%$. On the other hand, recent observations using the Keck Cosmic Web Imager (KCWI; Morrissey et al.,

2018) for a subset of the KBSS galaxy sample suggests that the ratio between the blueshifted and redshifted components of Ly α emission from the CGM increases with projected galactocentric distance (Erb, Steidel, and Chen, 2018; Chen et al, in prep.), and approaches 1:1 by $r \sim 50$ pkpc; unfortunately, the observations of individual galaxies with KCWI (or MUSE) are not yet sensitive enough to evaluate at $D_{\text{tran}} > 50$ pkpc¹⁵.

An obvious observational test of the hypothesis that emission filling significantly alters the strength of $W_{\lambda}(\text{Ly}\alpha)$ measured along background galaxy sightlines could be made using QSO sightlines, since QSOs are at least ~ 6 magnitudes brighter than the typical $z \sim 2.5$ background galaxy, so that foreground galaxy Ly α emission is expected to be negligible compared to the absorbed flux from the background source. Unfortunately, the sample size of QSO-galaxy pairs for $z_{\text{fg}} > 2$ is very small in comparison. We examined the velocity distribution of H I for QSO sightlines within $D_{\text{tran}} \approx 200$ pkpc of KBSS galaxies in Rudie et al. (2012) and Rudie et al. (2019). In the range of $50 < D_{\text{tran}}/\text{pkpc} < 200$, there are slightly more redshifted absorption components by number, but the excess is not statistically significant. When the high resolution QSO spectra are analyzed in the same way as the galaxy spectra by smoothing to reduce the spectral resolution and averaging the spectral regions near Ly α at the redshift of foreground galaxies – as done by Turner et al. (2014) (see Figure 2.6) – $W_{\lambda}(\text{Ly}\alpha)$ is larger by $\approx 50\%$ for the QSO sightlines for the bin at $D_{\text{tran}} \approx 90$ pkpc compared to the observed $W_{\lambda}(\text{Ly}\alpha)$ for the KGPS sightlines. Though the two measurements are still consistent with one another at the $\sim 2\sigma$ level, the difference is in the direction expected if the KGPS sample has been affected by Ly α emission. At smaller D_{tran} , where the expected effect of emission filling in the galaxy sightlines is larger, the QSO sightline samples are too small to provide a meaningful comparison (e.g., there are no QSO-galaxy pairs with $D_{\text{tran}} < 50$ pkpc in the KBSS sample used by Turner et al., 2014.)

In any case—whether or not it is responsible for the asymmetry in the current data—it is probably important to account for the effects of emission filling on $W_{\lambda}(\text{Ly}\alpha)$ in absorption, as a function of D_{tran} , which will depend on the relative brightness of the foreground and background sources. When we apply our estimate from above, the corrected $W_{\lambda}(\text{Ly}\alpha)$ vs. D_{tran} (Figure 2.17) accentuates the existence of two distinct “zones” in the behavior of Ly α absorption around KBSS galaxies: the

¹⁵Over the range of D_{tran} in common, the mean Ly α halo in the KCWI data is consistent in both shape and intensity with the mean Ly α halo presented by S2011.

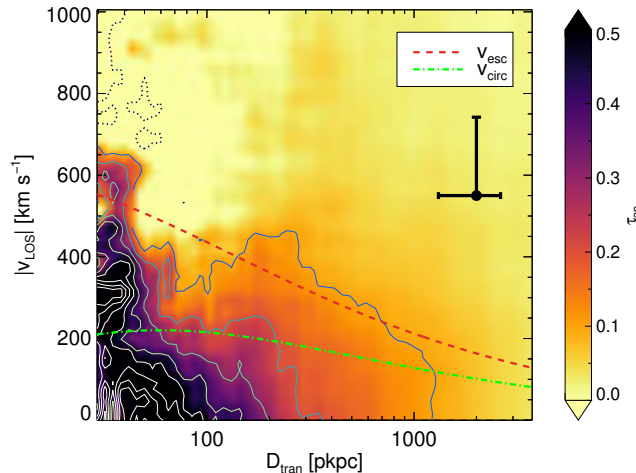


Figure 2.18: Same as the τ_{ap} map in Figure 2.8, with the radial dependence of the escape velocity (v_{esc} , red dashed) and circular velocity (v_{circ} , green dash-dotted) for an NFW halo with $M_{\text{h}} = 10^{12} M_{\odot}$ superposed (assuming that D_{tran} is equivalent to the galactocentric distance r .)

inner zone, at $D_{\text{tran}} \lesssim 100$ pkpc, where $W_{\lambda}(\text{Ly}\alpha) \propto D_{\text{tran}}^{-1.1}$, and an outer zone with $100 \lesssim D_{\text{tran}}/\text{pkpc} \lesssim 300$ kpc, over which $W_{\lambda}(\text{Ly}\alpha)$ remains remarkably flat.

Baryon Escape

A significant fraction of gas associated with galaxy-scale outflows is expected to be retained by relatively massive galaxies. Even if some gas does manage to escape to beyond the halo virial radius, theoretical expectations are that, for galaxies with halo masses $\simeq 10^{12} M_{\odot}$ at $z \gtrsim 2$, most will eventually be re-accreted by the galaxy through a process known as “recycling” (e.g., Oppenheimer et al., 2010; Muratov et al., 2015). It is of interest to ask whether the observed ensemble kinematics of circumgalactic HI we have presented in previous sections suggests the presence of neutral gas capable of escaping the potential well of the central galaxy. The most straightforward indicator would be significant absorption components of the CGM with $v_{\text{LOS}}(D_{\text{tran}}) > v_{\text{esc}}(r)$ where both are measured relative to the central galaxy systemic redshift (e.g., Adelberger et al., 2005a; Rudie et al., 2019.)

Figure 2.18 reproduces the folded map of τ_{ap} , with curves denoting the 3-D escape velocity (v_{esc}) for a $M_{\text{h}} = 10^{12} M_{\odot}$ NFW halo: since the map shows only projected distances and line-of-sight velocities, the actual galactocentric radius and 3-D space velocities of gas may be greater than D_{tran} and v_{LOS} , respectively. Considering only gravity as in §2.4, any gas with $v_{\text{LOS}} > v_{\text{esc}}$ would be capable of escaping the halo.

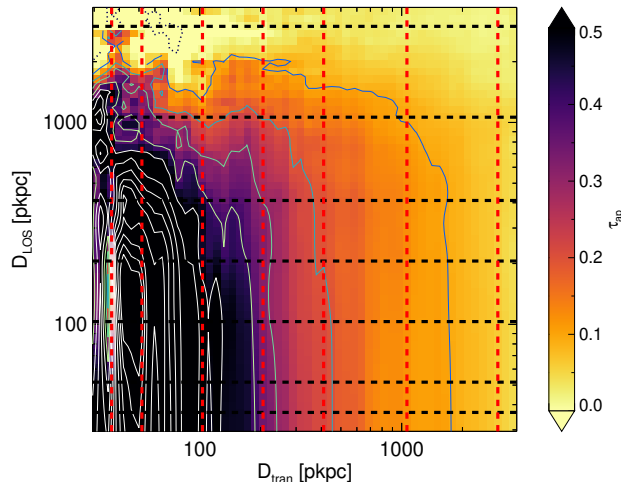


Figure 2.19: Same as the top-left plot of Figure 2.8, except here the y-axis has been converted to line-of-sight distance assuming that v_{LOS} is entirely due to Hubble expansion. The two axes have been adjusted so that any departures from symmetry indicate the presence of peculiar motions of gas with respect to the Hubble flow. The red vertical dashed lines and black horizontal dashed lines correspond to the locations of extracted profiles in Figure 2.20.

Conversely, gas with $v_{\text{LOS}} < v_{\text{esc}}$ is not guaranteed to be bound to the halo, but the chance of escape rapidly decreases as $|v_{\text{LOS}}| \rightarrow 0$. Clearly, judged on this basis, most of the relatively-high- τ_{ap} H I within $D_{\text{tran}} \lesssim 100$ pkpc is unlikely to escape the galaxy potential.

Nevertheless, it remains likely that some gas *does* escape, given the presence of significant τ_{ap} with v_{LOS} close to or exceeding v_{esc} . It is also likely that H I is not the best tracer of the fastest-moving gas, particularly at large galactocentric distances, based on both observations of high-ionization metals in nearby and high-redshift starburst galaxies (e.g., Strickland et al., 2004; Strickland and Heckman, 2009; Turner et al., 2015; Rudie et al., 2019) and on simulations such as those presented in §2.4.

Redshift-Space Distortions

In order to highlight the effects of peculiar velocities on the observations, we resampled the τ_{ap} map in the line-of-sight direction, assuming that v_{LOS} is due entirely to Hubble expansion, i.e., that $D_{\text{LOS}} = v_{\text{LOS}}/H(z)$. Figure 2.19 shows the re-sampled τ_{ap} map of the KGPS-Full sample with matching D_{LOS} and D_{tran} axes. Regions with $D > 100$ pkpc closely resemble similar results compiled using QSO sightlines

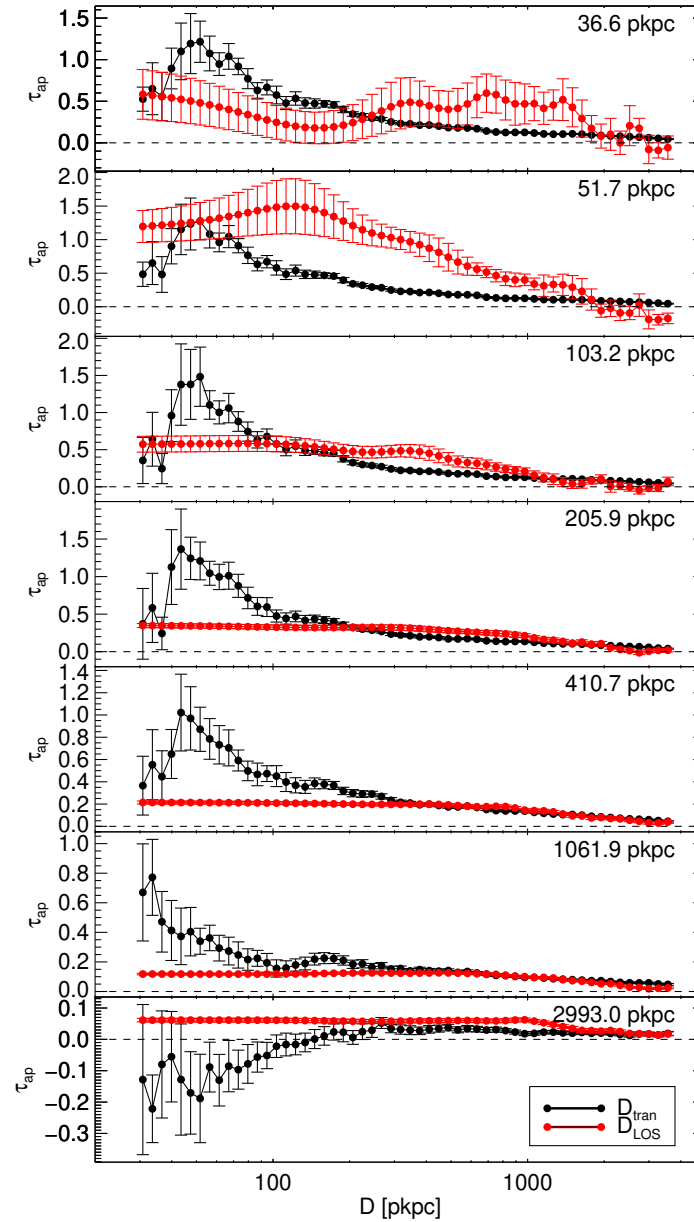


Figure 2.20: Comparison of the extracted τ_{ap} profiles (see Figure 2.19) in the D_{tran} (black) and D_{LOS} (red) directions. Numbers on the top-right corner of the plots are the distances in pkpc to the center of the galaxy in the direction orthogonal to that over which the profile is extracted.

from KBSS (Rudie et al., 2012; Rakic et al., 2012; Turner et al., 2014).

Figure 2.20 shows direct comparisons of τ_{ap} profiles extracted along the two axes (line of sight and transverse to the line of sight) for seven representative distances, randomly chosen from the figure. In the absence of peculiar velocities and redshift errors, the τ_{ap} profiles at fixed D_{LOS} and D_{tran} would be identical. In reality, the D_{LOS} and D_{tran} profiles differ significantly: e.g., at $D \lesssim 500$ pkpc, the D_{tran} cuts have similar shapes, while the corresponding D_{LOS} cuts on the same scales vary considerably. Most obvious is the “finger of God” elongation, known as the “Kaiser effect” (Kaiser, 1987), along the line of sight due to peculiar velocities of gas with $D_{\text{tran}} \lesssim 100$ pkpc. However, there is also a more subtle signature of infall in Figure 2.19 that is evident only at the lowest two contours in τ_{ap} , manifesting most clearly as a compression in the D_{LOS} direction between $D_{\text{tran}} \approx 100$ and $D_{\text{tran}} \approx 50$ pkpc as also noted previously.

At $D \gtrsim 500$ pkpc (upper-right corner of Figure 2.19), the D_{tran} and D_{LOS} cuts begin to match, indicating diminishing redshift-space distortion.

In addition to the KBSS-based studies mentioned above, there have been a number of other studies, focused on establishing the cross-correlation between “absorbers” along QSO sightlines and galaxies in the surrounding volumes at $z < 1$ (e.g., Chen et al., 2005; Ryan-Weber, 2006; Chen and Mulchaey, 2009; Tejos et al., 2014), $0.7 \lesssim z \lesssim 1.5$ (Shone et al., 2010), and $z \approx 2 - 3$ (Adelberger et al., 2003; Adelberger et al., 2005a; Tummuangpak et al., 2014; Bielby et al., 2017). Care must be exercised in comparing the results of these studies with those presented in this work, for two reasons: first, the aforementioned studies have cast the results in terms of auto- and cross-correlation functions, in co-moving coordinates, so that all length scales in the present work must be suitably adjusted¹⁶; second, most of these studies were not well-suited to measuring galaxy-gas correlations on scales smaller than ~ 1 cMpc (~ 300 pkpc at $\langle z \rangle = 2.2$) either due to redshift errors ($z > 2$ studies), paucity of absorber-galaxy pairs, or both. We note that the redshift space distortion in the KGPS map – both the “finger of God” at $D_{\text{tran}} \lesssim 50$ pkpc and the “compression” on scales of $50 \lesssim D_{\text{tran}} \lesssim 200$ pkpc, would probably have gone unrecognized. Otherwise, on scales larger than ~ 1 cMpc, there is reasonable agreement: for example, one of the conclusions of Tejos et al., 2014 is that there is little evidence for either infall or outflows of gas with peculiar velocities larger

¹⁶In comoving coordinates, the transverse scale for the 2D map in, e.g., Figure 2.7 would need to be multiplied by a factor of ≈ 3.2 for direct comparison, i.e., our measurements extend to transverse a transverse scale of $D_{\text{tran,com}} \approx 12.8h_{70}^{-1}$ cMpc.

than $\sim 120 \text{ km s}^{-1}$; our results are in agreement - recall that we found that infall velocities of $\sim 100 \text{ km s}^{-1}$ gave the best fits for our simple model. However, there are much larger peculiar velocities acting on scales smaller than $\simeq 150 \text{ pkpc}$ (0.5 cMpc), within the CGM.

Finally, we note that the values of τ_{ap} for the D_{tran} profile evaluated at $D_{\text{LOS}} = 2993 \text{ pkpc}$ (black points and curve in the bottom panel of Figure 2.20) are consistently negative for $D_{\text{tran}} \lesssim 100 \text{ pkpc}$. Because most of the points are correlated and each is individually consistent with $\tau_{\text{ap}} = 0$, we believe the most likely culprits are sample variance and continuum uncertainties exacerbated by the relatively small sample size. Meanwhile, as discussed in §2.4, it is possible that Ly α emission from the CGM of the foreground galaxy has a significant effect on the measured strength of Ly α absorption in the spectrum of faint background continuum sources, and that the magnitude of the effect would be largest at small D_{tran} . Scattered Ly α emission in down-the-barrel spectra of the galaxies tends to be dominated by a redshifted component, and it is not unusual for the red wing of Ly α to extend well beyond $v_{\text{LOS}} \sim 600 \text{ km s}^{-1}$; if the Ly α emission strength exceeds the flux removed by absorption against the continuum of the background source, it is possible in principle to have “negative” net Ly α absorption.

2.5 Summary

In this paper, we assembled 2862 spectroscopically-identified galaxies from KBSS ($1.9 \lesssim z \lesssim 3.3$; $\langle z \rangle = 2.51$) into $\sim 200,000$ unique angular pairs of physically-unrelated galaxies; we then used the spectra of the background galaxies to probe the H I content of the CGM/IGM of the foreground galaxies as a function of projected physical distance over the range of $30 \lesssim D_{\text{tran}}/\text{pkpc} \lesssim 4000$.

To maximize the utility of composite spectra for mapping the strength and kinematics of Ly α absorption surrounding galaxies, we used the $\simeq 45\%$ of galaxies with precise and accurate nebular emission line measurements to re-calibrate the relationship between the galaxy systemic redshift from z_{neb} and redshifts measured using spectral features in the rest-frame far-UV, $z_{\text{Ly}\alpha}$ and/or z_{IS} , which are biased by the effects of outflowing gas. We created composite spectra, stacked in bins of D_{tran} , of background galaxy spectra shifted to the rest frame of the corresponding foreground galaxy in each pair. The very large number of distinct galaxy-galaxy pairs allowed us to construct a well-sampled ensemble map of neutral H surrounding the average foreground galaxy in the sample. In particular, the improved sampling within

$D_{\text{tran}} \lesssim 100$ pkpc is crucial in probing the effects of galaxy-scale outflows on the H I kinematics.

We compared the observed Ly α map with cosmological zoom-in simulations and with a simple analytic model of outflows and infall surrounding a galaxy hosted by a dark matter halo of mass $M_{\text{h}} \approx 10^{12} M_{\odot}$. The principal results are summarized below:

1. The Ly α equivalent width as a function of impact parameter D_{tran} can be approximated as a power law, $W_{\lambda}(\text{Ly}\alpha) \propto D_{\text{tran}}^{-0.4}$ over the full range observed, but there are at least three distinct impact parameter zones for the run of $W_{\lambda}(\text{Ly}\alpha)$ vs. D_{tran} : $D_{\text{tran}} < 100$ pkpc (slope ≈ -1.0), $100 < D_{\text{tran}}/\text{pkpc} \lesssim 300$ (slope ≈ 0), and $300 \lesssim D_{\text{tran}}/\text{pkpc} \lesssim 2000$ (slope ≈ -0.5) (§2.3).
2. The 2-D map of apparent Ly α optical depth τ_{ap} (Figures 2.7, 2.8) in $v_{\text{LOS}}-D_{\text{tran}}$ space exhibits a dense “core” at $|v_{\text{LOS}}| < 500 \text{ km s}^{-1}$ and $D_{\text{tran}} < 100$ pkpc, that transitions to a diffuse component that becomes broader with increasing D_{tran} . The maps using the full KGPS sample and the sub-sample for which nebular redshifts are available for the foreground galaxy show consistent features. (§2.3)
3. Comparison of the τ_{ap} map with the projected N_{HI} map of a simulation with similar halo mass to the observed sample from the FIRE project shows that the dense “core”, and the outer “envelope” match remarkably well in both v_{LOS} and D_{tran} . (§2.4)
4. A simple, two-component analytic model with radial inflow and outflow can reproduce the general features of the observed 2-D τ_{ap} map; however, the model fails to fit abrupt features in the Ly α absorption kinematics at particular values of D_{tran} , which clearly indicate a level of complexity that is not captured by the adopted model parametrization. (§2.4)
5. The τ_{ap} map exhibits significant asymmetry in velocity relative to the galaxy systemic redshifts, the strongest of which is at projected distances $50 \lesssim D_{\text{tran}}/\text{pkpc} \lesssim 200$ and $200 \text{ km s}^{-1} \lesssim |v_{\text{LOS}}| \lesssim 500 \text{ km s}^{-1}$. The asymmetry is significant, and is unlikely to be explained by unaccounted-for systematic errors in galaxy redshifts. We suggest that the most plausible explanation is contamination of the Ly α absorption signal by diffuse Ly α emission associated

with the extended Ly α halo of the foreground galaxy scattering into the slit apertures used to measure the spectra of the background galaxies. Estimates of the expected effect of Ly α emission contamination on measurements of $W_\lambda(\text{Ly}\alpha)$ suggest that it should be non-negligible for any sample that uses background sources that are comparably bright to the foreground galaxies being probed. (§2.4)

6. Matching the $\tau_{\text{ap}}-D$ profile in D_{LOS} and D_{tran} axes shows strong redshift-space distortion at small D , and similar τ_{ap} profiles in the two directions at large D , suggesting that the redshift-space distortion becomes less prominent as $D \gtrsim 500$ pkpc. (§2.4)
7. The range of projected distance $50 \lesssim D_{\text{tran}}/\text{pkpc} \lesssim 150$ marks a transition in both the $W_\lambda(\text{Ly}\alpha)-D_{\text{tran}}$ relation, and the 2-D τ_{ap} map, suggesting that outflows gradually cede to infall as the dominant source of absorbing gas within that range. This inference is also supported by the narrow velocity profile of absorption in the same range of D_{tran} , consistent with the effective resolution of the observed map, indicating a local minimum dispersion in v_{LOS} where the confluence of infall, outflow, and Hubble expansion create a caustic-like feature in v_{LOS} space. (§2.4)

Our results for the spatial distribution and kinematics of H I could be compared with cosmological zoom-in simulations to test additional physical effects or feedback prescriptions (e.g., Hummels et al., 2013), and it is certainly possible to devise more realistic semi-analytic CGM models. Meanwhile, the clear distinction between outflow and inflow in the $v_{\text{LOS}}-D_{\text{tran}}$ space and the transition D_{tran} between the two provides vital information on the interaction between galaxies and their surroundings during the periods of rapid galaxy growth.

Similar observations using metal-line absorption from CGM gas can provide information on gas with a wider range of physical conditions, further constraining the distribution, kinematics, and physical conditions of baryons around galaxies. It will also be intriguing to compare the H I kinematics in absorption and emission *for the same galaxies* with aid of deep IFU spectroscopy, which will provide more nuanced view of the structure and kinematics of the CGM and how it affects the radiative transfer of Ly α . We are pursuing both of these approaches in forthcoming work.

Acknowledgments

Based on data obtained at the W. M. Keck Observatory, which is operated as a scientific partnership among the California Institute of Technology, the University of California, and the National Aeronautics and Space Administration. The Observatory was made possible by the generous financial support of the W. M. Keck Foundation.

This paper has included data obtained using Keck/LRIS (Oke et al., 1995; Steidel et al., 2004; Rockosi et al., 2010) and Keck/MOSFIRE (McLean et al., 2010; McLean et al., 2012). We thank the W.M. Keck Observatory staff for their assistance with the observations over two decades.

The following software packages have been crucial to preparing for this paper: the IDL Astronomy User's Library¹⁷, the Coyote IDL library¹⁸, Astropy (Price-Whelan et al., 2018), Emcee (Foreman-Mackey et al., 2013), the yt project (Turk et al., 2011), and Trident (Hummels, Smith, and Silvia, 2017).

This work was supported in part by grant AST-1313472 from the U.S. NSF, and by a grant from the Caltech/JPL President's and Director's Program. CAFG was supported by NSF through grants AST-1517491, AST-1715216, and CAREER award AST-1652522, by NASA through grant 17-ATP17-0067, by STScI through grants HST-GO-14681.011, HST-GO-14268.022-A, and HST-AR-14293.001-A, and by a Cottrell Scholar Award from the Research Corporation for Science Advancement.

We would like to thank the anonymous referee for providing valuable feedback. YC would like to thank Hongjie Zhu for her continuous encouragements when preparing for this paper. We would like to acknowledge Yiqiu Ma, E. Sterl Phinney, and Mateusz Matuszewski, for their constructive discussions. Finally, we thank collaborators Kurt L. Adelberger, Matthew P. Hunt, David R. Law, Olivera Rakic, and Monica L. Turner for their contributions to the KBSS survey over the course of nearly two decades.

Data Availability

The processed data underlying this article are available on the KBSS website (<http://ramekin.caltech.edu/KBSS>) with DOI: 10.22002/D1.1458.

¹⁷<https://idlastro.gsfc.nasa.gov/>

¹⁸<http://www.idlcoyote.com/>

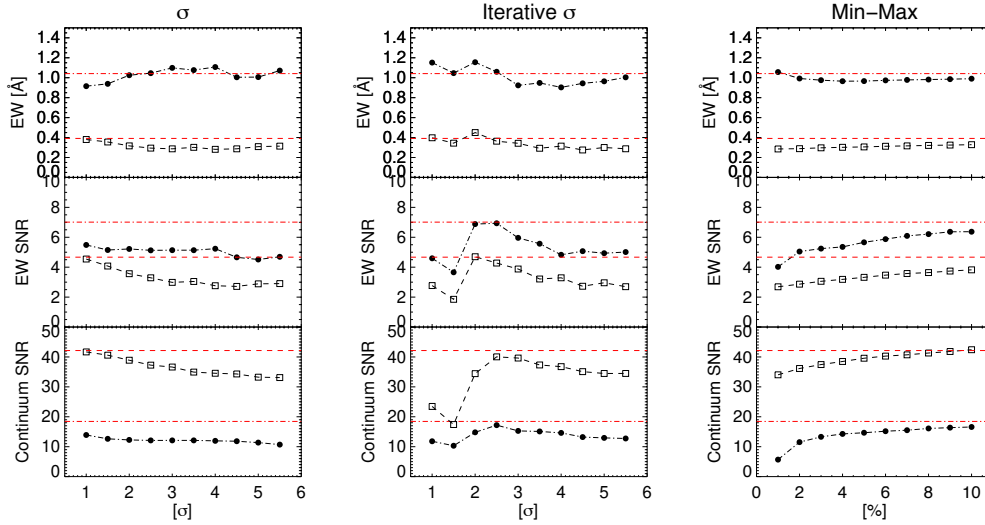


Figure 2.21: The impact of different stacking methods on $W_\lambda(\text{Ly}\alpha)$ measurements: each panel shows $W_\lambda(\text{Ly}\alpha)$ (top); the SNR of $W_\lambda(\text{Ly}\alpha)$ (middle); the SNR of the continuum near $\text{Ly}\alpha$ (bottom). The 3 panels (left to right) show the results for sigma clipping, *iterative* sigma clipping, and min-max rejection. For min-max rejection, the x-axis shows the fraction of data points rejected from each side of the sample distribution. Within each panel, the black filled points correspond to a sample with $(D_{\text{tran}}/\text{pkpc}) \leq 100$ and the skeletal boxes to a sample with $500 \leq (D_{\text{tran}}/\text{pkpc}) \leq 550$; the horizontal red lines show the corresponding values for a median stack with no other rejection algorithm applied.

Appendix

Stacking Method

To optimize the SNR of stacked spectra, we tested several different stacking methods: 1) sigma-clipped mean, 2) *iterative* sigma-clipped mean, 3) min-max clipped mean, and 4) median. For all cases, the error was estimated from bootstrap resampling of the sightlines within each bin using 2000 realizations. We select two D_{tran} bins – one with $(D_{\text{tran}}/\text{pkpc}) \leq 100$ and the other with $500 \leq (D_{\text{tran}}/\text{pkpc}) \leq 550$ from the KGPS-Full sample to demonstrate the effect of clipping on strong and weak $\text{Ly}\alpha$ absorption in Figure 2.21. $W_\lambda(\text{Ly}\alpha)$ was measured in the same way as in §2.3. The SNR of the continua is defined as the median flux density divided by the median error within two windows of rest-wavelength, $[1207, 1211] \text{ \AA}$ and $[1220, 1224] \text{ \AA}$.

While keeping most of the data points in the mean stacks does not alter the value of $W_\lambda(\text{Ly}\alpha)$ for either strong or weak lines, it significantly affects the SNR. On the other hand, achieving SNR similar to that obtained for median stacks requires more aggressive rejection ($\sim 2\sigma$ or $\sim 8\%$) for the sigma clipping and min-max rejection,

respectively. For iterative sigma clipping, we find that the optimal SNR is achieved at $\sim 2.5\sigma$, where the SNR of $W_\lambda(\text{Ly}\alpha)$ for weak lines and that of the continuum near strong lines are close to those of the median stack. Otherwise, the SNR remains $\sim 10\%$ smaller than for spectra combined using a median stack; this suggests that the data values at each wavelength pixel are not normally distributed, and therefore outliers are not easily removed by sigma clipping. Given that the spectral continuum of the pre-stacked spectra are not normalized, part of this is contributed by the variations of the stellar continuum in the spectra of the background galaxies. In addition, we find that in some regimes, the systematic effects of clipping methods have the opposite signs for strong and weak $W_\lambda(\text{Ly}\alpha)$ (top panel of Figure 2.21). Since the median stack consistently returns values close to the optimal clipped mean, both in terms of measured $W_\lambda(\text{Ly}\alpha)$ and $\text{SNR}(W_\lambda(\text{Ly}\alpha))$, we subsequently adopted the median stack for producing all composite spectra used in this paper.

Effective Spectral Resolution in Composite Spectra

Having a reliable measurement of the effective spectral resolution of the stacked spectra is crucial because some of the features in the 2D map are only marginally resolved. We stack spectra from the KGPS sample in the rest frame of z_{bg} and use the strong down-the-barrel UV features to estimate the effective resolution. We used the C II $\lambda 1334$ line since it does not suffer from significant contamination from other lines, and has the most consistent W_λ (RMS $\lesssim 5\%$) in the stacks of different subsamples.

Assuming that the observed line width can be expressed as,

$$\sigma_{\text{obs}} = \sqrt{\sigma_0^2 + \sigma_{\text{eff}}^2} \quad (2.22)$$

$$= \sqrt{\sigma_0^2 + \sigma_{\text{inst}}^2 + f_{\text{zuv}}\sigma_{\text{zuv}}^2}, \quad (2.23)$$

where σ_0 is the intrinsic width, σ_{eff} is the effective velocity resolution, σ_{inst} is the resolution of the spectrograph, and f_{zuv} is the fraction of spectra in stacks that use calibration from $z_{\text{Ly}\alpha}$ and z_{abs} as z_{sys} , and σ_{zuv} is the uncertainty of the calibration in velocity space. In this case, σ_{inst} and σ_{zuv} can be estimated separately. We assume that the redshift uncertainty is negligible when using z_{neb} as z_{sys} .

Since essentially all our LRIS observations used either the 400/3400 or 600/4000 gratings, σ_{inst} can be further divided into,

$$\sigma_{\text{inst}} = \sqrt{f_{400}\sigma_{400}^2 + f_{600}\sigma_{600}^2}, \quad (2.24)$$

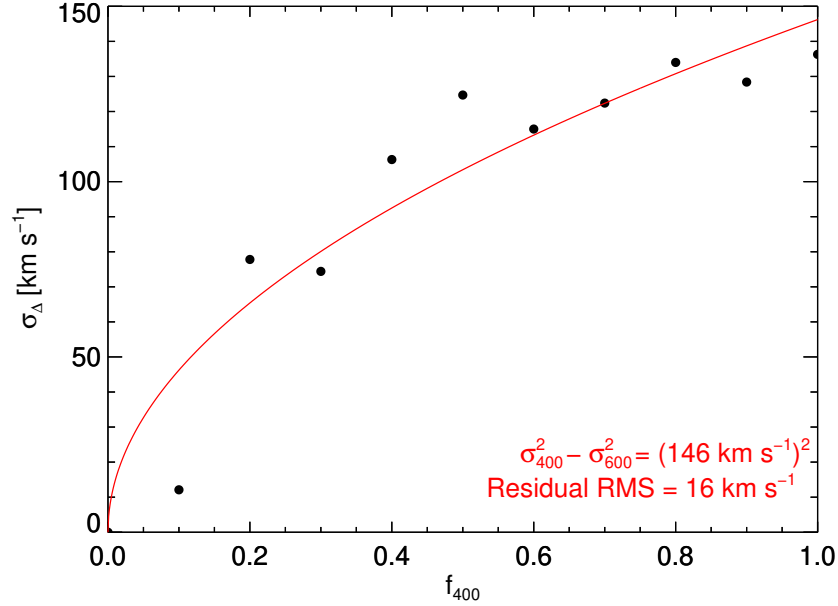


Figure 2.22: Width of the Gaussian kernel (σ_{Δ}) used in convolution to match the line profile of C II $\lambda 1334$, between stacks with pure 600/4000 spectra and ones with a fraction of the 400/3400 grism spectra (f_{400}). The red line is the best-fit model using Equation 2.25.

where σ_{400} and σ_{600} are the instrument resolution for the 400/3400 and 600/4000 grisms, and f_{400} and f_{600} are the fractions of spectra observed with the two grisms in the stack. To measure the absolute values of σ_{400} and σ_{600} , we constructed 11 samples. Each has different ratio of f_{400}/f_{600} , ranging from 100% of the spectra observed by the 400/3400 grism to 100% observed by the 600/4000 grism. All are based on exactly the same 95 objects, which have been observed with both 400/3400 and 600/4000 grisms, and have their systemic redshift measured from nebular lines. We fit the 10 stacks with non-zero contribution of 600/4000 spectra by convolving the 100% 600/4000 stack with a Gaussian kernel, whose standard deviation (σ_{Δ}) is the only free parameter. The best- χ^2 fits of σ_{Δ} are summarized in Figure 2.22. Based on Equation 2.24,

$$\sigma_{\Delta} = \sqrt{f_{400}(\sigma_{400}^2 - \sigma_{600}^2)}. \quad (2.25)$$

Therefore, $\sqrt{\sigma_{400}^2 - \sigma_{600}^2} = 146 \text{ km s}^{-1}$, obtained by fitting the equation above to the measured points in Figure 2.22.

Another ingredient for estimating the absolute value of σ_{400} and σ_{600} is the ratio of $\sigma_{400}/\sigma_{600}$. Figure 2.23 shows the instrument resolution of the two grisms for an

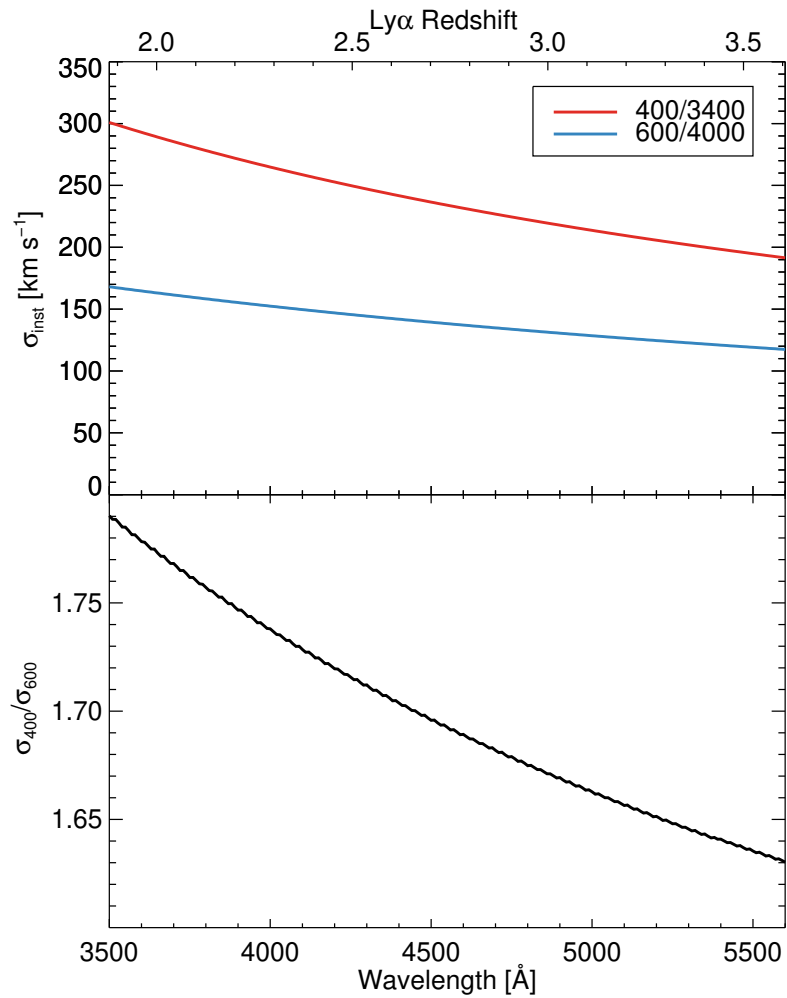


Figure 2.23: Spectroscopic resolution for 400/3400 and 600/4000 gratings plotted as 1- σ error in velocity space. *Top*: Absolute value estimated from arc spectra with 1.2-arcsec slit width. *Bottom*: Ratio between σ_{400} and σ_{600} , which remains unchanged with varying object size in slits.

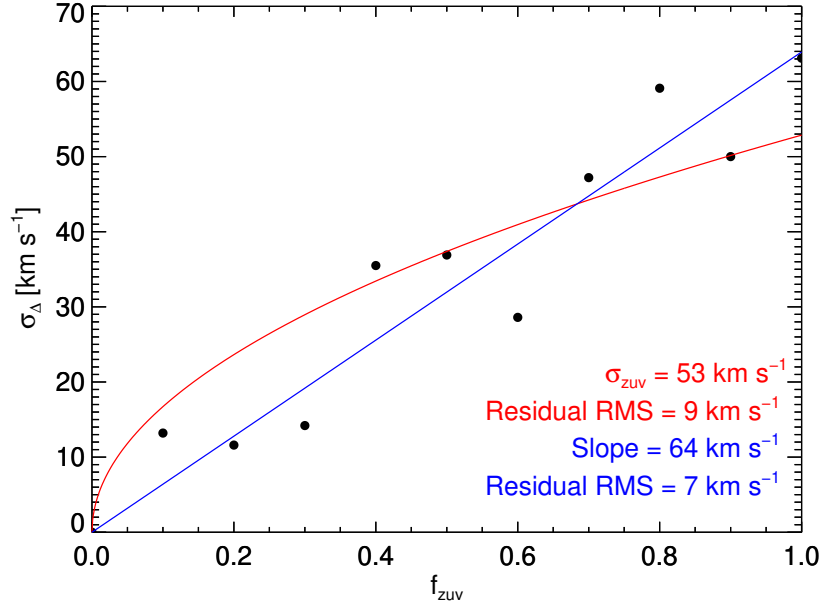


Figure 2.24: Similar to Figure 2.22, but the x-axis is the fraction of objects in the stacks whose z_{sys} is determined using rest-UV spectral features (f_{zuv}). The red curve is the best-fit of Equation 2.23, and the blue line is a simple linear fit.

object with uniform illumination of a 1.2 arcsec slit, estimated from the arc spectra taken during afternoon calibrations. For a median redshift of 2.4 in our DTB stacks, the observed wavelength of C II $\lambda 1334$ is 4559 Å, which gives $\sigma_{400}/\sigma_{600} \sim 1.69$. Therefore, $\sigma_{400} = 181 \text{ km s}^{-1}$, $\sigma_{600} = 107 \text{ km s}^{-1}$. This suggests a typical galaxy size of FWHM = 0.9 arcsec. We then convert this measurement to the resolution that would be obtained for Ly α at $z_{\text{med}} = 2.2$. Assuming the λ -dependence of σ as in Figure 2.23, the velocity resolutions are $\sigma_{400}(\text{Ly}\alpha) = 211 \text{ km s}^{-1}$ ($R = 604$), and $\sigma_{600}(\text{Ly}\alpha) = 121 \text{ km s}^{-1}$ ($R = 1055$).

To test the reliability, we also made a stack with the same objects and combined all 400/3400 and 600/4000 spectra together, weighted by the number of objects instead of the number of spectra to reproduce the scenario in §2.2. With 45% of the weight given to 400/3400 spectra, this yields a σ_{Δ} of 98 km s^{-1} , consistent with Equation 2.25 within 10%. For our typical foreground stacks in §2.2, $\sim 70\%$ of weight is contributed by 400/3400 spectra, and 600/4000 spectra make up the remaining 30%. Therefore, the effective resolution, $\sigma_{\text{inst}}(\text{Ly}\alpha) = 189 \text{ km s}^{-1}$.

The absolute value of σ_{zuv} in Equation 2.22 can be obtained using a similar method. We constructed 11 stacks with 382 objects that have redshift measurements with both nebular and rest-UV features. In these stacks, we randomly select f_{zuv} fraction

of objects and use the calibrated UV redshift (z_{UV}) instead of the precise z_{neb} . We use a similar method to fit the 10 stacks with non-zero f_{zuv} by convolving a Gaussian kernel with the 100% z_{neb} stack. The resulting kernel width as a function of f_{zuv} is shown in Figure 2.24. As can be seen in the figure, the relationship between σ_{Δ} and f_{zuv} can be better represented by a linear function rather than a square-root function, and the redshift errors associated with the use of UV features to estimate z_{sys} are smaller than derived in §2.2. We suspect that the reason for the apparent discrepancy is that a large fraction of the derived σ_z in §2.2 is caused by noise in the measurement of individual UV features in the spectra of individual galaxies, whereas the calibration between z_{neb} and z_{UV} effectively averages out such random noise. Nevertheless, we provide results for the two separate fits and use both in our final estimation. For a typical $f_{zuv} = 50\%$ in our foreground stacks for the KGPS-Full sample, $\sigma_{\Delta} = 37$ (square-root) or 32 (linear) km s^{-1} . Putting all components together in Equation 2.22, the effective resolution for the KGPS-Full sample is $\sigma_{\text{eff}}(\text{Ly}\alpha) = 192 \text{ km s}^{-1}$ for both the square-root and the linear fit.

In summary, the effective spectral resolution for the KGPS- z_{neb} and KGPS-Full sample is nearly identical: $\sigma_{z_{neb}} = 189 \text{ km s}^{-1}$ ($R = 676$) and $\sigma_{\text{full}} = 192 \text{ km s}^{-1}$ ($R = 665$), respectively. The uncertainty associated with the estimates is $\sim 15 \text{ km s}^{-1}$, based on the rms residuals of the fits for σ_{Δ} - f_{400} and σ_{Δ} - f_{zuv} relations.

References

- Adelberger, Kurt L., Charles C. Steidel, Alice E. Shapley, and Max Pettini (Feb. 2003). “Galaxies and Intergalactic Matter at Redshift $z \sim 3$: Overview”. *ApJ* 584.1, pp. 45–75. DOI: 10.1086/345660. arXiv: astro-ph/0210314 [astro-ph].
- Adelberger, Kurt L. et al. (May 2004). “Optical Selection of Star-forming Galaxies at Redshifts $1 < z < 3$ ”. *ApJ* 607.1, pp. 226–240. DOI: 10.1086/383221. arXiv: astro-ph/0401445 [astro-ph].
- Adelberger, Kurt L. et al. (Aug. 2005a). “The Connection between Galaxies and Intergalactic Absorption Lines at Redshift $2 \lesssim z \lesssim 3$ ”. *ApJ* 629.2, pp. 636–653. DOI: 10.1086/431753. arXiv: astro-ph/0505122 [astro-ph].
- Adelberger, Kurt L. et al. (Feb. 2005b). “The Spatial Clustering of Star-forming Galaxies at Redshifts $1.4 < z < 3.5$ ”. *ApJ* 619.2, pp. 697–713. DOI: 10.1086/426580. arXiv: astro-ph/0410165 [astro-ph].
- Anglés-Alcázar, Daniel et al. (Oct. 2017). “The cosmic baryon cycle and galaxy mass assembly in the FIRE simulations”. *MNRAS* 470.4, pp. 4698–4719. DOI: 10.1093/mnras/stx1517. arXiv: 1610.08523 [astro-ph.GA].

- Bahcall, John N. and Jr. Spitzer Lyman (May 1969). “Absorption Lines Produced by Galactic Halos”. *ApJ* 156, p. L63. DOI: 10.1086/180350.
- Bielby, R. M. et al. (Oct. 2017). “The VLT LBG redshift survey - VI. Mapping H I in the proximity of $z \sim 3$ LBGs with X-Shooter”. *MNRAS* 471.2, pp. 2174–2186. DOI: 10.1093/mnras/stx1772. arXiv: 1610.09144 [astro-ph.GA].
- Burchett, Joseph N. et al. (Dec. 2016). “A Deep Search for Faint Galaxies Associated with Very Low Redshift C IV Absorbers. III. The Mass- and Environment-dependent Circumgalactic Medium”. *ApJ* 832.2, 124, p. 124. DOI: 10.3847/0004-637X/832/2/124. arXiv: 1512.00853 [astro-ph.GA].
- Chen, Hsiao-Wen, Kenneth M. Lanzetta, John K. Webb, and Xavier Barcons (Oct. 2001). “The Gaseous Extent of Galaxies and the Origin of Ly α Absorption Systems. V. Optical and Near-Infrared Photometry of Ly α -absorbing Galaxies at $z < 1$ ”. *ApJ* 559.2, pp. 654–674. DOI: 10.1086/322414. arXiv: astro-ph/0107137 [astro-ph].
- Chen, Hsiao-Wen and John S. Mulchaey (Aug. 2009). “Probing The Intergalactic Medium-Galaxy Connection At $z < 0.5$. I. A Galaxy Survey In Qso Fields And A Galaxy-Absorber Cross-Correlation Study”. *ApJ* 701.2, pp. 1219–1242. DOI: 10.1088/0004-637X/701/2/1219. arXiv: 0906.3293 [astro-ph.CO].
- Chen, Hsiao-Wen, Jason X. Prochaska, Benjamin J. Weiner, John S. Mulchaey, and Gerard M. Williger (Aug. 2005). “Probing the Intergalactic Medium-Galaxy Connection toward PKS 0405-123. II. A Cross-Correlation Study of Ly α Absorbers and Galaxies at $z < 0.5$ ”. *ApJ* 629.1, pp. L25–L28. DOI: 10.1086/444377. arXiv: astro-ph/0507621 [astro-ph].
- Chen, Hsiao-Wen et al. (Dec. 2010). “What Determines the Incidence and Extent of Mg II Absorbing Gas Around Galaxies?” *ApJ* 724.2, pp. L176–L182. DOI: 10.1088/2041-8205/724/2/L176. arXiv: 1011.0735 [astro-ph.CO].
- Crighton, N. H. M. et al. (June 2011). “The VLT LBG Redshift Survey- II. Interactions between galaxies and the IGM at $z \sim 3$ ”. *MNRAS* 414.1, pp. 28–49. DOI: 10.1111/j.1365-2966.2011.17247.x. arXiv: 1006.4385 [astro-ph.CO].
- Dijkstra, Mark (Oct. 2014). “Ly α Emitting Galaxies as a Probe of Reionisation”. *Publ. Astron. Soc. Australia* 31, e040, e040. DOI: 10.1017/pasa.2014.33. arXiv: 1406.7292 [astro-ph.CO].
- Erb, Dawn K., Charles C. Steidel, and Yuguang Chen (July 2018). “The Kinematics of Extended Ly α Emission in a Low-mass, Low-metallicity Galaxy at $z = 2.3$ ”. *ApJ* 862.1, L10, p. L10. DOI: 10.3847/2041-8213/aacff6. arXiv: 1807.00065 [astro-ph.GA].
- Erb, Dawn K. et al. (Aug. 2006a). “H α Observations of a Large Sample of Galaxies at $z \sim 2$: Implications for Star Formation in High-Redshift Galaxies”. *ApJ* 647.1, pp. 128–139. DOI: 10.1086/505341. arXiv: astro-ph/0604388 [astro-ph].

- Erb, Dawn K. et al. (June 2006b). “The Mass-Metallicity Relation at $z > \sim 2$ ”. *ApJ* 644.2, pp. 813–828. DOI: 10.1086/503623. arXiv: astro-ph/0602473 [astro-ph].
- Erb, Dawn K. et al. (July 2006c). “The Stellar, Gas, and Dynamical Masses of Star-forming Galaxies at $z \sim 2$ ”. *ApJ* 646.1, pp. 107–132. DOI: 10.1086/504891. arXiv: astro-ph/0604041 [astro-ph].
- Faucher-Giguère, Claude-André, Dušan Kereš, Mark Dijkstra, Lars Hernquist, and Matias Zaldarriaga (Dec. 2010). “Ly α Cooling Emission from Galaxy Formation”. *ApJ* 725.1, pp. 633–657. DOI: 10.1088/0004-637X/725/1/633. arXiv: 1005.3041 [astro-ph.CO].
- Faucher-Giguère, Claude-André, Jason X. Prochaska, Adam Lidz, Lars Hernquist, and Matias Zaldarriaga (July 2008). “A Direct Precision Measurement of the Intergalactic Ly α Opacity at $2 \leq z \leq 4.2$ ”. *ApJ* 681.2, pp. 831–855. DOI: 10.1086/588648. arXiv: 0709.2382 [astro-ph].
- Faucher-Giguère, Claude-André et al. (May 2015). “Neutral hydrogen in galaxy haloes at the peak of the cosmic star formation history”. *MNRAS* 449.1, pp. 987–1003. DOI: 10.1093/mnras/stv336. arXiv: 1409.1919 [astro-ph.GA].
- Faucher-Giguère, Claude-André et al. (Sept. 2016). “A stellar feedback origin for neutral hydrogen in high-redshift quasar-mass haloes”. *MNRAS* 461.1, pp. L32–L36. DOI: 10.1093/mnrasl/plw091. arXiv: 1601.07188 [astro-ph.GA].
- Foreman-Mackey, Daniel et al. (Mar. 2013). *emcee: The MCMC Hammer*. ascl:1303.002.
- Franx, Marijn, Garth D. Illingworth, Daniel D. Kelson, Pieter G. van Dokkum, and Kim-Vy Tran (Sept. 1997). “A Pair of Lensed Galaxies at $z = 4.92$ in the Field of CL 1358+62”. *ApJ* 486.2, pp. L75–L78. DOI: 10.1086/310844. arXiv: astro-ph/9704090 [astro-ph].
- Hafen, Zachary et al. (Sept. 2019). “The origins of the circumgalactic medium in the FIRE simulations”. *MNRAS* 488.1, pp. 1248–1272. DOI: 10.1093/mnras/stz1773. arXiv: 1811.11753 [astro-ph.GA].
- Hopkins, Philip F. et al. (Nov. 2014). “Galaxies on FIRE (Feedback In Realistic Environments): stellar feedback explains cosmologically inefficient star formation”. *MNRAS* 445.1, pp. 581–603. DOI: 10.1093/mnras/stu1738. arXiv: 1311.2073 [astro-ph.CO].
- Hopkins, Philip F. et al. (Oct. 2018). “FIRE-2 simulations: physics versus numerics in galaxy formation”. *MNRAS* 480.1, pp. 800–863. DOI: 10.1093/mnras/sty1690. arXiv: 1702.06148 [astro-ph.GA].
- Hummels, Cameron B., Greg L. Bryan, Britton D. Smith, and Matthew J. Turk (Apr. 2013). “Constraints on hydrodynamical subgrid models from quasar absorption line studies of the simulated circumgalactic medium”. *MNRAS* 430.3, pp. 1548–1565. DOI: 10.1093/mnras/sts702. arXiv: 1212.2965 [astro-ph.GA].

- Hummels, Cameron B., Britton D. Smith, and Devin W. Silvia (Sept. 2017). “Trident: A Universal Tool for Generating Synthetic Absorption Spectra from Astrophysical Simulations”. *ApJ* 847.1, 59, p. 59. DOI: 10.3847/1538-4357/aa7e2d. arXiv: 1612.03935 [astro-ph.IM].
- Hummels, Cameron B. et al. (Sept. 2019). “The Impact of Enhanced Halo Resolution on the Simulated Circumgalactic Medium”. *ApJ* 882.2, 156, p. 156. DOI: 10.3847/1538-4357/ab378f. arXiv: 1811.12410 [astro-ph.GA].
- Ji, Suoqing, S. Peng Oh, and Phillip Masterson (July 2019). “Simulations of radiative turbulent mixing layers”. *MNRAS* 487.1, pp. 737–754. DOI: 10.1093/mnras/stz1248. arXiv: 1809.09101 [astro-ph.GA].
- Johnson, Sean D., Hsiao-Wen Chen, and John S. Mulchaey (May 2015). “On the possible environmental effect in distributing heavy elements beyond individual gaseous haloes”. *MNRAS* 449.3, pp. 3263–3273. DOI: 10.1093/mnras/stv553. arXiv: 1503.04199 [astro-ph.GA].
- Johnson, Sean D., Hsiao-Wen Chen, John S. Mulchaey, Joop Schaye, and Lorrie A. Straka (Nov. 2017). “The Extent of Chemically Enriched Gas around Star-forming Dwarf Galaxies”. *ApJ* 850.1, L10, p. L10. DOI: 10.3847/2041-8213/aa9370. arXiv: 1710.06441 [astro-ph.GA].
- Kaiser, Nick (July 1987). “Clustering in real space and in redshift space”. *MNRAS* 227, pp. 1–21. DOI: 10.1093/mnras/227.1.1.
- Kakiichi, Koki and Mark Dijkstra (Nov. 2018). “A new model framework for circumgalactic Ly α radiative transfer constrained by galaxy-Ly α forest clustering”. *MNRAS* 480.4, pp. 5140–5159. DOI: 10.1093/mnras/sty2214. arXiv: 1710.10053 [astro-ph.GA].
- Klypin, Anatoly, Gustavo Yepes, Stefan Gottlöber, Francisco Prada, and Steffen Heß (Apr. 2016). “MultiDark simulations: the story of dark matter halo concentrations and density profiles”. *MNRAS* 457.4, pp. 4340–4359. DOI: 10.1093/mnras/stw248. arXiv: 1411.4001 [astro-ph.CO].
- Kriek, Mariska et al. (June 2015). “The MOSFIRE Deep Evolution Field (MOSDEF) Survey: Rest-frame Optical Spectroscopy for ~ 1500 H-selected Galaxies at $1.37 < z < 3.8$ ”. *ApJS* 218.2, 15, p. 15. DOI: 10.1088/0067-0049/218/2/15. arXiv: 1412.1835 [astro-ph.GA].
- Lanzetta, Kenneth M., David V. Bowen, David Tytler, and John K. Webb (Apr. 1995). “The Gaseous Extent of Galaxies and the Origin of Lyman-Alpha Absorption Systems: A Survey of Galaxies in the Fields of Hubble Space Telescope Spectroscopic Target QSOs”. *ApJ* 442, p. 538. DOI: 10.1086/175459.
- Law, David R. et al. (Jan. 2012). “An HST/WFC3-IR Morphological Survey of Galaxies at $z = 1.5$ -3.6. I. Survey Description and Morphological Properties of Star-forming Galaxies”. *ApJ* 745.1, 85, p. 85. DOI: 10.1088/0004-637X/745/1/85. arXiv: 1107.3137 [astro-ph.CO].

- Lowenthal, James D. et al. (May 1997). “Keck Spectroscopy of Redshift $z \sim 3$ Galaxies in the Hubble Deep Field”. *ApJ* 481.2, pp. 673–688. DOI: 10.1086/304092. arXiv: astro-ph/9612239 [astro-ph].
- Madau, Piero and Mark Dickinson (Aug. 2014). “Cosmic Star-Formation History”. *ARA&A* 52, pp. 415–486. DOI: 10.1146/annurev-astro-081811-125615. arXiv: 1403.0007 [astro-ph.CO].
- McLean, Ian S. et al. (July 2010). “Design and development of MOSFIRE: the multi-object spectrometer for infrared exploration at the Keck Observatory”. *Ground-based and Airborne Instrumentation for Astronomy III*. Ed. by Ian S. McLean, Suzanne K. Ramsay, and Hideki Takami. Vol. 7735. Society of Photo-Optical Instrumentation Engineers (SPIE) Conference Series, 77351E. DOI: 10.1117/12.856715.
- McLean, Ian S. et al. (Sept. 2012). “MOSFIRE, the multi-object spectrometer for infra-red exploration at the Keck Observatory”. *Ground-based and Airborne Instrumentation for Astronomy IV*. Ed. by Ian S. McLean, Suzanne K. Ramsay, and Hideki Takami. Vol. 8446. Society of Photo-Optical Instrumentation Engineers (SPIE) Conference Series, 84460J. DOI: 10.1117/12.924794.
- Mitchell, Peter D., Joop Schaye, Richard G. Bower, and Robert A. Crain (Apr. 2020). “Galactic outflow rates in the EAGLE simulations”. *MNRAS* 494.3, pp. 3971–3997. DOI: 10.1093/mnras/staa938. arXiv: 1910.09566 [astro-ph.GA].
- Morris, Simon L. and Buell T. Jannuzi (Apr. 2006). “The association between gas and galaxies - I. CFHT spectroscopy and pair analysis”. *MNRAS* 367.3, pp. 1261–1281. DOI: 10.1111/j.1365-2966.2006.10013.x. arXiv: astro-ph/0601200 [astro-ph].
- Morrissey, Patrick et al. (Sept. 2018). “The Keck Cosmic Web Imager Integral Field Spectrograph”. *ApJ* 864.1, 93, p. 93. DOI: 10.3847/1538-4357/aad597. arXiv: 1807.10356 [astro-ph.IM].
- Muratov, Alexander L. et al. (Dec. 2015). “Gusty, gaseous flows of FIRE: galactic winds in cosmological simulations with explicit stellar feedback”. *MNRAS* 454.3, pp. 2691–2713. DOI: 10.1093/mnras/stv2126. arXiv: 1501.03155 [astro-ph.GA].
- Navarro, Julio F., Carlos S. Frenk, and Simon D. M. White (May 1996). “The Structure of Cold Dark Matter Halos”. *ApJ* 462, p. 563. DOI: 10.1086/177173. arXiv: astro-ph/9508025 [astro-ph].
- Nelson, Dylan et al. (Dec. 2019). “First results from the TNG50 simulation: galactic outflows driven by supernovae and black hole feedback”. *MNRAS* 490.3, pp. 3234–3261. DOI: 10.1093/mnras/stz2306. arXiv: 1902.05554 [astro-ph.GA].
- Nielsen, Nikole M., Glenn G. Kacprzak, Stephanie K. Pointon, Christopher W. Churchill, and Michael T. Murphy (Dec. 2018). “MAGIICAT VI. The Mg II Intragroup Medium Is Kinematically Complex”. *ApJ* 869.2, 153, p. 153. DOI: 10.3847/1538-4357/aaedbd. arXiv: 1808.09562 [astro-ph.GA].

- Oke, J. B. and D. G. Korycansky (Apr. 1982). “Absolute spectrophotometry of very large redshift quasars”. *ApJ* 255, pp. 11–19. doi: 10.1086/159797.
- Oke, J. B. et al. (Apr. 1995). “The Keck Low-Resolution Imaging Spectrometer”. *PASP* 107, p. 375. doi: 10.1086/133562.
- Oppenheimer, Benjamin D. et al. (Aug. 2010). “Feedback and recycled wind accretion: assembling the $z = 0$ galaxy mass function”. *MNRAS* 406.4, pp. 2325–2338. doi: 10.1111/j.1365-2966.2010.16872.x. arXiv: 0912.0519 [astro-ph.CO].
- Pettini, Max et al. (June 2001). “The Rest-Frame Optical Spectra of Lyman Break Galaxies: Star Formation, Extinction, Abundances, and Kinematics”. *ApJ* 554.2, pp. 981–1000. doi: 10.1086/321403. arXiv: astro-ph/0102456 [astro-ph].
- Price-Whelan, A.M. et al. (2018). “The Astropy Project: Building an inclusive, open-science project and status of the v2.0 core package”. *arXiv preprint arXiv:1801.02634*.
- Prochaska, J. Xavier, B. Weiner, H. W. Chen, J. Mulchaey, and K. Cooksey (Oct. 2011). “Probing the Intergalactic Medium/Galaxy Connection. V. On the Origin of Ly α and O VI Absorption at $z < 0.2$ ”. *ApJ* 740.2, 91, p. 91. doi: 10.1088/0004-637X/740/2/91. arXiv: 1103.1891 [astro-ph.CO].
- Rakic, Olivera, Joop Schaye, Charles C. Steidel, and Gwen C. Rudie (June 2012). “Neutral Hydrogen Optical Depth near Star-forming Galaxies at $z \approx 2.4$ in the Keck Baryonic Structure Survey”. *ApJ* 751.2, 94, p. 94. doi: 10.1088/0004-637X/751/2/94. arXiv: 1109.4944 [astro-ph.CO].
- Rakic, Olivera et al. (Aug. 2013). “A measurement of galaxy halo mass from the surrounding H I Ly α absorption”. *MNRAS* 433.4, pp. 3103–3114. doi: 10.1093/mnras/stt950. arXiv: 1306.1563 [astro-ph.CO].
- Rauch, Michael, Wallace L. W. Sargent, and Tom A. Barlow (Apr. 1999). “Small-Scale Structure at High Redshift. I. Glimpses of the Interstellar Medium at Redshift ~ 3.5 ”. *ApJ* 515.2, pp. 500–505. doi: 10.1086/307060.
- Reddy, Naveen A. et al. (June 2006). “Star Formation and Extinction in Redshift $z \sim 2$ Galaxies: Inferences from Spitzer MIPS Observations”. *ApJ* 644.2, pp. 792–812. doi: 10.1086/503739. arXiv: astro-ph/0602596 [astro-ph].
- Reddy, Naveen A. et al. (Mar. 2008). “Multiwavelength Constraints on the Cosmic Star Formation History from Spectroscopy: The Rest-Frame Ultraviolet, H α , and Infrared Luminosity Functions at Redshifts $1.9 \lesssim z \lesssim 3.4$ ”. *ApJS* 175.1, pp. 48–85. doi: 10.1086/521105. arXiv: 0706.4091 [astro-ph].
- Reddy, Naveen A. et al. (July 2012). “The Characteristic Star Formation Histories of Galaxies at Redshifts $z \sim 2-7$ ”. *ApJ* 754.1, 25, p. 25. doi: 10.1088/0004-637X/754/1/25. arXiv: 1205.0555 [astro-ph.CO].

- Rockosi, C. et al. (July 2010). “The low-resolution imaging spectrograph red channel CCD upgrade: fully depleted, high-resistivity CCDs for Keck”. *Ground-based and Airborne Instrumentation for Astronomy III*. Vol. 7735. Society of Photo-Optical Instrumentation Engineers (SPIE) Conference Series, 77350R. DOI: 10.1117/12.856818.
- Rubin, Kate H. R., Aleksandar M. Diamond-Stanic, Alison L. Coil, Neil H. M. Crighton, and Kyle R. Stewart (Dec. 2018). “Galaxies Probing Galaxies in PRIMUS. II. The Coherence Scale of the Cool Circumgalactic Medium”. *ApJ* 868.2, 142, p. 142. DOI: 10.3847/1538-4357/aad566. arXiv: 1806.08801 [astro-ph.GA].
- Rudie, Gwen C., Charles C. Steidel, and Max Pettini (Oct. 2012). “The Temperature-Density Relation in the Intergalactic Medium at Redshift $z = 2.4$ ”. *ApJ* 757.2, L30, p. L30. DOI: 10.1088/2041-8205/757/2/L30. arXiv: 1209.0005 [astro-ph.CO].
- Rudie, Gwen C., Charles C. Steidel, Alice E. Shapley, and Max Pettini (June 2013). “The Column Density Distribution and Continuum Opacity of the Intergalactic and Circumgalactic Medium at Redshift $z = 2.4$ ”. *ApJ* 769.2, 146, p. 146. DOI: 10.1088/0004-637X/769/2/146. arXiv: 1304.6719 [astro-ph.CO].
- Rudie, Gwen C. et al. (May 2012). “The Gaseous Environment of High- z Galaxies: Precision Measurements of Neutral Hydrogen in the Circumgalactic Medium of $z \sim 2-3$ Galaxies in the Keck Baryonic Structure Survey”. *ApJ* 750.1, 67, p. 67. DOI: 10.1088/0004-637X/750/1/67. arXiv: 1202.6055 [astro-ph.CO].
- Rudie, Gwen C. et al. (Nov. 2019). “Column Density, Kinematics, and Thermal State of Metal-bearing Gas within the Virial Radius of $z \sim 2$ Star-forming Galaxies in the Keck Baryonic Structure Survey”. *ApJ* 885.1, 61, p. 61. DOI: 10.3847/1538-4357/ab4255. arXiv: 1903.00004 [astro-ph.GA].
- Ryan-Weber, Emma V. (Apr. 2006). “Cross-correlation of Lyman α absorbers with gas-rich galaxies”. *MNRAS* 367.3, pp. 1251–1260. DOI: 10.1111/j.1365-2966.2006.10010.x. arXiv: astro-ph/0601055 [astro-ph].
- Shapley, Alice E., Charles C. Steidel, Max Pettini, and Kurt L. Adelberger (May 2003). “Rest-Frame Ultraviolet Spectra of $z \sim 3$ Lyman Break Galaxies”. *ApJ* 588.1, pp. 65–89. DOI: 10.1086/373922. arXiv: astro-ph/0301230 [astro-ph].
- Shapley, Alice E. et al. (June 2005). “Ultraviolet to Mid-Infrared Observations of Star-forming Galaxies at $z \sim 2$: Stellar Masses and Stellar Populations”. *ApJ* 626.2, pp. 698–722. DOI: 10.1086/429990. arXiv: astro-ph/0503485 [astro-ph].
- Shone, Allen M., Simon L. Morris, Neil Crighton, and Richard J. Wilman (Mar. 2010). “The association between gas and galaxies - III. The cross-correlation of galaxies and Ly α absorbers† at $z \sim 1$ ”. *MNRAS* 402.4, pp. 2520–2538. DOI: 10.1111/j.1365-2966.2009.16056.x. arXiv: 0911.3400 [astro-ph.CO].

- Steidel, Charles C., Mauro Giavalisco, Max Pettini, Mark Dickinson, and Kurt L. Adelberger (May 1996). “Spectroscopic Confirmation of a Population of Normal Star-forming Galaxies at Redshifts $Z > 3$ ”. *ApJ* 462, p. L17. DOI: 10.1086/310029. arXiv: astro-ph/9602024 [astro-ph].
- Steidel, Charles C. et al. (Aug. 2003). “Lyman Break Galaxies at Redshift $z \sim 3$: Survey Description and Full Data Set”. *ApJ* 592.2, pp. 728–754. DOI: 10.1086/375772. arXiv: astro-ph/0305378 [astro-ph].
- Steidel, Charles C. et al. (Apr. 2004). “A Survey of Star-forming Galaxies in the $1.4 \lesssim Z \lesssim 2.5$ Redshift Desert: Overview”. *ApJ* 604.2, pp. 534–550. DOI: 10.1086/381960. arXiv: astro-ph/0401439 [astro-ph].
- Steidel, Charles C. et al. (July 2010). “The Structure and Kinematics of the Circumgalactic Medium from Far-ultraviolet Spectra of $z \sim 2-3$ Galaxies”. *ApJ* 717.1, pp. 289–322. DOI: 10.1088/0004-637X/717/1/289. arXiv: 1003.0679 [astro-ph.CO].
- Steidel, Charles C. et al. (Aug. 2011). “Diffuse Ly α Emitting Halos: A Generic Property of High-redshift Star-forming Galaxies”. *ApJ* 736.2, 160, p. 160. DOI: 10.1088/0004-637X/736/2/160. arXiv: 1101.2204 [astro-ph.CO].
- Steidel, Charles C. et al. (Nov. 2014). “Strong Nebular Line Ratios in the Spectra of $z \sim 2-3$ Star Forming Galaxies: First Results from KBSS-MOSFIRE”. *ApJ* 795.2, 165, p. 165. DOI: 10.1088/0004-637X/795/2/165. arXiv: 1405.5473 [astro-ph.GA].
- Steidel, Charles C. et al. (Dec. 2018). “The Keck Lyman Continuum Spectroscopic Survey (KLCS): The Emergent Ionizing Spectrum of Galaxies at $z \sim 3$ ”. *ApJ* 869.2, 123, p. 123. DOI: 10.3847/1538-4357/aaed28. arXiv: 1805.06071 [astro-ph.GA].
- Strickland, David K. and Timothy M. Heckman (June 2009). “Supernova Feedback Efficiency and Mass Loading in the Starburst and Galactic Superwind Exemplar M82”. *ApJ* 697.2, pp. 2030–2056. DOI: 10.1088/0004-637X/697/2/2030. arXiv: 0903.4175 [astro-ph.CO].
- Strickland, David K., Timothy M. Heckman, Edward J. M. Colbert, Charles G. Hoopes, and Kimberly A. Weaver (May 2004). “A High Spatial Resolution X-Ray and H α Study of Hot Gas in the Halos of Star-forming Disk Galaxies. II. Quantifying Supernova Feedback”. *ApJ* 606.2, pp. 829–852. DOI: 10.1086/383136. arXiv: astro-ph/0306598 [astro-ph].
- Strom, Allison L. et al. (Feb. 2017). “Nebular Emission Line Ratios in $z \approx 2-3$ Star-forming Galaxies with KBSS-MOSFIRE: Exploring the Impact of Ionization, Excitation, and Nitrogen-to-Oxygen Ratio”. *ApJ* 836.2, 164, p. 164. DOI: 10.3847/1538-4357/836/2/164. arXiv: 1608.02587 [astro-ph.GA].

- Tejos, Nicolas et al. (Jan. 2014). “On the connection between the intergalactic medium and galaxies: the H I-galaxy cross-correlation at $z \lesssim 1$ ”. *MNRAS* 437.3, pp. 2017–2075. doi: 10.1093/mnras/stt1844. arXiv: 1309.5950 [astro-ph.CO].
- Theios, Rachel L. et al. (Jan. 2019). “Dust Attenuation, Star Formation, and Metallicity in $z \sim 2$ -3 Galaxies from KBSS-MOSFIRE”. *ApJ* 871.1, 128, p. 128. doi: 10.3847/1538-4357/aaf386. arXiv: 1805.00016 [astro-ph.GA].
- Trainor, Ryan F. and Charles C. Steidel (June 2012). “The Halo Masses and Galaxy Environments of Hyperluminous QSOs at $z \sim 2.7$ in the Keck Baryonic Structure Survey”. *ApJ* 752.1, 39, p. 39. doi: 10.1088/0004-637X/752/1/39. arXiv: 1204.3636 [astro-ph.CO].
- Tumlinson, J. et al. (June 2011). “Multiphase Gas in Galaxy Halos: The O VI Lyman-limit System toward J1009+0713”. *ApJ* 733.2, 111, p. 111. doi: 10.1088/0004-637X/733/2/111. arXiv: 1103.5252 [astro-ph.CO].
- Tumlinson, Jason, Molly S. Peeples, and Jessica K. Werk (Aug. 2017). “The Circumgalactic Medium”. *ARA&A* 55.1, pp. 389–432. doi: 10.1146/annurev-astro-091916-055240. arXiv: 1709.09180 [astro-ph.GA].
- Tummuangpak, P. et al. (Aug. 2014). “The Very Large Telescope Lyman-Break Galaxy Redshift Survey - IV. Gas and galaxies at $z \sim 3$ in observations and simulations”. *MNRAS* 442.3, pp. 2094–2115. doi: 10.1093/mnras/stu828. arXiv: 1304.4598 [astro-ph.CO].
- Turk, Matthew J. et al. (Jan. 2011). “yt: A Multi-code Analysis Toolkit for Astrophysical Simulation Data”. *ApJS* 192.1, 9, p. 9. doi: 10.1088/0067-0049/192/1/9. arXiv: 1011.3514 [astro-ph.IM].
- Turner, Monica L., Joop Schaye, Charles C. Steidel, Gwen C. Rudie, and Allison L. Strom (Nov. 2014). “Metal-line absorption around $z \approx 2.4$ star-forming galaxies in the Keck Baryonic Structure Survey”. *MNRAS* 445.1, pp. 794–822. doi: 10.1093/mnras/stu1801. arXiv: 1403.0942 [astro-ph.CO].
- Turner, Monica L., Joop Schaye, Charles C. Steidel, Gwen C. Rudie, and Allison L. Strom (June 2015). “Detection of hot, metal-enriched outflowing gas around $z \approx 2.3$ star-forming galaxies in the Keck Baryonic Structure Survey”. *MNRAS* 450.2, pp. 2067–2082. doi: 10.1093/mnras/stv750. arXiv: 1410.8214 [astro-ph.GA].
- Turner, Monica L. et al. (Oct. 2017). “A comparison of observed and simulated absorption from H I, C IV, and Si IV around $z \approx 2$ star-forming galaxies suggests redshift-space distortions are due to inflows”. *MNRAS* 471.1, pp. 690–705. doi: 10.1093/mnras/stx1616. arXiv: 1703.00086 [astro-ph.GA].
- Wisotzki, L. et al. (Mar. 2016). “Extended Lyman α haloes around individual high-redshift galaxies revealed by MUSE”. *A&A* 587, A98, A98. doi: 10.1051/0004-6361/201527384. arXiv: 1509.05143 [astro-ph.GA].

Chapter 3

THE KBSS-KCWI SURVEY: THE CONNECTION BETWEEN
EXTENDED $\text{Ly}\alpha$ HALOS AND GALAXY AZIMUTHAL ANGLE
AT $z \sim 2-3$

Chen, Yuguang et al. (Apr. 2021). “The KBSS-KCWI Survey: The connection between extended $\text{Ly}\alpha$ halos and galaxy azimuthal angle at $z \sim 2-3$ ”, arXiv:2104.10173. (in press with MNRAS), arXiv:2104.10173. arXiv: 2104.10173 [astro-ph.GA].

Yuguang Chen¹, Charles C. Steidel¹, Dawn K. Erb², David R. Law³, Ryan F. Trainor⁴, Naveen A. Reddy⁵, Alice E. Shapley⁶, Anthony J. Pahl⁶, Allison L. Strom⁷, Noah R. Lamb⁸, Zhihui Li¹, and Gwen C. Rudie⁹

¹Cahill Center for Astronomy and Astrophysics, California Institute of Technology, 1200 E California Blvd, MC249-17, Pasadena, CA 91125, USA

²Center for Gravitation, Cosmology, and Astrophysics, Department of Physics, University of Wisconsin-Milwaukee, 3135 N. Maryland Avenue, Milwaukee, WI 53211, USA

³Space Telescope Science Institute, 3700 San Martin Drive, Baltimore, MD 21218, USA

⁴Department of Physics and Astronomy, Franklin & Marshall College, 637 College Ave., Lancaster, PA 17603, USA

⁵Department of Physics and Astronomy, University of California, Riverside, 900 University Avenue, Riverside, CA 92521, USA

⁶Department of Physics and Astronomy, University of California, Los Angeles, 430 Portola Plaza, Los Angeles, CA 90095, USA

⁷Department of Astrophysical Sciences, 4 Ivy Lane, Princeton University, Princeton, NJ 08544, USA

⁸Department of Physics, Drexel University, 32 S. 32nd Street, Philadelphia, PA 19104, USA

⁹The Observatories of the Carnegie Institution for Science, 813 Santa Barbara Street, Pasadena, CA 91101, USA

Abstract

We present the first statistical analysis of kinematically-resolved, spatially-extended $\text{Ly}\alpha$ emission around $z = 2 - 3$ galaxies in the Keck Baryonic Structure Survey (KBSS) using the Keck Cosmic Web Imager (KCWI). Our sample of 59 star-forming galaxies ($z_{\text{med}} = 2.29$) comprises the subset with typical KCWI integration times of ~ 5 hours and with existing imaging data from the Hubble Space Telescope and/or

adaptive optics-assisted integral field spectroscopy. The high resolution images were used to evaluate the azimuthal dependence of the diffuse Ly α emission with respect to the stellar continuum within projected galactocentric distances of $\lesssim 30$ proper kpc. We introduce cylindrically-projected 2D spectra (CP2D) that map the averaged Ly α spectral profile over a specified range of azimuthal angle, as a function of impact parameter around galaxies. The averaged CP2D spectrum of all galaxies shows clear signatures of Ly α resonant scattering by outflowing gas. We stacked the CP2D spectra of individual galaxies over ranges of azimuthal angle with respect to their major axes. The extended Ly α emission along the galaxy principal axes are statistically indistinguishable, with residual asymmetry of $\leq 2\%$ ($\sim 2\sigma$) of the integrated Ly α emission. The symmetry implies that the Ly α scattering medium is dominated by outflows in all directions within 30 kpc. Meanwhile, we find that the blueshifted component of Ly α emission is marginally stronger along galaxy minor axes for galaxies with relatively weak Ly α emission. We speculate that this weak directional dependence of Ly α emission becomes discernible only when the Ly α escape fraction is low. These discoveries highlight the need for similar analyses in simulations with Ly α radiative transfer modeling.

3.1 Introduction

Extended “halos” of diffuse Lyman-alpha (Ly α) emission, extending to many times larger radii than starlight, are nearly ubiquitous around rapidly-star-forming galaxies at redshift $z > 2$ (e.g. Steidel et al., 2011; Wisotzki et al., 2016; Leclercq et al., 2017; Wisotzki et al., 2018). While there is not yet consensus on the dominant physical mechanism giving rise to diffuse Ly α halos, there is general agreement on the list of potential sources, all of which depend on substantial cool hydrogen gas in the circumgalactic medium (CGM; e.g., Ouchi, Ono, and Shibuya, 2020): (1) resonant scattering of Ly α produced by recombination of gas photoionised by massive stars or active galactic nuclei (AGN), i.e., a central source, where Ly α photons are subsequently scattered until they find optically-thin channels to escape; (2) *in situ* photoionization of H I by the metagalactic ultra-violet (UV) ionising radiation field combined with local sources and followed by recombination (sometimes called “fluorescence”); (3) accreting gas losing energy via collisional excitation of Ly α (sometimes referred to as “gravitational cooling”); (4) emission from unresolved satellite galaxies in the halos of larger central galaxies. In principle, the observed surface brightness, spatial distribution, and kinematics of Ly α emission can discriminate between the various mechanisms and, perhaps more importantly,

can provide direct information on the degree to which gas in the CGM is accreting, outflowing, or quiescent. Ly α emission from the CGM, if interpreted correctly, can provide a detailed map of the cool component of the dominant baryon reservoir associated with forming galaxies, as well as constraints on large-scale gas flows that are an essential part of the current galaxy formation paradigm.

Because a Ly α photon is produced by nearly every photoionisation of hydrogen, the intrinsic Ly α luminosity of a rapidly star-forming galaxy can be very high, and thus easily detected (Partridge and Peebles, 1967). However, due to its very high transition probability, Ly α is resonantly scattered until the last scattering event gives it an emitted frequency and direction such that the optical depth remains low along a trajectory that allows it to escape from the host galaxy. When the Ly α optical depth is high in all directions, the vastly increased effective path length – due to large numbers of scattering events during the time the photon is radiatively trapped – increases the probability that the photon is destroyed by dust or emitted via two-photon mechanism. But Ly α photons that are not absorbed by dust grains or converted to two-photon radiation must eventually escape, with the final scattering resulting in the photon having a frequency and direction such that the photon can freely stream without further interaction with a hydrogen atom. The radiative transfer of Ly α thus depends in a complex way on the distribution, clumpiness, and kinematics of H I within the host galaxy, as well as on where and how the photon was produced initially. But the added complexity is counter-balanced by the availability of a great deal of information about the scattering medium itself that is otherwise difficult or impossible to observe directly: i.e., the neutral hydrogen distribution and kinematics in the CGM.

Since the commissioning of sensitive integral-field spectrometers on large ground-based telescopes – the Multi Unit Spectroscopic Explorer (MUSE; Bacon et al., 2010) on the Very Large Telescopes (VLT) of the European Southern Observatory (ESO) and the Keck Cosmic Web Imager (KCWI; Morrissey et al., 2018) at the Keck Observatory – it has become possible to routinely detect diffuse Ly α emission halos around individual galaxies at high redshift (e.g., Wisotzki et al., 2016; Leclercq et al., 2017), and to simultaneously measure the spatially-resolved Ly α kinematics (e.g., Erb, Steidel, and Chen, 2018; Claeysens et al., 2019; Leclercq et al., 2020). Such observations can then be interpreted in terms of simple expectations based on Ly α radiative transfer; for example, a generic expectation is that most Ly α emission involving scattered photons (i.e., those that must pass through an H I gas distribution

before escaping their host) will exhibit a “double-peaked” spectral profile, where the relative strength of the blue-shifted and red-shifted peaks may be modulated by the net velocity field of the emitting gas. In the idealised case of a spherical shell of outflowing (infalling) gas, one predicts that an external observer will measure a dominant red (blue) peak (Verhamme, Schaerer, and Maselli, 2006). The fact that most ($\sim 90\%$) of star-forming galaxy “down the barrel” (DTB) spectra with Ly α in emission in the central portions exhibit dominant red peaks (e.g., Pettini et al., 2001; Steidel et al., 2010; Kulas et al., 2012; Trainor et al., 2015; Verhamme et al., 2018; Matthee et al., 2021) has led to the conclusion that outflowing gas dominates Ly α radiative transfer, at least at small galactocentric distances.

Essentially every simulation of galaxy formation (Faucher-Giguère et al., 2010) predicts that gaseous accretion is also important – particularly at high redshifts ($z \gtrsim 2$) – and this has focused attention on systems in which a double Ly α profile with a blue-dominant peak is observed, often cited as evidence for on-going accretion of cool gas (e.g., Vanzella et al., 2017; Martin et al., 2014; Martin et al., 2016; Ao et al., 2020). Quantitative predictions of Ly α emission from accreting baryons depend sensitively on the thermal state and the small-scale structure of the gas (e.g., Kollmeier et al., 2010; Faucher-Giguère et al., 2010; Goerdt et al., 2010), leading to large uncertainties in the predictions. The role played by “local” sources of ionising photons over and above that of the metagalactic ionising radiation field is likely to be substantial for regions near QSOs (Cantalupo et al., 2014; Borisova et al., 2016; Cai et al., 2019; O’Sullivan et al., 2020) but much more uncertain for star-forming galaxies, where the escape of scattered Ly α photons is much more likely than that of ionising photons.

Models of Ly α radiative transfer have attempted to understand the dominant physics responsible for producing Ly α halos around galaxies. Using photon-tracing algorithms with Monte-Carlo simulations, Verhamme, Schaerer, and Maselli (2006), Dijkstra (2014), Gronke and Dijkstra (2016), and Gronke et al. (2016) have explored the effects of resonant scattering on the emergent central Ly α line profile using various idealised H I geometries and velocity fields; in most cases, simple models can be made to fit the observed 1-D profiles (Gronke, 2017; Song, Seon, and Hwang, 2020). There have also been attempts to model or predict spatially-resolved Ly α which almost certainly depends on a galaxy’s immediate environment (Zheng et al., 2011; Kakiichi and Dijkstra, 2018), including both outflows and accretion flows, as well as the radiative transfer of Ly α photons from the site of initial production

to escape (e.g. Faucher-Giguère et al., 2010; Lake et al., 2015; Smith et al., 2019; Byrohl et al., 2020). However, the conclusions reached as to the dominant process responsible for the extended Ly α emission have not converged, indicating that more realistic, high resolution, cosmological zoom-in simulations may be required to capture all of the physical processes. Despite the variety of Ly α radiative transfer models to date, as far as we are aware, no specific effort has been made to statistically compare full 2-D model predictions (simultaneous spatial and kinematic) to observed Ly α halos.

Some insight into the relationship between galaxy properties and the kinematics and spatial distribution of cool gas in the CGM has been provided by studies at lower redshifts, where galaxy morphology is more easily measured. Statistical studies using absorption line probes have clearly shown that the strength of low-ionization metal lines such as Mg II, Fe II depends on where the line of sight passes through the galaxy CGM relative to the projected major axis of the galaxy – the “azimuthal angle” – (e.g. Bordoloi et al., 2011; Bouché et al., 2012; Kacprzak, Churchill, and Nielsen, 2012; Nielsen et al., 2015; Lan and Mo, 2018; Martin et al., 2019), and the inclination of the galaxy disk relative to the line of sight (e.g., Steidel et al., 2002; Kacprzak et al., 2011). More recently, clear trends have also been observed for high ions (O VI) (Kacprzak et al., 2015). In general, these trends support a picture of star-forming galaxies in which high-velocity, collimated outflows perpendicular to the disk are responsible for the strongest absorption lines in both low and high ions, with low ions also being strong near the disk plane. Theoretically at least, accretion flows might also be quasi-collimated in the form of cold streams of gas that would tend to deposit cool gas near the disk plane (see, e.g., Tumlinson, Peebles, and Werk, 2017). It is less clear how such a geometry for gas flows in the CGM would manifest as emission in a resonantly-scattered line like Ly α . One might expect that Ly α photons would escape most readily along the minor axis, since the large velocity gradients and lower H I optical depths of outflowing material both favour Ly α escape from the host galaxy. This picture is consistent with Verhamme et al. (2012), who showed that Ly α escape is enhanced when the simulated galaxies are viewed face-on.

Observations of low-redshift, spatially resolved Ly α emission have so far been limited to small samples – e.g., in the local universe ($z < 0.2$), using the Hubble Space Telescope (HST), the “Ly α reference sample” (LARS; Östlin et al., 2014) has obtained images probing Ly α emission around galaxies in great spatial detail,

reaffirming the complex nature of Ly α radiative transfer and its relation to the host galaxies. In most cases LARS found evidence that extended Ly α emission is most easily explained by photons produced by active star formation that then diffuse into the CGM before a last scattering event allows escape in the observer’s direction. Although there are small-scale enhancements associated with outflows, even for galaxies observed edge-on the Ly α emission is perhaps smoother than expected (Duval et al., 2016).

At $z > 2$, Ly α emission is more readily observed, but detailed analyses are challenged by the relatively small galaxy sizes (both physical and angular) and the need for high spatial resolution to determine the morphology of the stellar light. In this paper, we present a statistical sample of $z > 2$ galaxies drawn from a survey using KCWI of selected regions within the Keck Baryonic Structure Survey (KBSS; Rudie et al., 2012; Steidel et al., 2014; Strom et al., 2017). Since the commissioning of KCWI in late 2017, we have obtained deep IFU data (~ 5 hour integrations) for > 100 KBSS galaxies with $z = 2-3.5$, so that the Ly α line is covered within the KCWI wavelength range; some initial results from the survey have been presented by Erb, Steidel, and Chen (2018) and Law et al. (2018). The 59 galaxies included in our current analysis are those that, in addition to the KCWI data, have also been observed at high spatial resolution by either HST or adaptive-optics-assisted near-IR spectroscopy using Keck/OSIRIS. The overarching goal of the study is to evaluate the spatial and spectral distribution of Ly α emission within ≈ 5 arcseconds as compared to the principle axes defined by the galaxy morphology on smaller angular scales by each galaxy’s UV/optical continuum emission. In particular, we seek to use the observed kinematics and spatial distribution of Ly α emission to evaluate whether the cool gas in the CGM of forming galaxies shows evidence for directional dependence – e.g., inflows or outflows along preferred directions – with respect to the central galaxy.

This paper is organized as follows. In §3.2, we describe the KBSS-KCWI sample; §3.3 introduces the high-resolution imaging and IFU dataset; §3.4 covers the details on the measurement of the galaxy principle axes providing the definition of the galactic azimuthal angle; §3.5 presents results on the connection between Ly α halos and galactic azimuthal angle. §3.6 looks into the connection between the Ly α azimuthal asymmetry and the overall Ly α emission properties. §3.7 checks higher order azimuthal asymmetry of Ly α emission by dividing the sample into finer azimuthal bins. §3.8 discusses the implications of the results, with a summary in §3.9. Throughout the paper, we assume a Λ CDM cosmology with $\Omega_m = 0.3$,

$\Omega_\Lambda = 0.7$, and $h = 0.7$. Distances are given in proper units, i.e., physical kpc (pkpc).

3.2 The KBSS-KCWI Galaxy Sample

In late 2017, we began using the recently-commissioned Keck Cosmic Web Imager (KCWI; Morrissey et al., 2018) on the Keck II 10m telescope to target selected regions within the survey fields of the Keck Baryonic Structure Survey (KBSS; Rudie et al., 2012; Steidel et al., 2014; Strom et al., 2017). The main goal of the KCWI observations has been to detect diffuse emission from the CGM (within impact parameter, $D_{\text{tran}} \lesssim 100$ pkpc) of a substantial sample of rapidly star-forming galaxies and optically-faint AGN host galaxies, reaching surface brightness sensitivity of $\sim 5 \times 10^{-20}$ ergs s $^{-1}$ cm $^{-2}$ arcsec $^{-2}$ (1σ) for unresolved emission lines. Such limiting surface brightness would allow detection of the extended Ly α halos of individual galaxies at redshifts $z \sim 2 - 3$ (e.g., Steidel et al., 2011), and would be capable of detecting extended diffuse UV metallic cooling line emission as predicted by simulations of galaxies with comparable mass and redshift (e.g., Sravan et al., 2016).

KCWI offers three selectable image slicer scales, each of which can be used with three different regimes of spectral resolving power, $R \equiv \lambda/\Delta\lambda$. All of the observations used in the present study were obtained using the “medium” slicer scale and low resolution grating (BL), providing integral field spectra over a contiguous field of view (FoV) of $20''.3 \times 16''.5$ covering the common wavelength range 3530-5530 Å with resolving power $\langle R \rangle = 1800$.

Given the relatively small solid angle of the KCWI FoV, and the total integration time desired for each pointing of ~ 5 hours, it was necessary to choose the KCWI pointings carefully. In general, we chose KCWI pointings to maximize the number of previously-identified KBSS galaxies with $2 \lesssim z \lesssim 3.4$ within the field of view, so that the KCWI spectra would include the Ly α line as well as many other rest-frame far-UV transitions. Most of the targeted galaxies within each pointing were observed as part of KBSS in both the optical (Keck/LRIS; Oke et al., 1995; Steidel et al., 2004) and the near-IR (Keck/MOSFIRE; McLean et al., 2012; Steidel et al., 2014). The pointings were chosen so that the total sample of KBSS catalog galaxies observed would span the full range of galaxy properties represented in the KBSS survey in terms of stellar mass (M_*), star formation rate (SFR), Ly α emission strength, and rest-optical nebular properties. Most of the KCWI pointings were also directed

within the regions of the KBSS survey fields that have been observed at high spatial resolution by HST.

As of this writing, the KBSS-KCWI survey comprises 39 pointings of KCWI, including observations of 101 KBSS galaxies, of which 91 have $2 \leq z \leq 3.4$ placing Ly α within the KCWI wavelength range. In this work, we focus only on galaxies without obvious spectroscopic or photometric evidence for the presence of an AGN, and have therefore excluded 14 objects with spectroscopic evidence for the presence of AGN, to be discussed elsewhere. The remaining objects show no sign of significant AGN activity – e.g., they lack emission lines of high ionisation species in the rest-UV KCWI and existing LRIS spectra, their nebular line ratios in the rest-frame optical are consistent with stellar excitation based on spectra taken with Keck/MOSFIRE (see e.g. Steidel et al., 2014), they lack power-law SEDs in the NIR-MIR, etc. Because measurements of galaxy morphology are important to the analysis, we considered only the subset of the star-forming (non-AGN) galaxies that have also been observed at high spatial resolution using HST imaging or Keck/OSIRIS IFU spectroscopy behind adaptive optics (§3.3).

In addition to the known KBSS targets, many of the KCWI pointings include continuum-detected serendipitous galaxies whose KCWI spectra constitute the first identification of their redshifts. A total of 50 galaxies with $z > 2$ (most of which are fainter in the optical continuum than the KBSS limit of $\mathcal{R} = 25.5$) have been identified. We have included 10 such objects in our analysis sample, based on their having HST observations with sufficient S/N for determination of morphology.

A minimum total integration of 2.5 hours (5 hours is more typical) at the position of a galaxy in the KCWI data cube was also imposed, in order to ensure the relative uniformity of the data set. Ultimately, after inspection of the high resolution images (§3.3), 6 galaxies were removed because of source ambiguity or obvious contamination from nearby unrelated objects in the images, and two were excluded because they were not sufficiently resolved by HST to measure their position angle reliably (see §3.4).

The final sample to be considered in this work contains 59 galaxies, listed in Table 3.1. The redshifts given in Table 3.2 are based on MOSFIRE nebular spectra for 38 of the 59 galaxies, which have a precision of $\sim \pm 20 \text{ km s}^{-1}$ and should accurately reflect the galaxy systemic redshift. In the remaining cases, features in the rest-frame UV spectra including Ly α emission and strong interstellar absorption features (e.g., Si II, Si IV, C II, C IV, O I) were used to estimate the systemic redshift

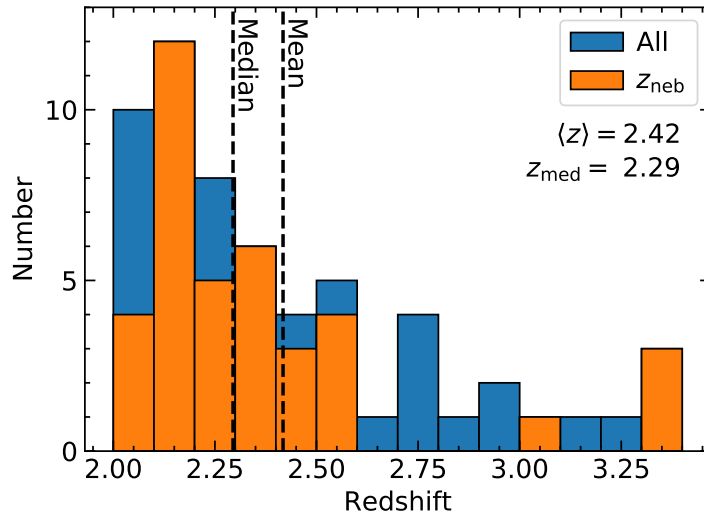


Figure 3.1: Redshift distribution of the galaxy sample. The blue histogram represents the full sample of 59 galaxies. The orange histogram shows the distribution for the 38 galaxies with nebular redshift measurements from MOSFIRE near-IR spectra, while the rest are calibrated based on Chen et al. (2020b) using rest-UV absorption lines or Ly α emission from Keck/LRIS and/or KCWI spectra. The mean (median) redshift of the full sample is 2.42 (2.29).

of the galaxy, using the calibration described by Chen et al. (2020b). Briefly, the method uses the statistics – based on several hundred KBSS galaxies with both nebular and UV observations – of the velocity offsets between nebular redshifts and redshifts defined by UV spectral features for samples divided by their UV spectral morphology, i.e., Ly α emission only, Ly α emission and interstellar absorption, or interstellar absorption only. The mean offsets for the appropriate sub-sample were applied to the UV-based redshifts in cases where nebular redshifts are not available; systemic redshifts obtained using such calibrations have an uncertainty of $\approx 100 \text{ km s}^{-1}$ when the rest-UV spectra are of high quality (see, e.g., Steidel et al., 2018.) Figure 3.1 shows the redshift distribution of the KCWI sample, which has $z_{\text{med}} = 2.29 \pm 0.40$ (median and standard deviation), for which the conversion between angular and physical scales is $8.21 \text{ pkpc}''$ with our assumed cosmology.

Reliable SED fits are available for 56 of the 59 galaxies using the BPASSv2.2 stellar population synthesis model (Stanway and Eldridge, 2018) and SMC extinction curve. This choice of SED model has been shown to predict internally consistent stellar mass (M_*) and star-formation rate (SFR) for high-redshift galaxies having properties similar to those in our sample (see, e.g., Steidel et al., 2016; Strom et al., 2017; Theios

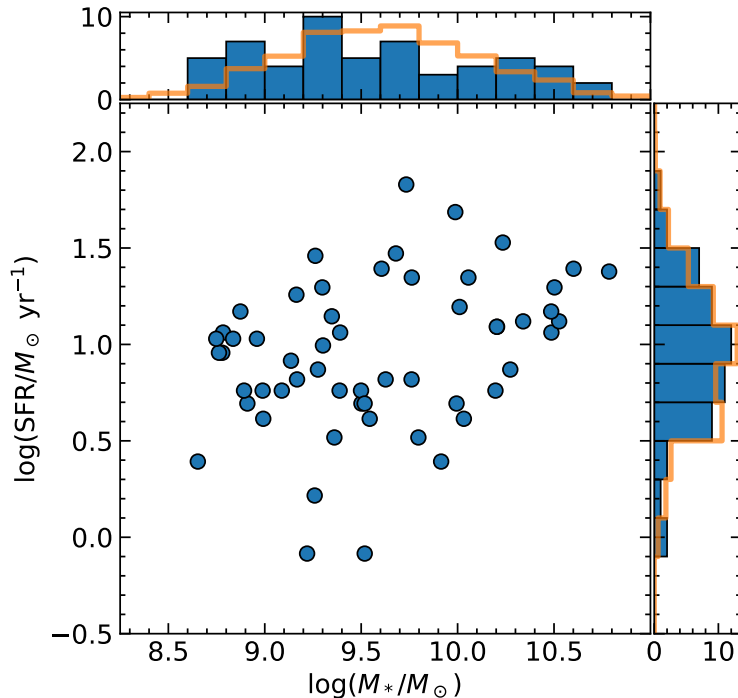


Figure 3.2: Distribution of SFR and M_* of 56/59 galaxies in this sample; the remaining 3 galaxies have insufficient photometric measurements for reliable SED fitting. The normalized distributions of the parent KBSS sample are shown in the orange 1-D histograms. The SFR and M_* of galaxies used in this work are similar to those of the parent KBSS sample; the values are all based on the BPASS-v2.2-binary spectral synthesis models (Stanway and Eldridge, 2018), assuming stellar metallicity $Z = 0.002$, SMC extinction as described by Theios et al. (2019), and a Chabrier (2003) stellar initial mass function.

et al., 2019), i.e., $8.5 \lesssim \log(M_*/M_\odot) \lesssim 11$, and $1 \lesssim \text{SFR}/(M_\odot \text{ yr}^{-1}) \lesssim 100$. The distributions of M_* and SFR (Figure 3.2) are similar to those of the full KBSS galaxy sample, albeit with a slight over-representation of $\log(M_*/M_\odot) \lesssim 9$ galaxies¹.

In order to facilitate comparison of the Ly α emission line strength of sample galaxies with those in the literature, Tables 3.1 and 3.2 includes the rest-frame Ly α equivalent width ($W_\lambda(\text{Ly}\alpha)$) based on extraction of 1-D spectra from the KCWI data cubes over

¹For direct comparison of our sample with the so-called “star-formation main-sequence” (SFMS), we note that SED fits that assume solar metallicity SPS models from Bruzual and Charlot (2003) and attenuation curve from Calzetti et al. (2000) result in a distribution of SFR vs. M_* entirely consistent with the published SFMS at $z \sim 2$ (e.g., Whitaker et al., 2014).

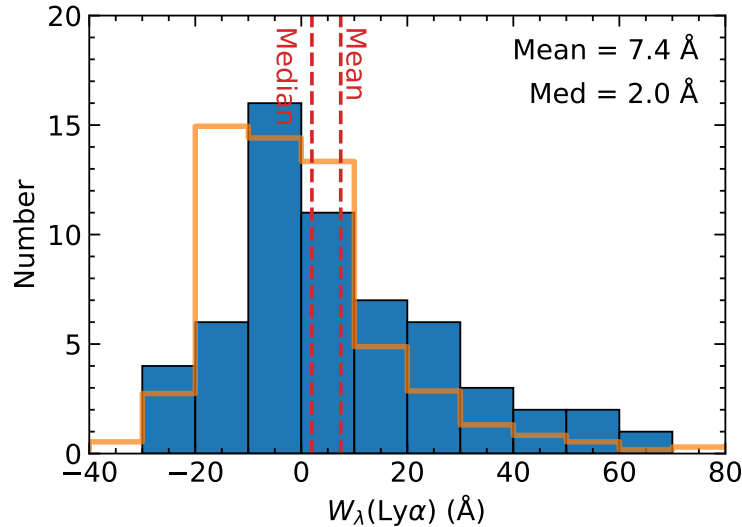


Figure 3.3: Distribution of $W_\lambda(\text{Ly}\alpha)$ for the sample (blue histogram). The orange skeletal histogram shows the normalized $W_\lambda(\text{Ly}\alpha)$ distribution from Reddy and Steidel (2009), which is a subset of the current KBSS sample large enough to be representative. The sample discussed in this work is slightly biased toward Ly α -emitting galaxies compared to the parent sample of $z \sim 2 - 3$ KBSS galaxies.

a spatial aperture defined by the extent of the UV continuum light of each galaxy². The values of $W_\lambda(\text{Ly}\alpha)$ in Table 3.2 were measured using the method described in Kornei et al. (2010) (see also Reddy and Steidel, 2009), where positive values indicate net emission and negative values net absorption. Aside from a slight over-representation of galaxies with the strongest Ly α emission ($W_\lambda(\text{Ly}\alpha) \gtrsim 40 \text{ \AA}$), the sample in Table 3.2 is otherwise typical of UV-continuum-selected galaxies in KBSS, by construction. The $W_\lambda(\text{Ly}\alpha)$ distribution for the sample in Table 3.2 is shown in Figure 3.3. In addition to $W_\lambda(\text{Ly}\alpha)$, we also measured the total Ly α flux ($F_{\text{Ly}\alpha}$) and the ratio between the blue- and red-shifted components of emission for the entire Ly α halo ($F_{\text{Ly}\alpha}(\text{blue})/F_{\text{Ly}\alpha}(\text{red})$), which are discussed further in §3.6.

3.3 Observations and Reductions

KCWI

The KCWI data discussed in the present work were obtained between 2017 September and 2020 November, in all cases using the medium-scale slicer made up of 24

²In general, the Ly α emission evaluated within a central aperture represents only a fraction of the total that would be measured in a large aperture that accounts for the diffuse Ly α halos with spatial extent well beyond that of the FUV continuum (see, e.g., Steidel et al., 2011; Wisotzki et al., 2016); however, the central $W_\lambda(\text{Ly}\alpha)$ is a closer approximation to values measured in most spectroscopic galaxy surveys.

Table 3.1: Summary of the galaxy sample and the observations (I).

Object ^a Identifier	RA (J2000.0)	DEC (J2000.0)	t_{exp} (KCWI) (hr)
Q0100-BX210	01:03:12.02	+13:16:18.5	5.4
Q0100-BX212	01:03:12.51	+13:16:23.2	5.2
Q0100-C7	01:03:08.24	+13:16:30.1	5.1
Q0100-D11	01:03:08.25	+13:16:37.6	5.1
Q0142-BX165	01:45:16.87	-09:46:03.5	5.0
Q0142-BX188	01:45:17.79	-09:45:05.6	5.3
Q0142-BX195-CS10	01:45:17.11	-09:45:06.0	4.5
Q0142-NB5859	01:45:17.54	-09:45:01.2	5.8
Q0207-BX144	02:09:49.21	-00:05:31.7	5.0
Q0207-MD60	02:09:53.69	-00:04:39.8	4.3
Q0449-BX88	04:52:14.94	-16:40:49.3	6.3
Q0449-BX88-CS8	04:52:14.79	-16:40:58.6	5.2
Q0449-BX89	04:52:14.80	-16:40:51.1	6.3
Q0449-BX93	04:52:15.41	-16:40:56.8	6.3
Q0449-BX110	04:52:17.20	-16:39:40.6	5.0
Q0821-MD36	08:21:11.41	+31:08:29.4	2.7
Q0821-MD40	08:21:06.96	+31:07:22.8	4.3
Q1009-BX215	10:11:58.71	+29:41:55.9	4.0
Q1009-BX218	10:11:58.96	+29:42:07.5	5.3
Q1009-BX222	10:11:59.09	+29:42:00.5	5.3
Q1009-BX222-CS9	10:11:58.92	+29:42:02.6	5.3
Q1009-D15	10:11:58.73	+29:42:10.5	5.3
Q1549-BX102	15:51:55.98	+19:12:44.2	5.0
Q1549-M17	15:51:56.06	+19:12:52.7	3.3
Q1623-BX432	16:25:48.74	+26:46:47.1	3.6
Q1623-BX436	16:25:49.10	+26:46:53.4	3.6
Q1623-BX453	16:25:50.85	+26:49:31.2	4.8
Q1623-BX453-CS3	16:25:50.35	+26:49:37.1	4.7
Q1623-C52	16:25:51.20	+26:49:26.3	4.8
Q1700-BX490	17:01:14.83	+64:09:51.7	4.3
Q1700-BX561	17:01:04.18	+64:10:43.8	5.0
Q1700-BX575	17:01:03.34	+64:10:50.9	5.0
Q1700-BX581	17:01:02.73	+64:10:51.3	4.7
Q1700-BX710	17:01:22.13	+64:12:19.3	5.0
Q1700-BX729	17:01:27.77	+64:12:29.5	4.7
Q1700-BX729-CS4	17:01:28.95	+64:12:32.4	3.0
Q1700-BX729-CS9	17:01:27.49	+64:12:25.1	4.7
Q1700-MD103	17:01:00.21	+64:11:55.6	5.0
Q1700-MD104	17:01:00.67	+64:11:58.3	5.0

Table 3.1: —*continued.*

Object ^a Identifier	RA (J2000.0)	DEC (J2000.0)	t_{exp} (KCWI) (hr)
Q1700-MD115	17:01:26.68	+64:12:31.7	4.7
Q2206-MD10	22:08:52.21	-19:44:13.9	5.0
DSF2237b-MD38	22:39:35.64	+11:50:27.5	3.7
Q2343-BX379	23:46:28.96	+12:47:26.0	4.0
Q2343-BX389	23:46:28.90	+12:47:33.5	4.0
Q2343-BX391	23:46:28.07	+12:47:31.8	4.0
Q2343-BX417	23:46:26.27	+12:47:46.7	3.0
Q2343-BX418	23:46:18.57	+12:47:47.4	4.9
Q2343-BX418-CS8	23:46:18.73	+12:47:51.6	5.1
Q2343-BX429	23:46:25.26	+12:47:51.2	5.2
Q2343-BX442	23:46:19.36	+12:47:59.7	4.6
Q2343-BX513	23:46:11.13	+12:48:32.1	4.8
Q2343-BX513-CS7	23:46:10.55	+12:48:30.9	4.8
Q2343-BX587	23:46:29.17	+12:49:03.4	5.2
Q2343-BX587-CS3	23:46:28.24	+12:49:07.2	4.8
Q2343-BX587-CS4	23:46:28.62	+12:49:04.8	5.2
Q2343-BX610	23:46:09.43	+12:49:19.2	5.3
Q2343-BX660	23:46:29.43	+12:49:45.6	5.0
Q2343-BX660-CS7	23:46:29.82	+12:49:38.7	4.2
Q2343-MD80	23:46:10.80	+12:48:33.2	4.8

^a The “CS” objects are continuum serendipitous objects discussed in §3.2. Their naming follows nearby KBSS galaxies that are previously known, and may not be physically associated to the CS objects.

slices of width $0''.69$ and length $20''.3$ on the sky. The instrumental setup uses the BL volume phase holographic (VPH) grating with an angle of incidence that optimizes the diffraction efficiency near 4200 \AA , with the camera articulation angle set to record the spectra of each slice with a central wavelength of $\sim 4500 \text{ \AA}$. A band-limiting filter was used to suppress wavelengths outside of the range $3500\text{--}5600 \text{ \AA}$ to reduce scattered light; the useful common wavelength range recorded for all 24 slices in this mode is $3530\text{--}5530 \text{ \AA}$, with a spectral resolving power ranging from $R \simeq 1400$ at 3530 \AA to $R \simeq 2200$ at 5530 \AA . At the mean redshift of the sample ($\langle z \rangle = 2.42$), $\text{Ly}\alpha$ falls at an observed wavelength of $\sim 4160 \text{ \AA}$, where $R \sim 1650$.

The E2V $4\text{k}\times 4\text{k}$ detector was binned 2×2 , which provides spatial sampling along slices of $0''.29 \text{ pix}^{-1}$. Because each slice samples $0''.68$ in the dispersion direction, the effective spatial resolution element is rectangular on the sky, with an aspect ratio of $\sim 2.3 : 1$. We adopted the following approach to the observations, designed

Table 3.2: Summary of the galaxy sample and the observations (II).

Object Identifier	Redshift ^a	$W_1(\text{Ly}\alpha)^b$ (Å)	$F_{\text{Ly}\alpha}(\text{tot})^c$ $10^{-17} \text{ erg s}^{-1} \text{ cm}^{-2}$	$\frac{F_{\text{Ly}\alpha}(\text{blue})^d}{F_{\text{Ly}\alpha}(\text{red})}$	Imaging ^e Data	PA_0^f (deg)	PA_0^g Method
Q0100-BX210	2.2769	-3 ± 2	6.3 ± 0.5	0.08 ± 0.05	F160W	37	(i), (ii)
Q0100-BX212	2.1063	-4 ± 3	2.3 ± 0.7	0.5 ± 0.29	F160W	-57	(i), (ii)
Q0100-C7	3.0408	12 ± 1	9.0 ± 0.4	0.15 ± 0.03	F160W	16	(i), (ii)
Q0100-D11	2.5865	6 ± 1	1.7 ± 0.4	0.11 ± 0.14	F160W	-12	(i), (ii)
Q0142-BX165	2.3576	51 ± 3	37.5 ± 0.5	0.28 ± 0.01	F160W	14	(ii)
Q0142-BX188	2.0602	-6 ± 1	4.6 ± 0.7	0.47 ± 0.15	F160W	66	(i), (ii)
Q0142-BX195-CS10	2.7382 (UV)	-1 ± 3	2.2 ± 0.5	0.47 ± 0.24	F160W	29	(ii)
Q0142-NB5859	2.7399 (UV)	20 ± 2	3.7 ± 0.4	0.65 ± 0.14	F160W	42	(i), (ii)
Q0207-BX144	2.1682	25 ± 3	44.9 ± 0.6	0.29 ± 0.01	F140W	-74	(i), (ii)
Q0207-MD60	2.5904	-27 ± 2	1.4 ± 0.5	-0.16 ± 0.21	F140W	-64	(ii)
Q0449-BX88	2.0086	-7 ± 3	3.3 ± 0.8	0.16 ± 0.16	F160W	10	(ii)
Q0449-BX88-CS8	2.0957 (UV)	4 ± 1	3.9 ± 0.8	0.34 ± 0.17	F160W	-39	(i), (ii)
Q0449-BX89	2.2570 (UV)	22 ± 2	7.6 ± 0.4	0.05 ± 0.03	F160W	-32	(i), (ii)
Q0449-BX93	2.0070	-7 ± 2	7.4 ± 0.8	0.6 ± 0.13	F160W, OSIRIS	-18	(i), (ii), (iii)
Q0449-BX110	2.3355	35 ± 2	20.4 ± 0.6	0.47 ± 0.03	F160W	-48	(i), (ii)
Q0821-MD36	2.583	75 ± 10	23.1 ± 0.6	0.16 ± 0.02	F140W	37	(i), (ii)
Q0821-MD40	3.3248	27 ± 3	11.0 ± 0.4	0.34 ± 0.03	F140W	-7	(ii)
Q1009-BX215	2.5059	1 ± 1	3.7 ± 0.8	0.34 ± 0.15	F160W	-20	(i), (ii)
Q1009-BX218	2.1091	-6 ± 3	4.0 ± 0.6	0.18 ± 0.11	F160W	-43	(i), (ii)
Q1009-BX222	2.2031	-4 ± 1	4.7 ± 0.5	0.28 ± 0.08	F160W	-83	(i), (ii)
Q1009-BX222-CS9	2.6527 (UV)	-1 ± 4	1.0 ± 0.4	—	F160W	76	(i), (ii)
Q1009-D15	3.1028 (UV)	-18 ± 6	4.2 ± 0.4	0.28 ± 0.08	F160W	28	(i), (ii)
Q1549-BX102	2.1934	50 ± 3	19.5 ± 0.5	0.51 ± 0.03	F606W	-87	(i), (ii)

Table 3.2: —continued.

Object Identifier	Redshift ^a	$W_\lambda(\text{Ly}\alpha)^b$ (Å)	$F_{\text{Ly}\alpha}(\text{tot})^c$ $10^{-17} \text{ erg s}^{-1} \text{ cm}^{-2}$	$\frac{F_{\text{Ly}\alpha}(\text{blue})^d}{F_{\text{Ly}\alpha}(\text{red})}$	Imaging ^e Data	PA_0^f (deg)	PA_0^g Method
Q1549-M17	3.2212 (UV)	27 ± 5	4.3 ± 0.5	0.0 ± 0.05	F606W	72	(ii)
Q1623-BX432	2.1825	17 ± 1	10.8 ± 0.7	0.46 ± 0.06	F160W	16	(ii)
Q1623-BX436	2.0515 (UV)	-12 ± 2	2.6 ± 1.0	—	F160W	12	(ii)
Q1623-BX453	2.1821	10 ± 2	2.8 ± 0.5	0.33 ± 0.14	F160W, OSIRIS	31	(iii)
Q1623-BX453-CS3	2.0244 (UV)	17 ± 2	5.6 ± 0.9	0.3 ± 0.11	F160W	-66	(i), (ii)
Q1623-C52	2.9700 (UV)	4 ± 1	8.5 ± 0.4	0.22 ± 0.03	F160W	-13	(ii)
Q1700-BX490	2.3958	-3 ± 4	12.8 ± 0.5	0.39 ± 0.03	F814W, OSIRIS	86	(i), (ii), (iii)
Q1700-BX561	2.4328	-3 ± 3	8.5 ± 0.6	0.51 ± 0.08	F814W	9	(ii)
Q1700-BX575	2.4334	0 ± 2	5.2 ± 0.6	0.14 ± 0.08	F814W	-34	(ii)
Q1700-BX581	2.4022	9 ± 4	10.6 ± 0.7	0.28 ± 0.05	F814W	27	(i), (ii)
Q1700-BX710	2.2946	-10 ± 3	8.1 ± 0.6	0.51 ± 0.09	F814W	-19	(i), (ii)
Q1700-BX729	2.3993	14 ± 2	12.9 ± 0.5	0.17 ± 0.03	F814W	-3	(i), (ii)
Q1700-BX729-CS4	2.2921 (UV)	14 ± 3	5.8 ± 1.1	0.21 ± 0.12	F814W	40	(ii)
Q1700-BX729-CS9	2.4014 (UV)	35 ± 2	1.1 ± 0.5	-0.19 ± 0.21	F814W	-59	(i), (ii)
Q1700-MD103	2.3151	-24 ± 1	-0.5 ± 0.5	—	F814W	55	(ii)
Q1700-MD104	2.7465 (UV)	6 ± 2	8.2 ± 0.4	0.11 ± 0.03	F814W	7	(i), (ii)
Q1700-MD115	2.9081 (UV)	33 ± 7	7.8 ± 0.5	0.05 ± 0.03	F814W	3	(i), (ii)
Q2206-MD10	3.3269	5 ± 2	4.0 ± 0.5	0.07 ± 0.08	F160W	41	(i), (ii)
DSF2237b-MD38	3.3258	2 ± 2	3.0 ± 0.5	0.44 ± 0.16	F606W	52	(i), (ii)
Q2343-BX379	2.0427 (UV)	-7 ± 2	6.4 ± 1.3	0.64 ± 0.23	F140W	-60	(i), (ii)
Q2343-BX389	2.1712	-16 ± 1	1.6 ± 0.6	0.65 ± 0.49	F140W	-50	(ii)
Q2343-BX391	2.1738	-16 ± 1	3.3 ± 0.7	—	F140W	21	(i), (ii)

Table 3.2: —continued.

Object Identifier	Redshift ^a	$W_\lambda(\text{Ly}\alpha)^b$ (Å)	$F_{\text{Ly}\alpha}(\text{tot})^c$ $10^{-17} \text{ erg s}^{-1} \text{ cm}^{-2}$	$\frac{F_{\text{Ly}\alpha}(\text{blue})^d}{F_{\text{Ly}\alpha}(\text{red})}$	Imaging ^e Data	PA_0^f (deg)	PA_0^g Method
Q2343-BX417	2.2231 (UV)	-9 ± 6	4.8 ± 0.7	0.49 ± 0.15	F160W	-38	(ii)
Q2343-BX418	2.3054	46 ± 3	40.5 ± 0.6	0.46 ± 0.01	F140W, OSIRIS	2	(i), (ii), (iii)
Q2343-BX418-CS8	2.7234 (UV)	66 ± 15	6.7 ± 0.4	0.15 ± 0.04	F140W	-67	(i), (ii)
Q2343-BX429	2.1751	-8 ± 5	3.0 ± 0.5	0.31 ± 0.15	F160W	28	(i), (ii)
Q2343-BX442	2.175	-18 ± 4	1.6 ± 0.7	0.38 ± 0.52	OSIRIS	-12	(iv)
Q2343-BX513	2.1082	10 ± 1	18.6 ± 0.7	0.71 ± 0.05	F140W, OSIRIS	-9	(i), (ii), (iii)
Q2343-BX513-CS7	2.0144 (UV)	-22 ± 2	4.2 ± 1.0	0.53 ± 0.26	F140W	71	(i), (ii)
Q2343-BX587	2.2427	-4 ± 3	7.2 ± 0.5	0.22 ± 0.05	F160W	44	(i), (ii)
Q2343-BX587-CS3	2.5727 (UV)	2 ± 2	1.3 ± 0.4	0.17 ± 0.26	F140W	-53	(i), (ii)
Q2343-BX587-CS4	2.8902 (UV)	-13 ± 1	2.8 ± 0.4	0.08 ± 0.08	F140W	-59	(i), (ii)
Q2343-BX610	2.2096	8 ± 2	13.5 ± 0.7	0.26 ± 0.04	F140W	22	(ii)
Q2343-BX660	2.1742	20 ± 3	25.7 ± 0.6	0.26 ± 0.02	F140W, OSIRIS	37	(i), (ii), (iii)
Q2343-BX660-CS7	2.0788 (UV)	41 ± 1	2.3 ± 0.9	—	F140W	89	(ii)
Q2343-MD80	2.0127	-26 ± 3	2.8 ± 0.8	0.22 ± 0.24	F140W	9	(i), (ii)

^a If marked as “UV”, the systemic redshift was estimated from features in the rest-UV spectra, calibrated as described by Chen et al. (2020b). The typical uncertainties on UV-estimated systemic redshifts are $\delta v \equiv c\delta z_{\text{sys}}/(1 + z_{\text{sys}}) \simeq 100 \text{ km s}^{-1}$. Otherwise, z_{sys} was measured from nebular emission lines in rest-optical (MOSFIRE) spectra, with $\delta v \simeq 20 \text{ km s}^{-1}$.

^b Rest-frame Ly α equivalent width. Details discussed in §3.2.

^c Total Ly α flux. See §3.6 for more details.

^d Flux ratio between the blueshifted and redshifted components of Ly α emission. Details in §3.6.

^e F140W and F160W images obtained using HST-WFC3-IR, F606W and F814W images from HST-ACS.

^f Typical uncertainty: $\pm 10^\circ$.

^g Methods used to measure PA_0 : (i) using GALFIT on HST images; (ii) using the pixel intensity second moment on HST images; (iii) pixel intensity second moment on OSIRIS H α map; (iv) kinematics of H α emission. Details on the methods are shown in §3.4.

to ensure that the slicer geometry with respect to the sky is unique on each 1200s exposure so that the effective spatial resolution on the final stacked data cube is close to isotropic. Typically, a total integration of ~ 5 hours is obtained as a sequence of 15 exposures of 1200s, each obtained with the sky position angle (PA) of the instrument rotated by 10-90 degrees with respect to adjacent exposures. Each rotation of the instrument field of view is accompanied by a small offset of the telescope pointing before the guide star is reacquired. In this way, a given sky position is sampled in 15 different ways by the slicer.

KCWI Data Reduction

Each 1200s exposure with KCWI was initially reduced using the data reduction pipeline (DRP) maintained by the instrument team and available via the Keck Observatory website³. The DRP assembles the 2D spectra of all slices into a 3D data cube (with spaxels of $0''.29 \times 0''.69$, the native scale) using a suite of procedures that can be customised to suit particular applications. The procedures include cosmic-ray removal, overscan subtraction and scattered light subtraction, wavelength calibration, flat-fielding, sky-subtraction, differential atmospheric refraction (DAR) correction, and flux-calibration. Wavelength calibration was achieved using ThAr arc spectra obtained using the internal calibration system during the afternoon prior to each observing night. Flat-fielding was accomplished using spectra of the twilight sky at the beginning or end of each night, after dividing by a b-spline model of the solar spectrum calculated using the information from all slices. For each frame, the sky background was subtracted using the sky-modeling feature in the DRP, after which the sky-subtracted image (still in the 2-D format) is examined in order to mask pixels, in all 24 slices, that contain significant light from sources in the field. The frame was then used to make a new 2-D sky model using only unmasked pixels, and the sky-subtracted image is reassembled into a wavelength-calibrated (rebinned to 1 \AA per wavelength bin) data cube, at which time a variance cube, an exposure cube, and a mask cube are also produced.

Next, we removed any remaining low frequency residuals from imperfect sky background subtraction by forming a median-filtered cube after masking obvious continuum and extended emission line sources using a running 3D boxcar filter. The typical dimensions of the filter are 100 \AA (100 pixels) in the wavelength direction, 16 pixels ($4''.6$) along slices, and 1 pixel ($0''.69$) perpendicular to the slices, with the last

³<https://github.com/Keck-DataReductionPipelines/KcwiDRP>

ensuring slice-to-slice independence. Minor adjustments to the filter dimensions were made as needed. If the running boxcar encounters a large region with too few unmasked pixels to allow a reliable median determination, then the pixel values in the filtered cube were interpolated from the nearest adjacent regions for which the median was well-determined. Finally, the median-filtered cube for each observed frame was subtracted from the data. We found that this method proved effective for removing scattered light along slices caused by bright objects within the KCWI field of view.

Because neither Keck II nor KCWI has an atmospheric dispersion corrector, each cube is corrected for differential atmospheric refraction (DAR) (i.e., apparent position of an object as a function of wavelength) using the elevation and parallactic angle at the midpoint of the exposure and a model of the atmosphere above Maunakea. Finally, each cube was flux-calibrated using observations obtained with the same instrument configuration of one or more spectrophotometric standard stars selected from a list recommended by the KCWI documentation.

Prior to stacking reduced data cubes of individual exposures covering the same sky region, they must be aligned spatially and rotated to account for differences in the PA of the instrument with respect to the sky on different exposures. To accomplish this, we averaged the DAR-corrected cubes along the wavelength axis to create pseudo-white-light images, rotated each to the nominal sky orientation (N up and E left) based on the World Coordinate System (WCS) recorded in the header, and cross-correlated the results to determine the relative offsets in RA and Dec, which we found to have a precision of ≈ 0.03 -arcsec (root mean square, RMS). The offsets were applied to the WCS in the header of each cube, and all cubes for a given pointing were then resampled to a common spatial grid with spatial sampling of $0''.3 \times 0''.3$ using a 2D *drizzle* algorithm in the *Montage* package⁴, with drizzle factor of 0.7. If the wavelength grid is different among cubes, the spectrum in each spaxel was resampled to a common grid using cubic spline. Finally, we stacked the resampled cubes by averaging, weighted by exposure time. A white light image of the final stacked data cube was used to determine small corrections to the fiducial RA and Dec to align with other multiwavelength data of the same region.

⁴<http://montage.ipac.caltech.edu/>

Table 3.3: Summary of HST observations

Field	Inst.	Filter	Prog. ID	PI	t_{exp} (s) ^a
DSF2237b	ACS	F606W	15287	A. Shapley ^b	6300
Q0100	WFC3	F160W	11694	D. Law ^c	8100
Q0142	WFC3	F160W	11694	D. Law ^c	8100
Q0207	WFC3	F140W	12471	D. Erb	800
Q0449	WFC3	F160W	11694	D. Law ^c	8100
Q0821	WFC3	F140W	12471	D. Erb	800
Q1009	WFC3	F160W	11694	D. Law ^c	8100
Q1549	ACS	F606W	12959	A. Shapley ^d	12000
Q1623	WFC3	F160W	11694	D. Law ^c	8100
Q1700	ACS	F814W	10581	A. Shapley ^e	12500
Q2206	WFC3	F160W	11694	D. Law ^c	8100
Q2343	WFC3	F140W	14620	R. Trainor	5200
Q2343	WFC3	F160W	11694	D. Law ^c	8100

^a Defined as the median exposure time across the whole FoV.

^b Pahl et al. (2021).

^c Law et al. (2012b) and Law et al. (2012a).

^d Mostardi et al. (2015).

^e Peter et al. (2007).

High Spatial Resolution Imaging

For galaxies in the mass range of our sample at $z \sim 2.5$, the typical half-light diameter is ~ 4 pkpc, which corresponds to $\simeq 0''.5$ (Law et al., 2012a). To obtain reliable measurements of the orientation of the galaxy’s projected major and minor axes (see §3.4), high resolution images are crucial. We gathered existing data from two sources: space-based optical or near-IR images from the HST/ACS or HST/WFC3; alternatively, $H\alpha$ maps obtained using the Keck/OSIRIS integral field spectrometer (Larkin et al., 2006) behind the WMKO laser guide star adaptive optics (LGSAO) system, which typically provides spatial resolution of $0''.11 - 0''.15$ (Law et al., 2007; Law et al., 2009; Law et al., 2012c).

The *HST/WFC3-IR* images in this work were obtained using either the F140W or F160W filters, from programs listed in Table 3.3, with spatial resolution of $\sim 0''.16$ and $\sim 0''.18$, respectively. The HST/ACS images were taken in either the F606W or F814W filters, with spatial resolution of $\sim 0''.09$ (full width at half maximum; FWHM). In all cases, overlapping exposures were aligned and combined using *DrizzlePac*⁵. For the Q2343 field, where galaxies have been observed with comparably deep observations in two filters, we selected the image with the smaller estimated

⁵<https://www.stsci.edu/scientific-community/software/drizzlepac>

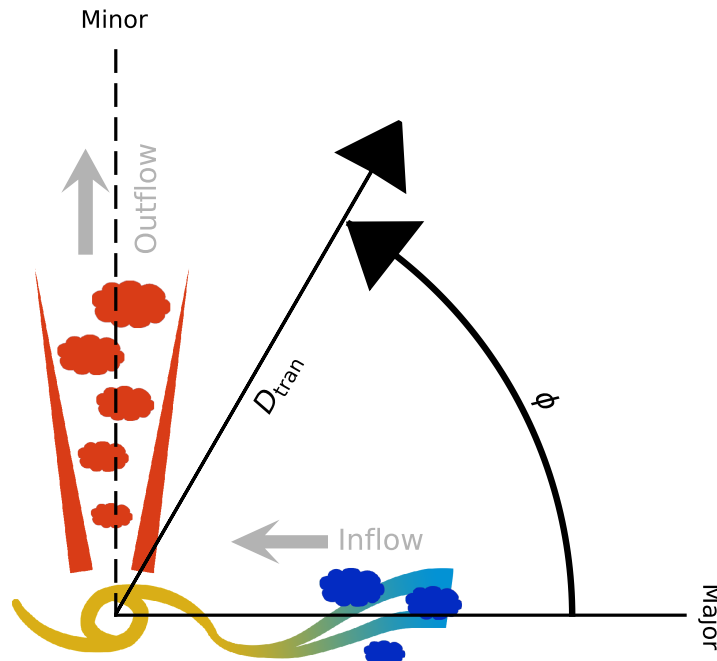


Figure 3.4: A schematic diagram of how the galaxy azimuthal angle (ϕ) is defined in this work and how it might be related to the origin and kinematics of gas in the CGM under common assumptions of a bi-conical outflow with accretion along the disk plane. Suppose that we are viewing a galaxy projected on the sky in this diagram, naively, one would expect to see inflow aligning with the projected galaxy major axis, and outflow aligning with the minor axis. Impact parameter, D_{tran} is defined as the projected distance from the center of the galaxy. The galaxy azimuthal angle, ϕ is defined as the projected angle on the sky with respect to the center of the galaxy, and starts from the projected galaxy major axis.

uncertainty in the measured position angle (see §3.4). The Keck/OSIRIS $H\alpha$ maps of six galaxies included in the sample are presented by Law et al. (2007), Law et al. (2009), Law et al. (2012c), and Law et al. (2018); details of the observations and data reduction can be found in those references.

3.4 Galaxy Azimuthal Angle

Motivation

The physical state of the CGM is controlled by the competition between accretion of new material onto the galaxy, and outflows driven by processes originating at small galactocentric radii. In what one might call the “classic” picture (see Veilleux, Cecil, and Bland-Hawthorn, 2005; Tumlinson, Peeples, and Werk, 2017 for review articles), based on observations of nearby starburst galaxies, inflowing and

outflowing gas occurs preferentially along the major and minor axes, respectively, as in the schematic diagram in Figure 3.4. It is well-established around star-forming galaxies at $z \lesssim 1$ that outflows driven by energy or momentum from stellar feedback (radiation pressure from massive stars, supernovae) originating near the galaxy center tend to escape along the direction that minimizes the thickness of the ambient interstellar medium (ISM) that would tend to slow or prevent outflows from escaping the galactic disk. Meanwhile, accretion of cool gas from the intergalactic medium (IGM) is believed to occur in quasi-collimated filamentary flows that carry significant angular momentum and thus would tend to approach the inner galaxy in a direction parallel to the disk plane (Nelson et al., 2019; Péroux et al., 2020). If feedback processes are sufficiently vigorous, the accretion is also most likely along directions that do not encounter strong outflows. When projected onto the plane of the sky, these considerations would tend to intersect outflowing material along the polar direction (the projected minor axis) and accreting material when the azimuthal angle (see Figure 3.4) is closer to the PA of the projected major axis.

At redshifts $z \lesssim 1$, there is strong support for this general geometric picture from the statistics of the incidence and strength of rest-UV absorption lines observed in the spectra of background sources, as a function of the azimuthal angle of the vector connecting the sightline and the center of the galaxy. As might be expected from a picture similar to Fig. 3.4, sightlines with ϕ close to the minor axis intersect gas with a large range of velocities, which kinematically broadens the observed absorption complexes comprised of many saturated components (e.g., Bordoloi et al., 2011; Bouché et al., 2012; Kacprzak, Churchill, and Nielsen, 2012; Schroetter et al., 2019). For azimuthal angles ϕ close to the major axis, the absorption features are strong due to the high covering fraction and column density of low-ionization gas near the disk plane, and broadened by the kinematics of differential rotation. The same picture has been supported by cosmological simulations where the gas metallicity, radial velocity, and the amount of outflowing mass all show significant differences along the galaxy major and minor axes (Nelson et al., 2019; Péroux et al., 2020).

It remains unclear, however, whether this geometric picture should be applied to galaxies at $z \sim 2$, where a large fraction of galaxies, particularly those with $\log(M_*/M_\odot) \lesssim 10$, appear to be “dispersion dominated”, where the rotational component of dynamical support (V_{rot}) is significantly smaller than that of apparently random motion (σ) (Law et al., 2009; Förster Schreiber et al., 2009), and where the central dynamical mass of the galaxy may be dominated by cold gas rather

than stars – and therefore any disk would be highly unstable. For such galaxies, there is not always a clear connection between the morphology of starlight and the principal kinematic axes (e.g., Erb et al., 2004; Law et al., 2012a). Meanwhile, a WFC3 survey conducted by Law et al. (2012a) for similar galaxies strongly supports 3D triaxial morphology, instead of inclined disk, to be the most suitable model to describe these galaxies. The fact that the vast majority of galaxies with “down the barrel” spectra at $z > 2$ have systematically blueshifted interstellar absorption lines and systematically redshifted Ly α emission suggests that outflows cannot be confined to a small range of azimuth (Shapley et al., 2003; Steidel et al., 2010; Jones, Stark, and Ellis, 2012 etc.).

The spatial and spectral distribution of the Ly α emission surrounding galaxies may provide crucial insight into the degree of axisymmetry and the dominant magnitude and direction of gas flows in the CGM. In any case, IFU observations of Ly α , where both the geometry and kinematics of the extended emission can be mapped, complement information available from absorption line studies.

In the analysis below, we define the galaxy azimuthal angle (ϕ) as the absolute angular difference between the vector connecting the galaxy centroid and a sky position at projected angular distance of θ_{tran} (or projected physical distance D_{tran}) and PA $_0$, the PA of the galaxy major axis measured from the galaxy stellar continuum light, as illustrated schematically in Figure 3.4,

$$\phi = |\text{PA} - \text{PA}_0|. \quad (3.1)$$

The zero point for measurements of position angle is arbitrary, but for definiteness we measure PA as degrees east (E) of north (N), so that angles increase in the counter-clockwise direction when N is up and E to the left. The use of Equation 3.1 to define ϕ implies that $0 \leq \phi/\text{deg} \leq 90$, and that $\phi = 0$ (90) deg corresponds to the projected major (minor) axis.

Methods

In order to obtain reliable measurements of ϕ , it is important to measure PA $_0$ accurately and consistently. We used up to four different methods to determine PA $_0$ for each galaxy. The choice of method depends on the information available; these are briefly summarized as follows:

⁶Since the HST WFC3-IR/F160W image of Q1623-BX453 is unresolved, its PA $_0$ is only derived from the OSIRIS H α map.

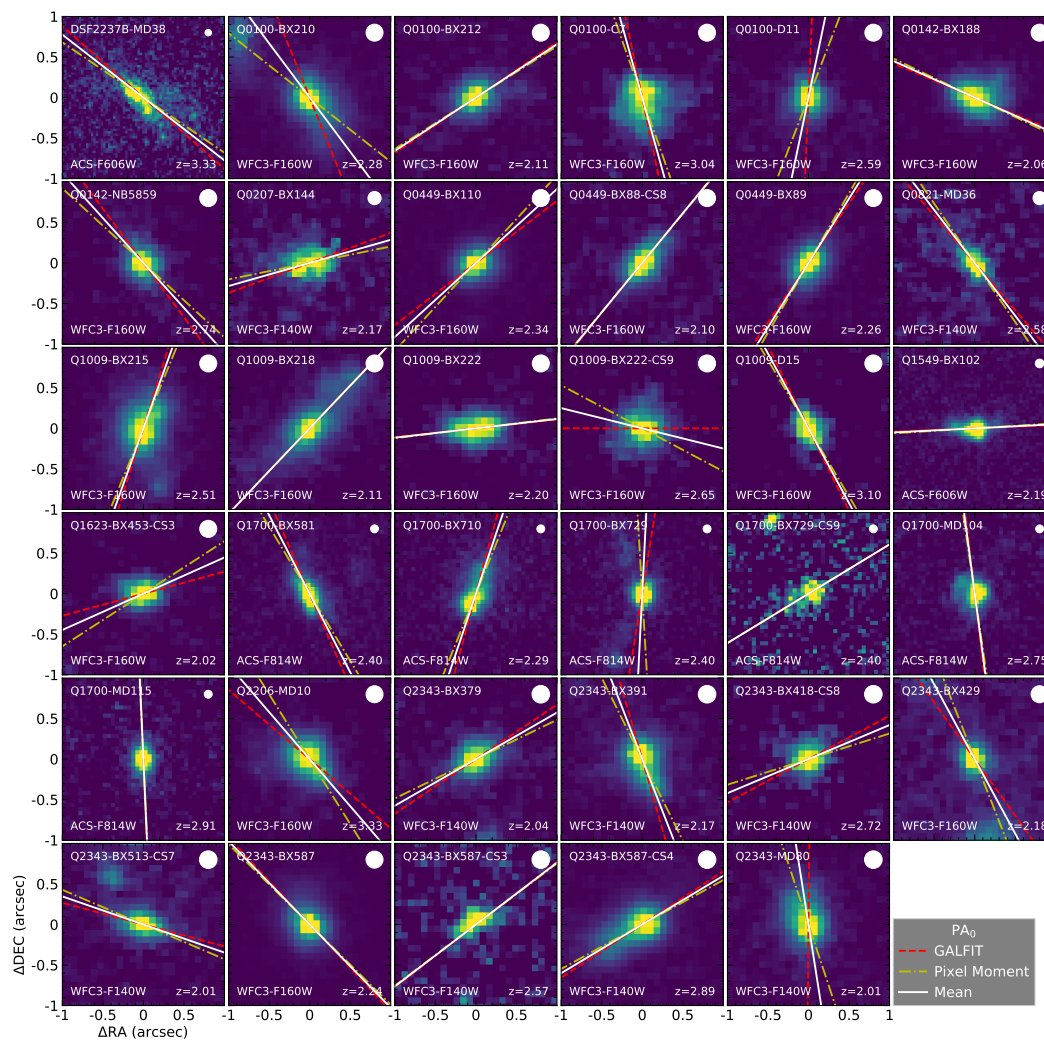


Figure 3.5: HST images of the 35 galaxies whose PA_0 were determined from Methods i and ii. For each image, shown in the four corners, from top-left in clockwise direction, are the KBSS identifier, the FWHM of PSF, redshift, and the instrument and filter that the image was taken with. The dashed red line, dash-dotted yellow line, and the solid white line indicate the direction of PA_0 measured from GALFIT, pixel moment, and the average between the two.

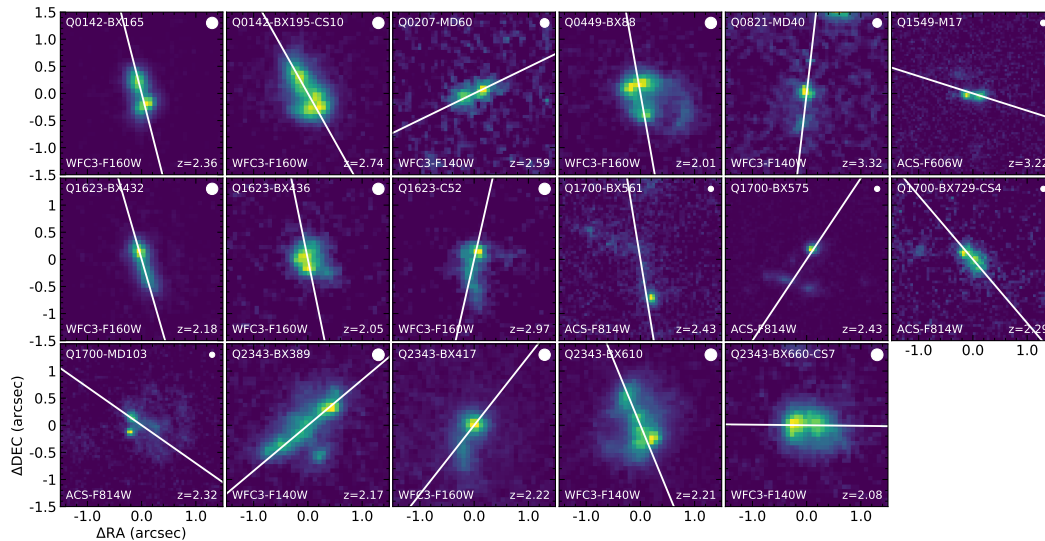


Figure 3.6: Same as Figure 3.5, except that the galaxies do not have a clear central SB peak. Therefore, their PA_0 were determined only from the pixel moment (white solid line).

- (i) *Sérsic profile fitting of HST images*: In this method, we fit a 2D Sérsic profile (Sérsic, 1963) to the host galaxy by using *GALFIT* (Peng et al., 2002; Peng et al., 2010), and determined PA_0 from the best-fit model parameters. The point-spread function (PSF) was measured by selecting stellar sources over the full HST pointing using the star classifier in *SExtractor*, which calculates a “stellarity index” for each object based on a neural network. We then examined sources with the highest 3% stellarity indices by eye, and normalized and stacked them to form an empirical PSF. Our fiducial model consists of a 2D elliptical Sérsic profile convolved with the PSF. We also included the first-order Fourier mode to handle the asymmetric morphology in most cases. However, over- or under-fitting can cause failure of convergence or unreasonably large fitting errors and residuals. In most cases, the cause of the failure and the required adjustment are obvious in the original galaxy image and the model residual. For example, if the residual reveals an additional source, we would add an additional Sérsic component or a simple scaled PSF to the model, depending on the size of the additional source. Meanwhile, if the primary source shows a triangular morphology, we would add the third-order Fourier mode⁷ associated with the Sérsic profile. However, in certain cases, obtaining a successful fit requires experimenting with the model by adding or removing cer-

⁷The second-order Fourier mode is degenerate with the ellipticity.

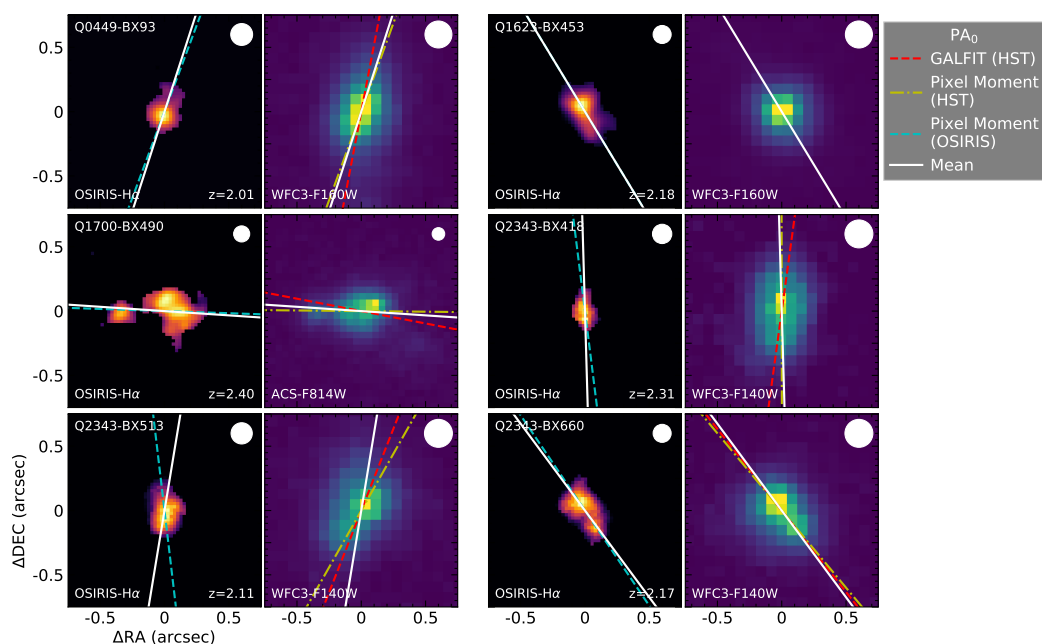


Figure 3.7: Similar to Figure 3.5, showing the PA_0 of galaxies with both Keck/OSIRIS $H\alpha$ maps from Law et al. (2009) and HST continuum images. For each panel, the left image shows the OSIRIS $H\alpha$ map, in which the cyan dashed line is PA_0 measured from this map using second pixel moment. The right image shows the HST image, where the red dashed line and the yellow dash-dotted line show the PA_0 measured from GALFIT fitting and second moment from this image when present. The white solid lines are the final PA_0 determined for each galaxy by averaging the OSIRIS and HST measurements⁶.

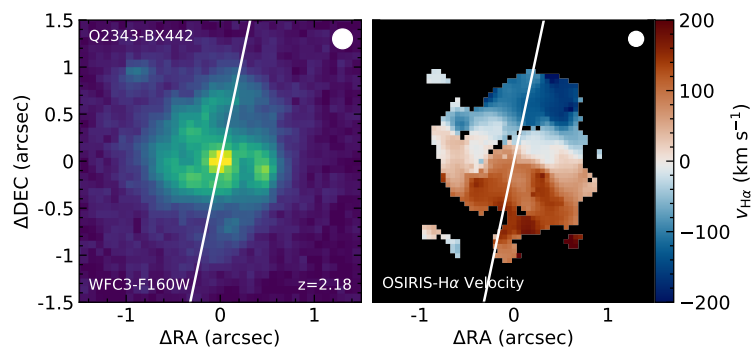


Figure 3.8: *Left*: HST WFC3-F160W image of Q2343-BX442. *Right*: $H\alpha$ velocity map of Q2343-BX442 by Law et al. (2012c). The PA_0 (white solid line) is defined to be perpendicular to its rotational axis.

tain degrees of freedom. The rule of thumb is that we add or remove degrees of freedom one at a time, and adopt the adjustment if it makes the fit converge, or significantly diminishes the reduced χ^2 and the fitted error of PA_0 . In the end, 23 galaxies were fit with the fiducial model. Nine galaxies (Q0100-C7, Q0821-MD36, Q1009-BX222, Q1009-D15, Q1623-BX453-CS3, Q1700-BX729-CS9, Q2343-BX418, Q2343-BX418-CS8, Q2343-BX660) were fit without the Fourier modes. Five galaxies (Q1009-BX218, Q1700-BX490, Q1700-BX710, Q1700-BX729, Q2343-BX513-CS7) were fit with additional sources. Three galaxies (Q2343-BX391, Q2343-BX587-CS3, Q2343-BX587-CS4) were fit with third-order Fourier modes. Galaxies with unsuccessful fits require using alternative methods, detailed below. Successful Sérsic fits were obtained for 40 of 59 galaxies, shown in Figures 3.5 and 3.7; galaxies with successful applications of this method tend to be isolated and to have a dominant central high-surface-brightness component.

- (ii) *Second moment of pixel intensity on HST images:* This method calculates the flux-weighted pixel PA arithmetically derived from the second moment of the pixel intensity,

$$\tan(2PA_0) = \frac{2\langle xy \rangle}{\langle x^2 \rangle - \langle y^2 \rangle}, \quad (3.2)$$

where x and y are the pixel positions relative to the center of the galaxy in the x - and y -directions, and “ $\langle \dots \rangle$ ” indicates the arithmetic mean of the pixel coordinates weighted by pixel flux. Galaxy centers were defined as the point where $\langle x \rangle = 0$ and $\langle y \rangle = 0$. Especially for the galaxies that are morphologically complex, we found that the PA_0 measurements using this method are sensitive to the surface brightness threshold used to define the outer isophotes, and to the spatial resolution of the HST image. Therefore, all ACS images (which have higher spatial resolution than those taken with WFC3-IR) were convolved with a 2D Gaussian kernel to match the PSF to those of the WFC3-IR/F160W images. We tested various surface brightness thresholds, and found that a threshold of 50% of the peak SB after convolution provides the most consistent measurements between the PA_0 measured using (i) and (ii) has an RMS of 10.8 degrees.

- (iii) *Second moment of pixel intensity of OSIRIS H α maps:* This method uses the same algorithm as in (ii), applied to Keck/OSIRIS H α maps rather than HST continuum images. The SB threshold follows Law et al. (2009). There are 6 galaxies whose major axes were determined using this method, including one (Q1623-BX453) whose F160W image is unresolved. For the remaining 5 galaxies, the RMS between PA₀ measured from the HST images and this method is ~ 15 degrees. All 6 galaxies are shown in Figure 3.7.
- (iv) *H α Kinematics:* As the only galaxy in this sample that demonstrates not only rotational kinematics from H α emission, but also clear disk morphology (Law et al., 2012c), the galaxy major axis of Q2343-BX442 is defined to be perpendicular to its rotational axis (Figure 3.8). Because of its complex morphology, we did not apply method (i) to this galaxy. Method (ii) is likely dominated by the inner spiral structure and leads to a PA₀ that is ~ 90 deg apart from that determined from kinematics, while method (iii) is consistent with this method within 15 deg.

Table 3.2 lists the adopted measurement of PA₀ for each galaxy in the sample, as well as the methods used to determine it. In cases where multiple methods were applied, we used the average PA₀ of the OSIRIS and HST measurements, where the latter value is an average of the results obtained using methods (i) and (ii). This way, more weight is given to method (iii) results when available, since it utilizes entirely independent data from a different instrument. The robustness of PA₀ measurements is discussed in the following two subsections.

Relationship between the Kinematic and Morphological Major Axes

An important issue for the interpretation of morphological measurement of PA₀ is the extent to which it is likely to be a proxy for the *kinematic* major axis. Two of the 17 galaxies in Figure 3.6 (Q2343-BX389 and Q2343-BX610) were studied as part of the SINS IFU survey by Förster Schreiber et al. (2018, hereafter FS18), and were subsequently re-observed with the benefit of adaptive optics by FS18; the latter found that both have clear rotational signatures and that the inferred difference between their morphological major axis PA₀ and the kinematic major axis PA_{kin} are $\Delta\text{PA} \equiv |\text{PA}_0 - \text{PA}_{\text{kin}}| = 2 \pm 5$ deg and 27 ± 10 deg for Q2343-BX389 and Q2343-BX610, respectively. From their full sample of 38 galaxies observed at AO resolution, FS18 found $\langle\Delta\text{PA}\rangle = 23$ deg (mean), with median $\Delta\text{PA}_{\text{med}} = 13$ deg.

Among the 6 galaxies which also have $H\alpha$ velocity maps from Law et al. (2009) (used for method (iii) above), two (Q0449-BX93 and Q1623-BX453) show no clear rotational signature, so that PA_{kin} is indeterminate. Small amounts of velocity shear were observed for Q2343-BX513 and Q2343-BX660, both having PA_{kin} consistent with PA_0 ⁸. However, for Q2343-BX418, the implied PA_{kin} is nearly perpendicular to its morphology-based PA_0 . For Q1700-BX490, the kinematic structure is complicated by the presence of two distinct components: the brighter, western component appears to have $PA_{\text{kin}} \simeq 20$ deg, which would be consistent with PA_0 measured from its $H\alpha$ intensity map; however, if the eastern component, which has a slightly blue-shifted velocity of $\sim 100 \text{ km s}^{-1}$, is included as part of the same galaxy, we found $PA_0 = 86$ deg.

As summarized in Tables 3.1 and 3.2 and Figures 3.5-3.7, most of the galaxy sample has PA_0 measured using 2 or more of the methods described above, and generally the morphologically-determined major axis PA_0 agree with one another to within ~ 10 deg. We caution that no high-spatial-resolution *kinematic* information is available for most of the sample; based on the subset of 9 that do have such measurements, approximately two-thirds show reasonable agreement between PA_0 and PA_{kin} .

Distribution and robustness of PA_0 measurements

To estimate the systematic uncertainty of the PA_0 measurements, we compare values measured using different methods for the same objects in Figure 3.9. Between methods (i) and (ii), which are both based on HST images, the measured PA_0 for 40 galaxies are well-centred along the 1-to-1 ratio, with $\text{RMS} \simeq 10.8$ deg. Values of PA_0 measured using method (iii) are based on spectral line maps from an IFU rather than continuum light in a direct image, so that the 5 PA_0 values measured using methods (i) and (iii) exhibit larger scatter, with $\text{RMS} \simeq 15.6$ deg relative to a 1:1 ratio. Therefore, we conclude that the uncertainty in final PA_0 measurements is $\lesssim 15$ deg.

Figure 3.10 shows the normalized Kernel Density Estimator (KDE) and the individual measurements of PA_0 . There is an apparent excess in the occurrence rate of values between $PA_0 \sim 10 - 40^\circ$. To evaluate its possible significance, we conducted 1000 Monte-Carlo realizations of a sample of 58 galaxies with randomly assigned PA_0 ; we find that there is a $\simeq 5\%$ probability that a similar excess is caused by

⁸Q2343-BX513 was also observed by FS18, who found $PA_{\text{kin}} = -35$ deg and $\Delta PA = 40 \pm 12$ deg; our adopted $PA_0 = -9$ deg differs by 26 deg from their PA_{kin} value.

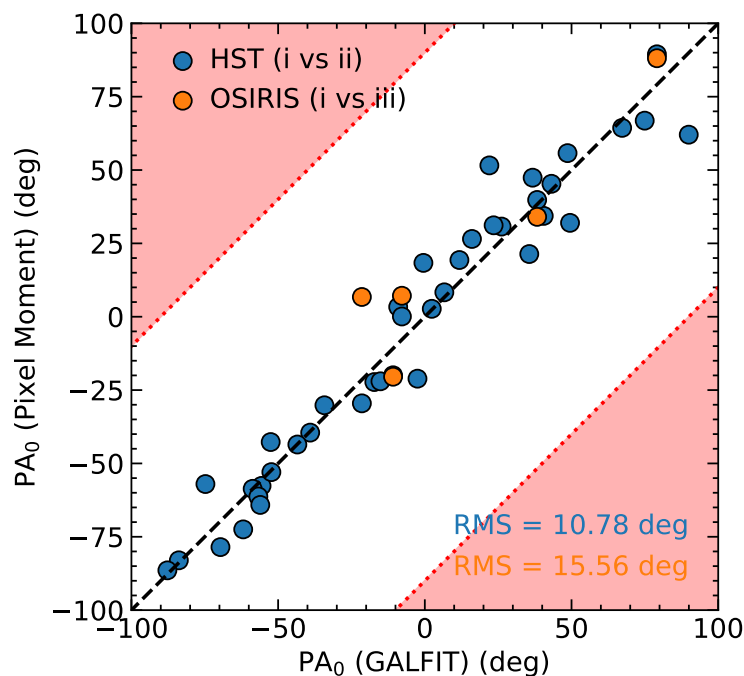


Figure 3.9: Comparison of PA_0 values measured using different methods. Blue points compare methods (i) and (ii), while orange points compare methods (i) and (iii). The overall RMS = 11.4 deg.

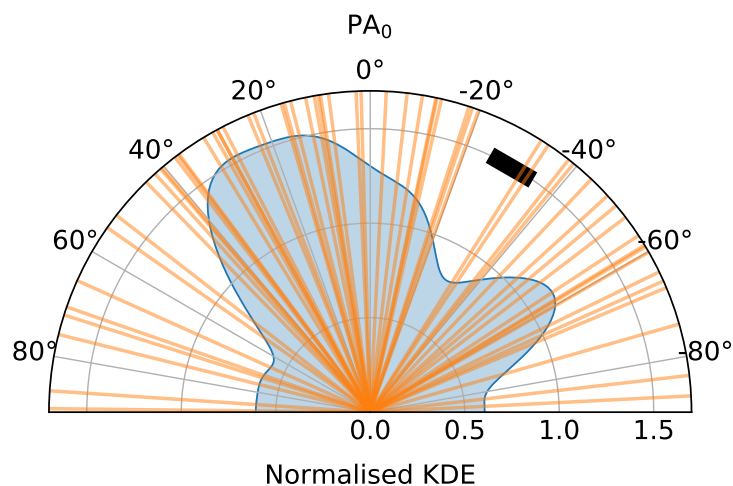


Figure 3.10: The kernel density estimate (KDE; blue shaded region) of PA_0 for the galaxy sample, normalized so that a uniform distribution would have a constant $KDE = 1$. The KDE was constructed using Gaussian kernels of fixed $\sigma = 10^\circ$, corresponding to an opening angle represented by the black block at the top-right. The orange solid lines indicate the values of PA_0 for the individual galaxies. There is an apparent excess in the KDE of galaxies with $PA_0 \approx 10 - 40^\circ$, which we attribute to sample variance.

chance, thus is not statistically significant, and is consistent with that expected from sample variance.

Furthermore, because the HST and OSIRIS images used to measure PA_0 were rotated to the nominal North up and East left orientation prior to measurement, we tested whether significant bias might result from the choice of pixel grid by re-sampling all images with pixel grids oriented in five different directions. We found that the values measured for PA_0 were consistent to within 10 deg (RMS).

The possible systematic bias introduced by an uneven PA_0 distribution is mitigated by our observational strategy of rotating the KCWI instrument PA between individual exposures. We define PA_{Slicer} as the position angle along the slices for each 1200 s exposure, and

$$\phi_{\text{slicer}} = |PA_{\text{Slicer}} - PA_0|. \quad (3.3)$$

Figure 3.11a shows the distribution of ϕ_{slicer} in units of total exposure time. There is a slight tendency for the observations to align with the galaxy major axis (i.e., $\phi_{\text{slicer}} \sim 0$) that results from our usual practice of beginning a sequence of exposures of a given pointing with one at $PA_{\text{slicer}} = 0$ deg and the aforementioned excess of galaxies with $PA_0 \sim 20^\circ$.

In order to characterize the PSF of our final KCWI data cubes, and to show that it is effectively axisymmetric, Figure 3.11b shows various composite images of the galaxy sample. Prior to forming the stack, each individual data cube was rotated to align the galaxy major (minor) axis with the X (Y) coordinate of the stacked image. The KCWI stacked galaxy continuum image [panel (i)] was made by integrating each aligned data cube along the wavelength axis over the range $1224 \leq \lambda_0/\text{\AA} \leq 1236$ in the galaxy rest frame (i.e., $2000 < \Delta v/\text{km s}^{-1} \leq 5000$). This integration window was chosen to be representative of the UV continuum near $\text{Ly}\alpha$ without including the $\text{Ly}\alpha$ line itself, and to be unaffected by $\text{Ly}\alpha$ absorption from the IGM. The center of the galaxy is determined with high confidence (see §3.5) by fitting a 2D Gaussian function to the individual galaxy continuum image. A similar approach – aligning the principal axes in the high-resolution HST images prior to stacking – was used to produce the HST stacked continuum image shown in panel (ii), except that the centers in the HST images were measured using the first moment of pixel intensity. Both stacks were conducted in units of observed surface brightness. The FWHM of the stacked HST image along the major and minor axes are $0''.55$ and $0''.35$, respectively. The stacked KCWI continuum image is well reproduced by the

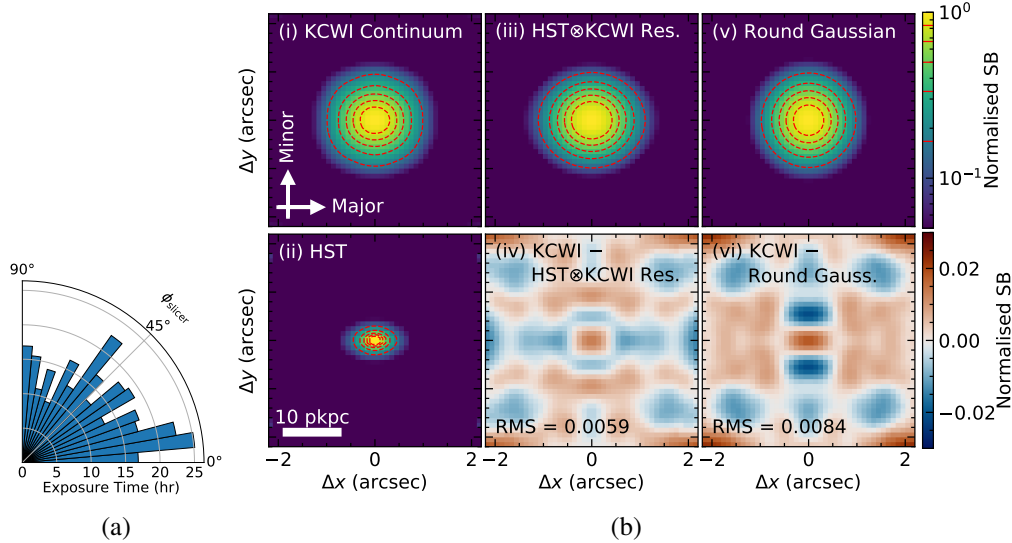


Figure 3.11: (a) Histogram of the relative contribution of measurements made at different slicer azimuthal angles (ϕ_{slicer}) in units of total exposure time. The distribution of ϕ_{slicer} is relatively uniform, with a small excess near $\phi_{\text{slicer}} \sim 10^\circ$. (b) Stacks of the galaxy continuum images for which the major and minor axes of each galaxy were aligned with the X and Y axes prior to averaging. Each panel shows (i) the pseudo-narrow-band image (rest frame $1230 \pm 6 \text{ \AA}$) of the KCWI galaxy continuum, (ii) the stacked HST continuum image, after aligning the principal axes in the same way, (iii) the HST image convolved with a Gaussian kernel of FWHM = $1''.02$ to match the KCWI continuum, (iv) the residual between the KCWI continuum and the HST image convolved with the KCWI PSF, (v) a 2D circular Gaussian profile with FWHM = 1.21 arcsec as the best symmetric Gaussian profile from a direct fit of the KCWI continuum image, and (vi) the residual between the KCWI continuum and the model in (v) isotropic Gaussian profile. The color map of (i), (ii), (iii), and (v) is in log scale, with linear red contours in the decrement of 0.17. The color map of (iv) and (vi) is in linear scale. The residual map in panel (vi) shows a clear dipole residual in the Y (minor axis) direction that is not present in (iv). The RMS values in panels (iv) and (vi) were calculated within $|\Delta x| < 1$ arcsec and $|\Delta y| < 1$ arcsec to reflect the dipole residual. The “boxiness” of the KCWI stack is likely due to the undersampling of KCWI in the spatial direction. Taken together, (b) demonstrates that the KCWI PSF is axisymmetric (with FWHM = $1''.02$), and that the KCWI continuum image is capable of distinguishing the galaxy major and minor axes.

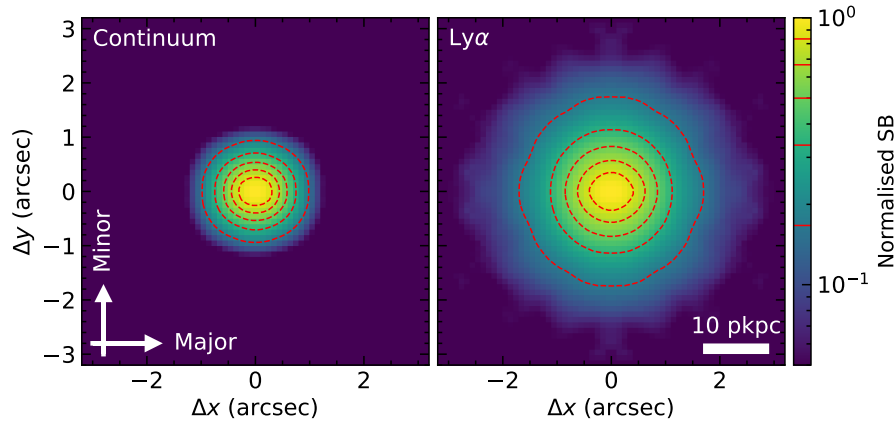


Figure 3.12: Stacked images of the galaxy continuum (*Left*) and the continuum-subtracted $\text{Ly}\alpha$ emission (*Right*) with the X- and Y-axes aligned with the galaxy major and minor axes, respectively. The color coding is on a log scale, while the contours are linear. The intensity scales have been normalized to have the same peak surface brightness intensity at the center. The $\text{Ly}\alpha$ emission is more extended than the continuum emission.

convolution of the PA_0 -aligned stacked HST image [panel (ii) of Fig. 3.11b] with an axisymmetric 2-D Gaussian profile with $\text{FWHM} = 1''.02$ [see panels (iii) and (iv) of Fig. 3.11b].

Comparing the convolution of HST and KCWI [panel (iii)] with the best direct fit of a symmetric Gaussian profile to the KCWI continuum image ($\text{FWHM} = 1''.21$) [panel (v)] show that even at the $\approx 1''.02$ resolution of KCWI one can clearly distinguish the major axis elongation. The residual map assuming a symmetric Gaussian profile [panel (vi)] shows a clear dipole residual compared to panel (iv). Thus, Figure 3.11 shows that (1) the PSF of the KCWI cubes is axisymmetric and thus has not introduced a bias to the azimuthal light distribution measurements and (2) the spatial resolution is sufficient to recognize non-axisymmetry even on sub-arcsec angular scales of the continuum light.

3.5 Analyses

$\text{Ly}\alpha$ Spatial Profile

To study the dependence of the $\text{Ly}\alpha$ emission profile on galaxy azimuthal angle, we first analyse the $\text{Ly}\alpha$ surface brightness (SB) profile as a function of the impact parameter (or transverse distance, D_{tran}). Figure 3.12 compares the stacked continuum and continuum-subtracted narrow-band $\text{Ly}\alpha$ emission, composed in the same way as in Figure 3.11. The integration window of the $\text{Ly}\alpha$ image is

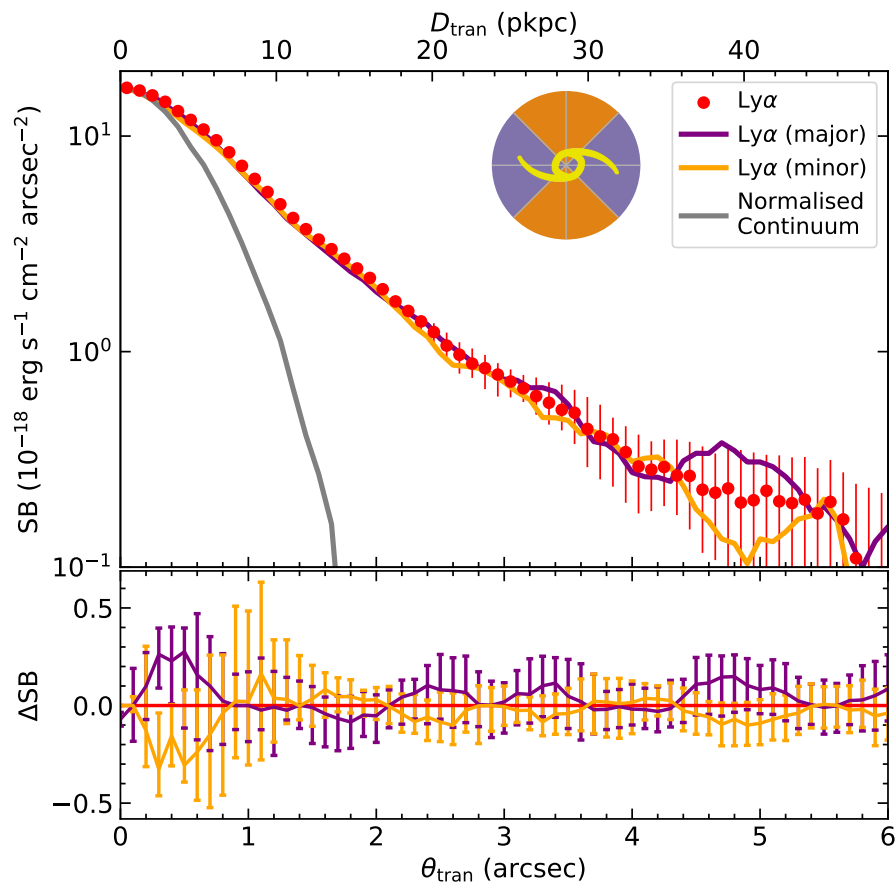


Figure 3.13: *Top panel:* The average Ly α surface brightness profile of the continuum-subtracted composite Ly α image shown the righthand panel of Figure 3.12. Red points represent the median surface brightness evaluated over all azimuthal angles ($0^\circ < \phi \leq 90^\circ$) as a function of projected distance from the galaxy center. Orange and purple curves show the profiles evaluated over $0^\circ < \phi \leq 45^\circ$ (major axis) and $45^\circ < \phi < 90^\circ$ (minor axis) azimuthal angles. Dashed cyan curve shows the best-fit profile of the two-component exponential model. Dotted cyan curves show the two component separately. The grey profile shows the normalized continuum for comparison. *Bottom:* The residual surface brightness profile formed by subtracting the all-azimuth average from the major and minor axis profiles. The residuals are consistent with zero aside from a marginally-significant difference at $\theta_{\text{tran}} < 1''.0$, where the Ly α emission is slightly stronger along the major axis. Unless otherwise noted, the conversion between θ_{tran} and D_{tran} for this and later figures assumes a redshift of 2.3, the median redshift of the sample.

$-700 < \Delta v / (\text{kms}^{-1}) \leq 1000$ ($1213 \text{ \AA} - 1220 \text{ \AA}$) to include most of the Ly α emission (as shown later in Figure 3.14). Continuum subtraction throughout this work was done spaxel-by-spaxel in the data cube of each target galaxy by subtracting the average flux density in two windows flanking the position of Ly α , with $2000 < |c\Delta v_{\text{sys}} / \text{km s}^{-1}| < 5000$, where Δv_{sys} is the velocity separation relative to rest-frame Ly α (i.e., two windows each of width $\simeq 12 \text{ \AA}$ in the rest frame, [1195-1207] and [1224-1236] \AA). Similar to §3.4, the center of the galaxy in the KCWI data was determined by fitting a 2D Gaussian profile to the KCWI continuum image. The fitting box was chosen by eye to include all of the signal from the galaxy, but excluding nearby contamination. Despite the arbitrary box size, we found that the derived centroid is very robust: varying the box size by 4 pixels ($1''.2$), the fit result does not change by more than $0''.01$. The typical fitting error propagated from the reduced χ^2 is also $\sim 0''.01$ (median), i.e., much smaller than the seeing disk.

A 2D Gaussian fit to the profiles finds that the FWHM values are $1''.279 \pm 0''.003$ (major axis) $\times 1''.182 \pm 0''.003$ (minor axis) (or a $\sim 8\%$ difference) for the continuum emission and $1''.689 \pm 0''.005 \times 1''.705 \pm 0''.005$ ($< 1\%$ difference between major and minor axes) for the Ly α emission. Therefore, the Ly α emission in the stacked image is both more symmetric and more spatially extended than the continuum emission.

Figure 3.13 shows the median Ly α SB as a function of D_{tran} (red). Each point represents the median SB of a bin of pixels with $\Delta D_{\text{tran}} = 0.1 \text{ pkpc}$. The Ly α surface brightness profile falls off much more slowly than the continuum (grey). Following Wisotzki et al. (2016), we fit the Ly α SB profile with a two-component model – a compact “core” component and an extended “halo” component. Both components are exponential profiles convolved with the KCWI PSF with the amplitudes, exponential radii, and a uniform background term as free parameters. Further details of the model fitting will be described in a future work (R. Trainor & N. Lamb, in prep.). The best-fit exponential radii $r_{\text{exp}} = 3.71_{-0.04}^{+0.06} \text{ pkpc}$ and $15.6_{-0.4}^{+0.5} \text{ pkpc}$. The r_{exp} of the halo component is close to Steidel et al. (2011) (for KBSS galaxies observed with narrow-band Ly α imaging), which found the median-stacked Ly α profile has $r_{\text{exp}} = 17.5 \text{ pkpc}$, but slightly more extended than Wisotzki et al. (2018) for SF galaxies at $z > 3$ (see also Matsuda et al., 2012; Momose et al., 2014; Leclercq et al., 2017). Dividing the SB profiles into two subsamples with $0^\circ \leq \phi < 45^\circ$ (purple) and $45^\circ \leq \phi \leq 90^\circ$ (orange) that represent the galaxy major and major axes respectively, one can see that the resulting profiles are consistent with one another to within 1σ , or within $\lesssim 2 \times 10^{-19} \text{ erg s}^{-1} \text{ cm}^{-2} \text{ arcsec}^{-2}$. The possible exception is

at the smallest projected distances ($D_{\text{tran}} < 1$ arcsec, or $\lesssim 8$ pkpc), where the Ly α emission is marginally enhanced; if real, the difference in profiles (the asymmetry) represents $< 2\%$ of the total Ly α flux. Thus, the composite Ly α intensity is remarkably symmetric, suggesting an overall lack of a strong statistical connection between the morphology of the starlight and that of the extended Ly α emission surrounding individual star-forming galaxies at $z \sim 2 - 3$.

Cylindrical Projection of 2D Spectra

The similarity of the Ly α surface brightness profile along galaxy major and minor axes suggests that extended Ly α emission depends little on the galaxy orientation. However, the KCWI data cubes allow for potentially finer discrimination through examination of both the surface brightness and kinematics of Ly α emission as a function of projected galactocentric distance. To facilitate such comparison, we introduce “cylindrical projections” of 2D Ly α emission. The basic idea behind cylindrical projection, illustrated in Figure 3.14, is to provide an intuitive visualization of spatial and spectral information simultaneously.

Compared to the standard 2D spectrum one obtains from slit spectroscopy, the cylindrical 2D spectrum replaces the 1D spatial axis (i.e., distance along a slit) with projected distance, by averaging spaxels in bins of D_{tran} or, equivalently, θ_{tran} . When projected as in the righthand panel of Figure 3.14, it can also be viewed as the Ly α spectrum at every projected radial distance (averaged, in this case, over all azimuthal angles) or as the average radial profile at each slice of wavelength or velocity.

Figure 3.14 shows the stacked cylindrical 2D spectrum formed by averaging the continuum subtracted data cubes at wavelengths near rest-frame Ly α for all 59 galaxies in Table 3.1. This composite cylindrical 2D spectrum, analogous to a “down-the-barrel” Ly α spectrum in 1D, but evaluated as a function of galactocentric distance, shows that the Ly α emission line is comprised of distinct redshifted and blueshifted components extending to ± 1000 km s $^{-1}$ with respect to $v_{\text{sys}} = 0$, with a minimum close to $v_{\text{sys}} = 0$. The vast majority of individual galaxies, and therefore also the average in the stacked profile, has $F_{\text{Ly}\alpha}(\text{blue})/F_{\text{Ly}\alpha}(\text{red}) \simeq 0.3$, and is thus “red peak dominated”. The two-component spectral morphology extends to at least $\theta_{\text{tran}} \simeq 3$ arcsec or $D_{\text{tran}} \simeq 25$ pkpc. This overall spectral morphology is most readily explained as Ly α photons being resonantly scattered by outflowing material, whereby redshifted photons are scattered from the receding (opposite) side are more likely to escape in the observer’s direction than blue-shifted photons e.g. Pettini

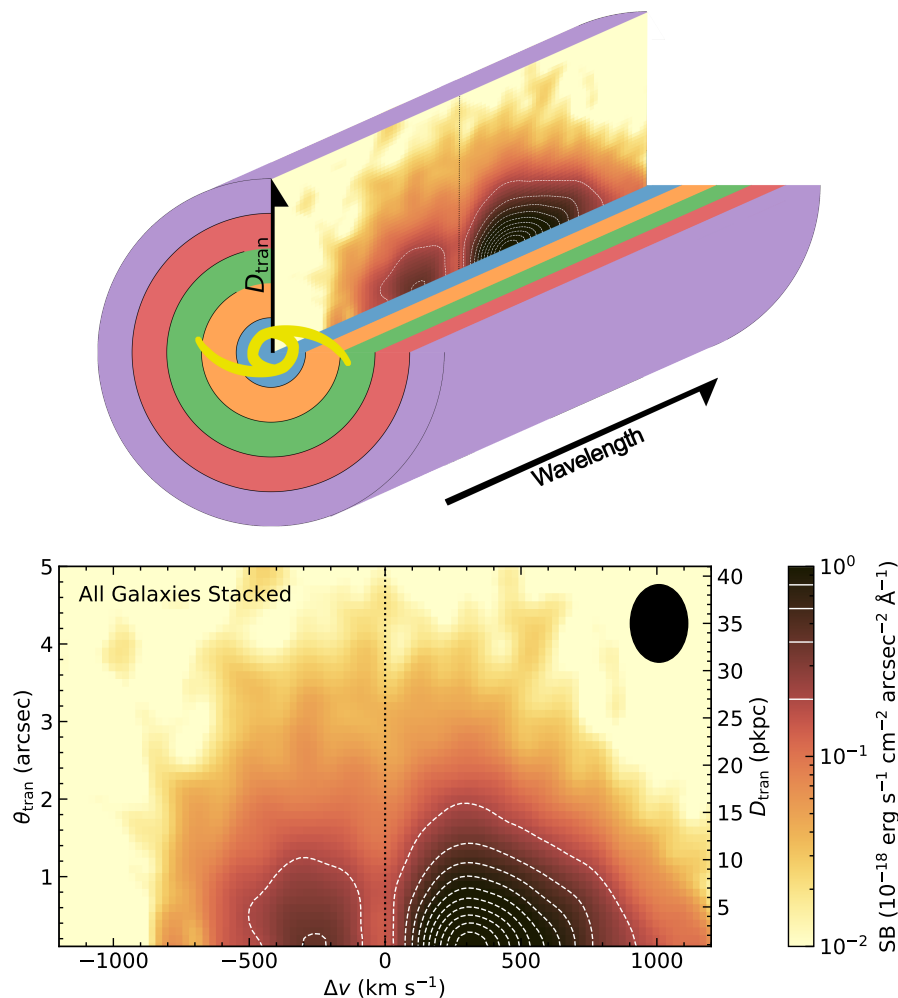


Figure 3.14: *Top:* A schematic diagram explaining cylindrically projected 2D (CP2D) spectra. Spaxels with similar D_{tran} are averaged to create the emission map in $D_{\text{tran}}-\Delta v$ space. *Bottom:* The composite CP2D spectra of the continuum-subtracted Ly α emission line map averaged over all 59 galaxies, at all azimuthal angles (ϕ). The color-coding of the Ly α surface intensity is on a log scale to show the full extent of the emission, whereas the contours are spaced linearly and marked as white lines in the colorbar. The stack was formed by shifting the wavelengths of each galaxy data cube to the rest frame, leaving the surface brightness in observed units. The black ellipse at the top right shows the effective resolution of the stacked maps, with principal axes corresponding to the spectral resolution FWHM and the spatial resolution FWHM (see §3.4). Pixels with $\theta_{\text{tran}} < 0.1$ arcsec have been omitted to suppress artifacts owing to the singularity in the cylindrical projection.

et al., 2001; Steidel et al., 2010; Dijkstra, 2014.

As D_{tran} increases and the Ly α SB decreases exponentially, the two Ly α peaks become less distinct and merge into a symmetric “halo” centered on $\Delta v = 0$. The vast majority of the Ly α emission is within $-700 < \Delta v/\text{km s}^{-1} < 1000$. However, we caution that the apparent blue edge at $\Delta v \sim -700 \text{ km s}^{-1}$ of Ly α emission in this composite 2D spectrum is likely caused by continuum over-subtraction resulting from the relatively simple technique that we used in this work. The continuum subtraction assumed a linear interpolation of the continuum spectrum underneath the Ly α emission (see §3.5), which tends to over-estimate the continuum flux blueward of the systemic redshift of the galaxy due to intrinsic Ly α absorption in the stellar spectrum and residual effects of the often-strong Ly α absorption damping wings on which Ly α emission is superposed. To improve on this would require a more sophisticated continuum-subtraction method in the inner $\approx 1''.0$ of the galaxy profile; however, since most of the remainder of this work will involve comparison of 2D cylindrical projections with one another, the imperfections in continuum subtraction at small θ_{tran} are unlikely to affect the results.

Dependence on azimuthal angle of cylindrically projected 2D (CP2D) spectra

To investigate how Ly α emission depends on the galaxy azimuthal angle, we split each CP2D spectrum of individual galaxies averaged over two independent bins of azimuthal angle (ϕ) with respect to the galaxy’s major axis: $0^\circ \leq \phi < 45^\circ$ (“major axis”) and $45^\circ \leq \phi \leq 90^\circ$ (“minor axis”), as in §3.5 and Figure 3.13. The CP2D stacks covering these azimuth ranges were combined separately to form CP2D composites that we refer to as “Major Axis” and “Minor Axis”. To reveal subtle differences in surface brightness and/or velocity along these two directions, we subtracted one from the other – Figure 3.15 shows the result.

The difference between the CP2D spectra along the major and minor axes (top right of Figure 3.15) shows excess emission along the galaxy major axis at $\Delta v \approx +300 \text{ km s}^{-1}$ – consistent with the velocity of the peak of the redshifted component in the full composite CP2D spectrum – within $\theta_{\text{tran}} \lesssim 2''$ ($D_{\text{tran}} \lesssim 15 \text{ pkpc}$). The Ly α flux of this asymmetric component of Ly α amounts to $\lesssim 2\%$ of the total, and has a peak intensity $\approx 5\%$ that of the peak of the redshifted Ly α component shown in Fig. 3.13.

The significance map in the bottom-right panel of Figure 3.15 is based on the standard deviation of 100 independent mock CP2D stacks, each made by assigning

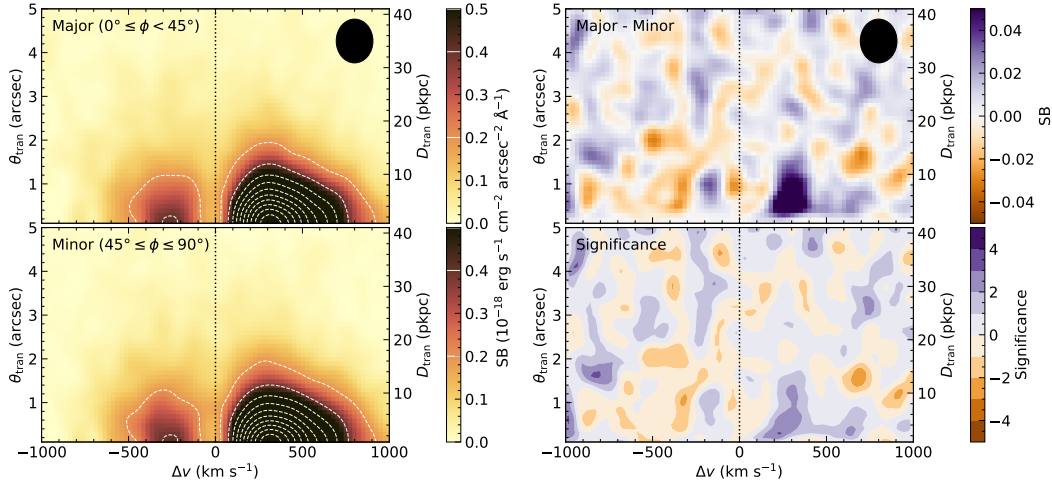


Figure 3.15: *Left*: The stacked CP2D spectra along the galaxy major ($0^\circ \leq \phi < 45^\circ$; top) and minor ($45^\circ \leq \phi \leq 90^\circ$; bottom) axes. Both the color-coding and the contours are on linear scales. *Right*: The residual CP2D maps: the top panel shows the difference between the Major axis and Minor axis maps, in the same units of surface intensity as in the lefthand panels, where blue colors indicate regions with excess Ly α surface intensity along the Major axis; orange colors indicate regions where Ly α is brighter in the Minor axis map. The bottom panel shows the same residual map in units of the local noise level. The most prominent feature is excess Ly α emission along the galaxy major axis relative to that along the minor axis), at $\Delta v \sim +300 \text{ km s}^{-1}$, extending to $\theta_{\text{tran}} \sim 2''.0$ or $D_{\text{tran}} \sim 15 \text{ pkpc}$.

random PA₀ to the galaxies in our sample before combining. The mock stacks were then used to produce a 2D map of the RMS residuals evaluated in the same way as the observed data. Considering the effective resolution, the overall significance (compared to the standard deviation) of the most prominent feature in the top-right panel of Figure 3.15 is $\simeq 2 - 2.5\sigma$ per resolution element. Thus, while the residual (excess) feature may be marginally significant statistically, the level of asymmetry relative to the total Ly α flux is in fact very small.

The robustness of residual Ly α asymmetry

Despite the marginally significant detection of the excess Ly α emission along galaxy major axes, its robustness is subject to scrutiny. In particular, we would like to determine whether the apparent detection is typical of the population or is caused by a few outlier objects having very asymmetric Ly α as a function of azimuthal angle.

Figure 3.16 shows histograms of the difference in integrated Ly α flux between the major and minor axis bins of azimuthal angle. We calculated the differences

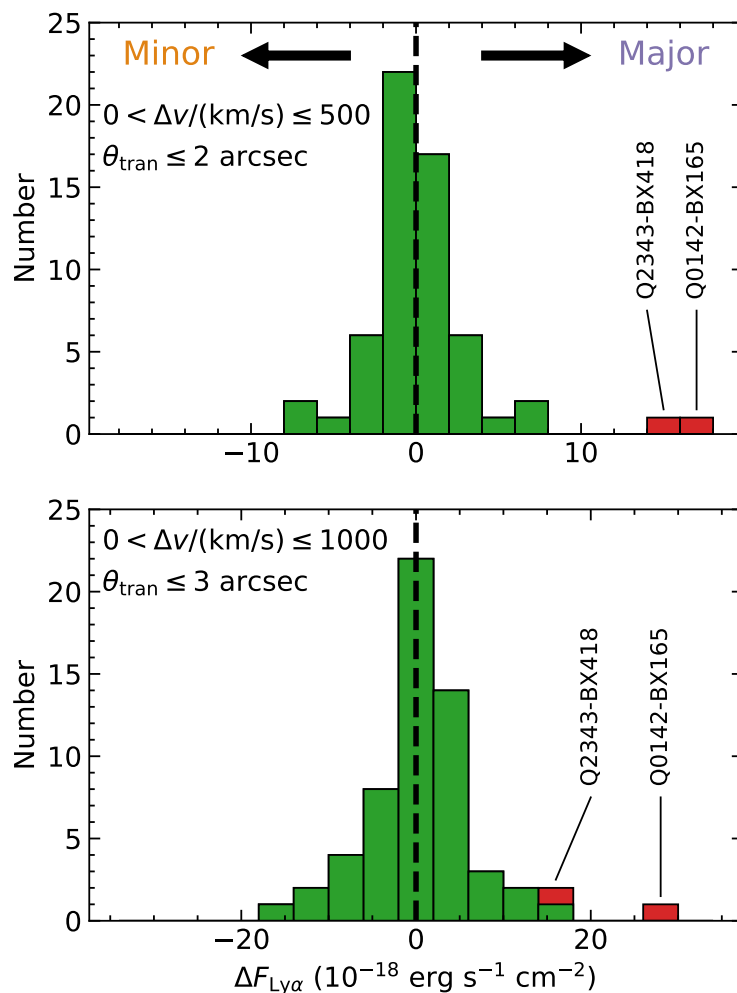


Figure 3.16: Distribution of the difference in Ly α flux integrated over velocity and angular distance in the bins of azimuthal angle corresponding to “major” and “minor” axes. Positive (negative) values indicate that Ly α emission is stronger along the major (minor) axis. The integration is conducted within $0 < \Delta v / (\text{km s}^{-1}) < 500$ and $\theta_{\text{tran}} \leq 2$ arcsec (top) and $0 < \Delta v / (\text{km s}^{-1}) < 1000$ and $\theta_{\text{tran}} \leq 3$ arcsec (bottom). There are two outliers in the first integration (top panel), while one remains in the second (bottom panel).

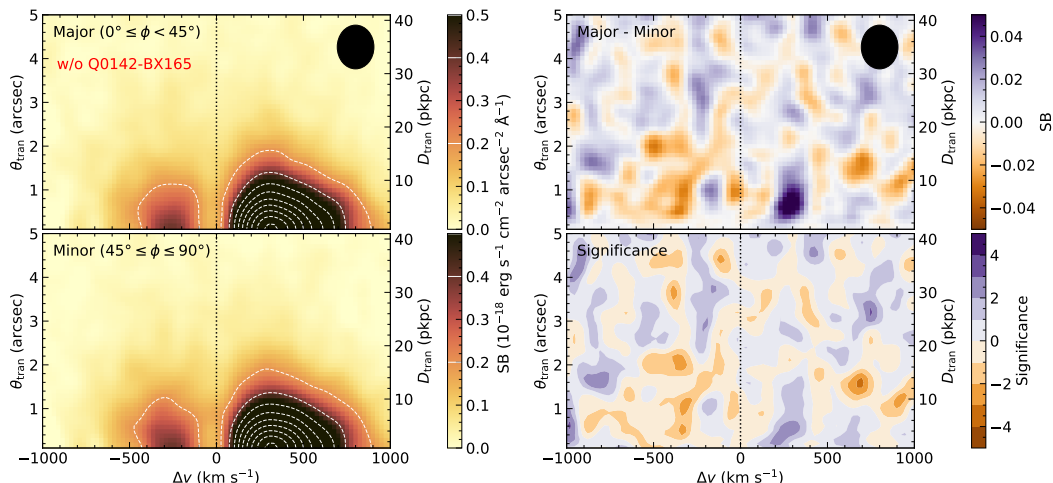


Figure 3.17: Same as Figure 3.15, but without Q0142-BX165, which is the strongest outlier in terms of excess Ly α emission along the galaxy major axis.

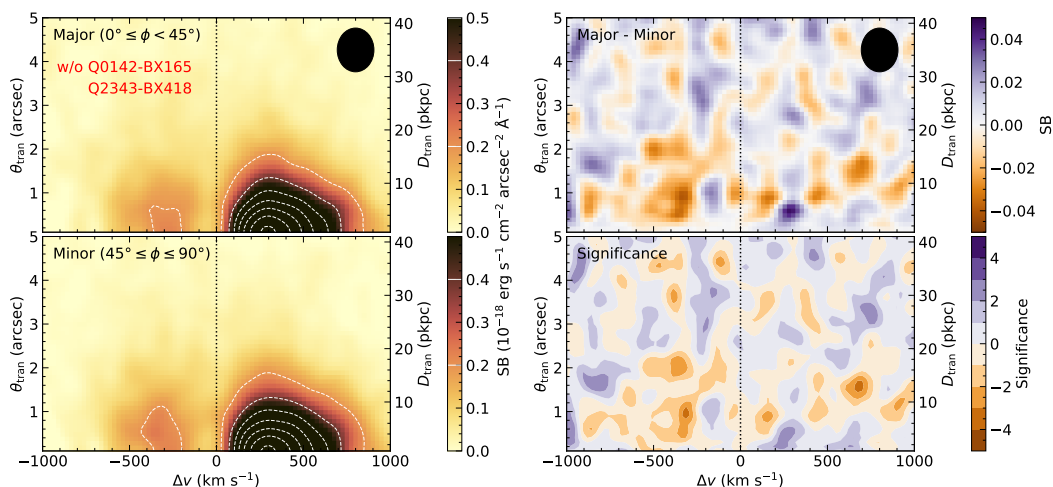


Figure 3.18: Same as Figure 3.15, but without Q0142-BX165 and Q2343-BX418, the two most significant outliers in the top panel of Figure 3.16. Significant excess emission that is larger than a resolution element for the redshifted peak no longer exists.

integrated over two different ranges of Δv and θ_{tran} ; (1) the range where the excess shown in Figure 3.15 is most prominent, $\theta_{\text{tran}} \leq 2''$ and $0 \leq (\Delta v)/\text{km s}^{-1} \leq 500$, shown in the top panel, and (2) the range which encapsulates most of the redshifted component of Ly α $\theta_{\text{tran}} \leq 3''$ and $0 \leq (\Delta v)/\text{km s}^{-1} \leq 1000$, shown in the bottom panel. Two galaxies – Q0142-BX165 and Q2343-BX418 – are clearly outliers in (1), while only Q0142-BX165 stands out in (2). The distribution of $\Delta F_{\text{Ly}\alpha}$ for the other 56 galaxies in the sample is relatively symmetric around $\Delta F_{\text{Ly}\alpha} = 0$.

Figures 3.17 and 3.18 show the stacked Ly α profiles as in Figure 3.15, but with the strongest outliers removed from the stack. After removing both outliers (Figure 3.18), the excess Ly α emission along the galaxy major axis at $\Delta v \simeq 300 \text{ km s}^{-1}$ becomes consistent with noise. Although Q2343-BX418 is not an extreme outlier in terms of the overall Ly α asymmetry of the integrated redshifted component of Ly α emission (bottom panel of Fig. 3.16), when only Q0142-BX165 is removed from the stack (Fig. 3.17) the composite 2D spectra still show obvious excess Ly α emission along the galaxy major axis, albeit with slightly reduced significance. Meanwhile, when both outliers are removed from the stack (Figure 3.18), one can see an emerging excess Ly α emission along the *minor* axis, for the *blue* peak, with $-700 \lesssim \Delta v / (\text{km s}^{-1}) \lesssim -200$ and $\theta_{\text{tran}} \lesssim 2''.5$ with integrated significance $\sim 2\sigma$. The flux of the excess blueshifted emission comprises $\sim 10\%$ of the total blueshifted Ly α flux, with a peak amplitude $\sim 1\%$ of the peak Ly α intensity (i.e., the redshifted peak).

We conducted an analysis on the *blueshifted* emission similar to that done for the redshifted asymmetry, with results summarized in Figure 3.19. There is no obvious outlier in the difference in integrated Ly α flux between the major and minor axis azimuth bins except for Q0142-BX165, for which the excess again favors the *major* axis (i.e., it is in the direction opposite to the apparent blueshifted asymmetry identified in Figure 3.18). We also consecutively removed from the Ly α stack galaxies with extreme excess emission along the minor axis, and found no sudden and significant changes in the composite spectra. Evidently, the blueshifted excess along the minor axis, while of about the same significance as the redshifted excess in the major axis direction, is a general property of the full sample rather than a result of a small number of outliers.

In summary, we found excess emission along the galaxy major axis for the redshifted component of Ly α near $\Delta v \simeq 300 \text{ km s}^{-1}$. However, this particular excess emission appears to be caused by galaxy outliers with extreme emission along the major axis. After removing them from the composite CP2D spectra we found excess emission along the galaxy minor axis for the blue peak within $-700 \lesssim \Delta v / (\text{km s}^{-1}) \lesssim -200$ that is not apparently affected by the extreme scenarios. Both detections are not particularly significant at the $\sim 2\sigma$ level.

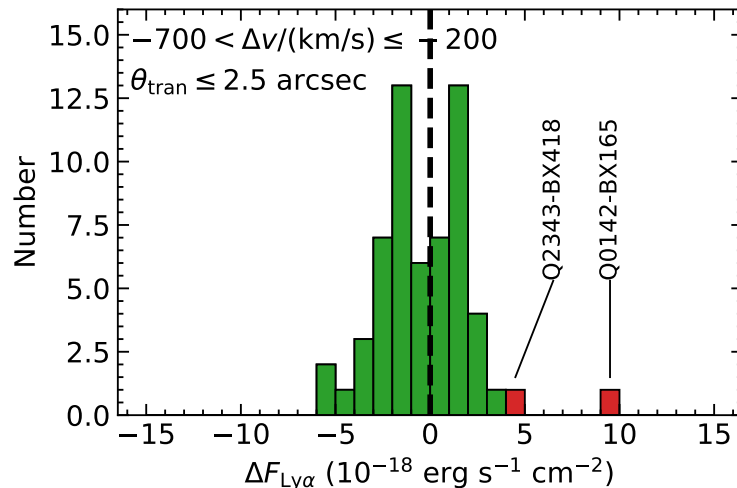


Figure 3.19: Same as Figure 3.16, but with a different velocity range of $-700 < \Delta v / (\text{km s}^{-1}) \leq -200$ and $\theta_{\text{tran}} \leq 2.5$ arcsec that focuses on the blueshifted component of Ly α emission. No individual galaxy is an extreme outlier in terms of excess blueshifted Ly α along the minor axis.

A Closer Look at the Extreme Cases

Figure 3.20 shows the residual between the cylindrically projected 2D spectra extracted along the major and minor axes of Q0142-BX165, as well as continuum images from both HST and KCWI. Q0142-BX165 has two comparably bright components separated by ≈ 3.5 pkpc ($\approx 0''.4$). Careful inspection of Keck/LRIS and Keck/MOSFIRE spectra of this system revealed no sign of an object at a different redshift. There is no significant offset between the KCWI continuum and Ly α centroids (≤ 0.5 pix $\sim 0''.15$ separation), indicating that the apparent directional asymmetry in the CP2D spectra is not caused by a spatial shift between the continuum and Ly α emission. Instead, the narrow-band Ly α map shows that the Ly α emission is elongated approximately along the N-S direction. However, after aligning the KCWI and HST astrometry with reference to a nearby compact galaxy, we found that both the KCWI stellar continuum near Ly α and the narrow-band Ly α emission are centered near the SW component (see Figure 3.20). It is possible that the SW component alone is responsible for the Ly α emission, in which case its PA $_0$ would be -59° , $\sim 70^\circ$ off from what was determined in §3.4. However, adopting PA $_0 = -59^\circ$ would cause BX165 to become an outlier with excess Ly α emission along the *minor* axis. Meanwhile, the elongation of the KCWI continuum aligns with the direction of the separation of the two components, and is roughly consistent with the direction of the Ly α elongation as well. This seems to suggest that the Ly α

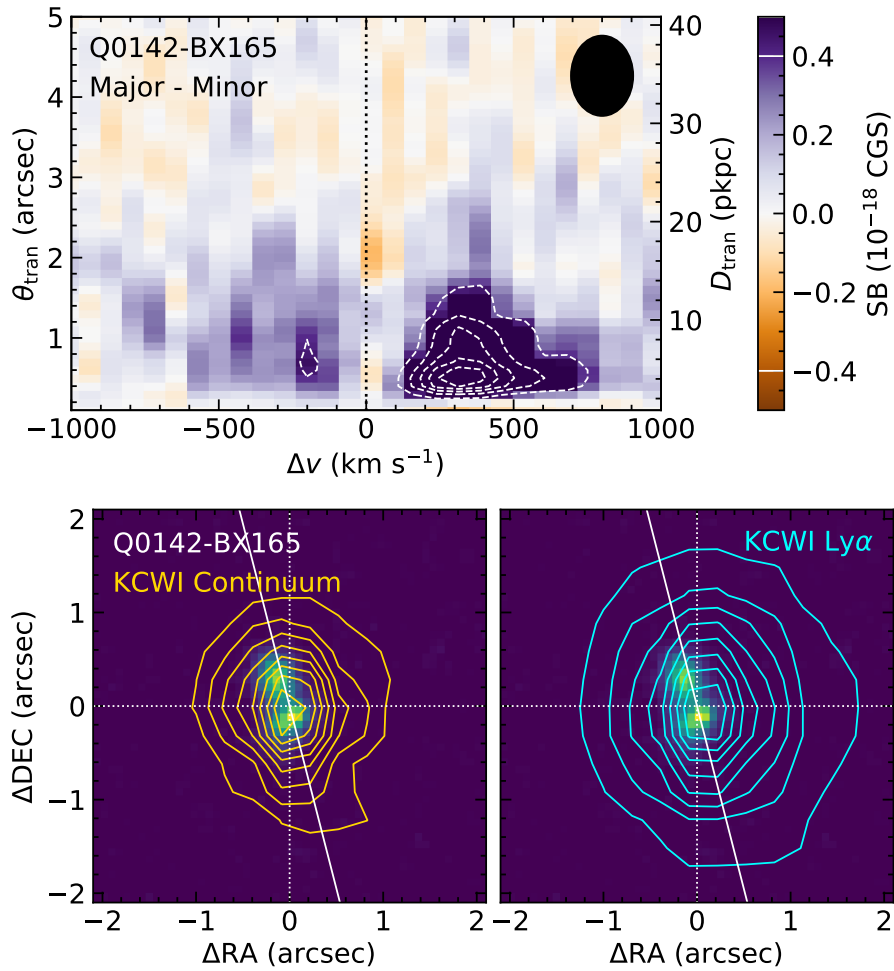


Figure 3.20: *Top*: Same as the top-right panel of Figure 3.15, but for a single galaxy, Q0142-BX165, which has the strongest excess Ly α emission along the galaxy major axis. Note that the color scale is 10 times that of Figure 3.15. *Bottom*: The HST F160W image of Q0142-BX165, overlaid with contours from the KCWI continuum image (left) and the narrow-band Ly α image (right).

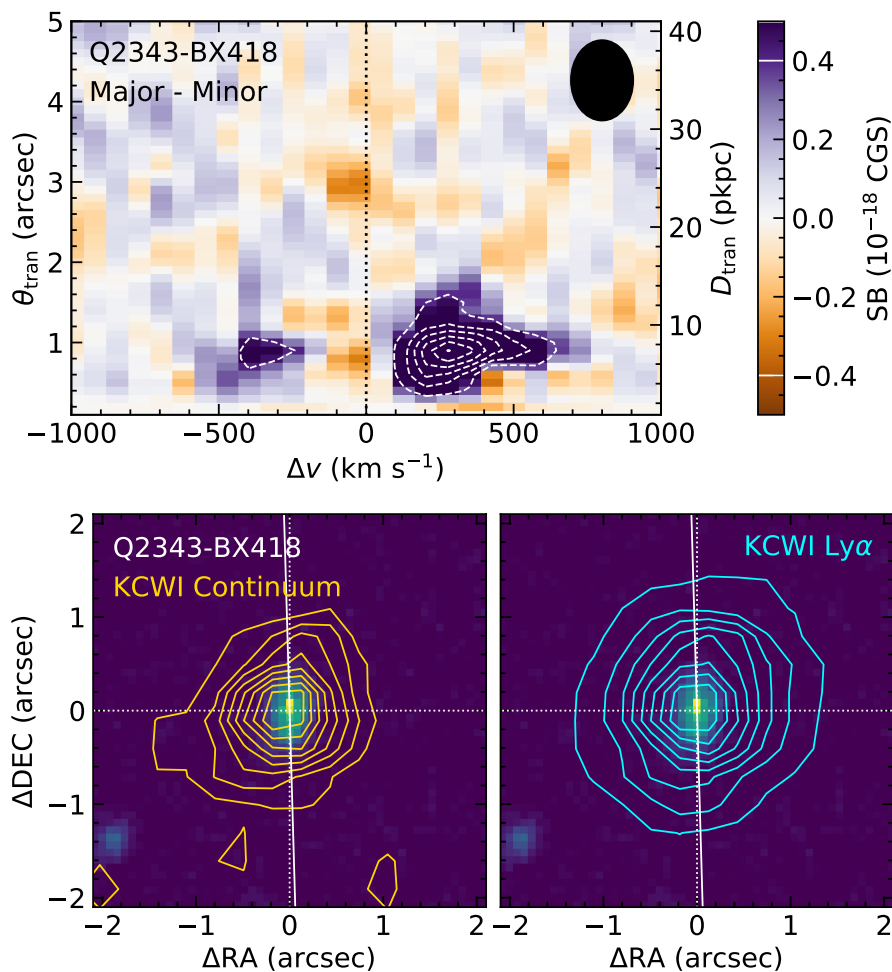


Figure 3.21: Same as Figure 3.20, but for Q2343-BX418, the object with the second strongest major axis Ly α asymmetry.

elongation simply reflects the asymmetry of the continuum source, albeit on a larger angular scale; however, as shown in Figure 3.6, many galaxies in the sample possess similar morphologies, but Q0142-BX165 is the only one that shows extraordinary asymmetry in Ly α emission. In any case, Q0142-BX165 has a uniquely asymmetric Ly α halo, possibly due to source confusion. Consequently, we exclude it from most of the analysis that follows.

The KCWI data cube for Q2343-BX418 has been analysed previously by Erb, Steidel, and Chen (2018); here, we consider it in the context of the analysis of Q0142-BX165 above (see Figure 3.21). The difference in peak SB between the major and minor axis CP2D spectra is nearly equal to that of Q0142-BX165 ($2.4 \times 10^{-18} \text{ erg s}^{-1} \text{ cm}^{-2} \text{ arcsec}^{-2} \text{ \AA}^{-1}$ for both). However, the spatial extent of the

excess emission is significantly smaller for Q2343-BX418. The HST/WFC3, KCWI continuum, KCWI Ly α images, and OSIRIS-H α images all show Q2343-BX418 comprise a single component whose centroids in the various images are consistent with one another. Despite its extreme SB asymmetry in Ly α , Q2343-BX418 exhibits no other obviously peculiar property compared to the rest of the sample.

3.6 Integrated Line Flux and Azimuthal Asymmetry

As shown in the previous sections, the degree of Ly α halo azimuthal asymmetry varies from case to case in our $z \approx 2.3$ sample, but the correlation with the morphology of the central galaxy is sufficiently weak that, on average, Ly α halos are remarkably symmetric and appear to be nearly independent – both kinematically and spatially – of the apparent orientation of the galaxy at the center.

Thus far we have treated the blueshifted and redshifted components of Ly α emission separately. However, the overall Ly α profile is expected to provide clues to the geometry and velocity field of circumgalactic H I. In this section, we compare the dependency between excess Ly α emission and $W_\lambda(\text{Ly}\alpha)$, total Ly α flux $F_{\text{Ly}\alpha}(\text{tot})$, and the ratio of the total flux of blueshifted and redshifted components of Ly α emission [$F_{\text{Ly}\alpha}(\text{blue})/F_{\text{Ly}\alpha}(\text{red})$]. The integration windows used to compute the values in Table 3.2 are $F_{\text{Ly}\alpha}(\text{tot})$: $\theta_{\text{tran}} \leq 3$ arcsec and $-700 < \Delta v/(\text{km s}^{-1}) \leq 1000$; $F_{\text{Ly}\alpha}(\text{blue})$: $\theta_{\text{tran}} \leq 2.5$ arcsec and $-700 < \Delta v/(\text{km s}^{-1}) \leq 0$; $F_{\text{Ly}\alpha}(\text{red})$: $\theta_{\text{tran}} \leq 3$ arcsec and $0 < \Delta v/(\text{km s}^{-1}) \leq 1000$. Different integration windows were used for the two components in order to optimize the S/N of the integral; they were chosen based on the detected extent of each component in Figure 3.17, in both θ_{tran} and Δv .

Figure 3.22 examines whether or not there is a connection between major axis/minor axis asymmetry in Ly α flux and the overall Ly α halo properties mentioned above. For each pair of variables in Figure 3.22, we indicate the value of the Pearson coefficient (r) and the corresponding probability p that the observed data set could be drawn from an uncorrelated parent sample. We also performed a linear regression using Orthogonal Distance Regression (ODR) in *SciPy*, which accounts for the estimated uncertainty in both x- and y-variables. As can be seen from the figure, most of the Pearson tests show no significant correlation and linear regression yields slopes consistent with zero. However, the Pearson test for the relation between $F_{\text{major}}(\text{blue}) - F_{\text{minor}}(\text{blue})$ and $F_{\text{Ly}\alpha}(\text{tot})$ (middle left panel of Figure 3.22) yields $p = 0.02$, suggesting a marginally significant trend in which the asymmetry of the

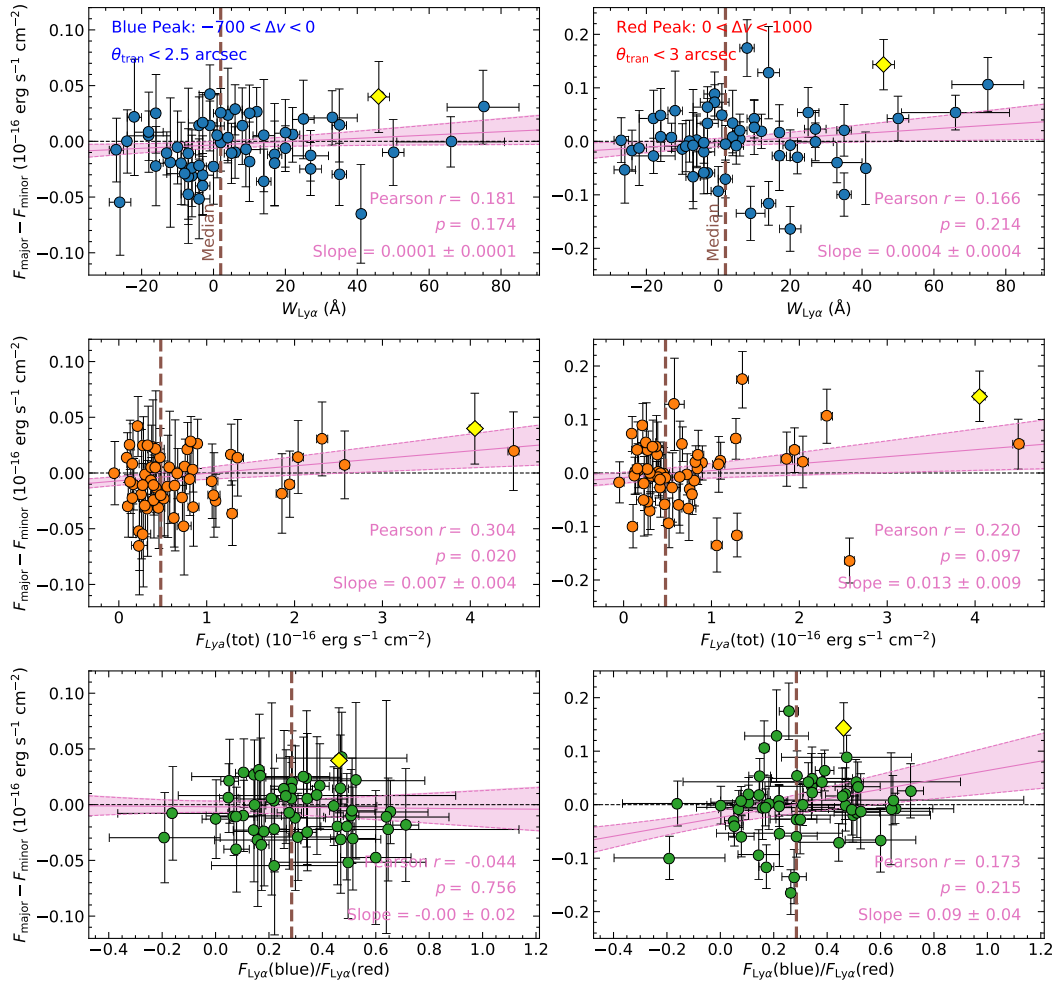


Figure 3.22: Relationship between the flux measurements of anisotropic (excess) Ly α emission ($\Delta F_{Ly\alpha} = F_{\text{major}} - F_{\text{minor}}$) of the blueshifted component (left) and redshifted component (right) of Ly α emission and properties of the integrated Ly α halo [Top: central Ly α equivalent width, $W_{\lambda}(Ly\alpha)$; Middle: total Ly α flux, $F_{Ly\alpha}(\text{tot})$; Bottom: the ratio between the total blueshifted and redshifted components, $F_{Ly\alpha}(\text{blue})/F_{Ly\alpha}(\text{red})$]. Galaxies without reliable F_{red} are omitted in the bottom panel since their $F_{Ly\alpha}(\text{blue})/F_{Ly\alpha}(\text{red})$ are dominated by noise. The pink lines and shaded regions show the results and their 1σ uncertainties of a linear regression accounting for the errors in both x- and y-directions. The vertical dashed line in each panel marks the median value of the (x-axis) property for the full sample. The yellow diamond in each panel marks the location of Q2343-BX418, the outlier that caused the excess emission of the redshifted peak along the galaxy major axis as discussed in §3.5.

blueshifted component of Ly α favors the minor axis when $F_{\text{Ly}\alpha}(\text{tot})$ is weak, and the major axis when $F_{\text{Ly}\alpha}(\text{tot})$ is strong.

The second relationship that stands out is $F_{\text{major}}(\text{red}) - F_{\text{minor}}(\text{red})$ and $F_{\text{Ly}\alpha}(\text{blue}) / F_{\text{Ly}\alpha}(\text{red})$ (bottom right panel of Figure 3.22), where a non-parametric test for correlation is not significant. The linear regression results in a marginally-significant positive slope, indicating that as the blueshifted component of Ly α approaches the strength of the redshifted component, there is a tendency for excess emission along the major axis; for galaxies with $F_{\text{Ly}\alpha}(\text{blue})/F_{\text{Ly}\alpha}(\text{red}) \lesssim 0.3$ (i.e., smaller than the median value for the sample), the tendency is for excess Ly α emission along the minor axis.

To further explore the reliability of the correlations, we split the sample in two halves according to the overall halo properties, and compared the subtracted CP2D spectra between the major and minor axes. Figure 3.23 shows the result. As discussed in §3.5, the excess Ly α emission along the galaxy major axis for the red peak at $\Delta v \simeq 300 \text{ km s}^{-1}$ within $\theta_{\text{tran}} \lesssim 1 \text{ arcsec}$ can be attributed to a single outlier (Q2343-BX418), which happens to fall above the median in all 3 quantities considered in Figure 3.23 (i.e., on the righthand panels of the figure). The subtracted CP2D spectra also indicate that essentially the entire excess Ly α emission for the blue peak along the minor axis – as identified earlier (§3.5) – is contributed by galaxies below the median $W_{\lambda}(\text{Ly}\alpha)$ and $F_{\text{Ly}\alpha}(\text{tot})$ (top and middle lefthand panels of Figure 3.23). In particular, the integrated significance within $-700 < \Delta v / (\text{ km s}^{-1}) \leq -200$ and $\theta_{\text{tran}} \leq 2''.5$ exceeds 2.5σ for the $W_{\lambda}(\text{Ly}\alpha) < \text{Median}$ bin. Comparison of the top two panels also illustrate the same trend of $F_{\text{major}}(\text{blue}) - F_{\text{minor}}(\text{blue})$ vs. $W_{\lambda}(\text{Ly}\alpha)$ and $F_{\text{Ly}\alpha}$ correlations suggested by Figure 3.22.

For the subsamples divided based on the value of $F_{\text{Ly}\alpha}(\text{blue})/F_{\text{Ly}\alpha}(\text{red})$, the differences between the major axis and minor axis range of azimuthal angle are less significant: there is a marginally significant excess of Ly α emission, more noticeable in the redshifted component, where it appears to extend over the range $\theta_{\text{tran}} \simeq 1 - 3 \text{ arcsec}$, and the bin with higher $F_{\text{Ly}\alpha}(\text{blue})/F_{\text{Ly}\alpha}(\text{red})$ appears to have a major axis excess over approximately the same range of angular distances. If Q2343-BX418 is removed from the stack of larger $F_{\text{Ly}\alpha}(\text{blue})/F_{\text{Ly}\alpha}(\text{red})$ galaxies, the residual remains, showing that it is not attributable to a single outlier. However, none of the residuals in the bottom panels of Figure 3.23 reaches a threshold of 2σ per resolution element.

In summary, a small statistical azimuthal asymmetry of Ly α halos persists when

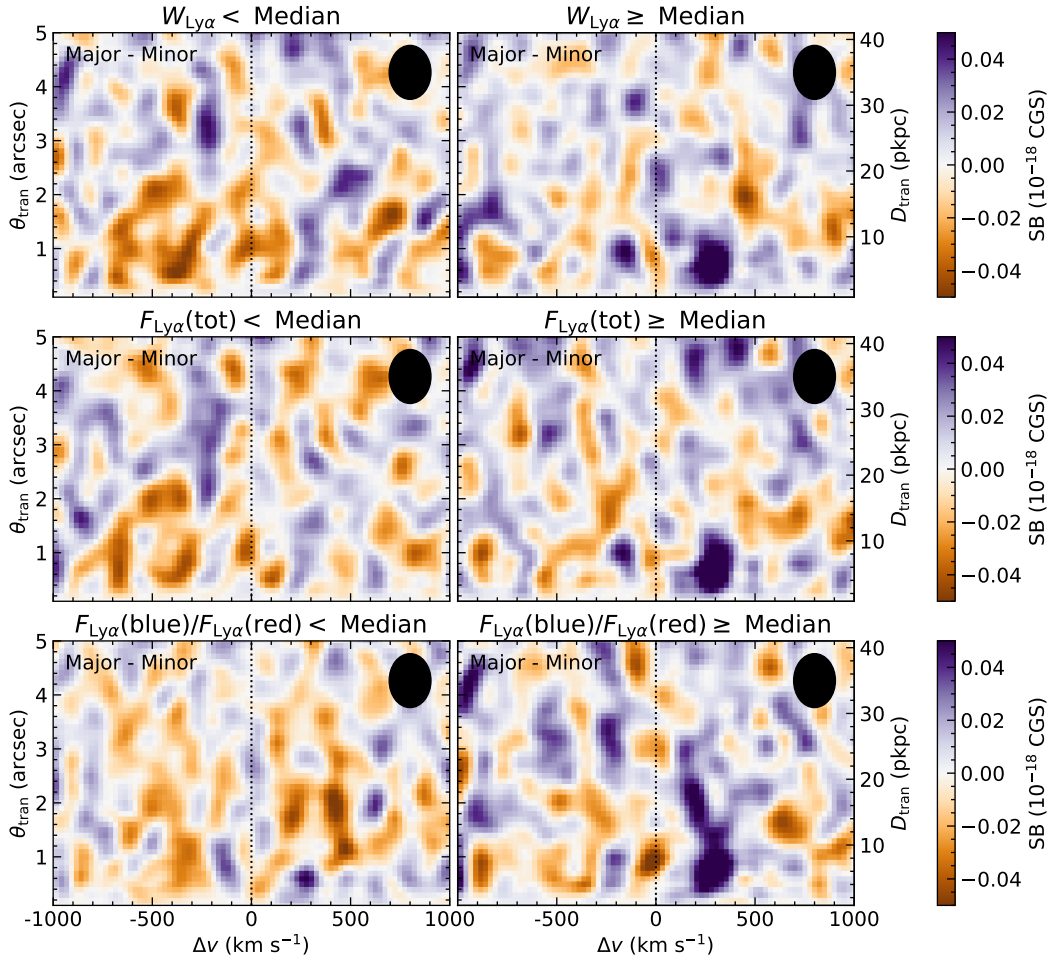


Figure 3.23: The difference between the CP2D spectra of Ly α emission for the major and minor axes. The maps show the residual for CP2D stacks for two sub-samples representing those below (left) and above (right) the sample median. From top to bottom, the Ly α halo properties are the central Ly α equivalent width ($W_{\lambda}(\text{Ly}\alpha)$), the integrated Ly α flux ($F_{\text{Ly}\alpha}(\text{tot})$), and the flux ratio between the blueshifted and redshifted components ($F_{\text{Ly}\alpha}(\text{blue})/F_{\text{Ly}\alpha}(\text{red})$). This figure confirms that the blueshifted excess Ly α emission favours weak Ly α emitting galaxies.

the galaxy sample is divided into two according to central $W_\lambda(\text{Ly}\alpha)$, total $F_{\text{Ly}\alpha}$, and the flux ratio of blueshifted and redshifted emission. Perhaps most intriguing is that galaxies with small or negative central $W_\lambda(\text{Ly}\alpha)$ have a tendency to exhibit excess $\text{Ly}\alpha$ emission along galaxy minor axes extending over a fairly large range of both θ_{tran} and velocity ($-700 < (\Delta v / \text{km s}^{-1}) < -200$). The apparent excess along the major axis of redshifted $\text{Ly}\alpha$ for the subsample with stronger $\text{Ly}\alpha$ emission and larger $F_{\text{Ly}\alpha}(\text{blue})/F_{\text{Ly}\alpha}(\text{red})$, on the other hand, is confined to a smaller range of (redshifted) velocities, again roughly coincident with the typical location of the “red peak”.

3.7 Finer Division of Galaxy Azimuthal Angles

At lower redshifts ($z < 1$), the covering fraction and column density of gas in various ionisation stages are commonly found to be related to the orientation of the gaseous disk relative to the line of sight. Many authors have used background QSO or galaxy sightlines to detect strong Mg II absorbers associated with galaxies at redshifts to allow the foreground galaxy orientations to be measured (e.g., Steidel et al., 2002; Bordoloi et al., 2011; Bouché et al., 2012; Schroetter et al., 2019; Lundgren et al., 2021). A common conclusion is that the sightlines giving rise to strong absorption tend to be those located at azimuthal angles corresponding to both the galaxy major and minor axes, but fewer (strong) absorbers are found at intermediate angles, $30^\circ < \phi < 60^\circ$. The kinematics of the absorbing gas also appear to be related to ϕ (e.g., Ho et al., 2017; Martin et al., 2019), with the broadest (and therefore strongest) systems found along the minor axis, presumably due to fast bi-conical outflows oriented perpendicular to the disk, followed by major axis sightlines sampling accreting or galactic fountain gas sharing the halo’s angular momentum and thus exhibiting disk-like rotation.

If the $\text{Ly}\alpha$ emission around $z = 2\text{--}3$ galaxies arises in CGM gas with properties similar to that of the low-ionization metallic absorbers at lower redshift, one might expect to see similar evidence for asymmetries along the two principal axes relative to intermediate azimuthal angles. We tested this possibility by expanding our analysis in §3.5 by dividing ϕ into three azimuthal bins – major axis ($0^\circ \leq \phi < 30^\circ$), minor axis ($60^\circ \leq \phi \leq 90^\circ$), and intermediate ($30^\circ \leq \phi \leq 60^\circ$). CP2D difference spectra among these 3 bins are shown in Figure 3.24.

Figure 3.24 shows no obvious sign of a bimodal distribution of $\text{Ly}\alpha$ emission with respect to ϕ , in which case the middle and right panels would show residuals of op-

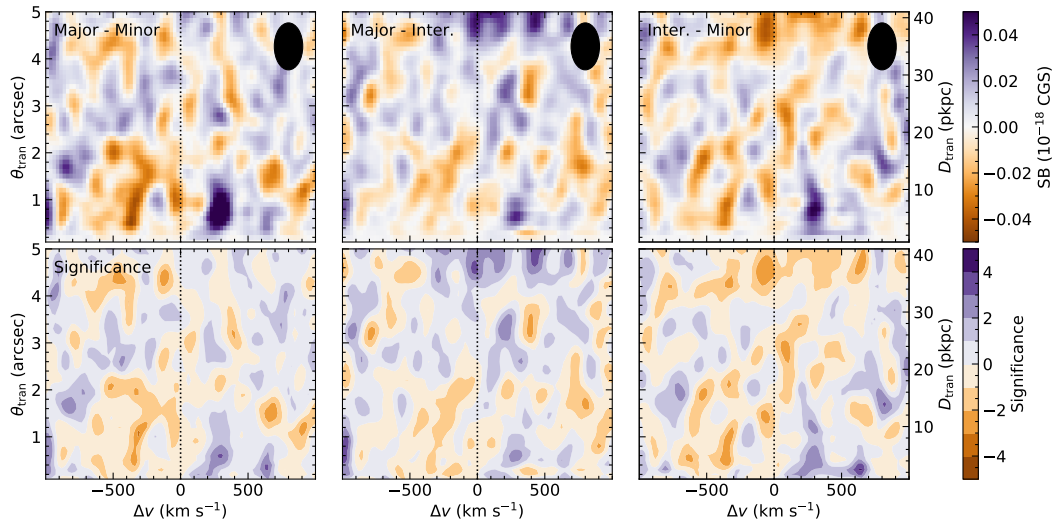


Figure 3.24: Similar to the right panel of Figure 3.15, but residual maps are between the major and minor (left), major and intermediate (middle), and intermediate and minor (right) axes with each bin size of only $\Delta\phi = 30^\circ$. The strong residual beyond $\theta_{\text{tran}} > 4$ arcsec is caused by a contaminating source near a single object. No sign of a bimodal distribution of Ly α emission is present. The sample in this figure is the same as in Figure 3.17. (Q0142-BX165: discarded; Q2343-BX418: included).

posite sign. Instead, the residual maps of “Major –Intermediate” and “Intermediate – Minor” suggest a gradual transition of the small asymmetries between major and minor axes in the larger bins of ϕ shown previously.

In any case, the main conclusion to draw from Figure 3.24 is once again that Ly α emission halos are remarkably similar in all directions with respect to the projected principal axes of $z \sim 2 - 3$ galaxies.

3.8 Discussion

Comparison to Previous Work

The morphology of Ly α emission from the CGM and its relation to the host galaxies has been analysed in various works between $z = 0$ and $z \lesssim 4$. However, analyses quantifying the Ly α emission with respect to the host-galaxy orientation is limited. In this section, we attempt to compare the existing research on Ly α halo morphology with our findings.

At very low redshifts ($z = 0.02 - 0.2$), Guaita et al. (2015) studied the Ly α halos of 14 Ly α -emitting galaxies in the Lyman Alpha Reference Sample (LARS; Östlin et al., 2014) and their connection to the host-galaxy morphologies. They found

that the Ly α halos for the subset of the sample that would be considered LAEs are largely axisymmetric, and there is no single galaxy morphological property that can be easily connected to the overall shape of the Ly α emitting regions. Indeed, the Ly α images of the individual galaxies in Hayes et al. (2014) appear to be independent of galaxy orientation beyond $D_{\text{tran}} \sim 2$ pkpc. Meanwhile, the stacked Ly α image of the LARS galaxies is elongated in the same direction as the far-UV continuum, i.e., along the major axis. However, this stack could be significantly affected by sample variance from galaxies that are particularly bright in rest-UV and Ly α , as we saw for the KBSS sample before removing outliers. Interestingly, Duval et al. (2016) studied a special galaxy in the LARS sample which is almost perfectly edge-on – they found two small Ly α emitting components (each of extent < 1 pkpc) near the disk consistent with Ly α emission escaping from the ISM through “holes” in the galactic disk, akin to that expected in a classical Galactic fountain (Bregman, 1980). While this is likely to be driven by stellar feedback allowing Ly α to escape in the direction perpendicular to the galaxy disk, the observed Ly α features are far closer to the galaxy than could be measured in our $z \sim 2 - 3$ sample. Moreover, most of the galaxies in our sample do not have organized thin disks, and so likely have much lower dust column densities obscuring active star forming regions.

At $z > 3$, Bacon et al. (2017) (and subsequent papers from the same group) conducted a systematic survey of Ly α emitting galaxies in the Hubble Ultra Deep Field using VLT/MUSE. For example, Leclercq et al. (2017) found significant variation of Ly α halo morphology among 145 galaxies, and identified correlations between the halo size and the size and brightness of the galaxy UV continuum. However, its connection with the galaxy morphological orientation remain to be investigated.

Meanwhile, Chen et al. (2020a) examined a case of a strongly-lensed pair of galaxies with extended Ly α emission at $z > 3$. The continuum image in the reconstructed source plane of their system A has at least three subcomponents extending over > 1 arcsec, which may be similar to the subsample of galaxies shown in our Figure 3.6, in terms of morphological complexity. In the context of the analysis we describe in the present work, this arrangement of Ly α with respect to continuum emission would be classified as excess minor axis Ly α emission. Unfortunately, the Ly α halo of a second $z > 3$ system is truncated in the source plane reconstruction.

In summary, we compared our result with galaxies and their Ly α emission morphology at $z \sim 0$ and $z > 3$ in previous work, finding that although our results are qualitatively consistent with earlier results, the comparison is hampered by limited

sample sizes, as well as by differences in redshift and intrinsic galaxy properties represented in each sample.

Theoretical Predictions

Many existing studies of the distribution and kinematics of CGM gas have focused on simulated galaxies within cosmological hydrodynamic simulations. Péroux et al. (2020) analysed how inflowing and outflowing gas might distribute differently as a function of the galactic azimuthal angle within the EAGLE and IllustrisTNG simulations, finding significant angular dependence of the flow rate and direction, as well as the CGM metallicity, with outflows of higher metallicity gas favoring the galaxy minor axis, and accretion of more metal-poor gas tending to occur along the major axis, at $z < 1$. Although Péroux et al. (2020) focused on $z \sim 0.5$ for their study, they made clear that the predicted trends would weaken significantly with increasing redshift.

At much higher redshifts ($z = 5 - 7$) around galaxies in the FIRE suite of simulations, Smith et al. (2019) found that Ly α escape is highly correlated with the direction of the H I outflow. Naively, one might expect that more Ly α would be found along the galaxy minor axis, which is the direction along which gaseous outflows would encounter the least resistance to propagation to large galactocentric radii. However, the galaxies experiencing the most active star formation at these redshifts tend to be altered on short timescales ($\sim 10^7$ yrs) by episodic accretion, star formation, and feedback events. Thus, the direction of outflows may change on similar timescales, while the CGM will evolve on a longer timescale, possibly erasing any clear signatures of alignment of outflows and Ly α emission. For the same reason, rapidly star-forming galaxies at $z \sim 2 - 3$, most of which have not yet established stable stellar disks, are likely to be surrounded by gas that is similarly turbulent and disordered.

Meanwhile, analytic or semi-analytic models of Ly α resonant scattering for idealised outflow geometries have focused primarily on the integrated Ly α emission profile from the entire galaxy or Ly α halo. Although many models account for the impact of the geometry and kinematics of gaseous outflows or accretion on the integrated Ly α emission profiles, there have been fewer efforts to predict the two-dimensional spatial and spectral profiles for detailed comparison to IFU observations.

For example, Carr et al. (2018) constructed a model to predict the Ly α spectral morphology assuming biconical H I outflows with resonant scattering. The model

predicts the integrated spectral profile without spatial information. In the context of the biconical outflow model, an integrated profile resembling our observation is predicted when the minor axis is perpendicular to the line of sight, with a large outflow having a small opening angle. However, this particular configuration would likely give rise to a highly asymmetric *spatial* distribution of Ly α emission, which we have shown is unlikely to be consistent with our observations.

Our results highlight the need for 3-D models of the cool gas in the CGM around rapidly-star-forming galaxies at high redshifts, prior to the development of stable disk configuration, for which the assumption of axisymmetry of outflows, at least on average, may be closer to reality. In any case, predicting the spatial and spectral properties of Ly α emission will require realistic treatment of the kinematics, small-scale structure, and radiative transfer of Ly α photons from the sites of production to their escape last scattering from the CGM toward an observer.

Gronke et al. (2016) has devised a model that assumes a two-phase CGM, composed of optically-thick clumps embedded in a highly-ionised diffuse “inter-clump” medium. This method has been used to fit the Ly α profiles at multiple locations within a spatially-resolved “Ly α blob” at $z \approx 3.1$ (LAB) (Li et al., 2020). More recently, Li et al., in prep, have shown that the clumpy outflow models can be applied successfully to fit multiple regions within a spatially resolved Ly α halo simultaneously, i.e., using a central source producing Ly α which then propagates through a clumpy medium with an axisymmetric outflow (see also Steidel et al., 2011, who showed that Ly α emission halos similar in extent to those presented in this paper are predicted naturally given the observed velocity fields of outflows viewed “down the barrel” to the galaxy center and the same radial dependence of clump covering fraction inferred from absorption line studies of background objects).

Implications for H I kinematics and Ly α Radiative Transfer

A spectral profile with a dominant redshifted component of Ly α emission line and a weaker blueshifted component – with peaks shifted by similar $|\Delta v|$ relative to the systemic redshift – is a typical signature of an expanding geometry, a central Ly α source function, and resonant scattering. It has also been shown that, for an ensemble of galaxies also drawn from the same KBSS redshift survey, the mean Ly α absorption signature measured in the spectra of background objects within $D_{\text{tran}} \lesssim 50$ pkpc ($\theta_{\text{tran}} \lesssim 6''$) are outflow-dominated (Chen et al., 2020b). However, although the observed Ly α halos and their dependence on galaxy properties may

be naturally explained by central Ly α sources scattering through the CGM, many authors have emphasized that collisionally-excited Ly α emission from accreting gas (i.e., gravitational cooling – see, e.g., Faucher-Giguère et al., 2010; Goerdt et al., 2010; Lake et al., 2015) and *in situ* photoionization by the UV background and/or local sources of ionizing photons (e.g., Leclercq et al., 2020) may also contribute significantly to extended Ly α halos.

Due to the complex nature of Ly α radiative transfer, our results cannot resolve this issue definitively. However, the fact that the stacked CP2D Ly α spectra show asymmetry of $< 2\%$ between the major and minor axis for the ensemble, combined with (1) the empirical correlation between the central Ly α line strength ($W_\lambda(\text{Ly}\alpha)$) and the Ly α flux integrated within the entire halo, and (2) the consistently red-peak-dominated kinematics of both the central and integrated Ly α line, all favor scattering of Ly α photons produced near the galaxy center through an outflowing, clumpy medium – at least within $D_{\text{tran}} \lesssim 30$ pkpc. The remarkable statistical symmetry of the full 2D profiles, both spatially and spectrally, suggests that most of the galaxies in our sample lack persistent disk-like configurations, an inference supported also by the ubiquity of blue-shifted absorption profiles in DTB spectra of similar galaxies and their lack of dependence on HST morphology (Law et al., 2012c; Law et al., 2012a). As a consequence, outflows do not behave in the manner expected for central starbursts in disk galaxies; in other words, $z \sim 2 - 3$ galaxies on average appear to be more axisymmetric than their lower-redshift counterparts. This may have important implications for the cycling of gas and metals into and out of forming galaxies.

On the other hand, we have detected marginal (2σ) excess Ly α emission along the galaxy major axis for the red peak, and along the galaxy minor axis for the blue peak. While most of the excess emission along the major axis can be easily explained by the relatively small sample size and the presence of one or two extreme cases, the excess blueshifted emission along the galaxy minor axis cannot be. While it is possible that the observed asymmetries indicate the prevalence of outflows along the major axis and inflows along the minor axis (i.e., the opposite of the behavior of galaxies at $z < 1$), we regard such an interpretation as unlikely. An important clue may be that most of the blueshifted, minor-axis excess is contributed by galaxies with weaker than the median Ly α emission strength – many in that subset have central $W_\lambda(\text{Ly}\alpha) < 0$, meaning that Ly α photons must scatter from higher-velocity material or in directions with a more porous distribution of optically thick gas to have

a high probability of escaping. Since we can only observe the photons that escape, galaxies with lower overall Ly α escape fractions will mean that those that do escape must take more extreme paths on average. As shown in §3.6, the galaxies with relatively weak emission also tend to have lower values of $F_{\text{Ly}\alpha}(\text{blue})/F_{\text{Ly}\alpha}(\text{red})$, which makes smaller absolute differences in emission strength vs. azimuthal angle more noticeable.

Finally, we would like to emphasise the fact that the lack of a strong statistical correlation between the morphology of extended Ly α emission and the galaxy orientation does *not* imply that the individual Ly α halos are symmetric. In fact, as shown in Figures 3.16, 3.19, and 3.22, individual Ly α halos are often asymmetric, particularly for objects with weak central Ly α emission. Rather, our results indicate that morphological variations of Ly α halos are uncorrelated with the apparent orientation of the host galaxy starlight.

3.9 Summary

In this paper, we have presented the first statistical results of an IFU survey of star-forming galaxies at $\langle z \rangle = 2.43$ drawn from the Keck Baryonic Structure Survey and observed with the Keck Cosmic Web Imager on the Keck 2 telescope. The 59 galaxies, with stellar mass and SFR typical of the full KBSS galaxy sample, comprise the subset of the KBSS-KCWI survey with both deep KCWI observations (typical exposure times of ~ 5 hours) and existing high-spatial-resolution images from Hubble Space Telescope and/or Keck/OSIRIS. The high resolution images were used to determine the direction of the projected major axis of the stellar continuum light of each galaxy; the KCWI IFU data cubes were used to detect spatially- and spectrally-resolved Ly α emission from the CGM around each galaxy to a limiting surface brightness of $\lesssim 1 \times 10^{-19}$ ergs s $^{-1}$ cm $^{-2}$ arcsec $^{-2}$ in the composite data (Figure 3.13), enabling detection of diffuse Ly α emission halos to projected distances of $\theta_{\text{tran}} \simeq 4''$ ($D_{\text{tran}} \simeq 30$ pkpc).

Our major findings are summarized below:

1. We introduced “cylindrically projected 2D spectra” (CP2D) in order to visualize and quantify Ly α spectra as a function of projected galactocentric distance D_{tran} . The CP2D spectra are averages of spaxels over a specified range of azimuthal angle (ϕ) at a common galactocentric distance, enabling statistical analyses of Ly α spectral profiles and their spatial varia-

tion simultaneously. The CP2D spectra clearly show distinct redshifted and blueshifted components of Ly α emission that remain distinct out to projected distances of at least 25 pkpc, with rest-frame velocity extending from $-700 \leq (\Delta v_{\text{sys}} / \text{km s}^{-1}) \lesssim 1000$ with respect to the galaxy systemic redshift, with blue and red peaks at $\simeq -300 \text{ km s}^{-1}$ and $\simeq +300 \text{ km s}^{-1}$, respectively. (§3.5)

2. We stacked the CP2D spectra of individual galaxies after aligning their continuum major axes, in bins of azimuthal angle ϕ measured with respect to the major axis. By creating difference images of the CP2D projections in independent ranges of ϕ , we showed that residual differences between “major axis” and “minor axis” – which would reflect asymmetries in either the spatial or spectral dimension along different ranges of ϕ – are very small, with amplitude: $\lesssim 2 \times 10^{-20} \text{ erg s}^{-1} \text{ cm}^{-2} \text{ arcsec}^{-2} \text{ \AA}^{-1}$, corresponding to asymmetries in Ly α flux amounting to $\leq 2\%$ of the total, between galaxy major and minor axis directions. (§3.5)
3. We found little evidence of statistically significant asymmetry of the Ly α emission, except for an excess ($\simeq 2\sigma$) of Ly α emission along galaxy major axes for the redshifted component of Ly α emission, with a peak near $\sim +300 \text{ km s}^{-1}$. However, closer inspection revealed that most of the signal was caused by two galaxies with unusually asymmetric Ly α halos. After discarding these outliers, another excess emission feature, with integrated significance $\simeq 2\sigma$, manifests as excess emission in the *blueshifted* component of Ly α along galaxy *minor* axes. This feature extends over a large range of velocity, and appears to be contributed primarily by galaxies with weaker than the sample median Ly α emission, and central Ly α equivalent width $W_\lambda(\text{Ly}\alpha) < 0$. The same weak-Ly α subsample includes many of highest M_* galaxies in the sample, as well as many of the galaxies with the smallest flux ratio between blueshifted and redshifted components ($F_{\text{Ly}\alpha}(\text{blue})/F_{\text{Ly}\alpha}(\text{red})$). We speculate that this asymmetry may indicate that significant azimuthal variation of Ly α emission morphology exists only for galaxies with the smallest Ly α escape fractions within the sample, i.e., weaker Ly α emitting galaxies possess more developed rotational structure. Evidently, one sees only the photons managing to find rare low- N_{HI} holes or that scatter from the highest velocity material, both of which are more likely along the minor axis (i.e., similar to expectations based on the standard picture of biconical starburst-driven outflows from disk-like

systems). (§3.5, §3.6)

4. Taken together, the results show that, statistically, the Ly α halo around galaxies in this sample (and, by extension, the population of relatively massive star-forming galaxies at $z \sim 2 - 3$) have remarkably little correlation – either kinematically or spatially – with the morphological distribution of stellar continuum light of the host galaxy. The observations suggest that most of the galaxies do not conform to expectations in which outflows are bi-conical and oriented along the minor axis of disk-like configurations, with accretion occurring preferentially along the major axis, suggested by observations of CGM gas in star-forming galaxies with $z < 1$. Instead, the lack of systematic variation in the kinematics and spatial extent with azimuthal angle of Ly α emission, together with the fact that $F_{\text{Ly}\alpha}(\text{blue})/F_{\text{Ly}\alpha}(\text{red})$ is universally smaller than unity, suggests that the bulk of Ly α at galactocentric distances $\lesssim 30$ pkpc is scattered from the inside out. The vast majority of scattered photons propagate through a scattering medium whose kinematics are dominated by outflows that statistically symmetric with respect to the apparent morphology of a galaxy’s starlight. (§3.8)

This paper marks the first attempt to understand the relationship between Ly α emission in the CGM and its host-galaxy properties in the KBSS-KCWI sample. As the central DTB Ly α emission was shown to be correlated with the host galaxy properties for the KBSS galaxies (e.g., Trainor et al., 2015; Trainor et al., 2016; Trainor et al., 2019), in forthcoming work, we will utilize the CP2D spectra to further investigate the connection between the Ly α halo and observable properties of the host galaxies (e.g., stellar mass, star-formation rate, star-formation rate surface density, etc.), to understand whether galaxies at $z = 2 - 3$ significantly impact the H I distribution in the CGM and *vice versa*, and to place additional constraints on the source functions and radiative transfer of Ly α in forming galaxies. With increased sample size and improved data reduction processes, we are also pushing to higher sensitivity in the stacked spectral cubes that allow us to probe the Ly α spectrum at larger galactocentric distances with high fidelity.

Acknowledgements

This work has included data from Keck/KCWI (Morrissey et al., 2018), Keck/OSIRIS (Larkin et al., 2006), Keck/MOSFIRE (McLean et al., 2012), Keck/LRIS-B (Steidel

et al., 2004), HST/WFC3-IR and HST/ACS. We appreciate the contribution from the staff of the W. M. Keck Observatory and the Space Telescope Science Institute.

The following software packages have been crucial to the results presented: Astropy (Astropy Collaboration et al., 2018), the SciPy and NumPy system (Virtanen et al., 2020; Harris et al., 2020), QFitsView⁹, CWITools (O’Sullivan and Chen, 2020), Montage¹⁰, GALFIT (Peng et al., 2002; Peng et al., 2010), and DrizzlePac¹¹.

This work has been supported in part by grant AST-2009278 from the US NSF, by NASA through grant HST-GO15287.001, and the JPL/Caltech President’s and Director’s Program (YC, CS).

The authors wish to recognize and acknowledge the very significant cultural role and reverence that the summit of Maunakea has always had within the indigenous Hawaiian community. We are most fortunate to have the opportunity to conduct observations from this mountain. We would like to thank the anonymous referee for providing constructive feedback. We would like to acknowledge Kurt Adelberger, Milan Bogosavljević, Max Pettini, and Rachel Theios for their contribution to the KBSS survey. It is a great pleasure for us to thank Don Neill, Mateusz Matuszewski, Luca Rizzi, Donal O’Sullivan, and Sebastiano Cantalupo for their help in handling the KCWI data, and Cameron Hummels and Max Gronke for insightful discussions. YC would like to acknowledge his grandfather, Chen Yizong, who passed away during the preparation of this manuscript.

Data Availability

The composite CP2D spectra and the Python program used to generate figures in this article are available upon reasonable request.

References

- Ao, Yiping et al. (Mar. 2020). “Infalling gas in a Lyman- α blob”. *Nature Astronomy* 4, pp. 670–674. DOI: 10.1038/s41550-020-1033-3. arXiv: 2003.06099 [astro-ph.GA].
- Astropy Collaboration et al. (Sept. 2018). “The Astropy Project: Building an Open-science Project and Status of the v2.0 Core Package”. *AJ* 156.3, 123, p. 123. DOI: 10.3847/1538-3881/aabc4f. arXiv: 1801.02634 [astro-ph.IM].

⁹<https://www.mpe.mpg.de/~ott/QFitsView/>

¹⁰<http://montage.ipac.caltech.edu/>

¹¹<https://www.stsci.edu/scientific-community/software/drizzlepac.html>

- Bacon, R. et al. (July 2010). “The MUSE second-generation VLT instrument”. *Ground-based and Airborne Instrumentation for Astronomy III*. Ed. by Ian S. McLean, Suzanne K. Ramsay, and Hideki Takami. Vol. 7735. Society of Photo-Optical Instrumentation Engineers (SPIE) Conference Series, p. 773508. DOI: 10.1117/12.856027.
- Bacon, Roland et al. (Dec. 2017). “The MUSE Hubble Ultra Deep Field Survey. I. Survey description, data reduction, and source detection”. *A&A* 608, A1, A1. DOI: 10.1051/0004-6361/201730833. arXiv: 1710.03002 [astro-ph.GA].
- Bordoloi, R. et al. (Dec. 2011). “The Radial and Azimuthal Profiles of Mg II Absorption around $0.5 < z < 0.9$ zCOSMOS Galaxies of Different Colors, Masses, and Environments”. *ApJ* 743.1, 10, p. 10. DOI: 10.1088/0004-637X/743/1/10. arXiv: 1106.0616 [astro-ph.CO].
- Borisova, Elena et al. (Nov. 2016). “Ubiquitous Giant Ly α Nebulae around the Brightest Quasars at $z \sim 3.5$ Revealed with MUSE”. *ApJ* 831.1, 39, p. 39. DOI: 10.3847/0004-637X/831/1/39. arXiv: 1605.01422 [astro-ph.GA].
- Bouché, N. et al. (Oct. 2012). “Physical properties of galactic winds using background quasars”. *MNRAS* 426.2, pp. 801–815. DOI: 10.1111/j.1365-2966.2012.21114.x. arXiv: 1110.5877 [astro-ph.CO].
- Bregman, J. N. (Mar. 1980). “The galactic fountain of high-velocity clouds.” *ApJ* 236, pp. 577–591. DOI: 10.1086/157776.
- Bruzual, G. and S. Charlot (Oct. 2003). “Stellar population synthesis at the resolution of 2003”. *MNRAS* 344.4, pp. 1000–1028. DOI: 10.1046/j.1365-8711.2003.06897.x. arXiv: astro-ph/0309134 [astro-ph].
- Byrohl, Chris et al. (Sept. 2020). “The physical origins and dominant emission mechanisms of Lyman-alpha halos: results from the TNG50 simulation in comparison to MUSE observations”. *arXiv e-prints*, arXiv:2009.07283, arXiv:2009.07283. arXiv: 2009.07283 [astro-ph.GA].
- Cai, Zheng et al. (Dec. 2019). “Evolution of the Cool Gas in the Circumgalactic Medium of Massive Halos: A Keck Cosmic Web Imager Survey of Ly α Emission around QSOs at $z \approx 2$ ”. *ApJS* 245.2, 23, p. 23. DOI: 10.3847/1538-4365/ab4796. arXiv: 1909.11098 [astro-ph.GA].
- Calzetti, Daniela et al. (Apr. 2000). “The Dust Content and Opacity of Actively Star-forming Galaxies”. *ApJ* 533.2, pp. 682–695. DOI: 10.1086/308692. arXiv: astro-ph/9911459 [astro-ph].
- Cantalupo, Sebastiano, Fabrizio Arrigoni-Battaia, J. Xavier Prochaska, Joseph F. Hennawi, and Piero Madau (Feb. 2014). “A cosmic web filament revealed in Lyman- α emission around a luminous high-redshift quasar”. *Nature* 506.7486, pp. 63–66. DOI: 10.1038/nature12898. arXiv: 1401.4469 [astro-ph.CO].

- Carr, Cody, Claudia Scarlata, Nino Panagia, and Alaina Henry (June 2018). “A Semi-analytical Line Transfer (SALT) Model. II: The Effects of a Bi-conical Geometry”. *ApJ* 860.2, 143, p. 143. doi: 10.3847/1538-4357/aac48e. arXiv: 1805.05981 [astro-ph.GA].
- Chabrier, Gilles (Apr. 2003). “The Galactic Disk Mass Function: Reconciliation of the Hubble Space Telescope and Nearby Determinations”. *ApJ* 586.2, pp. L133–L136. doi: 10.1086/374879. arXiv: astro-ph/0302511 [astro-ph].
- Chen, Mandy C., Hsiao-Wen Chen, Max Gronke, Michael Rauch, and Tom Broadhurst (Dec. 2020a). “Resolved galactic superwinds reconstructed around their host galaxies at $z > 3$ ”. *arXiv e-prints*, arXiv:2012.03959, arXiv:2012.03959. arXiv: 2012.03959 [astro-ph.GA].
- Chen, Yuguang et al. (Dec. 2020b). “The Keck Baryonic Structure Survey: Using foreground/background galaxy pairs to trace the structure and kinematics of circumgalactic neutral hydrogen at $z \sim 2$ ”. *MNRAS* 499.2, pp. 1721–1746. doi: 10.1093/mnras/staa2808. arXiv: 2006.13236 [astro-ph.GA].
- Claeysens, A. et al. (Nov. 2019). “Spectral variations of Lyman α emission within strongly lensed sources observed with MUSE”. *MNRAS* 489.4, pp. 5022–5029. doi: 10.1093/mnras/stz2492. arXiv: 1909.01692 [astro-ph.GA].
- Dijkstra, Mark (Oct. 2014). “Ly α Emitting Galaxies as a Probe of Reionisation”. *Publ. Astron. Soc. Australia* 31, e040, e040. doi: 10.1017/pasa.2014.33. arXiv: 1406.7292 [astro-ph.CO].
- Duval, Florent et al. (Mar. 2016). “The Lyman alpha reference sample. VI. Lyman alpha escape from the edge-on disk galaxy Mrk 1486”. *A&A* 587, A77, A77. doi: 10.1051/0004-6361/201526876. arXiv: 1512.00860 [astro-ph.GA].
- Erb, Dawn K., Charles C. Steidel, and Yuguang Chen (July 2018). “The Kinematics of Extended Ly α Emission in a Low-mass, Low-metallicity Galaxy at $z = 2.3$ ”. *ApJ* 862.1, L10, p. L10. doi: 10.3847/2041-8213/aacff6. arXiv: 1807.00065 [astro-ph.GA].
- Erb, Dawn K., Charles C. Steidel, Alice E. Shapley, Max Pettini, and Kurt L. Adelberger (Sept. 2004). “The Kinematics of Morphologically Selected $z \sim 2$ Galaxies in the GOODS-North Field”. *ApJ* 612.1, pp. 122–130. doi: 10.1086/422464. arXiv: astro-ph/0404235 [astro-ph].
- Faucher-Giguère, Claude-André, Dušan Kereš, Mark Dijkstra, Lars Hernquist, and Matias Zaldarriaga (Dec. 2010). “Ly α Cooling Emission from Galaxy Formation”. *ApJ* 725.1, pp. 633–657. doi: 10.1088/0004-637X/725/1/633. arXiv: 1005.3041 [astro-ph.CO].
- Förster Schreiber, N. M. et al. (Dec. 2009). “The SINS Survey: SINFONI Integral Field Spectroscopy of $z \sim 2$ Star-forming Galaxies”. *ApJ* 706.2, pp. 1364–1428. doi: 10.1088/0004-637X/706/2/1364. arXiv: 0903.1872 [astro-ph.CO].

- Förster Schreiber, N. M. et al. (Oct. 2018). “The SINS/zC-SINF Survey of $z \sim 2$ Galaxy Kinematics: SINFONI Adaptive Optics-assisted Data and Kiloparsec-scale Emission-line Properties”. *ApJS* 238.2, 21, p. 21. DOI: 10.3847/1538-4365/aadd49. arXiv: 1802.07276 [astro-ph.GA].
- Goerdt, Tobias et al. (Sept. 2010). “Gravity-driven Ly α blobs from cold streams into galaxies”. *MNRAS* 407.1, pp. 613–631. DOI: 10.1111/j.1365-2966.2010.16941.x. arXiv: 0911.5566 [astro-ph.CO].
- Gronke, M. and M. Dijkstra (July 2016). “Lyman- α Spectra from Multiphase Outflows, and their Connection to Shell Models”. *ApJ* 826.1, 14, p. 14. DOI: 10.3847/0004-637X/826/1/14. arXiv: 1604.06805 [astro-ph.GA].
- Gronke, Max (Dec. 2017). “Modeling 237 Lyman- α spectra of the MUSE-Wide survey”. *A&A* 608, A139, A139. DOI: 10.1051/0004-6361/201731791. arXiv: 1709.07008 [astro-ph.GA].
- Gronke, Max, Mark Dijkstra, Michael McCourt, and S. Peng Oh (Dec. 2016). “From Mirrors to Windows: Lyman-alpha Radiative Transfer in a Very Clumpy Medium”. *ApJ* 833.2, L26, p. L26. DOI: 10.3847/2041-8213/833/2/L26. arXiv: 1611.01161 [astro-ph.GA].
- Guaita, L. et al. (Apr. 2015). “The Lyman alpha reference sample. IV. Morphology at low and high redshift”. *A&A* 576, A51, A51. DOI: 10.1051/0004-6361/201425053. arXiv: 1501.02387 [astro-ph.GA].
- Harris, Charles R. et al. (Sept. 2020). “Array programming with NumPy”. *Nature* 585.7825, pp. 357–362. DOI: 10.1038/s41586-020-2649-2. arXiv: 2006.10256 [cs.MS].
- Hayes, Matthew et al. (Feb. 2014). “The Lyman Alpha Reference Sample. II. Hubble Space Telescope Imaging Results, Integrated Properties, and Trends”. *ApJ* 782.1, 6, p. 6. DOI: 10.1088/0004-637X/782/1/6. arXiv: 1308.6578 [astro-ph.CO].
- Ho, Stephanie H., Crystal L. Martin, Glenn G. Kacprzak, and Christopher W. Churchill (Feb. 2017). “Quasars Probing Galaxies. I. Signatures of Gas Accretion at Redshift Approximately 0.2”. *ApJ* 835.2, 267, p. 267. DOI: 10.3847/1538-4357/835/2/267. arXiv: 1611.04579 [astro-ph.GA].
- Jones, Tucker, Daniel P. Stark, and Richard S. Ellis (May 2012). “Keck Spectroscopy of Faint $3 < z < 7$ Lyman Break Galaxies. III. The Mean Ultraviolet Spectrum at $z \sim 4$ ”. *ApJ* 751.1, 51, p. 51. DOI: 10.1088/0004-637X/751/1/51. arXiv: 1111.5102 [astro-ph.CO].
- Kacprzak, Glenn G., Christopher W. Churchill, Jessica L. Evans, Michael T. Murphy, and Charles C. Steidel (Oct. 2011). “Morphological properties of $z \sim 0.5$ absorption-selected galaxies: the role of galaxy inclination”. *MNRAS* 416.4, pp. 3118–3137. DOI: 10.1111/j.1365-2966.2011.19261.x. arXiv: 1106.3068 [astro-ph.CO].

- Kacprzak, Glenn G., Christopher W. Churchill, and Nikole M. Nielsen (Nov. 2012). “Tracing Outflows and Accretion: A Bimodal Azimuthal Dependence of Mg II Absorption”. *ApJ* 760.1, L7, p. L7. DOI: 10.1088/2041-8205/760/1/L7. arXiv: 1205.0245 [astro-ph.CO].
- Kacprzak, Glenn G., Sowgat Muzahid, Christopher W. Churchill, Nikole M. Nielsen, and Jane C. Charlton (Dec. 2015). “The Azimuthal Dependence of Outflows and Accretion Detected Using O VI Absorption”. *ApJ* 815.1, 22, p. 22. DOI: 10.1088/0004-637X/815/1/22. arXiv: 1511.03275 [astro-ph.GA].
- Kakiichi, Koki and Mark Dijkstra (Nov. 2018). “A new model framework for circumgalactic Ly α radiative transfer constrained by galaxy-Ly α forest clustering”. *MNRAS* 480.4, pp. 5140–5159. DOI: 10.1093/mnras/sty2214. arXiv: 1710.10053 [astro-ph.GA].
- Kollmeier, Juna A. et al. (Jan. 2010). “Ly α Emission from Cosmic Structure. I. Fluorescence”. *ApJ* 708.2, pp. 1048–1075. DOI: 10.1088/0004-637X/708/2/1048. arXiv: 0907.0704 [astro-ph.CO].
- Kornei, Katherine A. et al. (Mar. 2010). “The Relationship between Stellar Populations and Ly α Emission in Lyman Break Galaxies”. *ApJ* 711.2, pp. 693–710. DOI: 10.1088/0004-637X/711/2/693. arXiv: 0911.2000 [astro-ph.CO].
- Kulas, Kristin R. et al. (Jan. 2012). “The Kinematics of Multiple-peaked Ly α Emission in Star-forming Galaxies at $z \sim 2-3$ ”. *ApJ* 745.1, 33, p. 33. DOI: 10.1088/0004-637X/745/1/33. arXiv: 1107.4367 [astro-ph.CO].
- Lake, Ethan et al. (June 2015). “On the Diffuse Ly α Halo around Ly α Emitting Galaxies”. *ApJ* 806.1, 46, p. 46. DOI: 10.1088/0004-637X/806/1/46. arXiv: 1502.01349 [astro-ph.CO].
- Lan, Ting-Wen and Houjun Mo (Oct. 2018). “The Circumgalactic Medium of eBOSS Emission Line Galaxies: Signatures of Galactic Outflows in Gas Distribution and Kinematics”. *ApJ* 866.1, 36, p. 36. DOI: 10.3847/1538-4357/aadc08. arXiv: 1806.05786 [astro-ph.GA].
- Larkin, James et al. (June 2006). “OSIRIS: a diffraction limited integral field spectrograph for Keck”. *Proc. SPIE*. Vol. 6269. Society of Photo-Optical Instrumentation Engineers (SPIE) Conference Series, 62691A. DOI: 10.1117/12.672061.
- Law, David R. et al. (Nov. 2007). “Integral Field Spectroscopy of High-Redshift Star-forming Galaxies with Laser-guided Adaptive Optics: Evidence for Dispersion-dominated Kinematics”. *ApJ* 669.2, pp. 929–946. DOI: 10.1086/521786. arXiv: 0707.3634 [astro-ph].
- Law, David R. et al. (June 2009). “The Kiloparsec-scale Kinematics of High-redshift Star-forming Galaxies”. *ApJ* 697.2, pp. 2057–2082. DOI: 10.1088/0004-637X/697/2/2057. arXiv: 0901.2930 [astro-ph.GA].

- Law, David R. et al. (Nov. 2012a). “A HST/WFC3-IR Morphological Survey of Galaxies at $z = 1.5$ -3.6. II. The Relation between Morphology and Gas-phase Kinematics”. *ApJ* 759.1, 29, p. 29. DOI: 10.1088/0004-637X/759/1/29. arXiv: 1206.6889 [astro-ph.CO].
- Law, David R. et al. (Jan. 2012b). “An HST/WFC3-IR Morphological Survey of Galaxies at $z = 1.5$ -3.6. I. Survey Description and Morphological Properties of Star-forming Galaxies”. *ApJ* 745.1, 85, p. 85. DOI: 10.1088/0004-637X/745/1/85. arXiv: 1107.3137 [astro-ph.CO].
- Law, David R. et al. (July 2012c). “High velocity dispersion in a rare grand-design spiral galaxy at redshift $z = 2.18$ ”. *Nature* 487.7407, pp. 338–340. DOI: 10.1038/nature11256. arXiv: 1207.4196 [astro-ph.CO].
- Law, David R. et al. (Oct. 2018). “Imaging Spectroscopy of Ionized Gaseous Nebulae around Optically Faint AGNs at Redshift $z \sim 2$ ”. *ApJ* 866.2, 119, p. 119. DOI: 10.3847/1538-4357/aae156. arXiv: 1809.04089 [astro-ph.GA].
- Leclercq, Floriane et al. (Dec. 2017). “The MUSE Hubble Ultra Deep Field Survey. VIII. Extended Lyman- α haloes around high- z star-forming galaxies”. *A&A* 608, A8, A8. DOI: 10.1051/0004-6361/201731480. arXiv: 1710.10271 [astro-ph.GA].
- Leclercq, Floriane et al. (Mar. 2020). “The MUSE Hubble Ultra Deep Field Survey. XIII. Spatially resolved spectral properties of Lyman α haloes around star-forming galaxies at $z > 3$ ”. *A&A* 635, A82, A82. DOI: 10.1051/0004-6361/201937339. arXiv: 2002.05731 [astro-ph.GA].
- Li, Zhihui, Charles C. Steidel, Max Gronke, and Yuguang Chen (Aug. 2020). “Revisiting the Gas Kinematics in SSA22 Lyman- α Blob 1 with Radiative Transfer Modeling in a Multiphase, Clumpy Medium”. *arXiv e-prints*, arXiv:2008.09130, arXiv:2008.09130. arXiv: 2008.09130 [astro-ph.GA].
- Lundgren, Britt F. et al. (Feb. 2021). “The Geometry of Cold, Metal-Enriched Gas Around Galaxies at $z \sim 1.2$ ”. *arXiv e-prints*, arXiv:2102.10117, arXiv:2102.10117. arXiv: 2102.10117 [astro-ph.GA].
- Martin, D. Christopher et al. (May 2014). “Intergalactic Medium Emission Observations with the Cosmic Web Imager. I. The Circum-QSO Medium of QSO 1549+19, and Evidence for a Filamentary Gas Inflow”. *ApJ* 786.2, 106, p. 106. DOI: 10.1088/0004-637X/786/2/106. arXiv: 1402.4816 [astro-ph.GA].
- Martin, D. Christopher et al. (June 2016). “A Newly Forming Cold Flow Protogalactic Disk, a Signature of Cold Accretion from the Cosmic Web”. *ApJ* 824.1, L5, p. L5. DOI: 10.3847/2041-8205/824/1/L5.
- Martin, D. Christopher et al. (July 2019). “Multi-filament gas inflows fuelling young star-forming galaxies”. *Nature Astronomy* 3, pp. 822–831. DOI: 10.1038/s41550-019-0791-2. arXiv: 1904.11465 [astro-ph.GA].

- Matsuda, Y. et al. (Sept. 2012). “Diffuse Ly α haloes around Ly α emitters at z=3: do dark matter distributions determine the Ly α spatial extents?”. *MNRAS* 425.2, pp. 878–883. DOI: 10.1111/j.1365-2966.2012.21143.x. arXiv: 1204.4934 [astro-ph.CO].
- Matthee, Jorjryt et al. (Feb. 2021). “The X-SHOOTER Lyman- α survey at z=2 (XLS-z2) I: the panchromatic spectrum of typical Lyman- α emitters”. *arXiv e-prints*, arXiv:2102.07779, arXiv:2102.07779. arXiv: 2102.07779 [astro-ph.GA].
- McLean, Ian S. et al. (Sept. 2012). “MOSFIRE, the multi-object spectrometer for infra-red exploration at the Keck Observatory”. *Ground-based and Airborne Instrumentation for Astronomy IV*. Ed. by Ian S. McLean, Suzanne K. Ramsay, and Hideki Takami. Vol. 8446. Society of Photo-Optical Instrumentation Engineers (SPIE) Conference Series, 84460J. DOI: 10.1117/12.924794.
- Momose, Rieko et al. (July 2014). “Diffuse Ly α haloes around galaxies at z = 2.2-6.6: implications for galaxy formation and cosmic reionization”. *MNRAS* 442.1, pp. 110–120. DOI: 10.1093/mnras/stu825. arXiv: 1403.0732 [astro-ph.CO].
- Morrissey, Patrick et al. (Sept. 2018). “The Keck Cosmic Web Imager Integral Field Spectrograph”. *ApJ* 864.1, 93, p. 93. DOI: 10.3847/1538-4357/aad597. arXiv: 1807.10356 [astro-ph.IM].
- Mostardi, R. E. et al. (Sept. 2015). “A High-Resolution Hubble Space Telescope Study of Apparent Lyman Continuum Leakers at z \sim 3”. *ApJ* 810.2, 107, p. 107. DOI: 10.1088/0004-637X/810/2/107. arXiv: 1506.08201 [astro-ph.GA].
- Nelson, Dylan et al. (Dec. 2019). “First results from the TNG50 simulation: galactic outflows driven by supernovae and black hole feedback”. *MNRAS* 490.3, pp. 3234–3261. DOI: 10.1093/mnras/stz2306. arXiv: 1902.05554 [astro-ph.GA].
- Nielsen, Nikole M., Christopher W. Churchill, Glenn G. Kacprzak, Michael T. Murphy, and Jessica L. Evans (Oct. 2015). “MAGIICAT V. Orientation of Outflows and Accretion Determine the Kinematics and Column Densities of the Circumgalactic Medium”. *ApJ* 812.1, 83, p. 83. DOI: 10.1088/0004-637X/812/1/83. arXiv: 1505.07167 [astro-ph.GA].
- Oke, J. B. et al. (Apr. 1995). “The Keck Low-Resolution Imaging Spectrometer”. *PASP* 107, p. 375. DOI: 10.1086/133562.
- Östlin, Göran et al. (Dec. 2014). “The Ly α Reference Sample. I. Survey Outline and First Results for Markarian 259”. *ApJ* 797.1, 11, p. 11. DOI: 10.1088/0004-637X/797/1/11. arXiv: 1409.8347 [astro-ph.GA].
- O’Sullivan, Donal and Yuguang Chen (Nov. 2020). “CWITools: A Python3 Data Analysis Pipeline for the Cosmic Web Imager Instruments”. *arXiv e-prints*, arXiv:2011.05444, arXiv:2011.05444. arXiv: 2011.05444 [astro-ph.IM].

- O’Sullivan, Donal B. et al. (May 2020). “The FLASHES Survey. I. Integral Field Spectroscopy of the CGM around 48 $z \simeq 2.3$ -3.1 QSOs”. *ApJ* 894.1, 3, p. 3. DOI: 10.3847/1538-4357/ab838c. arXiv: 1911.10740 [astro-ph.GA].
- Ouchi, Masami, Yoshiaki Ono, and Takatoshi Shibuya (Aug. 2020). “Observations of the Lyman- α Universe”. *ARA&A* 58, pp. 617–659. DOI: 10.1146/annurev-astro-032620-021859. arXiv: 2012.07960 [astro-ph.GA].
- Pahl, Anthony J., Alice Shapley, Charles C. Steidel, Yuguang Chen, and Naveen A. Reddy (Aug. 2021). “An uncontaminated measurement of the escaping Lyman continuum at $z \sim 3$ ”. *MNRAS* 505.2, pp. 2447–2467. DOI: 10.1093/mnras/stab1374. arXiv: 2104.02081 [astro-ph.GA].
- Partridge, R. B. and P. J. E. Peebles (Mar. 1967). “Are Young Galaxies Visible?” *ApJ* 147, p. 868. DOI: 10.1086/149079.
- Peng, Chien Y., Luis C. Ho, Chris D. Impey, and Hans-Walter Rix (July 2002). “Detailed Structural Decomposition of Galaxy Images”. *AJ* 124.1, pp. 266–293. DOI: 10.1086/340952. arXiv: astro-ph/0204182 [astro-ph].
- Peng, Chien Y., Luis C. Ho, Chris D. Impey, and Hans-Walter Rix (June 2010). “Detailed Decomposition of Galaxy Images. II. Beyond Axisymmetric Models”. *AJ* 139.6, pp. 2097–2129. DOI: 10.1088/0004-6256/139/6/2097. arXiv: 0912.0731 [astro-ph.CO].
- Péroux, Céline et al. (Dec. 2020). “Predictions for the angular dependence of gas mass flow rate and metallicity in the circumgalactic medium”. *MNRAS* 499.2, pp. 2462–2473. DOI: 10.1093/mnras/staa2888. arXiv: 2009.07809 [astro-ph.GA].
- Peter, Annika H. G. et al. (Oct. 2007). “Morphologies of Galaxies in and around a Protocluster at $z = 2.300$ ”. *ApJ* 668.1, pp. 23–44. DOI: 10.1086/521184. arXiv: 0706.2865 [astro-ph].
- Pettini, Max et al. (June 2001). “The Rest-Frame Optical Spectra of Lyman Break Galaxies: Star Formation, Extinction, Abundances, and Kinematics”. *ApJ* 554.2, pp. 981–1000. DOI: 10.1086/321403. arXiv: astro-ph/0102456 [astro-ph].
- Reddy, Naveen A. and Charles C. Steidel (Feb. 2009). “A Steep Faint-End Slope of the UV Luminosity Function at $z \sim 2$ -3: Implications for the Global Stellar Mass Density and Star Formation in Low-Mass Halos”. *ApJ* 692.1, pp. 778–803. DOI: 10.1088/0004-637X/692/1/778. arXiv: 0810.2788 [astro-ph].
- Rudie, Gwen C. et al. (May 2012). “The Gaseous Environment of High- z Galaxies: Precision Measurements of Neutral Hydrogen in the Circumgalactic Medium of $z \sim 2$ -3 Galaxies in the Keck Baryonic Structure Survey”. *ApJ* 750.1, 67, p. 67. DOI: 10.1088/0004-637X/750/1/67. arXiv: 1202.6055 [astro-ph.CO].
- Schroetter, Ilane et al. (Dec. 2019). “MusE GAs FLOW and Wind (MEGAFLOW) - III. Galactic wind properties using background quasars”. *MNRAS* 490.3, pp. 4368–4381. DOI: 10.1093/mnras/stz2822. arXiv: 1907.09967 [astro-ph.GA].

- Sérsic, J. L. (Feb. 1963). “Influence of the atmospheric and instrumental dispersion on the brightness distribution in a galaxy”. *Boletín de la Asociación Argentina de Astronomía La Plata Argentina* 6, pp. 41–43.
- Shapley, Alice E., Charles C. Steidel, Max Pettini, and Kurt L. Adelberger (May 2003). “Rest-Frame Ultraviolet Spectra of $z \sim 3$ Lyman Break Galaxies”. *ApJ* 588.1, pp. 65–89. DOI: 10.1086/373922. arXiv: astro-ph/0301230 [astro-ph].
- Smith, Aaron et al. (Mar. 2019). “The physics of Lyman α escape from high-redshift galaxies”. *MNRAS* 484.1, pp. 39–59. DOI: 10.1093/mnras/sty3483. arXiv: 1810.08185 [astro-ph.GA].
- Song, Hyunmi, Kwang-Il Seon, and Ho Seong Hwang (Sept. 2020). “Ly α Radiative Transfer: Modeling Spectrum and Surface Brightness Profiles of Ly α -emitting Galaxies at $Z = 3-6$ ”. *ApJ* 901.1, 41, p. 41. DOI: 10.3847/1538-4357/abac02. arXiv: 2007.08172 [astro-ph.GA].
- Pravnicu, Mihai et al. (Nov. 2016). “Strongly time-variable ultraviolet metal-line emission from the circum-galactic medium of high-redshift galaxies”. *MNRAS* 463.1, pp. 120–133. DOI: 10.1093/mnras/stw1962. arXiv: 1510.06410 [astro-ph.GA].
- Stanway, E. R. and J. J. Eldridge (Sept. 2018). “Re-evaluating old stellar populations”. *MNRAS* 479.1, pp. 75–93. DOI: 10.1093/mnras/sty1353. arXiv: 1805.08784 [astro-ph.GA].
- Steidel, Charles C. et al. (May 2002). “The Kinematic Connection between absorbing Gas toward QSOs and Galaxies at Intermediate Redshift”. *ApJ* 570.2, pp. 526–542. DOI: 10.1086/339792. arXiv: astro-ph/0201353 [astro-ph].
- Steidel, Charles C. et al. (Apr. 2004). “A Survey of Star-forming Galaxies in the $1.4 \lesssim Z \lesssim 2.5$ Redshift Desert: Overview”. *ApJ* 604.2, pp. 534–550. DOI: 10.1086/381960. arXiv: astro-ph/0401439 [astro-ph].
- Steidel, Charles C. et al. (July 2010). “The Structure and Kinematics of the Circumgalactic Medium from Far-ultraviolet Spectra of $z \sim 2-3$ Galaxies”. *ApJ* 717.1, pp. 289–322. DOI: 10.1088/0004-637X/717/1/289. arXiv: 1003.0679 [astro-ph.CO].
- Steidel, Charles C. et al. (Aug. 2011). “Diffuse Ly α Emitting Halos: A Generic Property of High-redshift Star-forming Galaxies”. *ApJ* 736.2, 160, p. 160. DOI: 10.1088/0004-637X/736/2/160. arXiv: 1101.2204 [astro-ph.CO].
- Steidel, Charles C. et al. (Nov. 2014). “Strong Nebular Line Ratios in the Spectra of $z \sim 2-3$ Star Forming Galaxies: First Results from KBSS-MOSFIRE”. *ApJ* 795.2, 165, p. 165. DOI: 10.1088/0004-637X/795/2/165. arXiv: 1405.5473 [astro-ph.GA].
- Steidel, Charles C. et al. (Aug. 2016). “Reconciling the Stellar and Nebular Spectra of High-redshift Galaxies”. *ApJ* 826.2, 159, p. 159. DOI: 10.3847/0004-637X/826/2/159. arXiv: 1605.07186 [astro-ph.GA].

- Steidel, Charles C. et al. (Dec. 2018). “The Keck Lyman Continuum Spectroscopic Survey (KLCS): The Emergent Ionizing Spectrum of Galaxies at $z \sim 3$ ”. *ApJ* 869.2, 123, p. 123. DOI: 10.3847/1538-4357/aaed28. arXiv: 1805.06071 [astro-ph.GA].
- Strom, Allison L. et al. (Feb. 2017). “Nebular Emission Line Ratios in $z \simeq 2-3$ Star-forming Galaxies with KBSS-MOSFIRE: Exploring the Impact of Ionization, Excitation, and Nitrogen-to-Oxygen Ratio”. *ApJ* 836.2, 164, p. 164. DOI: 10.3847/1538-4357/836/2/164. arXiv: 1608.02587 [astro-ph.GA].
- Theios, Rachel L. et al. (Jan. 2019). “Dust Attenuation, Star Formation, and Metallicity in $z \sim 2-3$ Galaxies from KBSS-MOSFIRE”. *ApJ* 871.1, 128, p. 128. DOI: 10.3847/1538-4357/aaf386. arXiv: 1805.00016 [astro-ph.GA].
- Trainor, Ryan F., Charles C. Steidel, Allison L. Strom, and Gwen C. Rudie (Aug. 2015). “The Spectroscopic Properties of Ly α -Emitters at $z \sim 2.7$: Escaping Gas and Photons from Faint Galaxies”. *ApJ* 809.1, 89, p. 89. DOI: 10.1088/0004-637X/809/1/89. arXiv: 1506.08205 [astro-ph.GA].
- Trainor, Ryan F., Allison L. Strom, Charles C. Steidel, and Gwen C. Rudie (Dec. 2016). “The Rest-frame Optical Spectroscopic Properties of Ly α -emitters at $Z \sim 2.5$: The Physical Origins of Strong Ly α Emission”. *ApJ* 832.2, 171, p. 171. DOI: 10.3847/0004-637X/832/2/171. arXiv: 1608.07280 [astro-ph.GA].
- Trainor, Ryan F. et al. (Dec. 2019). “Predicting Ly α Emission from Galaxies via Empirical Markers of Production and Escape in the KBSS”. *ApJ* 887.1, 85, p. 85. DOI: 10.3847/1538-4357/ab4993. arXiv: 1908.04794 [astro-ph.GA].
- Tumlinson, Jason, Molly S. Peeples, and Jessica K. Werk (Aug. 2017). “The Circumgalactic Medium”. *ARA&A* 55.1, pp. 389–432. DOI: 10.1146/annurev-astro-091916-055240. arXiv: 1709.09180 [astro-ph.GA].
- Vanzella, E. et al. (Mar. 2017). “Illuminating gas inflows/outflows in the MUSE deepest fields: Ly α nebulae around forming galaxies at $z \simeq 3.3$ ”. *MNRAS* 465.4, pp. 3803–3816. DOI: 10.1093/mnras/stw2442. arXiv: 1607.03112 [astro-ph.GA].
- Veilleux, Sylvain, Gerald Cecil, and Joss Bland-Hawthorn (Sept. 2005). “Galactic Winds”. *ARA&A* 43.1, pp. 769–826. DOI: 10.1146/annurev.astro.43.072103.150610. arXiv: astro-ph/0504435 [astro-ph].
- Verhamme, A., D. Schaerer, and A. Maselli (Dec. 2006). “3D Ly α radiation transfer. I. Understanding Ly α line profile morphologies”. *A&A* 460.2, pp. 397–413. DOI: 10.1051/0004-6361:20065554. arXiv: astro-ph/0608075 [astro-ph].
- Verhamme, A. et al. (Oct. 2012). “Lyman- α emission properties of simulated galaxies: interstellar medium structure and inclination effects”. *A&A* 546, A111, A111. DOI: 10.1051/0004-6361/201218783. arXiv: 1208.4781 [astro-ph.CO].
- Verhamme, A. et al. (July 2018). “Recovering the systemic redshift of galaxies from their Lyman alpha line profile”. *MNRAS* 478.1, pp. L60–L65. DOI: 10.1093/mnrasl/sly058. arXiv: 1804.01883 [astro-ph.GA].

- Virtanen, Pauli et al. (Feb. 2020). “SciPy 1.0: fundamental algorithms for scientific computing in Python”. *Nature Methods* 17, pp. 261–272. DOI: 10.1038/s41592-019-0686-2. arXiv: 1907.10121 [cs.MS].
- Whitaker, Katherine E. et al. (Nov. 2014). “Constraining the Low-mass Slope of the Star Formation Sequence at $0.5 < z < 2.5$ ”. *ApJ* 795.2, 104, p. 104. DOI: 10.1088/0004-637X/795/2/104. arXiv: 1407.1843 [astro-ph.GA].
- Wisotzki, L. et al. (Mar. 2016). “Extended Lyman α haloes around individual high-redshift galaxies revealed by MUSE”. *A&A* 587, A98, A98. DOI: 10.1051/0004-6361/201527384. arXiv: 1509.05143 [astro-ph.GA].
- Wisotzki, L. et al. (Oct. 2018). “Nearly all the sky is covered by Lyman- α emission around high-redshift galaxies”. *Nature* 562.7726, pp. 229–232. DOI: 10.1038/s41586-018-0564-6. arXiv: 1810.00843 [astro-ph.GA].
- Zheng, Zheng, Renyue Cen, Hy Trac, and Jordi Miralda-Escudé (Jan. 2011). “Radiative Transfer Modeling of Ly α Emitters. II. New Effects on Galaxy Clustering”. *ApJ* 726.1, 38, p. 38. DOI: 10.1088/0004-637X/726/1/38. arXiv: 1003.4990 [astro-ph.CO].

Chapter 4

CIRCUMGALACTIC $\text{Ly}\alpha$ EMISSION AND ITS HOST GALAXIES

In the previous chapter, we demonstrated that the correlation between $\text{Ly}\alpha$ emission in the CGM and the orientation of the host galaxies is insignificant. However, the connection between $\text{Ly}\alpha$ emission in the DTB spectra and other properties of the host galaxies has been well established observationally, e.g., M_* , SFR, E(B-V), and the luminosity of $\text{H}\alpha$ and [O III] emission (e.g., Steidel et al., 2010; Erb et al., 2016; Trainor et al., 2019; Weiss et al., 2021). However, the physical process that most directly responsible for these correlations remains uncertain. This has led to debates on what processes govern $\text{Ly}\alpha$ escape, and the implications of the variation of $\text{Ly}\alpha$ through the cosmic history, e.g., the decline of $\text{Ly}\alpha$ equivalent widths for star-forming galaxies at $z \simeq 7$ (Mesinger et al., 2015).

As of the end of April 2021, the KBSS-KCWI survey consists of 110 star-forming galaxies (excluding galaxies with known AGN activities, but including continuum serendipitous [“CS”] objects) at $z > 2$ and total integration time ≥ 2.5 hours. The details of the sample and the observations are provided in Chapter 3. Details of the data reduction process are provided in Appendix A.

The size and depth of the KBSS-KCWI survey provide an ideal dataset to explore the connections between the spatially resolved $\text{Ly}\alpha$ emission and host galaxy properties for the first time. In this chapter, we present some preliminary results that expand our analyses from previous chapters.

4.1 Continuum Subtraction

We conduct continuum-subtraction on the spaxels near the galaxies to isolate $\text{Ly}\alpha$ emission from the stellar continuum. One issue we encountered in Chen et al. (2021) (hereafter C21) is the over-subtraction of the $\text{Ly}\alpha$ profile blueward of the systemic redshift. This issue is caused by the fact that a simple interpolation of a constant continuum level between wavelengths above and below $\text{Ly}\alpha$ does not capture the complexity of the real spectra. Therefore, a more complex method is needed.

In this chapter, stellar-continuum subtraction is performed using stellar population synthesis (SPS) models, namely the “Binary Population and Spectral Synthesis”

(BPASS) v2.2 models (Stanway and Eldridge, 2018) with an upper mass cutoff of $100M_{\odot}$, assuming a stellar metallicity $Z_* = 0.002Z_{\odot}$, and adopting a constant star-formation history (SFH) with age $t = 10^8$ years. The above assumptions were previously found to be suitable to describe the KBSS galaxy sample in the FUV continuum by Steidel et al. (2016) and Theios et al. (2019). As shown below, the models work acceptably well for our purpose – to remove the stellar continuum near $\text{Ly}\alpha$ in composite spectra.

We apply the mean of Monte-Carlo models of “IGM+CGM” H I transmission curve as described by Steidel et al. (2018) (hereafter S18) at the redshift of the object to the SPS model. The curve was generated as the mean from Monte-Carlo simulations based on the best-fit H I incidence rate from Rudie et al. (2013). The attenuated spectrum is then reddened using an SMC extinction curve using the best-fit $E(B-V)$ required to match the observed the spectral shape of the 1D-extracted spectrum from the KCWI data¹. The fits were conducted with iterative sigma-clipping with $N_{\sigma} = 2.5$. Emission and absorption lines arising from the ISM and CGM gas are masked using the templates suggested by S18.

As shown by S18, H I absorption in the ISM has a crucial impact on the continuum shape near $\text{Ly}\alpha$ as well. Therefore, as a final step in the continuum modeling, we applied the “holes” model of S18 to the modeled spectra. This model assumes that the observed spectrum consists of two distinct components. One is covered by low-ionization gas including dust, which reddens the continuum shape; the second component is assumed to be uncontaminated by the ISM, emerging through holes. S18 found that the fraction of the galaxy continuum covered by optically thick H I (f_c) is linearly correlated with the observed $\text{Ly}\alpha$ equivalent width [$W_{\lambda}(\text{Ly}\alpha)$]. Pahl et al. (2021) subsequently updated the correlation parameters after removing a small number of blended objects, which gives,

$$1 - f_c = 0.58[W_{\lambda}(\text{Ly}\alpha)/110\text{\AA}]. \quad (4.1)$$

We adopt this correlation for individual galaxies in our sample, where $W_{\lambda}(\text{Ly}\alpha)$ were measured from 1D-extracted KCWI spectra. We further assumed that the H I column density, $\log(N_{\text{HI}}/\text{cm}^{-2}) = 20.61$, the best-fit value found by S18 for the “holes” model to the composite KLCS spectrum. The Doppler width and systemic velocity offset of this ISM component are assumed to be $b = 125 \text{ km s}^{-1}$ and $v_{\text{sys}} = -100 \text{ km s}^{-1}$, as in S18.

¹The extraction method for 1D continuum spectra were described in C21. It generates spectra that are similar to that observed by slit spectrographs and optimizes the S/N for the continuum.

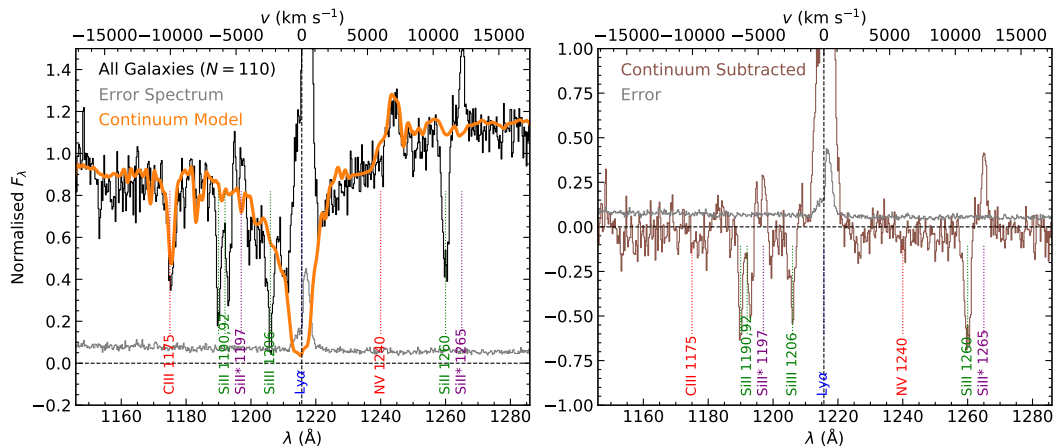


Figure 4.1: *Left*: The composite 1D spectrum of the full sample (black) and the composite stellar continuum model (orange). Before stacking, each individual galaxy spectrum was normalized with $F_\lambda(1450 \text{ \AA}) = 1$, and the stacking method was a sigma-clipped mean with $N_\sigma = 2.5$. *Right*: The composite continuum-subtracted spectrum (brown). In both panels, the grey spectrum is the 1σ error spectrum derived from bootstrap resampling. The vertical lines with labels mark the selected spectral features in the range, where different colors indicate their primary physical origin: ISM (green), nebular (blue), stellar (red), and non-resonant emission (purple). Our continuum model works well in continuum subtraction.

Finally, we emphasize that the model assumptions above were previously most successful for fitting with composite spectra (e.g., S18). Most notably, the IGM + CGM opacity curve is the average absorption strength of Ly α absorbers in the foreground Ly α forest at a given redshift that lowers the continuum level in the composite spectra. However, we needed to develop a method for fitting spectra individually, for which discrete Ly α forest absorption lines are present, rather than a smoothly leveled continuum, in order to measure Ly α emission robustly as shown in §4.2. We experimented with multiple methods, including fitting only the portion of spectra redward of Ly α , and/or fitting without accounting for IGM + CGM attenuation. In the end, we found that using iterative sigma clipping results in fits that are most consistent with fits to composite spectra over our redshift range. The difference between the the two versions of continuum spectra is $< 5\%$ (RMS) near Ly α .

Following the procedures outlined above, a continuum model is generated for every object in the sample; this continuum model is scaled to match the flux within the continuum footprint in the KCWI cube before being subtracted. Figure 4.1 shows the composite 1D spectrum, the best-fit model continuum spectrum, and the

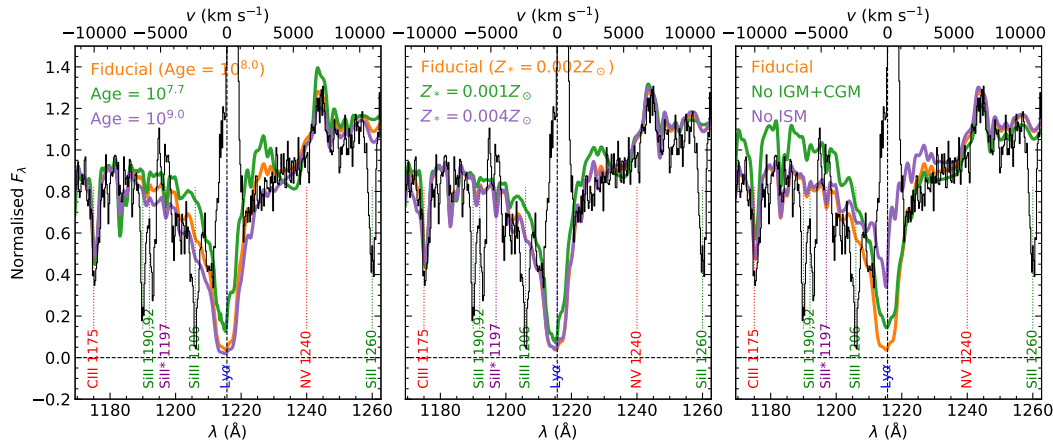


Figure 4.2: This figure shows how different parameters or assumptions affect the modeled continuum spectrum. The black and orange spectra are the same as in Figure 4.1, which show the composite 1D spectra of the galaxies and their fiducial continuum models. From left to right: The change of the continuum spectrum by varying age (left) and stellar metallicity (middle), and by ignoring the IGM + CGM component or the ISM component (right). Our fiducial model closely resembles the continuum around Ly α in the composite 1D spectrum.

continuum-subtracted spectrum, for all galaxies in the KCWI sample. Our model spectrum follows well with the continuum near Ly α . Figure 4.2 shows how age, Z_* , and the application of IGM + CGM and ISM attenuation affect the modeled continuum. The assumed age of the constant-star-formation model has a significant impact near Ly α , especially in the wings; it is somewhat degenerate to the assumed ISM column density. The impact of Z_* is minimal near Ly α except in the wings for models with extremely low metallicity. Note that without the H I covering of the ISM component, the model would significantly underpredict the absorption strength within 5000 km s^{-1} of Ly α . By ignoring the IGM + CGM opacity, the predicted continuum would be considerably higher than that observed blueward of Ly α . In summary, continuum models constructed using the assumptions above are suitable and adequate for isolating the Ly α emission component from the stellar continuum.

4.2 The Average Ly α Emission

In order to understand how the Ly α halos vary with the properties of the host galaxies, we begin by investigating the average Ly α emission profile for the full sample of 110 galaxies.

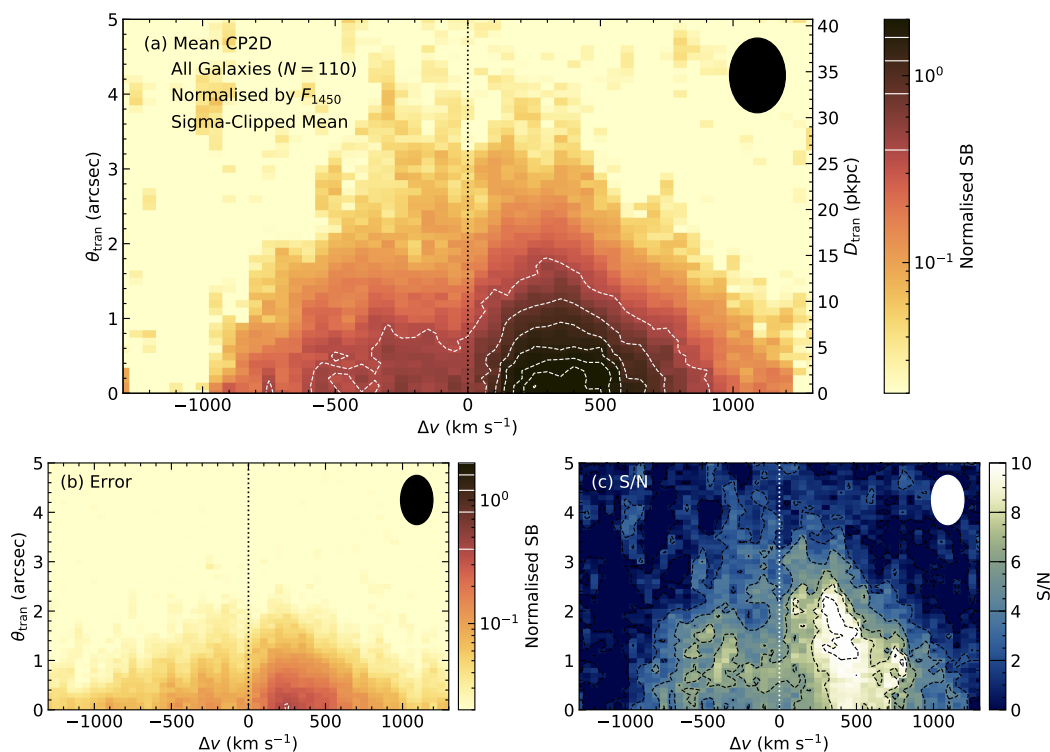


Figure 4.3: (a) The composite CP2D spectrum constructed from a stack of all 110 star-forming galaxies in the sample. Before stacking, the CP2D spectrum of each object was extracted and normalized based on its median flux density at 1400–1500 Å. The stacking was made with iterative sigma-clipped mean with $N_\sigma = 2.5$. The color map is on a log scale to highlight the low SB halo, while the white contours are linear increments of 0.4, as shown in the color bar. The ellipse on the top-right is the effective “beam” size of the map, where the vertical size is the FWHM of the typical seeing (1 arcsec), and the horizontal size corresponds to the typical spectral resolution (210 km s^{-1}), as estimated in C21. (b) Error of the composite CP2D spectrum, estimated using bootstrap resampling with 500 realizations. The color map is the same as in panel (a). (c) The S/N map of the composite CP2D spectrum formed by dividing panel (a) by panel (b). Both the color map and contours are on a linear scale.

The Ly α Cylindrically Projected 2D Spectrum

Figure 4.3 shows the average continuum-subtracted “cylindrically projected 2D” (CP2D) spectrum of the sample. The CP2D spectrum, introduced by C21, maps the mean Ly α SB as a function of velocity and projected distance (D_{tran}) or angular separation (θ_{tran}) around host galaxies. The CP2D spectrum in Figure 4.3 was constructed by stacking the individual CP2D spectra. Each spectrum was extracted from the continuum-subtracted 3D cube that was made using the method discussed in §4.1. The center of the object was taken by fitting a 2D Gaussian profile to the pseudo-white-light image of the corresponding KCWI data.

Before stacking, the individual CP2D spectra were resampled onto a common grid with $\Delta v = 50 \text{ km s}^{-1}$ and $\Delta\theta_{\text{tran}} = 0.1 \text{ arcsec}$. The covariance scale was estimated in a bootstrap style. First, we calculated the covariance matrix between every two pixels in the CP2D spectrum using bootstrap resampling. We found that after normalizing the covariance by the product of the SB of the two corresponding pixels, the normalized covariance only depends on the relative position between the two pixels, and can be roughly fit by a 2D Gaussian function. The FWHM of the Gaussian function is $\approx 0.8 \text{ arcsec}$ in the θ_{tran} and $\sim 110 \text{ km s}^{-1}$ in the Δv directions, which were determined to be the correlation scales. Note that these scales reflect the initial characteristic detector sampling of KCWI, and are smaller than the spatial and spectral resolution, which are set respectively by seeing and the choice of grating. The latter was estimated as 1 arcsec and 210 km s^{-1} as shown in C21.

Individual CP2D spectra were then normalized by the median f_{λ} between $1400 - 1500 \text{ \AA}$ ($F_{\lambda}(1450 \text{ \AA})$), which can be measured directly from the 1D-extracted spectra for galaxies with $z \lesssim 2.7$. At $z > 2.7$, the KCWI do not include the full $1400 - 1500 \text{ \AA}$ range in the rest frame. In which cases, we used the median flux derived from the best-fit continuum model as shown in §4.1. We chose to normalize individual spectra before stacking because, without normalization, the final stack may be dominated by objects that are the brightest in both the continuum and in Ly α . normalizing the flux by the continuum gives each galaxy roughly the same contribution to the final stack, and Ly α flux per unit continuum flux density reflects the Ly α emissivity relative to the continuum emissivity of stars. The choice of F_{1450} is motivated by the fact that the spectral range $1400 - 1500 \text{ \AA}$ is relatively free from strong UV absorption or emission lines, and has been used by many authors (e.g., Steidel et al., 2010; Chen et al., 2020) to make composite 1D spectra.

To reduce the effect of outliers, each pixel in the composite CP2D spectra is stacked

by using iterative sigma-clipped mean centred around the median as our stacking method with $N_\sigma = 2.5$. We found that $N_\sigma = 2.5$ can reproduce the median stack, but with higher S/N. The error spectrum was obtained from bootstrap reampling using the same $N_\sigma = 2.5$ sigma-clipped mean with 500 realizations.

Similar to that shown by C21, the composite CP2D spectrum shows a distinctive morphology for Ly α halo emission that is consistent with resonant scattering from outflowing H I (e.g., Pettini et al., 2001; Verhamme, Schaerer, and Maselli, 2006; Dijkstra, 2014). with a dominant redshifted emission component extending to ~ 40 pkpc, and a weaker blueshifted component, whose relative intensity relative to the redshifted component increases with increasing projected distance (Figure 4.4). The blue and redshifted emission gradually become indistinguishable at $D_{\text{tran}} \gtrsim 25$ pkpc, which results in a characteristic “triangular” envelope (Figure 4.3). Unlike C21, the more sophisticated continuum model allows us to recover much of the Ly α emission that was previously oversubtracted, especially for $\Delta v < 700 \text{ km s}^{-1}$. In the following subsections, we examine the spectral and spatial variations in more detail.

The Spatial Profile of Ly α Emission

The Ly α spatial profile as a function θ_{tran} is a common demonstration to show the spatial extent of the Ly α halo. Its variation as a function of the host galaxy properties may help understand the production and escape of Ly α photons.

Figure 4.4 shows the Ly α spatial profile of the full sample, extracted from the composite CP2D spectrum as shown in Figure 4.3. The spatial profile is continuum-subtracted, normalized by $F_\lambda(1450)$, and combined using sigma-clipped mean. The total Ly α profile was extracted by integrating within the velocity bin of $-1000 \text{ km s}^{-1} \leq \Delta v < 1200 \text{ km s}^{-1}$, with the red side slightly more extended than the blue side in velocity space to include the more extended signal as shown in Figure 4.3. Meanwhile, we also separately extracted the Ly α profiles of the blue- and redshifted emission: $-1000 \text{ km s}^{-1} \leq \Delta v < 0 \text{ km s}^{-1}$ for the blue side, and $0 \leq \Delta v < 1200 \text{ km s}^{-1}$ for the red side. We fit all three profiles (total, blueshifted, and redshifted) with an exponential function convolved with a Gaussian function with FWHM = $1''.02$ (see Chen et al., 2021), using the Markov-Chain Monte-Carlo (MCMC) method. The results are shown in Figure 4.4 as well.

The ratio between the blue- and redshifted emission components also varies significantly with projected distance: while the blueshifted component is weaker than

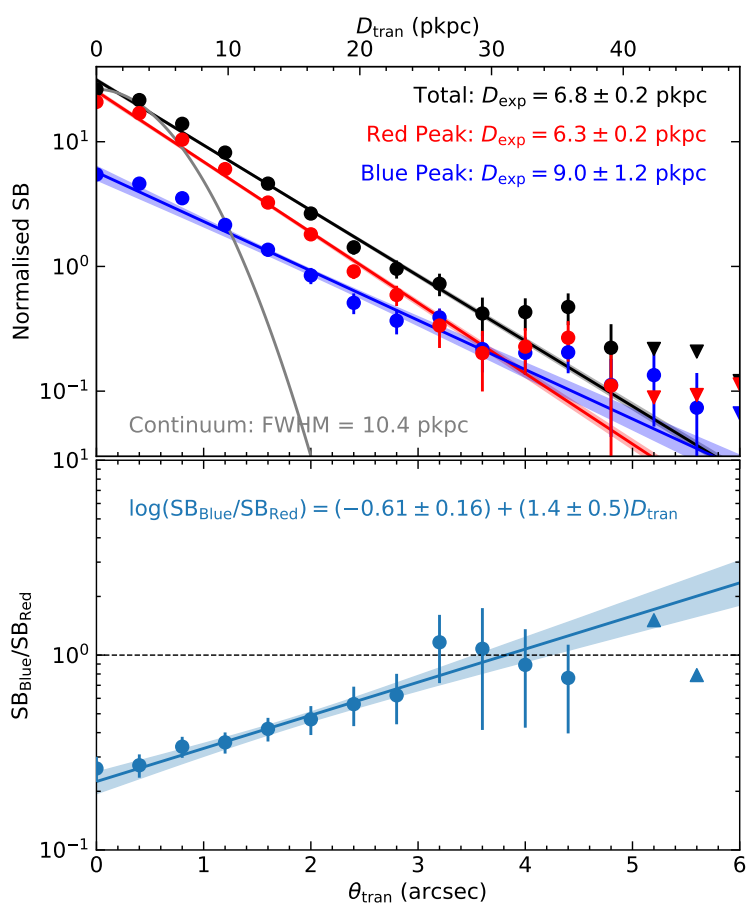


Figure 4.4: *Top:* The composite spatial profiles of the normalized Ly α surface brightness. The black points show the total Ly α emission. The red and blue points show the redshifted and blueshifted emission components accordingly. The black, red, and blue lines show the best-fit exponential profiles to the corresponding points. All profiles are continuum-subtracted. The gray line shows the continuum profile. *Bottom:* The ratio between the blue and redshifted emission as a function of θ_{tran} . The blue line is the best-fit line in log-linear space.

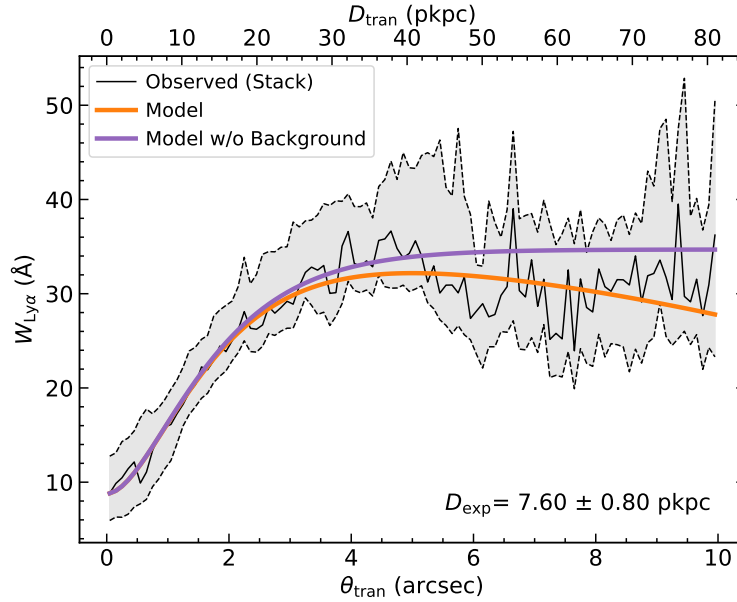


Figure 4.5: The $W_\lambda(\text{Ly}\alpha)$ spatial curve of growth for the stacked CP2D spectra as shown in Figure 4.3. The black curve is the measured value, with the gray shade marks the 1σ error. The orange curve is the best-fit model from an exponential profile with a constant background. The purple line shows this best-fit model, after removing the background component.

the redshifted component, when it is close to the galaxy center, the SB of the blueshifted emission becomes comparable to the redshifted emission at $\theta_{\text{tran}} > 3$ arcsec ($D_{\text{tran}} \gtrsim 25$ pkpc). There are hints that the blueshifted emission may be stronger than the red emission at $\theta_{\text{tran}} > 5$ arcsec, though this needs confirmation in the future with more reliable sky subtraction.

The $W_\lambda(\text{Ly}\alpha)$ Curve of Growth

The amount of $\text{Ly}\alpha$ emission escaped in the CGM and its relation to the projected galactocentric distance are important in understanding the $\text{Ly}\alpha$ emission mechanism and to constrain the radiative transfer models. Therefore, it is important to measure $W_\lambda(\text{Ly}\alpha)$ as a function of the spatial aperture size (or the so-called “curve of growth”, CoG; e.g., Steidel et al., 2011).

Figure 4.5 shows the stacked $W_\lambda(\text{Ly}\alpha)$ CoG for the full sample, measured from Figure 4.3. To achieve this measurement, we developed a robust way of measuring the integrated $W_\lambda(\text{Ly}\alpha)$ that is consistent with previous measurements (e.g., Reddy and Steidel, 2009). For the continuum flux, we use median flux within $1230\text{\AA} < \lambda < 1240\text{\AA}$ from the continuum model obtained in §4.1. The flux integration of

$\text{Ly}\alpha$ signal is conducted within $1208\text{\AA} < \lambda \leq 1221\text{\AA}$. By comparing the $W_\lambda(\text{Ly}\alpha)$ measured from this method and the $W_\lambda(\text{Ly}\alpha)$ measured using in the same standard as in Reddy and Steidel (2009) for the 1D-extracted DTB spectra of all galaxies in the sample. Except for 5 galaxies with low continuum flux, so that its value is difficult to be determined by eye consistently, the $W_\lambda(\text{Ly}\alpha)$ measured from the two methods of the remaining 105 galaxies are close to the 1-to-1 ratio, with an RMS of 13\AA . Throughout this work, $W_\lambda(\text{Ly}\alpha)$ is measured using this new robust method.

The measured $W_\lambda(\text{Ly}\alpha)$ CoG in Figure 4.5 was fit with the CoG of an exponential profile and a negative background term that contribute to the integration of $W_\lambda(\text{Ly}\alpha)$ proportion to the aperture size. This background term is motivated by the fact that the sky background is often slightly over-subtracted in data reduction, causing the measured $W_\lambda(\text{Ly}\alpha)$ CoG curve to turn down at $\theta_{\text{tran}} > 5$ arcsec. After removing the background component, the best-fit model can be expressed as,

$$W_\lambda(D_{\text{tran}}) = AD_{\text{exp}} \left(-\frac{D_{\text{tran}}}{D_{\text{exp}}} - 1 \right) \exp \left(-\frac{D_{\text{tran}}}{D_{\text{exp}}} \right) + B, \quad (4.2)$$

where $D_{\text{exp}} = 7.6 \pm 0.8$ pkpc, $A = 3.4 \pm 0.3\text{\AA} \text{ pkpc}^{-1}$, and $B = 35 \pm 2\text{\AA}$. For a typical aperture of 1-arcsec diameter, the $W_\lambda(\text{Ly}\alpha)$ measured within the aperture only consists of 33% of the total $\text{Ly}\alpha$ signal.

4.3 $\text{Ly}\alpha$ CP2D Spectrum and the Host Galaxies

In this section, we present preliminary results of the connection between $\text{Ly}\alpha$ CP2D spectra and their host galaxies.

Figures 4.6 to 4.13 show how the composite CP2D spectra vary with $E(B - V)$, M_* , SFR, sSFR (specific star formation rate = SFR/M_*), $F_{\text{H}\alpha}$ (without slit correction), $\log([\text{OIII}]/\text{H}\beta)$, $W_\lambda(\text{Ly}\alpha)$, and $F_{\text{blue}}(\text{tot})/F_{\text{red}}(\text{tot})$. $E(B - V)$, M_* , SFR, and sSFR were measured with 88 galaxies from SED fitting using the BPASSv2.2 stellar population synthesis model (Stanway and Eldridge, 2018) and SMC extinction curve by Steidel et al. (2016), Strom et al. (2017), and Theios et al. (2019). Of the 42 galaxies have $F_{\text{H}\alpha}$ measurements; 52 galaxies have $\log([\text{OIII}]/\text{H}\beta)$ measurements; both from previous Keck/MOSFIRE observations. DTB $W_\lambda(\text{Ly}\alpha)$ were measured from the 1D-extracted DTB spectra from KCWI data, using the method described in §4.2. $F_{\text{blue}}(\text{tot})/F_{\text{red}}(\text{tot})$ is the ratio between the blue- and redshifted emission of the total $\text{Ly}\alpha$ halo, measured by integrating flux within the aperture of $\theta_{\text{tran}} < 3$ arcsec and $-1000 \text{ km s}^{-1} < \Delta v < 0 \text{ km s}^{-1}$ (blue emission) and $0 < \Delta v < 1200 \text{ km s}^{-1}$ (red emission).

For each parameter, the galaxies were divided into three bins containing roughly equal numbers of galaxies. Their CP2D spectra were combined using sigma-clipped mean with $N_\sigma = 2.5$. The composite CP2D spectra show many of the same trends found previously using the DTB spectra. Specifically, since the Ly α produced in the galaxy will either escape or be absorbed by dust, low $E(B - V)$ would suggest a large Ly α escape fraction. Meanwhile, low M_* , large sSFR, strong H α , and high $\log([\text{O III}]/\text{H}\beta)$ emission often suggest strong ionizing radiation from young stars that would favor Ly α production (e.g., Trainor et al., 2019; Du et al., 2020; Weiss et al., 2021). On the other hand, some parameters do not affect the Ly α emission proportionally. For example, although the total Ly α emission per unit continuum flux density decreases significantly between the first and second bins of $E(B - V)$, with roughly the equal difference in the median $E(B - V)$, the second and third bins show similar levels of Ly α emission. This suggests that the dust attenuation only affects the Ly α escape when $E(B - V)$ is low. Intriguingly, although the total Ly α emission changes with the galaxy parameters, the characteristic triangular outer envelope reaches similar D_{tran} in all figures (also see Steidel et al., 2011), suggesting that the scattering of Ly α photons in the outer CGM is relatively independent of the host galaxy properties.

4.4 Looking Forward

Using preliminary results, we have demonstrated the potential of analyzing the composite CP2D spectra in the KBSS-KCWI survey, and the connection between Ly α emission and their host galaxies. We plan to expand our analyses in the following aspects.

We demonstrated that certain Ly α emission does not change proportionally to the host galaxy properties through CP2D spectra. This will be further quantified by measuring the change in Ly α spatial profile as shown in §4.2, which will demonstrate how the host galaxy affects Ly α emission in different parts of the CP2D spectrum.

Meanwhile, radiative transfer simulations have predicted that the spectral profile of Ly α emission reflects the H I gas properties in the CGM. For example, Gronke et al. (2016) showed that in an outflowing clumpy H I medium, $F_{\text{blue}}(\text{Ly}\alpha)/F_{\text{red}}(\text{Ly}\alpha)$ correlates with outflow velocity and covering factor. Since outflow velocity and covering factor can also affect other spectral properties of Ly α , e.g., peak separation, Figure 4.13 provides a testing ground for similar theoretical predictions. In the future, we will compare them quantitatively.

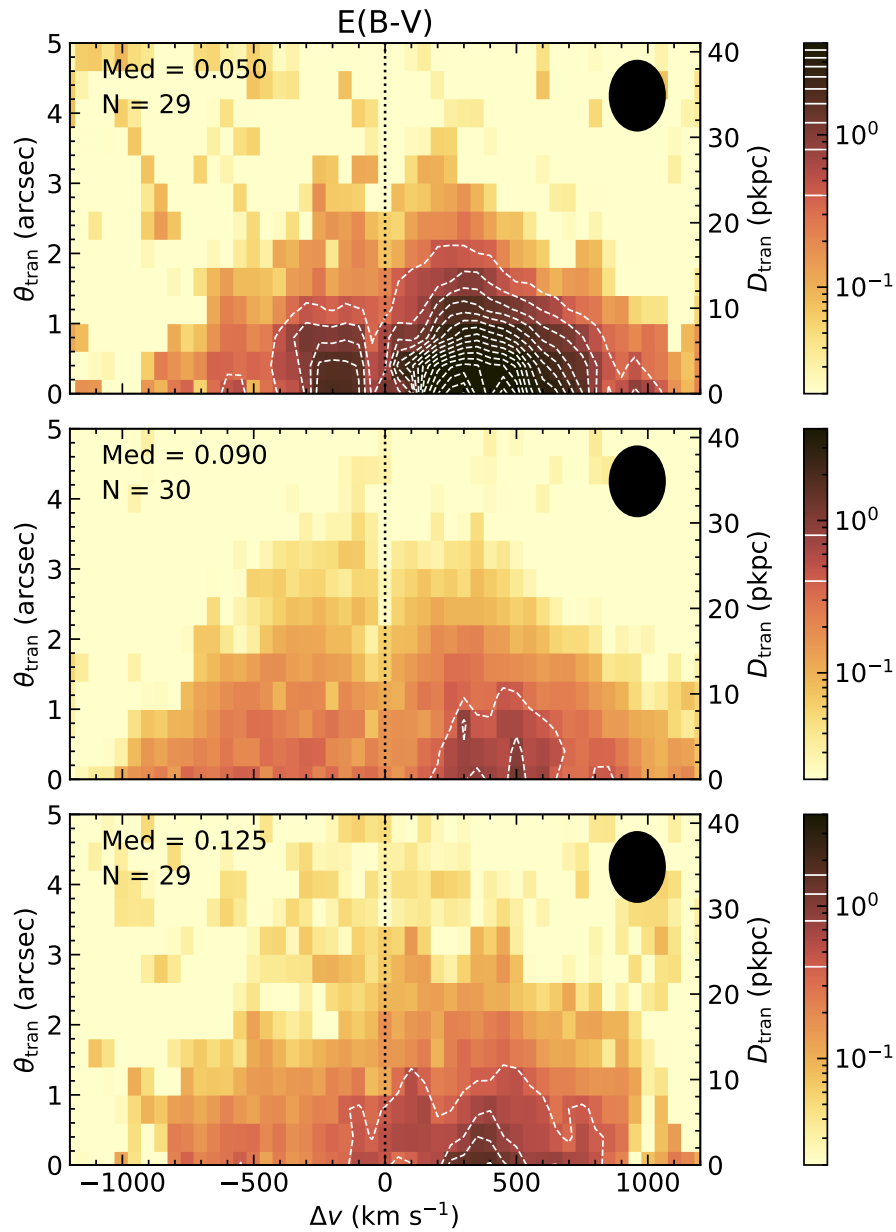


Figure 4.6: The composite CP2D spectra for three sets of galaxies divided into bins of $E(B-V)$. The top left corner of each panel shows the median value of $E(B-V)$, and the number of galaxies that went into each bin. The colormap is in log space, while the white contours are linear. Both are shown in the colorbars on the right side. The unit of the colorbars is normalized SB units.

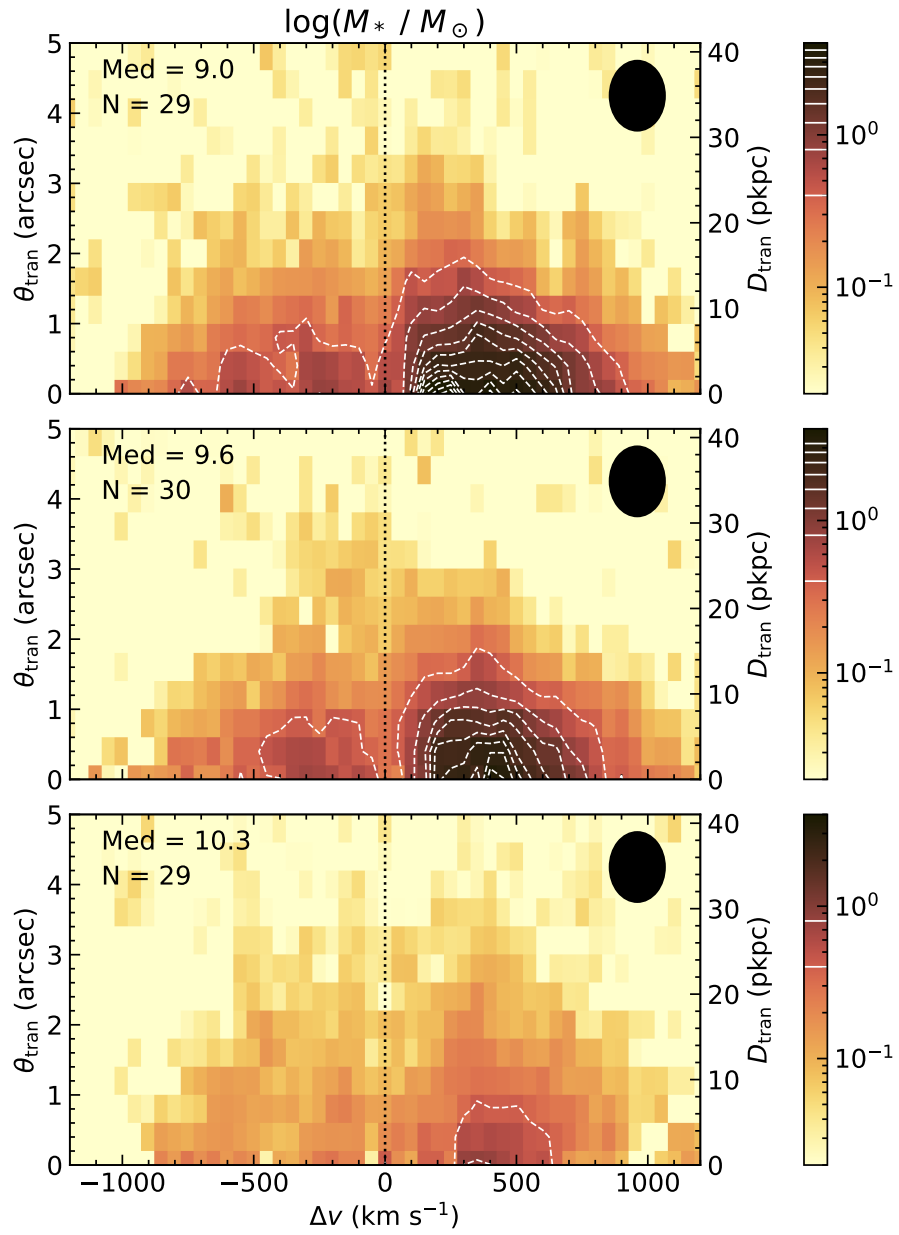


Figure 4.7: Same as in Figure 4.6, for galaxies binned in $\log(M_*/M_\odot)$.

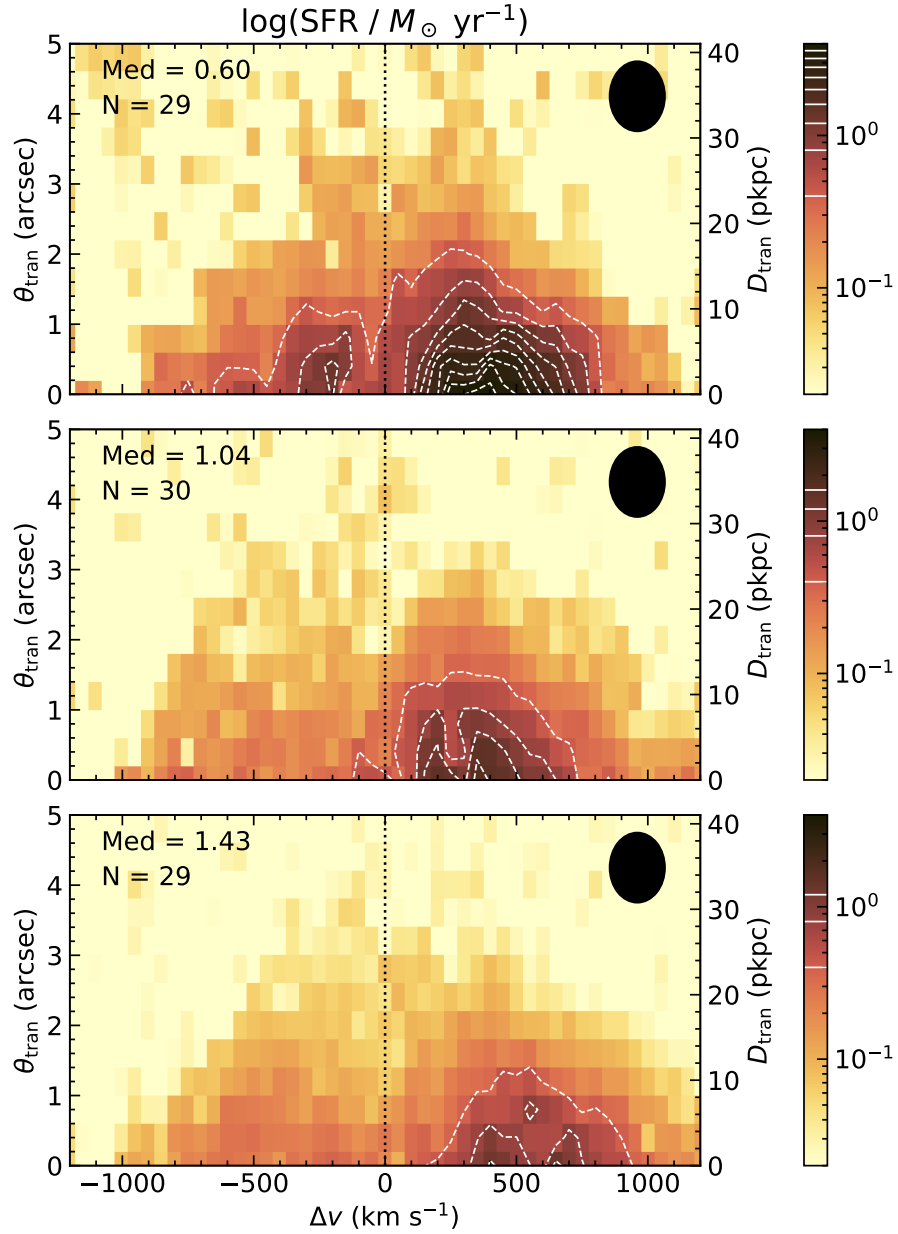


Figure 4.8: Same as in Figure 4.6, for galaxies binned in $\log(\text{SFR})$, where SFR is based on best-fit SED models.

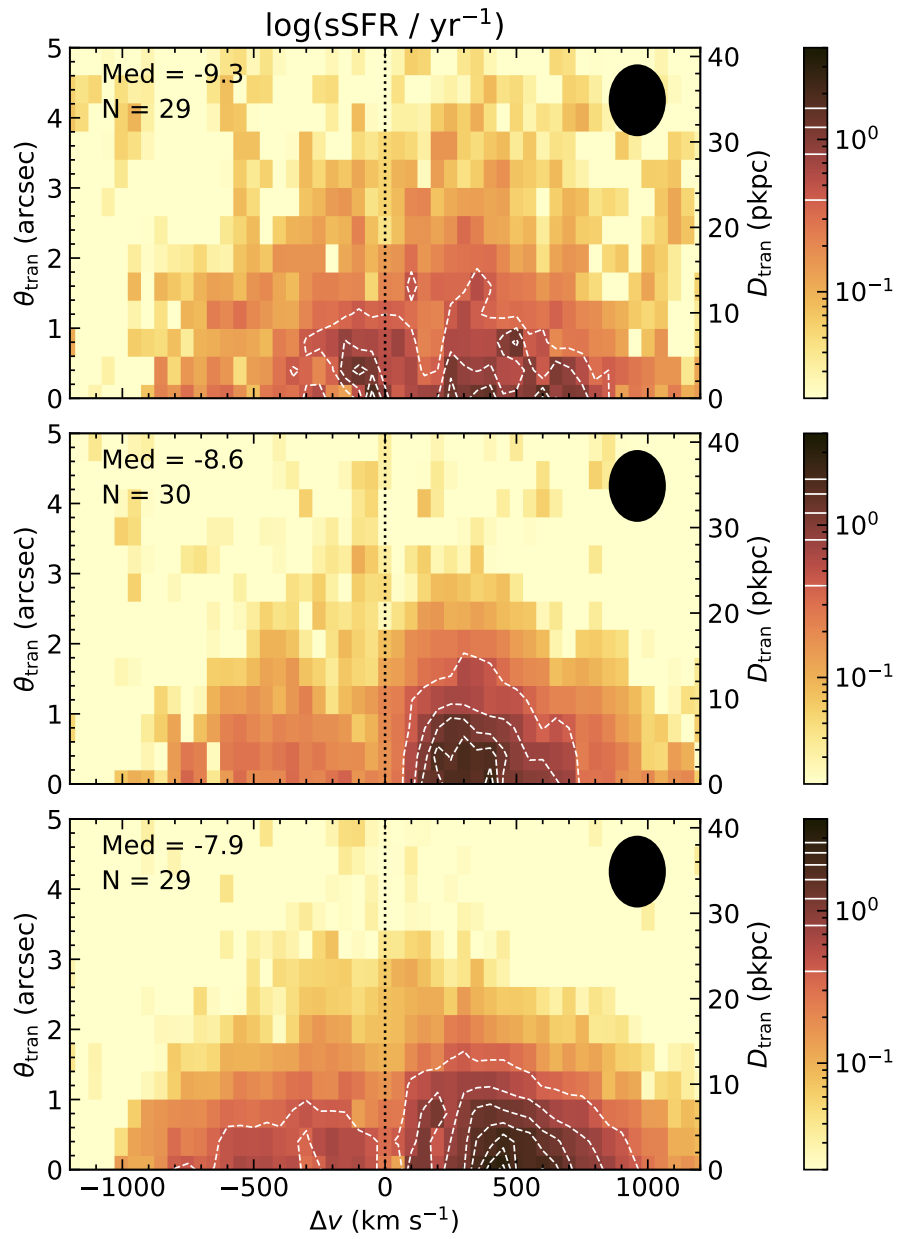


Figure 4.9: Same as in Figure 4.6, for galaxies binned in $\log(\text{sSFR})$.

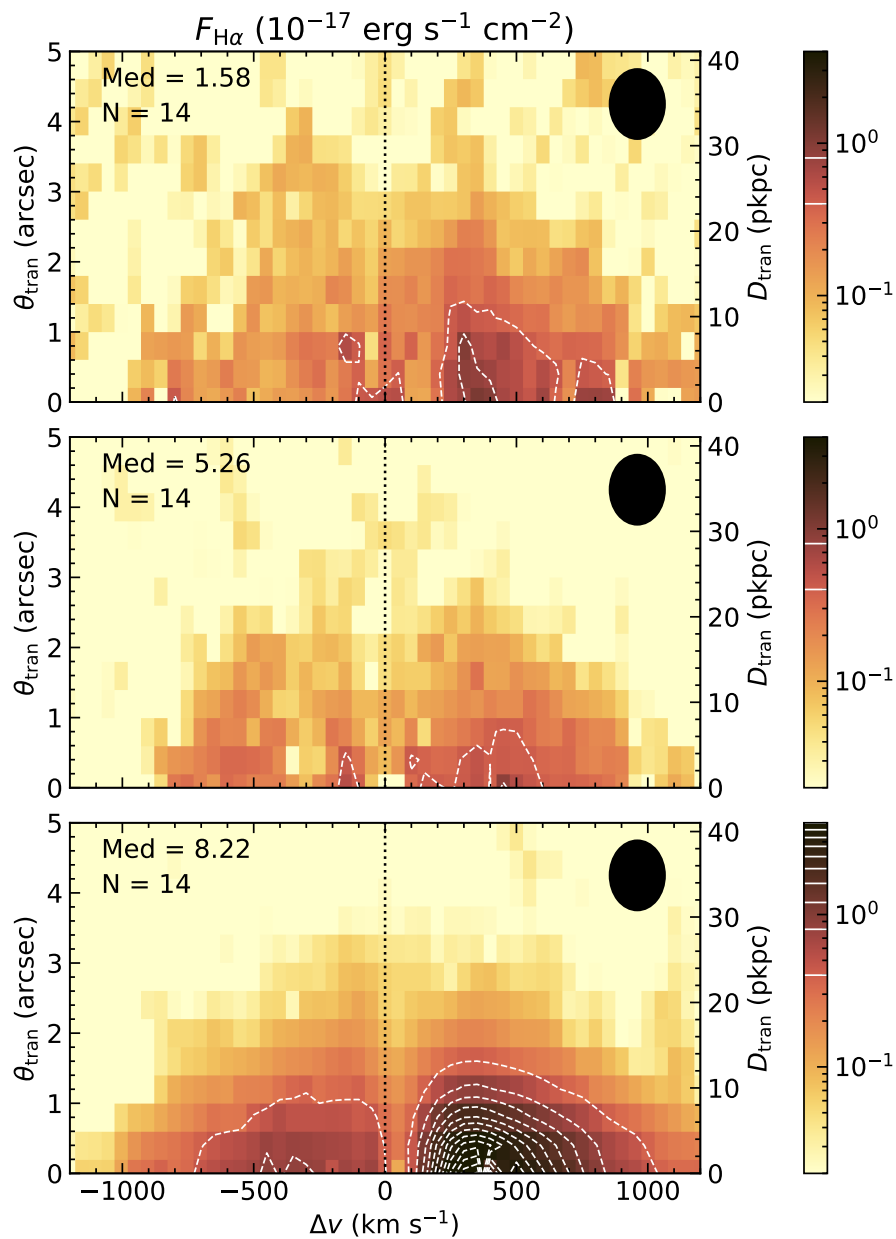


Figure 4.10: Same as in Figure 4.6, for galaxies binned in observed $F_{\text{H}\alpha}$ from 1D extracted slit-spectroscopy.

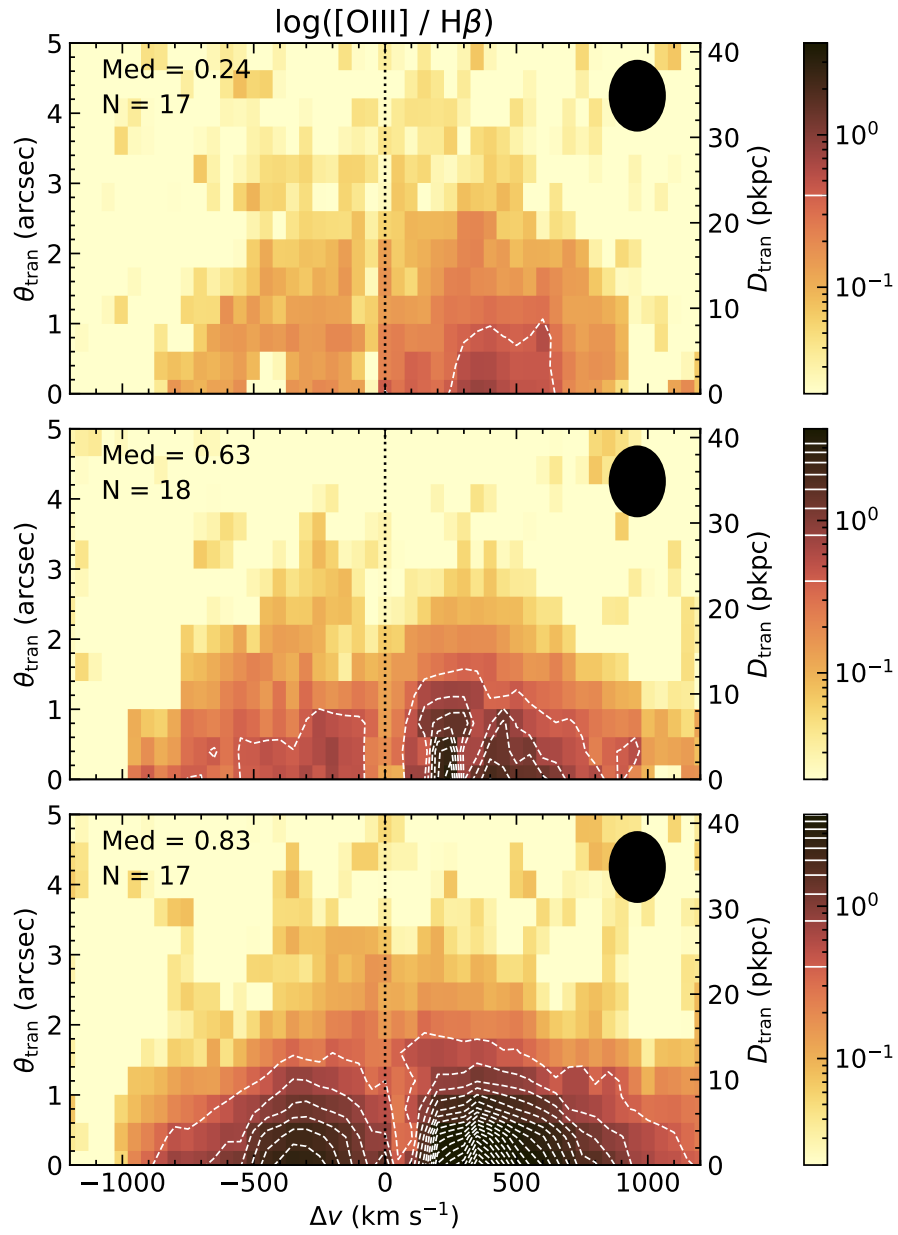


Figure 4.11: Same as in Figure 4.6, for galaxies binned in $\log([\text{OIII}]/\text{H}\beta)$.

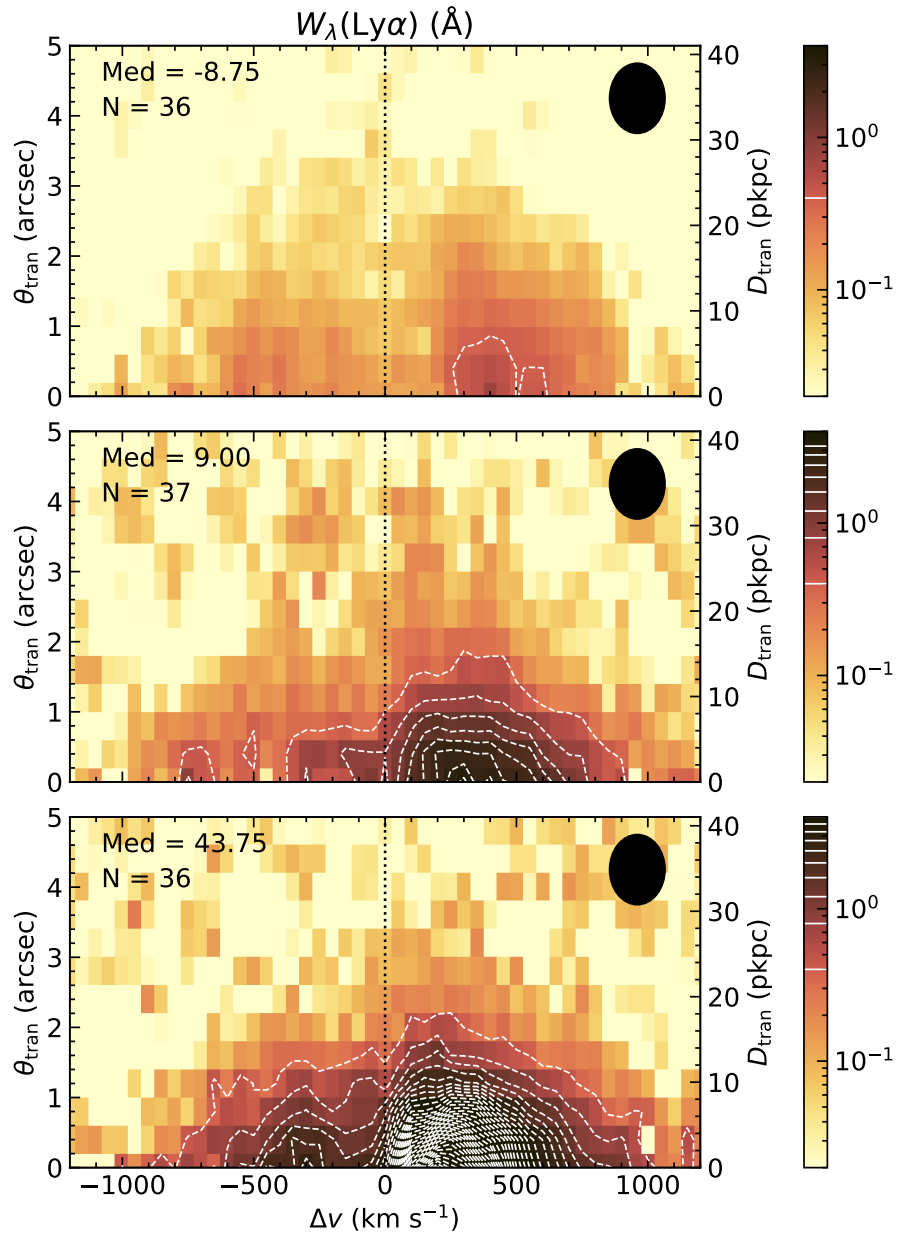


Figure 4.12: Same as in Figure 4.6, for galaxies binned in the DTB $W_{\lambda}(\text{Ly}\alpha)$.

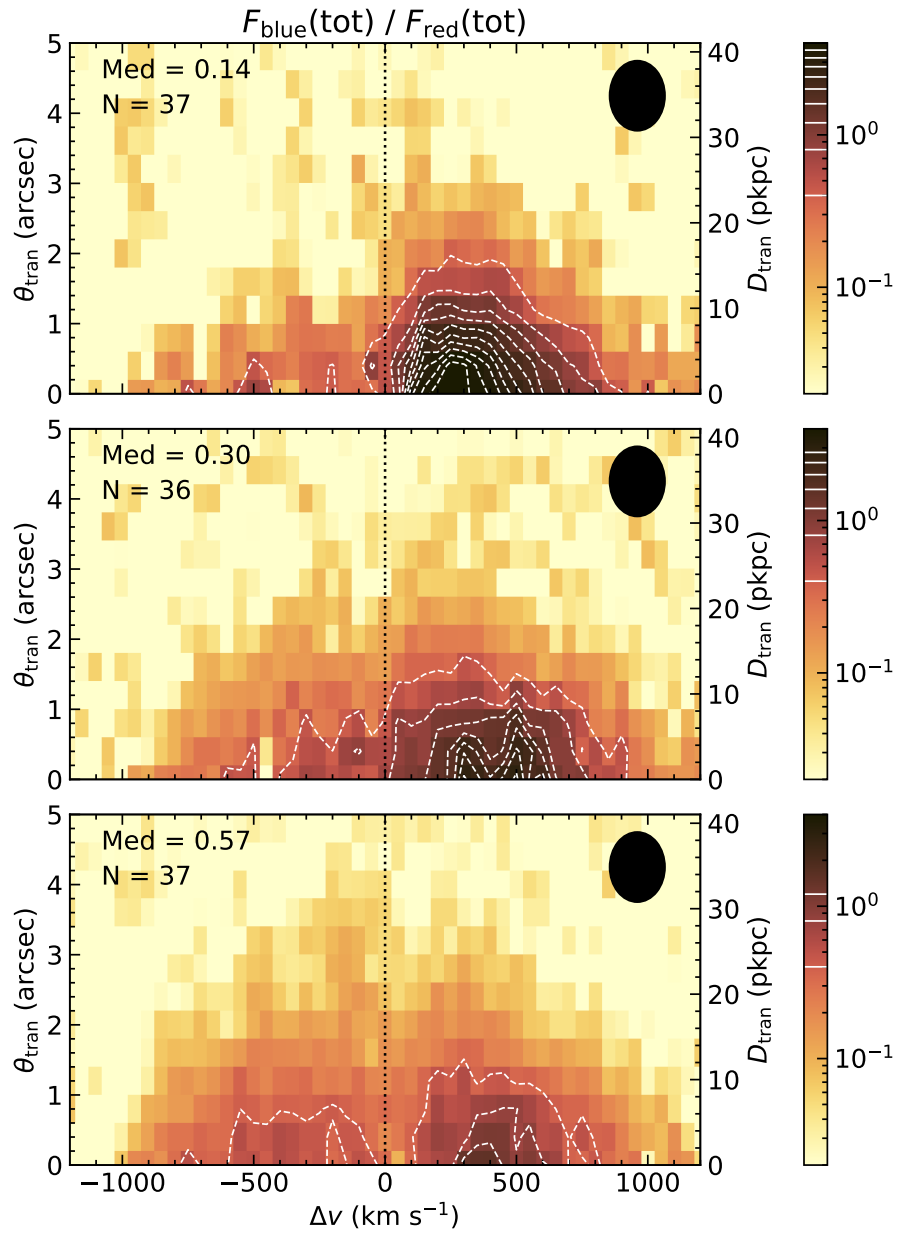


Figure 4.13: Same as in Figure 4.6, for galaxies binned in $F_{\text{blue}}(\text{tot})/F_{\text{red}}(\text{tot})$.

Furthermore, low-ionization metal lines in the 1D spectra of the host galaxies are indicators of the cold gas covering fraction. The rest-frame equivalent width of the combined metal absorption (W_{LIS}) was found to be correlated with the Ly α emission in DTB spectra (Shapley et al., 2003; Trainor et al., 2019). We will measure W_{LIS} in our sample, and measure its effect on the composite CP2D spectra.

References

- Chen, Yuguang et al. (Dec. 2020). “The Keck Baryonic Structure Survey: Using foreground/background galaxy pairs to trace the structure and kinematics of circumgalactic neutral hydrogen at $z \sim 2$ ”. *MNRAS* 499.2, pp. 1721–1746. DOI: 10.1093/mnras/staa2808. arXiv: 2006.13236 [astro-ph.GA].
- Chen, Yuguang et al. (Apr. 2021). “The KBSS-KCWI Survey: The connection between extended Ly α halos and galaxy azimuthal angle at $z \sim 2-3$ ”, arXiv:2104.10173. (in press with MNRAS), arXiv:2104.10173. arXiv: 2104.10173 [astro-ph.GA].
- Dijkstra, Mark (Oct. 2014). “Ly α Emitting Galaxies as a Probe of Reionisation”. *Publ. Astron. Soc. Australia* 31, e040, e040. DOI: 10.1017/pasa.2014.33. arXiv: 1406.7292 [astro-ph.CO].
- Du, Xinnan et al. (Feb. 2020). “Searching for $z > 6.5$ Analogs Near the Peak of Cosmic Star Formation”. *ApJ* 890.1, 65, p. 65. DOI: 10.3847/1538-4357/ab67b8. arXiv: 1910.11877 [astro-ph.GA].
- Erb, Dawn K. et al. (Oct. 2016). “A High Fraction of Ly α Emitters among Galaxies with Extreme Emission Line Ratios at $z \sim 2$ ”. *ApJ* 830.1, 52, p. 52. DOI: 10.3847/0004-637X/830/1/52. arXiv: 1605.04919 [astro-ph.GA].
- Gronke, Max, Mark Dijkstra, Michael McCourt, and S. Peng Oh (Dec. 2016). “From Mirrors to Windows: Lyman-alpha Radiative Transfer in a Very Clumpy Medium”. *ApJ* 833.2, L26, p. L26. DOI: 10.3847/2041-8213/833/2/L26. arXiv: 1611.01161 [astro-ph.GA].
- Mesinger, Andrei et al. (Jan. 2015). “Can the intergalactic medium cause a rapid drop in Ly α emission at $z > 6$?” *MNRAS* 446.1, pp. 566–577. DOI: 10.1093/mnras/stu2089. arXiv: 1406.6373 [astro-ph.CO].
- Pahl, Anthony J., Alice Shapley, Charles C. Steidel, Yuguang Chen, and Naveen A. Reddy (Aug. 2021). “An uncontaminated measurement of the escaping Lyman continuum at $z \sim 3$ ”. *MNRAS* 505.2, pp. 2447–2467. DOI: 10.1093/mnras/stab1374. arXiv: 2104.02081 [astro-ph.GA].
- Pettini, Max et al. (June 2001). “The Rest-Frame Optical Spectra of Lyman Break Galaxies: Star Formation, Extinction, Abundances, and Kinematics”. *ApJ* 554.2, pp. 981–1000. DOI: 10.1086/321403. arXiv: astro-ph/0102456 [astro-ph].

- Reddy, Naveen A. and Charles C. Steidel (Feb. 2009). “A Steep Faint-End Slope of the UV Luminosity Function at $z \sim 2-3$: Implications for the Global Stellar Mass Density and Star Formation in Low-Mass Halos”. *ApJ* 692.1, pp. 778–803. DOI: 10.1088/0004-637X/692/1/778. arXiv: 0810.2788 [astro-ph].
- Rudie, Gwen C., Charles C. Steidel, Alice E. Shapley, and Max Pettini (June 2013). “The Column Density Distribution and Continuum Opacity of the Intergalactic and Circumgalactic Medium at Redshift $z = 2.4$ ”. *ApJ* 769.2, 146, p. 146. DOI: 10.1088/0004-637X/769/2/146. arXiv: 1304.6719 [astro-ph.CO].
- Shapley, Alice E., Charles C. Steidel, Max Pettini, and Kurt L. Adelberger (May 2003). “Rest-Frame Ultraviolet Spectra of $z \sim 3$ Lyman Break Galaxies”. *ApJ* 588.1, pp. 65–89. DOI: 10.1086/373922. arXiv: astro-ph/0301230 [astro-ph].
- Stanway, E. R. and J. J. Eldridge (Sept. 2018). “Re-evaluating old stellar populations”. *MNRAS* 479.1, pp. 75–93. DOI: 10.1093/mnras/sty1353. arXiv: 1805.08784 [astro-ph.GA].
- Steidel, Charles C. et al. (July 2010). “The Structure and Kinematics of the Circumgalactic Medium from Far-ultraviolet Spectra of $z \sim 2-3$ Galaxies”. *ApJ* 717.1, pp. 289–322. DOI: 10.1088/0004-637X/717/1/289. arXiv: 1003.0679 [astro-ph.CO].
- Steidel, Charles C. et al. (Aug. 2011). “Diffuse Ly α Emitting Halos: A Generic Property of High-redshift Star-forming Galaxies”. *ApJ* 736.2, 160, p. 160. DOI: 10.1088/0004-637X/736/2/160. arXiv: 1101.2204 [astro-ph.CO].
- Steidel, Charles C. et al. (Aug. 2016). “Reconciling the Stellar and Nebular Spectra of High-redshift Galaxies”. *ApJ* 826.2, 159, p. 159. DOI: 10.3847/0004-637X/826/2/159. arXiv: 1605.07186 [astro-ph.GA].
- Steidel, Charles C. et al. (Dec. 2018). “The Keck Lyman Continuum Spectroscopic Survey (KLCS): The Emergent Ionizing Spectrum of Galaxies at $z \sim 3$ ”. *ApJ* 869.2, 123, p. 123. DOI: 10.3847/1538-4357/aaed28. arXiv: 1805.06071 [astro-ph.GA].
- Strom, Allison L. et al. (Feb. 2017). “Nebular Emission Line Ratios in $z \approx 2-3$ Star-forming Galaxies with KBSS-MOSFIRE: Exploring the Impact of Ionization, Excitation, and Nitrogen-to-Oxygen Ratio”. *ApJ* 836.2, 164, p. 164. DOI: 10.3847/1538-4357/836/2/164. arXiv: 1608.02587 [astro-ph.GA].
- Theios, Rachel L. et al. (Jan. 2019). “Dust Attenuation, Star Formation, and Metallicity in $z \sim 2-3$ Galaxies from KBSS-MOSFIRE”. *ApJ* 871.1, 128, p. 128. DOI: 10.3847/1538-4357/aaf386. arXiv: 1805.00016 [astro-ph.GA].
- Trainor, Ryan F. et al. (Dec. 2019). “Predicting Ly α Emission from Galaxies via Empirical Markers of Production and Escape in the KBSS”. *ApJ* 887.1, 85, p. 85. DOI: 10.3847/1538-4357/ab4993. arXiv: 1908.04794 [astro-ph.GA].

- Verhamme, A., D. Schaerer, and A. Maselli (Dec. 2006). “3D Ly α radiation transfer. I. Understanding Ly α line profile morphologies”. *A&A* 460.2, pp. 397–413. DOI: 10.1051/0004-6361:20065554. arXiv: astro-ph/0608075 [astro-ph].
- Weiss, Laurel H. et al. (May 2021). “The HETDEX Survey: The Ly α Escape Fraction from 3D-HST Emission-Line Galaxies at $z \sim 2$ ”. *ApJ* 912.2, 100, p. 100. DOI: 10.3847/1538-4357/abedb9. arXiv: 2103.12126 [astro-ph.GA].

Chapter 5

CONCLUSION

In this thesis, we have presented novel results from observations of the Ly α line – in both absorption and emission – in the circumgalactic medium surrounding galaxies in the Keck Baryonic Structure Survey at $z \simeq 2 - 3$. Figure 5.1 provides a schematic illustration of what has been discovered in this thesis.

We first constructed the KGPS sample with $> 200,000$ independent sightlines that have projected distances $\lesssim 3$ pMpc from the foreground galaxies. The average Ly α absorption shows distinctive spatial and spectral distributions. The apparent Ly α optical depth exhibits a “core” component at $D_{\text{tran}} \lesssim 50$ pkpc and $|\Delta v| < 500$ km s $^{-1}$. At $D_{\text{tran}} \gtrsim 100$ pkpc, the absorption gradually transitions to a diffuse component whose spectral profile broadens as D_{tran} increases. By comparing the observed τ_{ap} map with the projected N_{HI} distribution in the FIRE simulation, we found qualitative agreement. After fitting the observed absorption map to a simple analytic model consisting of outflow, inflow, and Hubble expansion, we found that outflow dominates the HI kinematics at $D_{\text{tran}} \lesssim 50$ pkpc. Accretion flows and Hubble expansion gradually takes over as we move outward, with Hubble expansion becoming dominant at $D_{\text{tran}} \gtrsim 150$ pkpc. Between $\simeq 50 - 150$ pkpc, Ly α absorption exhibits a narrow spectral profile that is consistent with the spectral resolution, where the confluence of outflow, accretion, and Hubble expansion create a caustic-like distortion in the v_{LOS} . By comparing the characteristic outflow velocity with the escape velocity, we also confirmed that the majority of the outflowing HI does not carry enough kinetic energy to escape from the gravitational potential of an NFW halo. Furthermore, by comparing the Ly α absorption profiles as functions of D_{LOS} (assuming pure Hubble expansion) and D_{tran} , we found that the peculiar velocity from inflow and outflow results in significant redshift-space distortion at $D_{\text{tran}} \lesssim 500$ pkpc.

The physical scale of outflows in the CGM is well reflected by the Ly α emission profile in the average CP2D spectrum from the KBSS-KCWI survey. The averaged CP2D spectrum shows a dominant redshifted component with $\Delta v \sim 300$ km s $^{-1}$ and a weaker blueshifted component at $\Delta v \sim -300$ km s $^{-1}$, matching the Ly α spectral profile expected from resonant scattering through a radially outflowing medium.

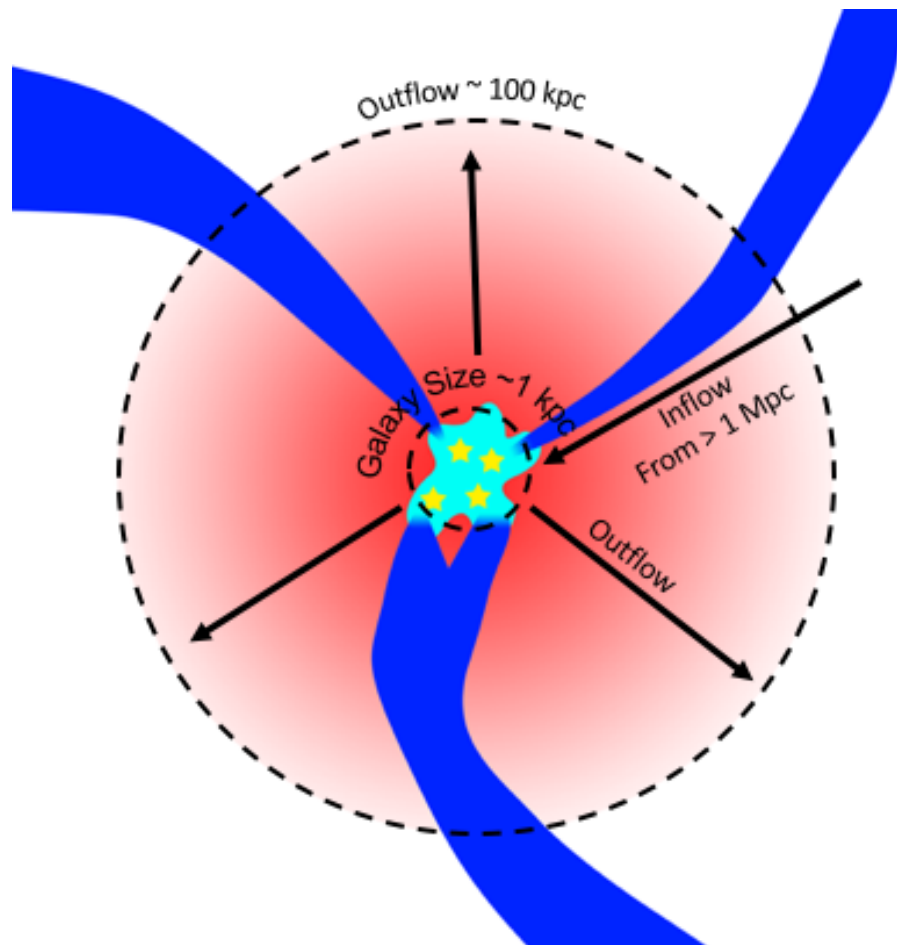


Figure 5.1: A schematic diagram for H I in the CGM around a typical star-forming galaxy at $z = 2 - 3$, as a qualitative summary of the major results of this thesis. Outflows originating from regions of rapid star formation inside galaxies from star-forming regions inside galaxies dominates the H I kinematics in all directions at $D_{\text{tran}} \lesssim 50 \text{ pkpc}$. At $D_{\text{tran}} \gtrsim 100 \text{ pkpc}$, accretion flows and/or ambient CGM that carries H I from $> 1 \text{ pMpc}$, likely in the form of “cold accretion” streams based on recent cosmological simulations, gradually takes over.

This characteristic spectral profile reaches at least $D_{\text{tran}} \simeq 30$ pkpc, suggesting that outflows dominate the CGM kinematics within this physical scale.

Perhaps most intriguingly, through Ly α absorption, we found that the average spectral profile is asymmetric relative to the galaxy systemic velocity at $50 \lesssim D_{\text{tran}}/\text{pkpc} \lesssim 200$. While the detection is marginal (2σ), we hypothesized that emission filling from the foreground Ly α halo may quantitatively explain the asymmetry. However, this suggests that Ly α emission at this distance range is dominated by blueshifted emission, which is consistent with the distance where outflow-dominant kinematics transitions to inflow-dominant. In fact, we observed that the blueshifted emission component in the average CP2D spectrum becomes comparable to the redshifted component at $D_{\text{tran}} \gtrsim 30$ pkpc, and may even be stronger than the redshifted component at $D_{\text{tran}} \gtrsim 40$ pkpc, though more comprehensive understanding of the systematic uncertainty is required for confirmation in the future.

For 59 galaxies in the KBSS-KCWI survey where high-resolution imaging data were available, we also compared the mean Ly α emission profile as a function of its azimuthal orientation relative to the projected galaxy major axis. We found that at $D_{\text{tran}} \lesssim 30$ pkpc, the Ly α emission is statistically indistinguishable, both spatially and spectrally, along the galaxy projected major and minor axes. This suggests that, statistically, the kinematics and spatial distribution of the Ly α scattering medium (dominated by outflows) is uncorrelated with the apparent morphology of the host galaxy starlight. Meanwhile, we found that the blueshifted component of Ly α emission is marginally stronger along galaxy minor axes for only for galaxies with relatively weak Ly α emission, suggesting the appearance of a weak directional dependence of Ly α emission when the overall Ly α escape fraction is low. This may indicate that galaxies with weaker Ly α emission possess more developed rotational structure, which allows more Ly α photons to escape from the minor axis.

Using preliminary results from 110 star-forming galaxies with $2 \leq z \leq 3.5$ in the KBSS-KCWI survey, we also found that at $D_{\text{tran}} \lesssim 30$ pkpc, Ly α emission in the CGM is affected both by the ability of host galaxies to produce Ly α photons and, once produced, by the availability of pathways for scattered photons to escape. However, the spatial profile of Ly α emission in the “outskirts” at $D_{\text{tran}} \sim 30$ pkpc, appears to be less affected by the host galaxy properties; such behavior suggests that once Ly α photons manage to find pathways through the most optically-thick regions of the inner CGM, the properties of the CGM scattering medium becomes nearly independent of the properties of the central host galaxy.

While this thesis offers a significant update to our understanding of the distribution and kinematics of H I in the CGM at $z \simeq 2-3$, our picture remains far from complete. Among the unresolved issues that are closely related to this thesis: 1) The details of the mapping between the spatial and spectral behavior of extended Ly α emission and the kinematics and geometry of H I in the CGM. Quantitative understanding of outflow and accretion rates will require relatively sophisticated, spatially resolved radiative transfer models. 2) The detailed structure, kinematics, and metal content of outflowing material near its launch point in the ISM and inner CGM of host galaxies will require relatively high resolution, high sensitivity observations of absorption along discrete lines of sight to multiple background objects with close angular offsets from the galaxy of interest; KCWI observations that are already in hand can be used as a starting point to address this issue. 3) The absorption line studies, particularly those sensitive to low and high-ionization metallic species, are needed to disentangle ambiguities inherent to Ly α radiative transfer, and to more closely probe the multiphase CGM and its connection to host galaxy properties. Both the KGPS and KBSS-KCWI datasets can be used effectively for this purpose. 4) From a technical perspective, to reach a reliable Ly α detection at $D_{\text{tran}} \gtrsim 50$ pkpc, or SB detection limit of $\lesssim 10^{-19}$ erg s $^{-1}$ cm $^{-2}$ arcsec $^{-2}$, requires a significant reduction of systematic uncertainties in background subtraction for reduced KCWI data cubes, which can be achieved with more sophisticated background subtraction algorithm. 5) Ionized gas - particularly the component that is at out of equilibrium at temperatures intermediate between the virial temperature of $T \sim 10^6$ K and that of quiescent photoionized gas at $T \sim 10^4$ K would provide the most direct link the feedback processes in the forming galaxies. Extremely sensitive KCWI observations of CGM emission such as those in the KBSS-KCWI survey offer the best prospect for the foreseeable future. 6) Resonance lines of ionic species other than Ly α , and their closely related non-resonance emission lines from the same excited state to excited fine structure levels just above the ground state (notably low-ionization metallic lines of Si II, C II for galaxies in the redshift range of our sample) – can be used to trace the run of optical depth with galactocentric distance using techniques similar to those described in this thesis.

All of the issues described above can be pursued using the same KBSS-KCWI dataset compiled for this thesis, toward a better understanding of the physics of feedback, accretion, and outflows in the CGM of forming galaxies.

Appendix A

THE STANDARD KBSS-KCWI REDUCTION PROCEDURE

The observations of the KBSS-KCWI survey are conducted using the Medium slicer (FoV: $\sim 16'' \times 20''$; spatial sampling: $0''.69 \times 0''.29$) and the BL VPH grating ($R \sim 1650$). For each pointing, the typical total integration time is ~ 5 hours. The exposure time of individual exposures is 20 min. Between exposures, a rotation of 10 – 90 degrees is applied, in order to regain some spatial resolution across the slicers. The standard data reduction procedure for the KBSS-KCWI survey was designed to take advantage of the observational strategy and the survey depth to generate multi-level data products with high quality. The data output consists of three levels, as shown in Figure A.1.

A.1 Level 1: Improved Data Reduction Pipeline

As of the writing of this thesis, the Level 1 data product of the KBSS-KCWI survey is built upon the standard IDL data reduction pipeline (DRP)¹ that re-assembles the 2D spectra of each slice into a 3D data cube for each exposure. The standard DRP procedures include cosmic-ray removal, overscan subtraction, scattered light subtraction, wavelength calibration, flat-fielding, sky-subtraction, differential atmospheric refraction (DAR) correction, and flux calibration. Details of these standard procedures are included in Chen et al. (2021). Aside from the standard DRP procedures, we developed additional methods to achieve higher reduction quality.

The standard sky-subtraction procedure in the DRP assumes that, except when an astronomical object is present, the sky spectrum in each frame is the same in all spaxels after flat-fielding. However, scattered light in sky flats and/or science exposures often have a small amount (~ 0.5 ADU) of low-frequency residual, which can be noticed when multiple wavelength layers are binned for a single frame (as shown in Figure A.2). Furthermore, when a bright object is in the FoV, it often leaves a trail of scattered light along the slices that the object is present. We introduced an additional step after sky subtraction to remove these residual signals. We construct a median-filtered data cube using a running 3D boxcar filter. The typical dimensions of the filter are 100 \AA (100 pixels) in the wavelength direction, 16 pixels ($4''.6$) along slices, and 1 pixel ($0''.69$) perpendicular to the slices, with the

¹<https://github.com/Keck-DataReductionPipelines/KcwiDRP>

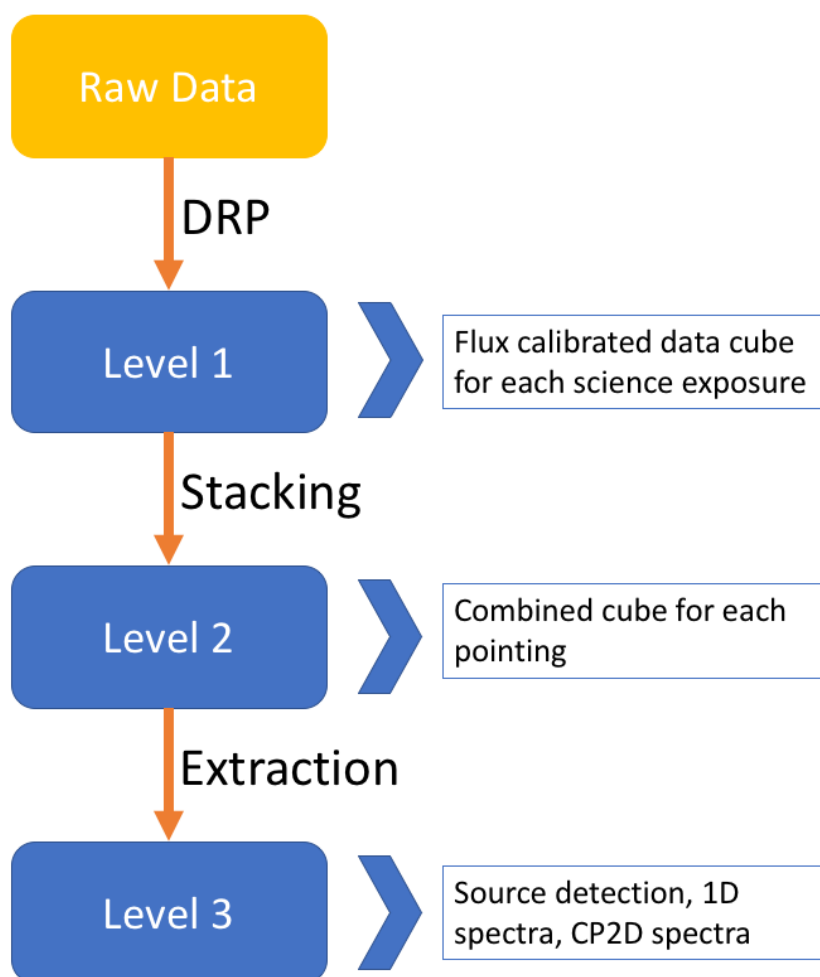


Figure A.1: Flowchart of the three-level data products of the KBSS-KCWI survey.

last ensuring slice-to-slice independence. Existing objects in the FoV, appearing either as continuum objects in the pseudo-white-light image, or as bright emission-line objects in each wavelength layer, are masked. The values of the masked pixels in the median-filtered cube are linearly interpolated from the nearby unmasked pixels. This median-filtered cube is subtracted from the science cube. As shown in Figure A.2, in the new data cube, the residual background and scattered light from bright objects can be removed using this method.

The standard DRP only uses one spectrophotometric standard star for flux calibration for each frame. This might introduce additional uncertainty in flux calibration, because a single exposure of a standard star might be affected by fog or cirrus that

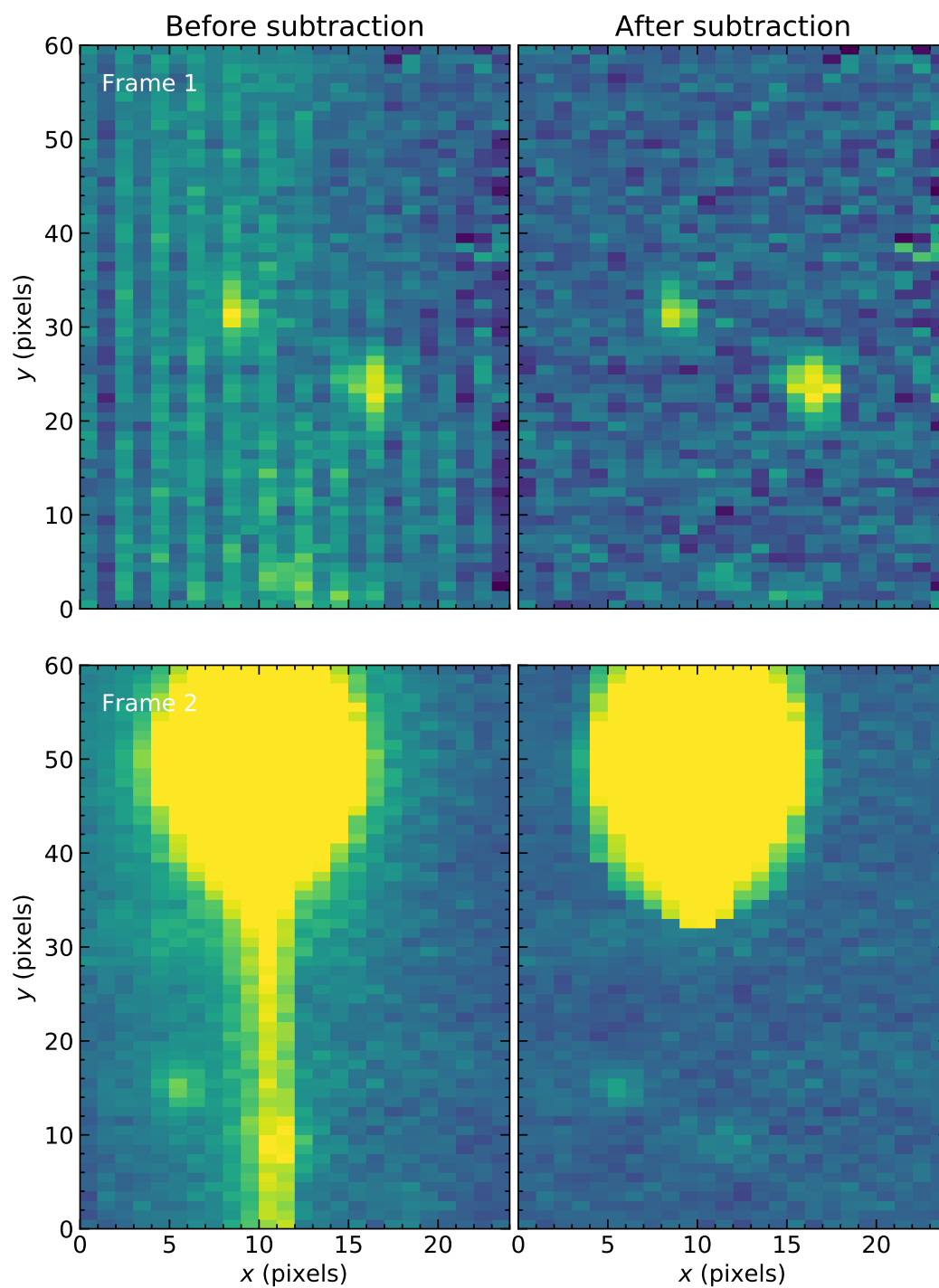


Figure A.2: Pseudo-white-light images before (*left*) and after (*right*) subtracting the median-filtered cube. This procedure is capable of removing low-frequency background (*top*) residuals and scattered light from bright objects (*bottom*).

can lower the atmospheric transmissivity. To achieve higher quality in flux calibration, we use the combined inverse-sensitivity curve (ISC) from every standard-star exposure in consecutive observing nights. Exposures with particularly low ADU counts (or high ISC) are discarded. Figure A.3 shows an example of the individual and combined ISC.

The final Level 1 product is the 3D data cubes of individual exposures. For each exposure, three data cubes: science (in the unit of flux per pixel), variance, bad-pixel mask cubes are generated.

A.2 Level 2: Stacked Data Cube for Each Pointing

Following the data cube generated by improved DRP for each exposure, our Level 2 data product combines the individual frames for each pointing. This step consists of the following procedures: aligning data frames in the spatial directions, stacking, and astrometry correction. Most of the procedures have been included in CWITools (O’Sullivan and Chen, 2020).

For a single pointing, to achieve ~ 5 -hour total integration time, the observations are often distributed in multiple nights, in which the target field needs to be reacquired for every night. Furthermore, when we rotate the FoV between exposures, the guide star needs to be reacquired after every rotation. This causes slight random offsets ($\sim 10''$) between the individual exposures that are not recorded in the world coordinate system (WCS). We first resample the pseudo-white-light images to a common grid with $0''.3 \times 0''.3$ pixel size based on the original WCS. We then correct this random offset by searching for the local maximum of the cross-correlated pseudo-white-light images of two cubes. A manually drawn alignment box is used for the cross-correlation. Figure A.4 shows an example. For one point, all frames are aligned to the first cube. The alignment precision is 0.1 pixels (or $0''.03$).

Before stacking the data cubes, we compare the flux values of pixels that are 2.5σ above the sky background at the same location but from different exposures, in case the atmospheric extinction is affected by passing cloud or fog. A correction factor, which is the median ratio between the pixels in other frames and the frame that the flux is significantly lower, is multiplied by the frame. After the necessary correction, each data cube is resampled to a common grid with $0''.3 \times 0''.3 \times 1 \text{ \AA}$ pixel size. The resampling is conducted using the “drizzle” algorithm, which is capable of regaining spatial resolution from undersampled pixels without introducing additional pixel correlation (Fruchter and Hook, 2002). The “drizzle factor” we used is 0.8. Ideally,

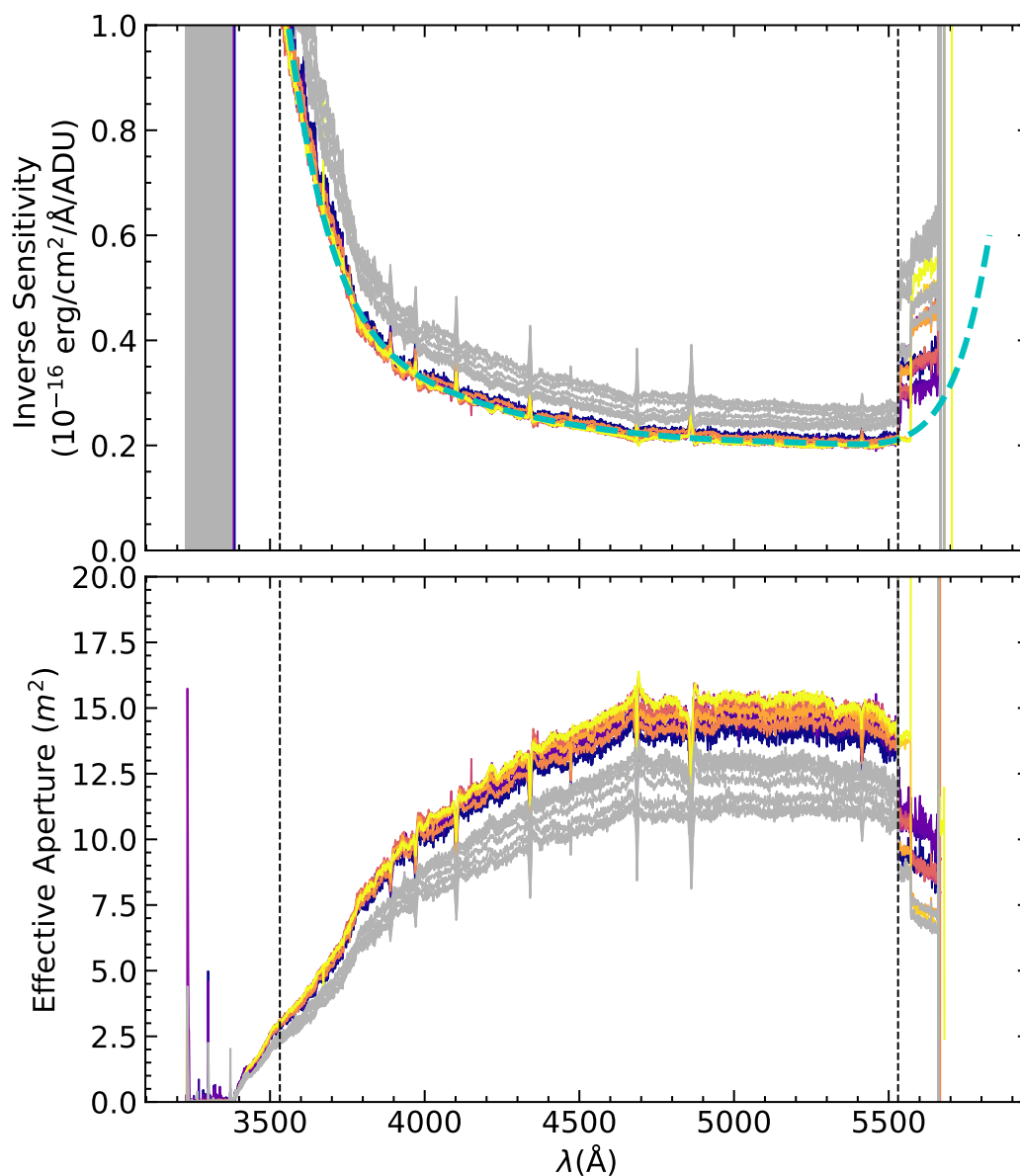


Figure A.3: The inverse sensitivity (*top*) and effective aperture curves of (*bottom*) measured from spectrophotometric two standard stars (Feige 34 and Feige 110). This figure includes data from three consecutive observing nights in November 2019. The colored curves are included in the final calibration. The gray ones were observed at either the end of the first night or the beginning of the second night when it was cloudy, and are discarded. The dashed cyan curve in the top panel is modeled ISC from all curves observed in clear conditions. The vertical dashed curves mark the boundary generated by the IDL DRP, in which the reduction is reliable.

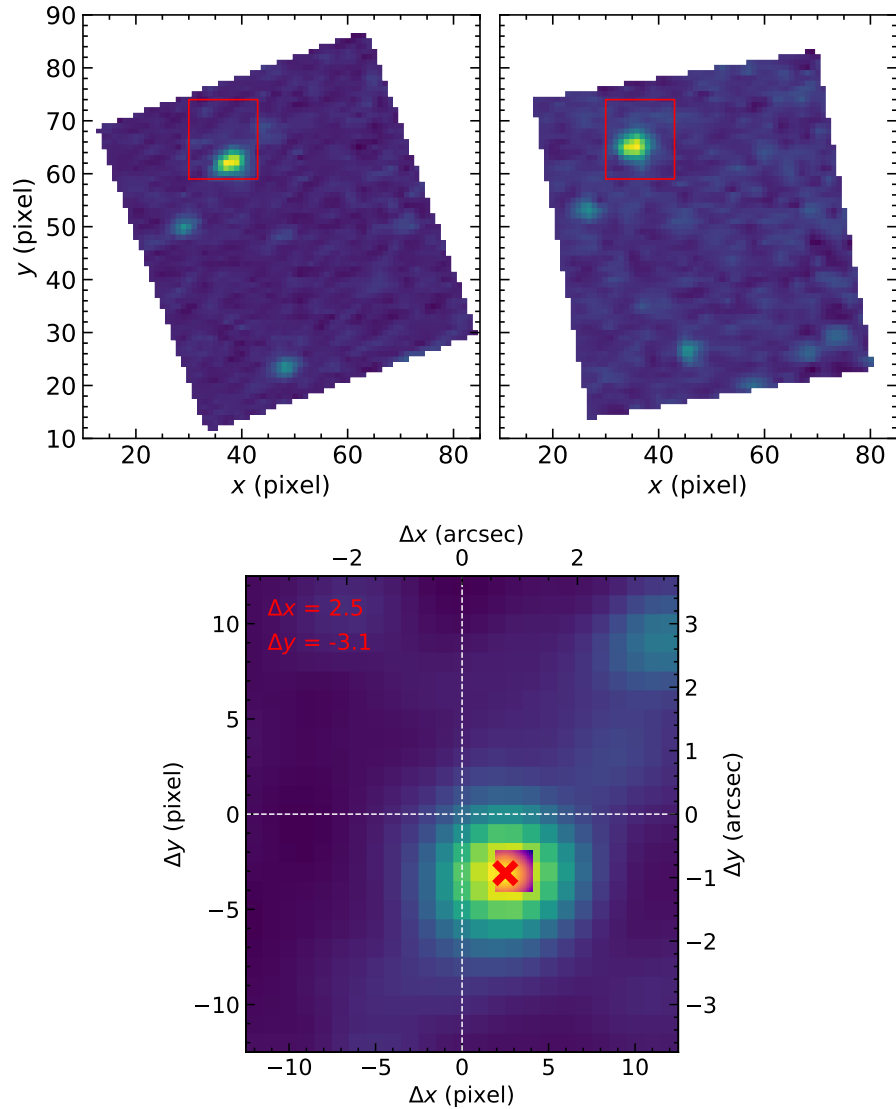


Figure A.4: *Top*: Pseudo-white-light images of two exposures on the same pointing. The red box marks the location of the alignment box, in which the cross-correlation is calculated. *Bottom*: The cross-correlation map of two images. The red cross marks the location of the local maximum, which is the relative offset between the two exposures.

to achieve the optimal S/N in the final stack, one would weight the pixels in the individual frames by inverse variance. However, the *caveat* is that the variance cubes are estimated from the sky background, assuming the noise is dominated by the sky background, and the sky flux itself is affected by Poisson noise. This causes the pixels with lower sky values to obtain higher weight, and the sky background in the final stack is oversubtracted. Therefore, the final stacking procedure uses the mean stack with bad pixels masked. For each frame, a weight of,

$$w_i = t_{\text{exp}} / f_{\text{ext}}^2, \quad (\text{A.1})$$

where t_{exp} is the exposure time, and f_{ext} is the extinction correction factor we mentioned earlier, is applied in the stacking process, in order to optimize the S/N ratio.

Finally, we register the stacked cube for each pointing to a known astrometric solution using a similar method to the alignment procedure. The reference images were obtained previously as part of the KBSS survey.

A.3 Level 3: Extracting Signal

The most advanced Level 3 data product consists of signals extracted from the combined data cube for further analyses. These procedures include: continuum object detection, the extraction of 1D spectra, and the extraction of cylindrically projected 2D (CP2D) spectra.

Before extracting the signals, we need to detect sources in the stacked data cubes. As of the time of writing this thesis, the source detection is only conducted on pseudo-white-light images data cube using SExtractor. The detection threshold is set to 1.5σ . The deblending algorithm is applied with the number of deblending of 32, and a contrast parameter of 0.005. Therefore, our source-detection only includes continuum-bright objects. Source detection of emission line objects with no continuum emission will be conducted in the future.

Using the segment map generated by SExtractor, we extract the 1D spectrum of each continuum object inside a segmented aperture. Before combining, the spaxels are weighted by the continuum flux squared in the pseudo-white-light image (F_{cont}^2) for optimal extraction (Horne, 1986). Weighting the flux, however, causes the unit of the 1D spectrum to be arbitrary. Therefore, we normalize the extracted 1D spectrum to the total flux in the aperture from the white-light image without weighting. This method, which optimizes the S/N of the continuum, also ensures that the extracted

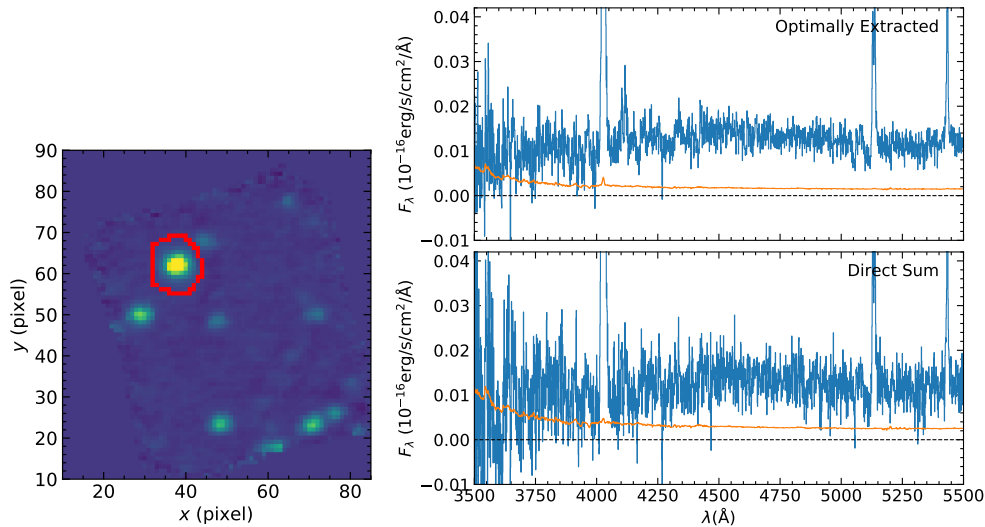


Figure A.5: *Left*: Pseudo-white-light image of a pointing in the KBSS-KCWI survey. The red circle marks the boundary, from which the 1D spectrum is extracted. The object in it is Q0100-BX172. The boundary is drawn from the segment map generated by SExtractor. *Right*: Comparison between the optimally extracted 1D spectrum (top) and a direct sum of the spaxels in the aperture (bottom). The direct sum is significantly noisier than the optimally extracted spectrum.

1D spectra are close to what is extracted from slit spectrographs. The error spectra are propagated using the variance cubes. However, a factor of 1.05 is multiplied by the propagated error spectra. This factor is to account for the pixel covariance and is estimated using the method similar to Husemann et al. (2013), Law et al. (2016), and O’Sullivan et al. (2020). In short, it compares the standard deviation of a series of signals extracted from apertures with the same size on the blank sky, to the median propagated error from the same aperture. Figure A.5 shows an example of the optimally extracted spectrum compared to using a direct sum.

The CP2D spectra, introduced in Chen et al. (2021), can be used to demonstrate the statistical Ly α emission in the CGM as a function of galactocentric distance D_{tran} . We extract the CP2D spectra by resampling the data cubes onto a 3D cylindrical grid [position angle (PA), D_{tran} , and wavelength] using cubic interpolation. The cube is then averaged in the position angle direction, so that the final 2D spectrum is in the space of D_{tran} and wavelength. The center of the galaxies is determined by fitting a 2D Gaussian profile to the continuum image with a positional error $\lesssim 0''.01$. Examples of CP2D spectra can be found in Chapters 3 and 4.

References

- Chen, Yuguang et al. (Apr. 2021). “The KBSS-KCWI Survey: The connection between extended Ly α halos and galaxy azimuthal angle at $z \sim 2-3$ ”, arXiv:2104.10173. (in press with MNRAS), arXiv:2104.10173. arXiv: 2104.10173 [astro-ph.GA].
- Fruchter, A. S. and R. N. Hook (Feb. 2002). “Drizzle: A Method for the Linear Reconstruction of Undersampled Images”. *PASP* 114.792, pp. 144–152. DOI: 10.1086/338393. arXiv: astro-ph/9808087 [astro-ph].
- Horne, K. (June 1986). “An optimal extraction algorithm for CCD spectroscopy.” *PASP* 98, pp. 609–617. DOI: 10.1086/131801.
- Husemann, B. et al. (Jan. 2013). “CALIFA, the Calar Alto Legacy Integral Field Area survey. II. First public data release”. *A&A* 549, A87, A87. DOI: 10.1051/0004-6361/201220582. arXiv: 1210.8150 [astro-ph.CO].
- Law, David R. et al. (Oct. 2016). “The Data Reduction Pipeline for the SDSS-IV MaNGA IFU Galaxy Survey”. *AJ* 152.4, 83, p. 83. DOI: 10.3847/0004-6256/152/4/83. arXiv: 1607.08619 [astro-ph.IM].
- O’Sullivan, Donal and Yuguang Chen (Nov. 2020). “CWITools: A Python3 Data Analysis Pipeline for the Cosmic Web Imager Instruments”. *arXiv e-prints*, arXiv:2011.05444, arXiv:2011.05444. arXiv: 2011.05444 [astro-ph.IM].
- O’Sullivan, Donal B. et al. (May 2020). “The FLASHES Survey. I. Integral Field Spectroscopy of the CGM around 48 $z \simeq 2.3-3.1$ QSOs”. *ApJ* 894.1, 3, p. 3. DOI: 10.3847/1538-4357/ab838c. arXiv: 1911.10740 [astro-ph.GA].